Hadron-Quark Phase Transitions in Hybrid Stars and Core-Collapse Supernovae

Inauguraldissertation

zur
Erlangung der Würde eines Doktors der Philosophie
vorgelegt der
Philosophisch-Naturwissenschaftlichen Fakultät
der Universität Basel

von

Oliver Philipp Heinimann

aus Zunzgen, Baselland

Basel, 2017

Genehmigt von der Philosophisch-Naturwissenschaftlichen Fakultät
auf Antrag von

Prof. Dr. Friedrich-Karl Thielemann
Fakultätsverantwortlicher

PD Dr. Matthias Hempel
Dissertationsleiter

Prof. Dr. Tomoya Takiwaki
Korreferent

Basel, den 21. März 2017

Prof. Dr. Martin Spiess

(Dekan)

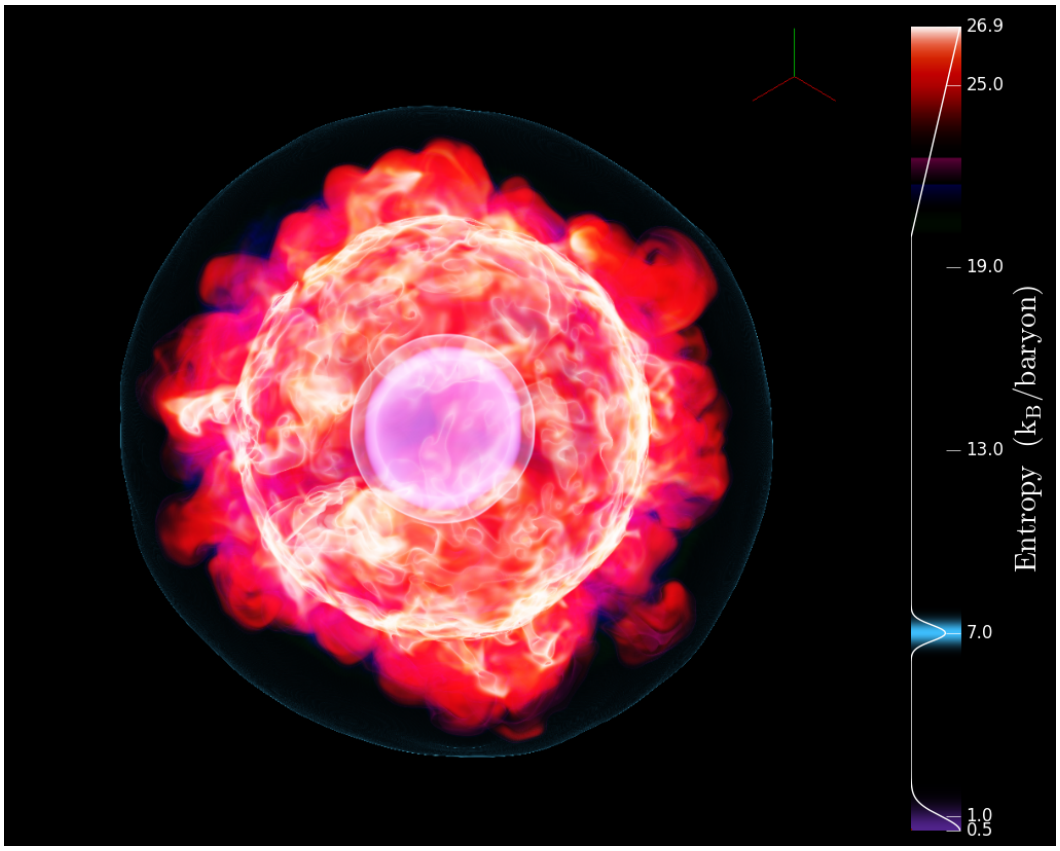

Volume-rendered entropy profile of ELEPHANT using the spherical-restart technique and applying the hybrid supernova equation of state BASQUARK. After the collapse of the protoneutron star, the newly formed shock wave (yellow) detached from the protoneutron star in the center (purple) and moves through the convection zone towards the standing accretion front (blue).

Dedicated to my parents Barbara and Stephan,
my grandparents, and my godfather Hampä

Abstract

Extreme temperatures and densities in core-collapse supernovae and one of their possible remnants, the so-called neutron stars, are likely to favor the appearance of new degrees of freedom such as hyperons and/or quark matter. This work is dedicated to the investigation of the hadron-quark phase transition in core-collapse supernovae and cold neutron stars. To this day, only a couple of supernova equations of state that consider quark matter have been developed and none of them fulfills the observational 2 $M_\odot$ neutron star mass constraint [56, 11, 70]. The phase transition from hadronic to quark matter can have an interesting impact on the post-bounce evolution of core-collapse supernovae: The phase transition is able to induce a collapse of the protoneutron star which ultimately can trigger an explosion, as shown in spherically-symmetric simulations [174, 65]. So far, this scenario has not been investigated in multi-dimensional core-collapse supernova simulations.

In the first part of this work, we analyze cold hybrid stars[1] by the means of a systematic parameter scan for the phase transition properties. The hadronic phase is described by the state-of-the-art supernova equation of state HS(DD2) and the quark phase by an equation of state with a constant speed of sound (CSS). Choosing a quark matter speed of sound of $c^2_{\mathrm{QM}} = 1/3$, we find promising cases which meet the 2 $M_\odot$ criterion and are interesting for core-collapse supernova explosions. We show that the very simple CSS equation of state is transferable into the well-known thermodynamic bag model, important for application in core-collapse simulations. Additionally, the occurrence of reconfinement and multiple phase transitions is discussed. The influence of hyperons in our parameter scan is studied as well. Including hyperons, no change in the general behavior is found, except for overall lower maximum masses. In both cases (with and without hyperons) we find that quark matter with $c^2_{\mathrm{QM}} = 1/3$ can increase the maximum mass only if reconfinement is suppressed or if quark matter is absolutely stable. The systematic parameter study is completed with an analogous analysis using $c^2_{\mathrm{QM}} = 1$, the maximum value to be still consistent with special relativity. The higher speed of sound leads to more parameter configurations consistent with the 2 $M_\odot$ criterion. Increasing the speed of sound to $c^2_{\mathrm{QM}} > 1/3$ is therefore an interesting case which increases the possibilities when constructing a future hybrid supernova equation of state.

On the basis of the best guess configuration obtained in the parameter scan for $c^2_{\mathrm{QM}} = 1/3$, we construct the new hybrid supernova equation of state BASQUARK. BASQUARK uses HS(DD2) for the hadronic part and a bag model to describe quark matter. The detailed analysis of BASQUARK with the sophisticated spherical

[1] Hybrid stars are neutron stars that contain quark matter.

supernova code AGILE-BOLTZTRAN shows an explosion for a 15 $M_\odot$ progenitor. Hence, BASQUARK is the first hybrid supernova equation of state that fulfills the 2 $M_\odot$ neutron star constraint and is known to trigger an explosion in spherical symmetry.

The second part of this work is dedicated to the analysis of BASQUARK in the 3D core-collapse supernova code ELEPHANT. To ensure an effective analysis at late post-bounce times without consuming a vast amount of computational resources, we develop a new method called the *spherical restart method*. This method allows us to perform a separate spherical AGILE-IDSA simulation, which is computationally very cheap, map its profile into ELEPHANT, and continue the simulation in three dimensions. The method shows that the obtained 3D profiles imitate well the profiles obtained in a consistently run simulation. If the collapse behavior of ELEPHANT up to bounce is considered in AGILE-IDSA, the spherical restart method is able to reproduce profiles that are on spherical average almost identical to such, obtained in consistently run ELEPHANT simulations. This allows the opportunity to increase the resolution for more detailed investigations.

Finally, we apply BASQUARK in ELEPHANT and use a 15 $M_\odot$ and a 40 $M_\odot$ progenitor. Both progenitors explode in spherical symmetry due to the phase-transition induced collapse of the protoneutron star. In initial tests, ab-intio calculations with ELEPHANT are executed with a low resolution of 2 km to proceed fast to the relevant post-bounce times. Both progenitors ultimately explode due to oscillations of the protoneutron star which are probably an artifact of the low resolution. This mechanism is not expected at higher resolution. The 15 $M_\odot$ progenitor does not show any indication of a collapse of the protoneutron star, but seems to be powered by the delayed-neutrino driven mechanism. In turn, the 40 $M_\odot$ progenitor shows indications of a failed collapse of the protoneutron star. By the use of the spherical restart method, the simulation is spherically restarted before the suspected collapse, using a resolution of 2 km, 1 km, and 500 m. The 2 km run indicates once more collapse features, but fails due to stability issues caused by the low resolution. Using a resolution of 1 km ultimately shows a collapse of the protoneutron star which results in the explosion of the star. 500 m resolution confirms the results using 1 km resolution and additionally helped the convection to develop. This is the first time, a phase-transition induced collapse and the succeeding explosion is simulated in a three-dimensional core-collapse supernova. We find that resolution is crucial for a correct description of quark matter in the center of the protoneutron star. In the near future, neutrino-quark rates and the IDSA treatment have to be investigated in more detail.

The results obtained with BASQUARK in ELEPHANT are preliminary yet. Nevertheless, this work opens the door into the new field of multi-dimensional core-collapse supernova simulations that consider quark matter and gives some clear indications on the subjects to be investigated in the future.

Acknowledgement

I would like to express my gratitude to a couple of persons. My thanks go to

- PD Dr. M. Hempel for his supervision as my PhD advisor. I am very grateful for his constant and steady support, the close supervision, as well as his encouragement during the three years of my PhD.
- Prof. Dr. F.-K. Thielemann for co-supervising my PhD and providing me with the opportunity to do this thesis in the best working environment. He always saw my work in the bigger picture and never failed to give good advice.
- Prof. Dr. M. Liebendörfer for unofficially co-supervising my PhD as my third advisor. Without hesitation, he introduced me into the world of 3D core-collapse supernova simulations and always answered my numerous questions.
- Prof. Dr. T. Takiwaki for his willingness to be the external expert of my dissertation. I will also not forget his commitment when organizing the "Many Riddles of Core-Collapse Supernovae" workshop at NAOJ in Tokyo where he gave me the opportunity to present my work to a very proficient audience.
- Dr. R. Cabézon and Dr. T. Kuroda for sharing the outpost office on the first floor with me. It was a great time with a lot of serious and sometimes not so serious discussions.
- K. Ebinger, J. Reichert, M. Frensel, and B. Wehmeyer for granting me asylum in their office in case of the need of a coffee/sandwich break and sharing the honor of representing the last PhD students of the Astroparticle Group in Basel. I appreciate the time with you and your friendship.
- Dr. A. Lohs for sharing the room with me at conferences, the great work and time together.
- Dr. K.-C. Pan for his steady support especially when it came down to compiling and visualization questions.
- the other past members of the Astroparticle group of the University of Basel for the cordial work ambiance.
- E. Cazzato, F. Cefála, and O. Müller who started studying physics with me and also ended up doing a PhD in theoretical Physics, for their friendship and the good time together.

- C. Ghellert and the other CSCS staff members who granted us great support with our code ELEPHANT.
- my family for their constant, altruistic support.
- my girlfriend Pascale for her constant and lovely support, and her patience with me while I was writing this thesis.

Contents

1 Introduction

> *Is this the real life, is this just fantasy*
> *Caught in a landslide, no escape from reality*
> *Open your eyes, look up to the skies and see*
>
> — **Freddie Mercury, Queen**
> Bohemian Rhapsody

1.1 Preface and motivation

Core-collapse supernovae are among the most energetic explosions observed in the Universe, even outshining an entire galaxy for a brief instant. Their possible remnants, so-called neutron stars, represent the densest stable objects (beside black holes) known. The description of matter under such extreme conditions is a demanding and still unsolved problem in which physicists around the world engage. The high densities and neutron-rich conditions reached in core-collapse supernovae and neutron stars are not accessible in terrestrial experiments. With increasing densities the description of matter becomes more uncertain. New degrees of freedom besides nucleons, such as hyperons and/or quark matter, can appear. The recent discoveries of neutron stars with masses around 2 $M_\odot$ [56, 11, 70] represent a strong constraint on the appearance and impact of the additional degrees of freedom on the equation of state (EOS), used to describe matter.

Another big challenge in astrophysics represents the *supernova problem*; the question why and how core-collapse supernovae take place. A lot of efforts have been done towards a solution of this problem during the last couple of decades, but a complete and consistent answer is missing up to this day. The most established and well-investigated explosion mechanism is the delayed neutrino-driven mechanism [48, 24]. Another mechanism for core-collapse supernovae is due to the appearance of quark matter in the protoneutron star which can have crucial impact on the dynamical evolution of the star. Sagert et al. [174] have shown in one-dimensional simulations that the appearance of quark matter can cause a collapse of the protoneutron star to a more compact configuration, which results in a second shock wave that travels outwards. This second shock wave can revive the stalled first shock and induce an explosion. This scenario is known as the QCD phase-transition mechanism. High explosion energies around and above 10^{51} erg [174] make this scenario especially interesting for further investigation. However, the hybrid equations of state applied in [174] have maximum masses much below 2 $M_\odot$. In the subsequent

works exploring this scenario [174, 68, 65, 66, 69, 150, 67] explosions could not be obtained if the maximum mass was sufficiently high.

To this day, only a few supernovae equations of state that consider quark matter (called hybrid supernovae equations of state) exist ([174, 65, 67, 69, 149]). Their phase-transition parameters were not chosen on the basis of a systematic investigation. The hadronic part of the hybrid equations of state are also in conflict with some results gained from nuclear experiments [153]. The hybrid supernova equations of state have only been tested on a few progenitors in one-dimensional simulations. A systematic progenitor investigation and an application in a multi-dimensional core-collapse supernova simulation are completely missing so-far.

Based on the introductory words above, this thesis has two main purposes: First, it shall provide a detailed analysis on possible phase-transition configurations in hybrid stars which are useful to construct future hybrid supernova equations of state. The best guess configuration will be used to construct a new hybrid supernova equation of state. This equation of state is going to be the first hybrid supernova equation of state that is in agreement with most experimental and observational constraints. Additionally, first results of its application in the spherical core-collapse supernova code AGILE-BOLTZTRAN will be shown. Second, we aim to show first results of 3D core-collapse supernova simulations considering quark matter. This has never been done before and is therefore completely new territory.

1.2 Organization of this thesis

This thesis is essentially structured in two parts. Part I consists of Chapters 2 - 7:

- Chapter 2 gives a general overview on the topic of supernovae, i.e. core-collapse supernovae and their explosion mechanisms.
- In Chapter 3, a short introduction on cold neutron stars i.e. on hybrid stars is provided. A special emphasis is put on the classification of hybrid stars and their connection to the QCD phase-transition explosion mechanism.
- In Chapter 4, a broad introduction on the equations of state used in this work is provided.
- Chapter 5 is devoted to the systematic analysis of the phase transition in cold hybrid stars.
- Chapter 6 deals with the newly constructed hybrid supernova equation of state with the name BASQUARK and its application in the spherical supernova code AGILE-BOLTZTRAN.
- Chapter 7 concludes the results gained up to this part.

Part II deals with the 3D supernova code ELEPHANT and the application of BASQUARK. It consists of Chapters 8 - 11.

- In Chapter 8, the theoretical background of the supernova code ELEPHANT is outlined. A special emphasis is put on the upgrades needed for simulations with quark matter.
- Chapter 9 deals with a newly developed method called the spherical-restart method. This method allows us to map a spherical profile from an AGILE-IDSA run into ELEPHANT and to continue the evolution in three dimensions.
- In Chapter 10, the hybrid supernova equation of state BASQUARK is used in ELEPHANT. This is the first time quark matter is considered in a core-collapse supernova simulation. We discuss the preliminary results obtained in ab-initio simulations and first results concerning a second collapse using the spherical restart technique to increase resolution.
- Chapter 11 concludes the results obtained in part II.

Finally, in Chapter 12 an overall conclusion, summary, and outlook is provided on the entire work presented in this thesis.

Please note that parts of this thesis are reproduced from the author's work which has been published as [87]

> Oliver Heinimann, Matthias Hempel, and Friedrich-Karl Thielemann:
> *Towards generating a new supernova equation of state:*
> *A systematic analysis of cold hybrid stars*
> Phys. Rev. D **94**, 103008 (2016)

Core-Collapse Supernovae

2

> *In the face of overwhelming odds, I'm left with only one option, I'm gonna have to science the shit out of this.*
>
> — **Mark Watney**
> The Martian

2.1 Historical and general remarks on supernovae

The term *supernovae* was introduced in 1934 by the two astronomers Baade and Zwicky. They realized that supernovae are by far more luminous and rarer than the, in certain stellar environments, very frequently observed *novae* [16, 15]. By this term Baade and Zwicky named a phenomenon which was already observed and documented as early as the second century A.D. by Chinese astronomers: *Guest stars* appeared for a limited time in the sky and faded away later [139, 23]. Nevertheless, it took centuries until it was understood that such an event remarks the violent death of a star whose brightness can outshine a whole Galaxy for a limited time. Within the last millennium, a total of six supernova events occurring in our galaxy and one in the Large Magellanic cloud were witnessed and recorded (see Tab. 2.1, published in [33]). It is believed that this historical number only represents around 20 % of the total number of galactic supernova events occurred during the last millennium. This can be justified by the fact that the *"majority of the supernovae was shrouded from the view by the dust that pervades the Milky Way"* [33]. Today, it is believed that there is around one supernova explosion in the universe every second and around one every 30-50 years in our galaxy [33].

Supernovae are classified into two physically fundamental different types: *core-collapse* and *thermonuclear* supernovae. Thermonuclear supernovae are not part of this thesis. It is believed that they arise from carbon-oxygen white dwarfs which accrete matter from a binary companion. They explode as soon as the Chandrasekhar mass limit for a degenerate electron gas is reached (~ 1.4 $M_\odot$). Through the thermonuclear nature of the explosion, no remnant is left over after the violent explosion [181].

In this thesis core-collapse supernovae are the objects, respectively events, of interest. In stars with masses $\gtrsim 8$ $M_\odot$ all nuclear burning stages up to iron are undergone. No elements beyond the iron group are obtained through nuclear fusion since the

Supernova	Year (AD)	Distance (kpc)	Peak visual magnitude
SN1006	1006	2.0	-9.0
Crab	1054	2.2	-4.0
SN 1181	1181	8.0	?
RXJ 0852-4642	$\sim$1300	$\sim$0.2	?
Tycho	1572	7.0	-4.0
Kepler	1604	10.0	-3.0
Cas A	$\sim$1680	3.4	$\sim$6.0?
SN1987A	1987	50$\pm$5	3.0

Tab. 2.1: "Historical" compilation of the observed supernovae in the Milky Way and the Large Magellanic Cloud during the last millennium. The table and information of this caption was published in [33]. Note that SN1987A exploded in the Large Magellanic Cloud which is one of the nearby satellite galaxies. Additionally included is RX J0852-4642, a recent supernova remnant whose recent birth went unrecorded, most probably since it was found in the Southern Hemisphere. Cas A, another supernova remnant, was born in historical times but the observation of the event is only based on ambiguous notes. In the table, astronomical magnitudes are logarithmic and given by the formula $M_V = -2.5\log_{10}(\text{brightness}) + \text{constant}$. Examples to compare with: Moon is near -12 magnitudes, Venus peaks at -4.4 magnitudes and good eyes can see down to almost +6 magnitudes.

fusion processes would be of endothermic nature [33]. What is left at the end of a massive star's thermonuclear life is a structure, which is often compared with an "onion skin " structure. An oxygen-neon-magnesium core or an iron core is placed in the center followed by shells of elements of progressively lower atomic weight at progressively lower densities and temperatures [33]. A typical final nesting is Fe $\rightarrow$ Si $\rightarrow$ O $\rightarrow$ He $\rightarrow$ H. The core of such massive stars becomes gravitationally unstable as soon as the radiation pressure of the nuclear burning in the center cannot counteract the gravitational pull anymore. This results in an gravitational collapse of the core and finally leads to the formation of a neutron star or a black hole [181]. The gravitational binding energy is released in the form of neutrinos ($\mathcal{O}(10^{53})$ erg) and kinetic energy of the explosion of the outer layers ($\mathcal{O}(10^{51})$ erg).

In astronomy, the classification of supernovae is not based on the explosion mechanism but on the specific observed optical spectra of the supernovae. Rudolph Minkowski discovered that the spectra of supernovae can be distinguished by the absence (Type I) or presence (Type II) of the hydrogen Balmer lines [145]. This initial scheme was further extended by an increased number of observations and more detailed analysis of the spectra with newer technology. Today, astronomers use a scheme as it is presented in a simplified version in Fig. 2.1 (see e.g. [64, 82, 40, 201]):

- Type Ia: This type of supernovae is characterized by the absence of hydrogen in its spectra and a deep absorption line around 6150 Å which is attributed to Si [64]. Due to their high luminosities and similar light curves, this type of supernova has been used as so-called "standard candles" to determine the

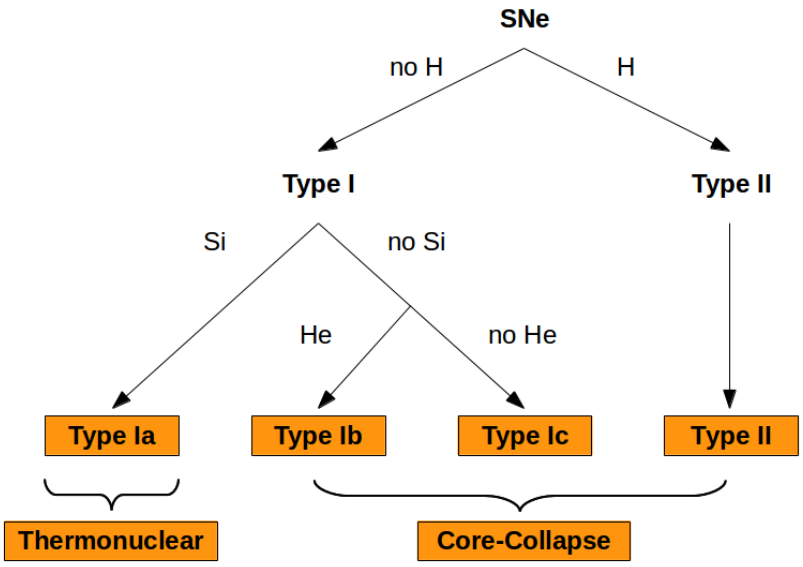

Fig. 2.1: Simplified astronomer's supernova classifications scheme [64, 82, 40, 201]. A distinction between two main classes of supernovae is carried out on the basis of the absence (Type I) and presence (Type II) of hydrogen lines in their spectra. A further subdivision of Type I supernovae is based on the presence (Ia) or absence (Ib,Ic) of Si lines. Type Ib and Ic can be distinguished by the occurrence of He lines (Ib) or not (Ic). Another, more fundamental distinction is based on the explosion mechanism: Theorists differ between thermonuclear (Type Ia) and core-collapse supernovae (Type II, Ib, Ic).

geometry of the Universe (see e.g. [164]). For more information see e.g. [127].

- Type Ib: This type of supernovae is characterized by the absence of hydrogen lines, weak or absent Si, and a strong He feature in its spectrum.
- Type Ic: This type of supernovae are distinguished by the absence of hydrogen lines, and weak or absent Si and He lines in its spectrum.
- Type II: Supernovae of the type II family do have distinctive hydrogen Balmer lines. More subtypes can be specified by the shape of their light curve (see e.g. [40, 201, 82]).

Finally, the importance of supernovae on the dynamical and chemical evolution of the Universe has to be stressed (see e.g. [206]). Many elements such as iron, calcium and silicon have their origin in supernovae. The major source of oxygen in the universe for example is the oxygen ejected during a core-collapse supernova [33].

2.2 Core-collapse supernovae

2.2.1 Stellar evolution

Stars are born in interstellar gas clouds mainly consisting of hydrogen and helium[1]. Such gas clouds collapse gravitationally and transform the gravitational energy into thermal energy and radiation. If the initial mass is above ~ 0.08 $M_\odot$, hydrogen is able to fuse to helium ("hydrogen burning"). This onset of nuclear burning leads to a halt of the gravitational compression and as soon as hydrogen fusion in the core becomes the only source of energy the star is considered in hydrostatic and thermal equilibrium. When hydrogen is exhausted in the core, most stars (i.e. if the mass is high enough) proceed to hydrogen shell burning. If the core is compressed sufficiently helium fusion starts in the core. As a product of the helium fusion mostly carbon and oxygen are left as ashes. Up to this stage, the exhaustion of one fuel was followed by the ignition of its successor.

Stars with masses below $\lesssim 6-8$ $M_\odot$ do not reach densities and temperatures high enough to ignite carbon burning. Therefore, their cores become electron-degenerate carbon-oxygen cores. In their final stage the outer layers are blown away forming planetary nebulae leaving behind the carbon-oxygen cores which will remain as a so-called white dwarf [214, 84].

Stars with masses $\gtrsim 6-8$ $M_\odot$ are able to ignite carbon burning which results in the production of oxygen, neon and magnesium ashes. In the narrow range between $8-10$ $M_\odot$, core temperatures are again not sufficient to ignite the further nuclear burning stages. As a consequence, the outer layers are blown away leaving behind an oxygen-neon-magnesium white dwarf. It is possible that such white dwarfs can lead to a special kind of core-collapse supernova [114] or undergo accretion-induced collapse [57, 1].

For stars with masses $\gtrsim 10$ $M_\odot$ a further contraction of the core is possible leading to the ignition of the successive burning stages where the ashes of the former stage build the fuel of the next stage. The last three distinct burning stages following the carbon burning are: neon burning, oxygen burning, and silicon burning [102, 214]. Finally, silicon burning leads to the production of the iron-group nuclei in the core. As mentioned in Sec. 2.1, no elements beyond the iron group are built since at this stage fusion would become endothermic or in other words, the nuclear binding energy per nucleon has reached its maximum in iron [33, 167]. As an example of a star at the end of its lifetime (presupernova configuration), a radial profile of a 15 $M_\odot$ star is shown in Fig. 2.2 [213]. The embedded iron core in an onion-like structure consisting of elements of progressively lower atomic weight at progressively lower densities and temperatures (also see Sec. 2.1) is clearly recognizable. However,

[1] The explanations in this subsection are mainly based on [102, 156].

the “onion shells” are not pure but mixtures of several elements and isotopes. The must abundant element determines the name of the shell.

A typical 15 $M_\odot$ star spends around 11.1 million years burning its hydrogen to helium and another 1.97 million years burning its helium [214]. The other burnings stages are tremendously shorter, peaking in the final silicon burning which only lasts around 18 days. These significantly shorter time scales are strongly influenced by important radiation neutrino losses that occur after the helium burning. It is the temperature sensitivity of such neutrino losses in combination with the need to go to higher temperature in order to burn the nuclear fuels that results in a fast acceleration during the last nuclear burning stages [214].

2.2.2 Core collapse and bounce

The iron core (consisting mostly of iron-group nuclei) in the center of the star grows steadily by the ashes of the silicon shell burning. The dominant pressure component acting against the gravitational compression is provided by the degenerate and relativistic electron gas while nuclear pressure is only small compared to it [23]. Such a degenerate, relativistic electron gas pressure scales as

$$P_e \sim Y_e^{4/3} \rho^{4/3} \,, \tag{2.1}$$

where Y_e represents the electron fraction and ρ the density. The factor $4/3$ represents the adiabatic index Γ for the extremely relativistic degenerate limit [23, 181]. The stability limit of the iron core is set by the Chandrasekhar mass limit [43], which is essentially the maximum mass that can be supported against gravity by an electron-degenerated gas in hydrostatic equilibrium. The Chandrasekhar mass including thermal corrections is given by [19, 214]

$$M_{\mathrm{Ch}} \approx 5.83 \bar{Y}_e^2 \left(1 + \left(\frac{\bar{s}_e}{\pi \bar{Y}_e} \right)^2 \right) \mathrm{M}_\odot \,, \tag{2.2}$$

where $\bar{Y}_e$ represents an average value of the electron fraction and $\bar{s}_e$ an average value of the electronic entropy per baryon in the iron core. Typical values for Y_e in the iron core of a 15 $M_\odot$ star reach from $Y_e = 0.42$ in the center to $Y_e = 0.48$ at the edge resulting in a reasonable average of $\bar{Y}_e = 0.45$ [214]. A typical value for $\bar{s}_e$ is ~ 0.52 [214]. Using these values in Eq. 2.2 results in an effective mass of $1.34\ \mathrm{M}_\odot$. Finally, the core mass exceeds the Chandrasekhar mass limit and the core becomes unstable; the collapse sets in. The combination of two physical effects accelerates the initial infall significantly: electron-captures (sometimes the term “neutronization” is used to describe this effect) and photodissociation (see e.g. [181]).

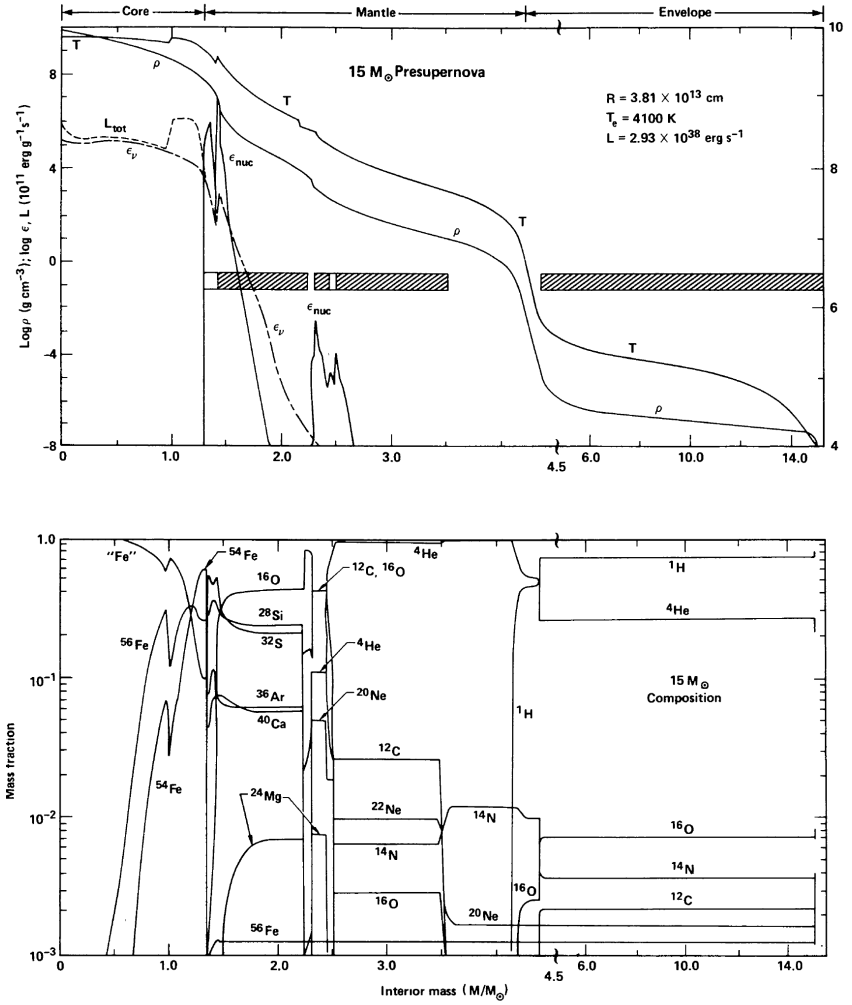

Fig. 2.2: Figure and part of the caption taken from [213]. Shown is the structure and composition of a typical 15 $M_\odot$ presupernova star at a time when the edge of its iron core begins to collapse at 1000 km/s. The upper panel shows the profile information in terms of density and temperature. $L_{\rm tot}$ indicates the total energy loss. The neutrino emission ϵ_ν dominates the energy loss throughout most of the iron core followed by peaks in the nuclear-energy generation rate $\epsilon_{\rm nuc}$ which show the location of the active burning shells. The lower panel shows detailed information on the composition of the "onion-like" structure of the star.

The most significant electron-capture reactions are [181]:

- Electron captures by nuclei,

$$e^- + (Z, A) \rightarrow \nu_e + (Z - 1, A) \ , \tag{2.3}$$

  where e^- are the electrons, ν_e the electron neutrinos, Z the charge number and A the atomic number.

- Electron captures by free protons,

$$e^- + p \rightarrow \nu_e + n \ , \tag{2.4}$$

  with p representing the proton and n the neutron.

At typical core densities ($\rho \gtrsim 10^9$ g/cm^3 electron captures on iron nuclei occur predominately by

$$^{56}\mathrm{Fe} + e^- \rightarrow 56^{\mathrm{Mn}} + \nu_e \ , \tag{2.5}$$

since the Fermi energy of the electrons

$$\mu_e = 11.1\mathrm{MeV} \left(\frac{\rho Y_e}{10^{10}\mathrm{gcm}^{-3}} \right)^{1/3} \tag{2.6}$$

exceeds the mass difference between the Fe and the Mn nuclei, namely $m_{\mathrm{Mn}} - m_{\mathrm{Fe}} = 3.7$ MeV (see [117]). Such reactions reduce Y_e and therefore also decrease the contribution of the degenerate electrons to the total pressure[2].

Photodissociation is the second process having an important influence on the pressure in the core. This endothermic process can take place at temperatures $T \gtrsim 5 \cdot 10^9$ K and typically dissolutes $^{56}_{26}$Fe nuclei to helium (alpha) cores [117]

$$\gamma + ^{56}_{26}\mathrm{Fe} \rightarrow 13\alpha + 4n - 124.4\mathrm{MeV} \ . \tag{2.7}$$

This leads to a reduction of the thermal pressure support [117]. Additionally, the internal energy produced by the contracting core is exhausted by this reaction [117]. At even higher temperatures, the present helium nuclei can further dissociate into free nucleons.

The iron core proceeds to contract under its self gravitation. The collapsing core is split into two parts: the homologously collapsing inner core and the supersonically infalling outer core. The matter inside the sonic point[3] still stays in communication and collapses homologously (velocity is approximately proportional to the radius) (see also [79, 181]). Matter outside the sonic point does not notice the inner collapse and is in quasi free-fall. For this reason, the outer shells are not moved or affected

[2] Note that up to a density of $\rho \approx 10^{12}$ g/cm^3 neutrinos are untrapped and can escape freely.
[3] The sonic point is defined as the point where the infall velocity equals the speed-of-sound velocity.

until the supernova shock wave generated in the core region collides with them and ejects them in the explosion.

As density increases above $\rho \approx 10^{12}$ g/cm^3 neutrinos are not escaping freely anymore but become trapped. This implies that they comove with the surrounding matter and build a semi-degenerate Fermi sea [181]. At such densities, the timescales for neutrinos to diffuse out of the core become comparable to the collapse timescales. Coherent scattering on nucleons

$$\nu + (Z, A) \rightarrow \nu + (Z, A) \ , \tag{2.8}$$

represents the dominant opacity source. The trapping of the neutrinos has enormous implications on the core collapse: Neutrinos from the electron captures cannot escape freely anymore but are trapped in the high density region. This implies that the lepton number per baryon $Y_l = Y_e + Y_\nu$ does not change but is constant. Additionally, neutrino trapping causes the collapse to proceed adiabatically to high approximation [181, 23]. Neutrinos can escape the trapped region when they reach the *neutrino sphere*. The neutrino sphere is defined as radial position where the neutrino optical depth

$$\tau(r, E_\nu) = \int_r^\infty \frac{dr}{\lambda_\nu}; \tag{2.9}$$

reaches 2/3, with E_ν the neutrino energy and λ_ν the neutrino mean free path. Note that during the collapse only electron neutrinos are emitted due to the electron captures.

After a few hundred milliseconds infall the homologous inner core reaches nuclear density $\rho_{\mathrm{nuc}} = 2.8 \cdot 10^{14}$ g/cm^3. At this point, pressure increases rapidly as the nuclear forces cause the nuclear equation of state to stiffen immediately [181]. Above ρ_{nuc} the pressure becomes high enough to halt the collapse. This causes the homologous core to "bounce" and rebound before it settles into the hydrostatic equilibrium. The rebounding inner core drives a hydrodynamical shock wave into the still infalling matter from the outer core[4].

2.2.3 Shock evolution and explosion mechanisms

The further evolution of the shock wave, initially created at core bounce, determines the fate of the star i.e. if the shock wave is finally able to push through the outer layers ultimately leading to a supernova explosion.
The initial shock wave propagates into the outer core region. During this propagation through the infalling matter the shock wave loses constantly energy due to the dissociation of nuclei into free nucleons. This happens at a cost of around 8.8 MeV per nucleon [23]. This corresponds to an energy loss of around $E_{\mathrm{loss}} = (1.6 - 1.8) \cdot 10^{51}$ erg per infalling 0.1 $M_\odot$ of material [147, 23]. Behind the shock wave this change of

[4] At the sonic point the pressure wave turns into a shock wave [117].

the matter composition results in even more energy loss: The emerging free protons behind the shock front become subject of electron captures

$$e^- + p \rightarrow n + \nu_e \ . \tag{2.10}$$

Such electron captures are significantly more effective than the ones on nuclei and therefore lead to the production of a huge number of electron neutrinos [110]. When the shock front passes the neutrino sphere these neutrinos are released suddenly. This electron neutrino burst (also called "neutronization burst" or "breakout burst" [117]) leads to peak luminosities above $\sim 10^{53}$ erg/s for a few milliseconds. Due to the immense loss of energy by dissociation of the nuclei and by neutrino emission, the shock finally stalls at around 100 - 200 km [117, 110]. The shock becomes the so-called *standing accretion shock*. The possibility that this initial "prompt shock" leads to a direct explosion is only possible for very special physical prerequisites (such as e.g. progenitor structure) (see e.g. [99, 12]). All other modern simulations did not show prompt explosions (see e.g., [110, 107] and references therein). Simultaneously to these events after core bounce, a compact remnant begins to form in the center of the star. Its mass is growing rapidly, forming a so-called protoneutron star. This object will either become a neutron star at later stages or collapse into a black hole, depending on the mass of the progenitor star and the explosion mechanism [84, 152].

During the collapse phase predominately electron neutrinos are produced. In the post-bounce phase neutrinos of the other flavors are produced as well. The slowly deleptonizing and cooling protoneutron star emits neutrinos of all flavors mainly via pair-production processes [29]. In this phase neutrinos of all flavors are emitted at a luminosity of $\sim 10^{52}$ erg/s due to the mass accretion onto the protoneutron star. After an eventual explosion this compact remnant becomes transparent to neutrinos which results in an exponential decay of the neutrino luminosities [34].

As stated above, the vast majority of the gravitational binding energy is converted into neutrinos. The intense neutrino burst represents a physically measurable observable. To this day, only a small number of neutrinos from SN1987A have been measured [100, 101]. These neutrinos confirm the basic picture of the supernova mechanism. Today, modern detectors such as Super-Kamiokande should be able to provide more detailed neutrino profiles in case of a nearby core-collapse supernova. This detailed information can provide crucial information on the explosion dynamics.

The first five panels in Fig. 2.3 illustrate the processes during a core-collapse supernova described in Sec. 2.2.2 and Sec. 2.2.3. The question that has been bothering physicists all around the world for the last few decades is how the standing accretion front can be revived and lead to the star's final explosion. In the following, a short overview over the recently discussed explosion mechanisms is given. For a more detailed review, see e.g. [107].

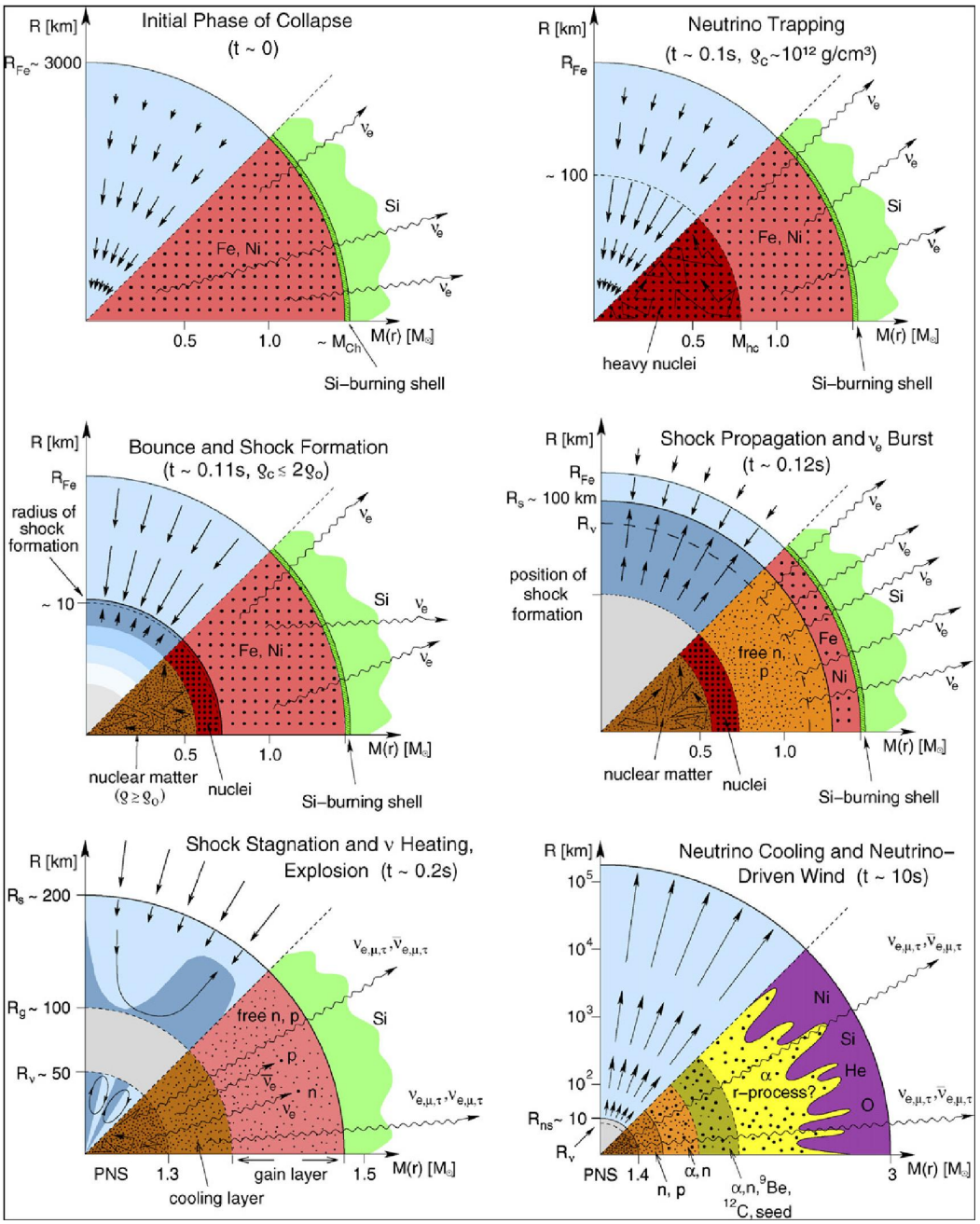

Fig. 2.3: Reprinted from [110], with permission from Elsevier. A set of schematic representations of the different stages in a core-collapse supernova. The upper half of the panels illustrate the dynamical conditions in the star with arrows indicating the velocities. The lower half of the panels shows the nuclear composition as well as the nuclear and weak processes. Mass information is given on the x-axis while radial information is provided on the y-axis. The different used variables represent the following quantities: $M_{\rm Ch}$ the Chandrasekhar mass, $M_{\rm hc}$ the mass of the collapsing homologous inner core, $R_{\rm Fe}$ the radius of the iron core, $R_{\rm S}$ the shock radius, $R_{\rm g}$ the gain radius, $R_{\rm ns}$ the neutron star radius, and R_ν the neutrinosphere.

Delayed neutrino-driven mechanism

The delayed neutrino-driven mechanism represents the most popular scenario for the supernova problem. The concept was initially proposed back in the 1960's by Colgate & White [48], and almost 20 years later numerically solved by Bethe & Wilson [24]. It is based on the fact that still a huge amount of the released gravitational binding energy is stored in the protoneutron star in the form of trapped neutrinos. The neutrinos streaming off the neutrino sphere are then supposed to deposit some of their energy in the outer layers between the protoneutron star and the standing accretion front. This energy deposition happens predominately via the ν_e and $\bar{\nu}_e$ absorptions on nucleons [24]:

$$\nu_e + n \rightarrow e^- + p \tag{2.11}$$

$$\bar{\nu}_e + p \rightarrow e^+ + n \; . \tag{2.12}$$

This neutrino heating is the cause for a pressure increase behind the shock. The heated layers expand and create a region of low density but relatively high temperature between the protoneutron star surface and the shock front. This region is sometime referred to as *hot bubble* [47]. The continuous energy input provided by the neutrinos keeps the pressure high in this region and eventually pushes the shock outwards again. Ultimately this may lead to an explosion. However, these processes happen on a time scale of a few 100 ms and requires that a few percent of the radiated neutrino energy are converted to thermal energy of nucleons, leptons, and photons [110]. Therefore, the mechanism is called the *delayed* neutrino-driven mechanism.

The success of the delayed neutrino-driven mechanism turned out to be very sensitive to the so-called *gain radius*. At this radial position the neutrino heating rate per nucleon equals the neutrino cooling rate per nucleon. Especially the extent of the net neutrino heating region and the magnitude of the net neutrino energy deposition therein are responsible for a successful explosion. Crucial factors in this region are the neutrino energy density and the neutrino flux outside the neutrino sphere [117]. This makes a detailed neutrino treatment indispensable for core-collapse supernova simulations. For a more detailed discussion on the gain radius see e.g. [110] and the references therein.

However, highly elaborated spherically symmetric simulations including e.g. full Boltzmann neutrino transport and general relativity failed in general to explode [133, 134]. Only for special low mass progenitors (O-Ne-Mg cores with masses between $\sim 8 - 10$ $\mathrm{M}_\odot$) were found to explode [114].

Multi-dimensional simulations on the other side showed successful explosions where spherically symmetric explosions failed (see e.g. [97, 37, 74, 73]). Fluid instabilities which only occur in multi-dimensional treatment lead an enhanced energy deposition

behind the shock front. The most important fluid instabilities include convection [97, 108] and the standing-accretion shock instability (SASI), see e.g. [31, 105, 137, 148, 176].

Magneto-rotational mechanism

In the case of rapidly rotating stars the so-called *magneto-rotational* or *magnetohydrodynamic* mechanism is possible. The concept is rather old and has already been proposed in the 1970's [142, 25]. With observation of highly magnetized neutron stars, so-called *magnetars*, this mechanism was reconsidered as a possible supernova mechanism [61]. The mechanism is based on the idea that during the collapse and in the post-bounce phase magnetic fields grow due to flux-freezing, increasing the number of field windings [142], and by the help of magnetorotational instabilities (MRI) [17, 2, 151]. These processes require differential rotation which is naturally developed in the case of rapid rotation during infall. Magnetic fields on the order of 10^{15} G are expected [2]. The resulting explosions are highly energetic ($\sim 10^{52}$ erg) and show well-collimated bipolar jets (see e.g. [38, 196] and references therein). Such high explosion energies make this mechanism favorable to explain hypernovae (see e.g. [210] and references therein).

Acoustic mechanism

The acoustic mechanism has been proposed by Burrows et al. [35, 36]. It has been found in 2D simulations where no explosions were found by the neutrino-heating mechanism. At late post-bounce times ($t \gtrsim 1$ s), the protoneutron star shows large-amplitude dipole gravity-mode oscillations which were excited by SASI sloshing motions and by anisotropic accretion downstreams [107]. The violent protoneutron star vibrations send strong sound waves into the surrounding medium which ultimately transform into shock waves that drive the explosion. Robust explosions were obtained for various tested progenitors. Nevertheless, other groups failed to reproduce this mechanism (see e.g. [137]) and a serious counterargument to this scenario has been proposed [207].

QCD core-collapse supernova mechanism

It has been shown that the conditions in core-collapse supernovae can favor a phase transition from hadronic to quark matter in the early post-bounce phase [194, 193, 195, 76, 60, 215]. In such simulations it was found that a second shock wave can form as a direct consequence of the phase transition [76]. However, due to the lack of an appropriate neutrino transport treatment, the evolution could only be followed for a few milliseconds. Only later, more detailed simulations where used to test equations of state considering quark matter [149]. Sagert et al. found in

their simulations using the sophisticated one-dimensional supernova code AGILE-BOLTZTRAN [130] with full Boltzmann neutrino transport that a shock wave created by the hadron-quark phase transition can indeed lead to an explosion [174, 65]. This is the only mechanism that shows explosions in spherical symmetry besides the simulations using an O-Ne-Mg progenitor (see discussion above).
In their models, Sagert et al. described quark matter using a simple, but widely used MIT bag model. The hybrid equation of state used was designed having an early onset of the phase transition. This leads to the appearance of quark matter already at core bounce. The successive evolution of the shock is initially similar to other simulations using a purely hadronic equation of state: The expanding shock looses energy due to the dissociation of nuclei and loss of neutrinos, especially at the neutrino burst. This transforms the outwards moving shock wave into a standing accretion shock. Meanwhile, in the core region of the protoneutron star the quark fraction rises until the reduced adiabatic index causes the protoneutron star to collapse. The collapse halts due to a stiffening of the equation of state and as consequence a subsonic accretion front forms at the border of the quark phase. The accretion front then detaches from this border turning into an accretion shock that later becomes a dynamic shock moving outwards with positive matter velocities (see Fig. 2.4). As soon as this expanding shock wave merges with the standing accretion shock the further evolution is similar to the neutrino-driven scenario. The revived shock wave is energetic enough to possibly lead to an explosion. The collapse of the protoneutron star and the subsequent shock wave release a second neutrino burst which is distinct enough to be measurable by current terrestrial neutrino experiments.

Unfortunately, this scenario has one big drawback: The equations of state used in [174, 65] do not support the observational 2 $M_\odot$ neutron star constraint [56, 70, 11]. Equations of state supporting the 2 $M_\odot$ neutron star constraint did not lead to explosions [66]. So far it is unclear if future hybrid equations of state that support the observational constraints can still lead to explosions. It was also criticized that the parameters determining the phase transition rely on a certain fine tuning to allow this scenario (see e.g. [107]).

To this day, there is no general agreement of theoretical astrophysicists on what might be *the* core-collapse supernova explosion mechanism. It is more likely that the explosion mechanism might: a) depend on the progenitor star's structure, its rotation, its magnetic field etc. and b) finally be a combination of some of the above mentioned mechanisms.

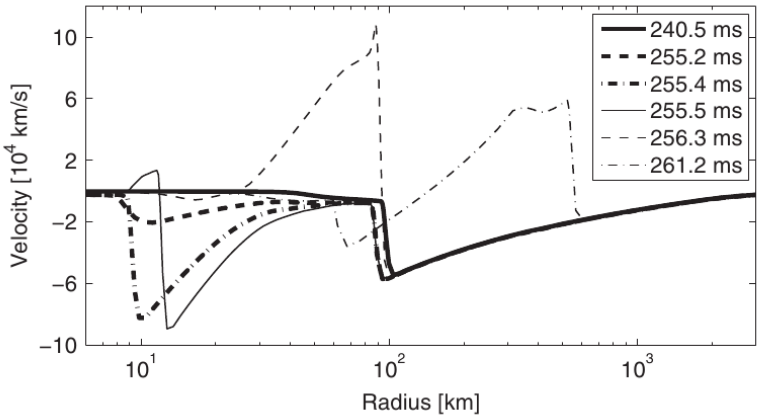

Fig. 2.4: Reprinted figure with permission from [174], copyright 2009 by the American Physical Society. Shown are the radial velocity profiles at different times during the post-bounce evolution of a 10 $M_\odot$ progenitor. The equation of state used is of a hybrid nature including additionally to hadronic matter also quark matter. Clearly visible are the second collapse of the protoneutron star which ultimately results in a strong explosion.

Neutron Stars and Hybrid Stars

3

> *I'm smart enough to know that I'm dumb.*
>
> **— Richard Feynman**

In this chapter, a short summary on the subject of neutron stars and especially hybrid stars is provided. Very detailed and profound information can be found in e.g. [78, 181]. In the last section of this chapter we provide new insights on the mass-radius curves at finite entropies and neutrino fractions which directly link the mass-radius curves to the second-collapse mechanism in core-collapse supernovae.

3.1 General remarks

Neutron stars are the objects with the highest densities found in the universe (besides black holes). Masses of up to two 2 $M_\odot$ are compressed to sphere-like objects (depending on rotation or magnetic fields) of radii between 8 and 20 km. The idea of such objects goes back to Baade & Zwicky in 1934 who proposed that a supernova represents *"the transition of an ordinary star into a neutron star, consisting mainly of neutrons."* [16, 15]. A few years later in 1939, the theoretical description of the structure of neutron stars was developed by Oppenheimer and Volkoff [155] and Tolman [199]. The first observational evidence of a neutron star was found in 1968 when the first pulsar (fast rotating neutron star) was discovered by Hewish et al. [98]. Today, more than 2000 pulsars have been detected [124]. Amongst these observations, the two most important measurements are two 2 $M_\odot$ neutron stars which represent the heaviest neutron stars observed with a high precision [56, 70, 11]. These two neutron stars set the mass constraint which every equation of state describing the matter of the neutron stars has to fulfill. Since in neutron stars physical quantities such as densities, pressures, magnetic fields etc. reach values not accessible in Earth-based experiments, these objects provide the ideal laboratory to test the description of matter under extreme conditions. The strongest constraint on the neutron star equation of state could be set by a single exact measurement of mass and radius at the same time. Since such a measurement is still missing up to present, the state of matter at such extreme densities is still unknown.

After the formation neutron stars cool down: the initial strong cooling happens via neutrino emission on a timescale of seconds. The neutron star temperature T can therefore assumed to be $T = 0$ (see discussion in Sec. 4.2.5 for more details).

Additionally, matter is assumed to be in beta equilibrium[1]. The internal structure of a neutron star can best be described by dividing the density profiles into different sections. In [181] the following density ranges are defined:

- **Surface:** $\rho \lesssim 10^6$ g cm^{-3}
- **Outer crust:** 10^6 g cm$^{-3} \lesssim \rho \lesssim 4.3 \times 10^{11}$ g cm^{-3}
- **Inner crust:** 4.3×10^{11} g cm$^{-3} \lesssim \rho \lesssim 0.5\rho_0$
- **Outer core:** $0.5\rho_0 \lesssim \rho \lesssim \rho_{core} \approx 2\rho_0$
- **Inner core:** $\rho \gtrsim \rho_{core} \approx 2\rho_0$,

where ρ_0 defines the density of nuclear matter at the saturation point of the nuclear forces[2]. A brief summary on the state of matter in the different layers is given in the following (for details see e.g. [78, 181, 41]):

Surface The surface of a neutron star is defined as where the pressure $P = 0$. ^{56}Fe is the matter with the lowest density in a neutron star and therefore forms the surface of the neutron star. ^{56}Fe is the most stable element which possesses the lowest energy per nucleon and therefore represents the lowest possible energy state at zero compression.

Outer crust In the most simple models, the outer crust at a given depth is a crystal of only one nuclear species. Matter is completely ionized. Due to the inverse β decay ($e^- + p \rightarrow n + \nu$), the ^{56}Fe atoms are altered step-by-step to more neutron-rich nuclei. The crystal structure is maintained, but atomic numbers can reach vast numbers.

Inner crust At the border of the outer crust to the inner crust, the neutron drip occurs. Free neutrons start to appear (neutrons that "dripped out of nuclei"). At the bottom of the inner crust, exotic nuclear matter configurations, so called "pastas" are possible (see [41] for a good review).

Outer core In this density regime, nuclei dissolve and build a strongly interacting Fermi liquid of nucleons. It is composed of neutrons, protons, electrons and μ^- mesons and therefore is often called $npe\mu$-composition.

Inner core This density regime is the most speculative part of a neutron star. It is the part of the core where hyperons and exotic matter is expected. Many different theories and models have been applied e.g. conversion of nucleons into hyperons[3], pion condensation, and conversion into quark matter.

[1] Beta equilibrium is defined via the relation $\mu_n = \mu_p + \mu_e$ with μ_n, μ_p, and μ_e as the chemical potentials of the neutrons, protons, and electrons. The neutrino chemical potential is neglected since the neutron star is transparent for neutrinos.

[2] For more details, see Sec. 4.1.3.

[3] Hyperons are baryons that contain at least on strange quark.

There is also the possibility that neutron stars could be built by pure quark matter. It is based on the idea that strange quark matter can be absolutely stable and considered as the true ground state of matter which was developed by Bodmer and Witten [209, 28]. However, in this work we will not consider such objects.

3.2 Neutron star structure equations

Since extreme masses and densities occur in neutron stars, they have to be treated as general relativistic objects. Starting from Einstein's field equation

$$G_{\mu\nu} = -\frac{8\pi G}{c^4} T_{\mu\nu} \ , \tag{3.1}$$

one arrives for an isotropic, general relativistic, static, ideal-fluid sphere in hydrostatic equilibrium at the so-called *Tolman - Oppenheimer - Volkoff equation* (TOV) [199, 155]:

$$\frac{dp}{dr} = -\frac{G\epsilon(r)m(r)}{c^2 r^2}\left(1+\frac{p(r)}{\epsilon(r)}\right)\left(1+\frac{4\pi r^3 p(r)}{m(r)c^2}\right)\left(1-\frac{2Gm(r)}{c^2 r}\right)^{-1} \ , \tag{3.2}$$

where p describes the pressure, ϵ the energy density which is determined by the equation of state $\epsilon(r) = \epsilon(p(r))$, m the enclosed mass up to radius r, and G the Newtonian gravitational constant. The second equation which describes the mass dependence reads as

$$\frac{dm}{dr} = \frac{4\pi r^2 \epsilon(r)}{c^2} \ . \tag{3.3}$$

In Eq. 3.2 three correction factors, compared to the structure equations obtained in a purely Newtonian treatment, can be identified (following [185]): The first two bracket terms represent the special relativity corrections of order v^2/c^2. In the non-relativistic limit they reduce to 1. The last bracket is a general relativistic correction. The factor $2GM/c^2R$ (M represents the total mass at radius R) determines whether general relativity has to be taken into account or not. The corresponding critical radius

$$R = \frac{2GM}{c^2} \tag{3.4}$$

is called the *Schwarzschild radius*. E.g.: The Schwarzschild radius of a 1 $M_\odot$ star is approximately $R \approx 3$ km. Since neutron star radii are of the order of ~ 10 km, general relativistic effects that have to be taken into account. Please note: all of the three terms written in brackets in Eq. 3.2 are bigger than one and therefore strengthen the term of the Newtonian gravity.

Equations 3.2 and 3.3 can be numerically solved starting from an initial central pressure p_0 and the boundary condition $m(r = 0) = 0$, until the surface of the neutron star is reached at $p = 0$. If the central pressure p_0 is varied as well a so-called mass-radius (M-R) relation can be produced. In such a representation

the masses of the neutron stars are plotted against their radii for a varied p_0. Since Eq. 3.2 and Eq. 3.3 only depend on the equation of state, the used equation of state generates a unique M-R relation. The maximum-mass configuration of the M-R relation has to be able to fulfill the observational 2 $M_\odot$ constraint.

3.3 Hybrid stars

Hybrid stars are defined as neutron stars that consist of both, hadronic matter and quark matter. The outer region is described by hadronic matter until at a certain transition pressure p_{trans} is reached where a phase transition to quark matter is undergone. This phase transition can be treated in two ways generally: Either there is a mixed region where both hadronic and quark matter coexist (Gibb's phase transition) or there is a sharp transition from hadronic to quark matter without a mixed phase (Maxwell phase transition). In this work we will use the Maxwell phase transition to model hybrid stars. Detailed information on the equations of state of hybrid stars will be given in Sec. 4.4.

Hybrid stars can have a special feature in their M-R curve; a so-called *third family*. Families of compact stars in M-R relations are defined as follows: First family stars are white dwarfs which are not subject of this thesis. Regular neutron stars are considered second family stars. In the M-R curves of neutron stars after a phase of instability[4] a third stable branch can build up, which consists of hybrid stars [77, 178] (see Fig. 3.1). The third family feature can be used to classify hybrid stars, as discussed in the following.

3.3.1 Classification

In Ref. [7] Alford et al. introduced four different cases to classify hybrid stars by their M-R relation as shown in Fig. 3.1. The classification is based on two criteria: the presence of a third family branch and the stability of hybrid stars at the onset of quark matter. Cases A and C have no third family branch and therefore only one maximum mass configuration. Case A ("absent") consists of only a hadronic branch. The point where quark matter sets in coincides with the maximum mass configuration. Case C ("connected") is similar to case A with the difference that there are stable hybrid star configurations which include quark matter up to the maximum mass. Cases B and D both have a third family branch in their M-R curve. Case B is identical to case C up to the first maximum. There is an unstable branch to the left of this point, followed by a third family branch ending in a second maximum. Case D is identical to case A up to the first maximum, but also has a third family branch in addition.

[4] Such hybrid star configurations are unstable with respect to radial perturbations [178].

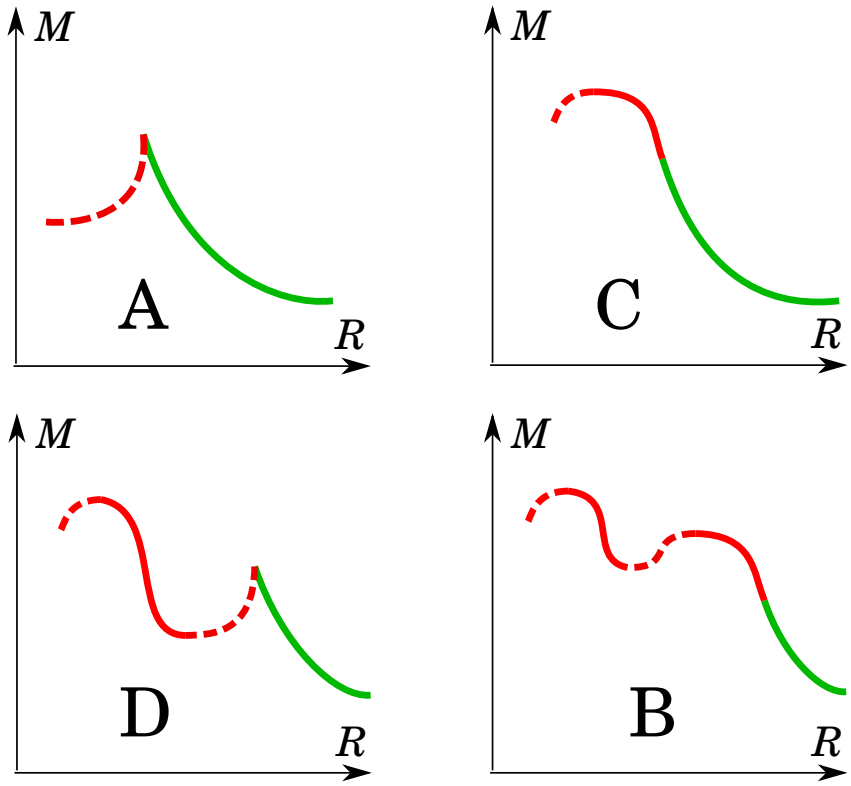

Fig. 3.1: M-R classification according to Alford et al. [7]. The straight green lines represent the purely hadronic stable configurations. Straight red lines represent stable hybrid star configurations and dashed red lines unstable hybrid star configurations.

For the supernova mechanism triggered by the hadron-quark phase transition, cases B and D are interesting. As we will learn in Sec. 3.3.2 they both have the potential to induce a second collapse in a supernova and a subsequent explosion (as described in Sec. 2.2.3).

3.3.2 Hot third families and their connection to core-collapse supernovae

In [93] we have shown that a connection between the third family features in M-R relations and the processes in a core-collapse supernova with a second collapse is present. The following discussion is based closely on [93].

Third family features do not necessarily have to be as distinct as shown in the illustrations in Fig. 3.1. More often, the feature is almost absent or very tiny in the case of cold compact stars respectively. The situation changes dramatically if one considers finite entropies. In [93] we had a closer look at two representative, already existing hybrid supernova equations of state which use a bag model to describe quark matter[5]: The B165 EOS uses a bag constant of $B^{1/4} = 165$ MeV and B139 EOS a bag constant of $B^{1/4} = 139$ MeV. While B139 EOS does fulfill the 2 $M_\odot$ constraint

[5] See Sec. 4.3.3 for a detailed discussion of the bag model

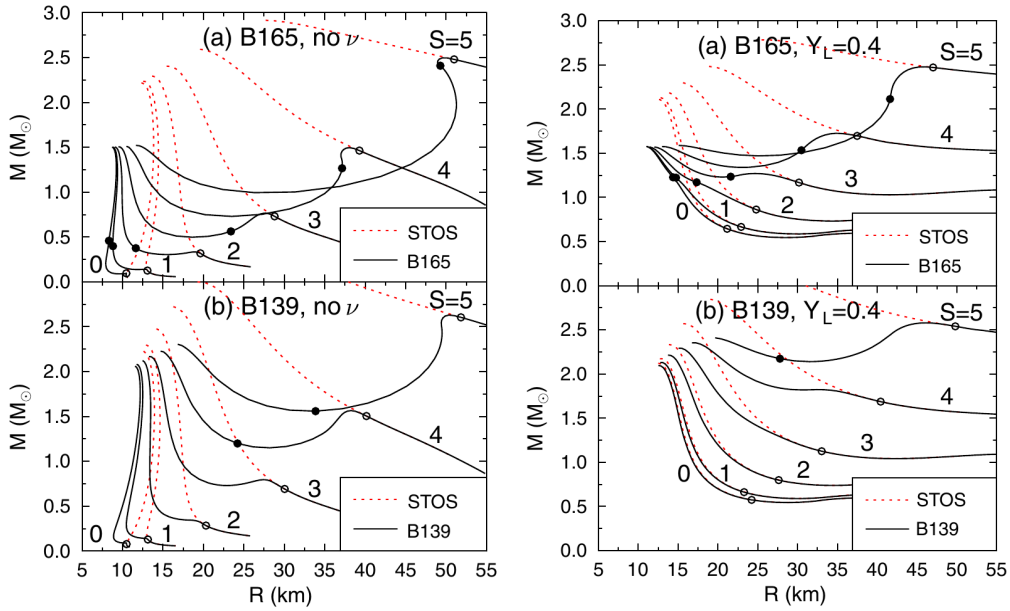

(a) Fig. 1 of [93]. No neutrinos are present. **(b)** Fig. 2 of [93]. Completely trapped neutrinos in beta equilibrium and a lepton fraction Y_L of 0.4.

Fig. 3.2: M-R curves for the B165 EOS and the B139 EOS for finite entropies per baryon S in beta equilibrium without (left panels) and with (right panels) neutrinos. The beginning a phase-coexistence regions is indicated with an open circle and the end with a full circle.

with a maximum mass of 2.04 $M_\odot$ the B165 EOS does not, having a maximum mass of only 1.50 $M_\odot$. However, it is only the B165 EOS that leads to explosions in spherical symmetric supernova simulations [174, 66, 67]. More information on these equations of state can be found in Chapter 4.

Figure 3.2a shows the M-R relations for the two hybrid supernova equations of state and their underlying hadronic equations of state for various entropies per baryon S, in beta equilibrium and without neutrinos. For cold hybrid stars, the third family is almost absent. With increasing entropies a second maximum develops which ultimately becomes the global maximum.

Comparing the B165 EOS with the B139 EOS we find that the third family branch appears already for lower entropies and is generally more pronounced than for the B139 EOS. The circles in Fig. 3.2a indicate the beginning (open circles) and the end (full circles) of the phase-coexistence region. Interestingly, using the B139 EOS pure quark matter is only obtained in hybrid stars at the highest entropies. For both equations of state a third family exists at $S = 5$. But, since the maximum total numbers of baryons in these third-family branches are below the one of the second family, such a third family cannot be reached by accretion. Consequently, a collapse from the maximum of the second family would result in the formation of a black hole as the number of baryons is conserved during a collapse.

In protoneutron stars not only finite entropies are present but also a finite neutrino fraction. Neutrinos are typically trapped in the core. To identify the effects of a finite neutrino fraction on the stability of a protoneutron star, we include completely trapped neutrinos in Fig. 3.2b using a constant lepton fraction $Y_L = 0.4$. It is clearly visible that neutrinos tend to decrease the phase transition effects and the resulting third-family feature. This can be explained by the fact that neutrinos contribute to the thermodynamic properties of both phases. Therefore, using a finite neutrino fraction, the third family features occur only at high entropies: for the B165 EOS at $S \geq 3$ and for the B139 EOS at $S \geq 4$. In any case, these results are not so realistic since in protoneutron stars the Y_L fraction is not constant. The results in actual simulations would lie somewhere between the results of Fig. 3.2a and Fig. 3.2b.

Such M-R relations with finite entropies and neutrino fractions can be connected with the second collapse mechanism in core-collapse supernovae [174, 66]. As long as shocks are absent and neutrinos trapped, S and Y_L are conserved quantities in core-collapse supernovae which are only advected with matter. Their values are similar to the ones in Fig. 3.2. In the post-bounce phase, matter is gradually accreted onto the protoneutron star increasing its mass and density. This would move the protoneutron star configuration from the right to the left in the M-R curves in Fig. 3.2. When the mostly hadronic protoneutron star has reached the maximum mass of the second family a collapse is induced. The collapse halts when high enough pressures are reached in the core to counterbalance the gravitational forces. Subsequently a second shock is formed which can lead to an explosion. It seems that only equations of state with a pronounced third family feature at finite entropies and neutrino fractions are favorable for explosions. Hence, the result that the B139 EOS, which only has a weakly pronounced third family feature, did not lead to explosions in spherically symmetric core-collapse supernova simulations is consistent with our explanation above.

4 Equations of State

> *A reader lives a thousand lives before he dies, said Jojen. The man who never reads lives only one.*
>
> **— George R.R. Martin**
> A Dance with Dragons

4.1 General purpose equation of state - theory

This section provides an overview of the equation of state theory used for astrophysical purposes. The discussion is mainly based on the review article of Oertel et al. [153] and the useful summary provided in the CompOSE manual[1] [203, 202]. The units used are $k_B = \hbar = c = 1$.

Even though in this work the term supernova equation of state (SN EOS) is often used, actually the term "general purpose equation of state" [153] is more accurate in a broader astrophysical context. Such a general purpose equation of state has to describe matter under extreme densities, extreme temperatures, and extreme isospin asymmetries which can be found in neutron stars, supernova explosions, collapse into black holes, and also neutron star mergers.

4.1.1 Definition - equation of state

Generally spoken, by the expression "equation of state" we mean any relation between thermodynamic state variables. In the following, we define this expression more precisely. If a thermodynamic potential $\Xi = \Xi(x_i, \xi_j)$ is known as a function of its n natural variables x_i and ξ_j (with the integers $i \in [1, n_1]$, $j \in [1, n_2]$ and $n = n_1 + n_2$), all the thermodynamic properties of a system are completely determined. The variables x_i can be identified as extensive and ξ_j as intensive variables. With this information, the thermodynamic equation of state can be determined as

$$\xi_i = \left.\frac{\partial \Xi}{\partial x_i}\right|_{x_k, k\neq i; \xi_j} = \xi_i(x_i, \xi_j) \tag{4.1}$$

and

$$x_j = \left.\frac{\partial \Xi}{\partial \xi_j}\right|_{\xi_k, k\neq j; x_i} = x_j(x_i, \xi_j). \tag{4.2}$$

[1] `http://compose.obspm.fr/`

The thermodynamic potential Ξ can be expressed as

$$\Xi = \Xi(x_i, \xi_j) = \sum_{i=1}^{n_1} \xi_i x_i \tag{4.3}$$

using Euler's theorem on homogeneous functions. Equation 4.3 shows that we can reconstruct the full thermodynamic potential if all equations of state are known. Useful for further thermodynamic considerations are the so-called Maxwell relations

$$\left.\frac{\partial \xi_l}{\partial x_k}\right|_{x_j, j\neq k} = \left.\frac{\partial \xi_k}{\partial x_l}\right|_{x_j, j\neq k}. \tag{4.4}$$

They are obtained using the information that for the mixed second derivative of a thermodynamic potential Ξ the order of differentiation must not be of relevance for the final result.

In the context of this work we are interested in applications of the equation of state to models that hydrodynamically describe a macroscopic system. There, matter is treated as a fluid and explicit effects from the present gravitational potential are not included into the thermodynamic description. The equation of state is constructed under the assumption that in each local system a thermodynamic equilibrium holds. In such systems the intensive thermodynamic variables (e.g. temperature T, pressure p or chemical potential μ) are typically well defined and thermal, mechanical, and chemical equilibrium hold[2].

In typical general purpose equations of state for dense matter the natural variables of choice are; temperature T [MeV], volume V [fm^3], and the set of particle numbers N_i $i \in [1, N_{\text{part}}]$ [ ]. These variables correspond to the (Helmholtz) free energy $F = F(T, V, N_i)$ [MeV] as the thermodynamic potential[3]. Since in the thermodynamic limit the actual value of V is not of relevance, meaning that all the extensive variables show the same scaling behavior, it is convenient to define important quantities as ratios of V, some of which we will list in the following. The free energy density is defined as

$$f(T, n_i) = \frac{F}{V} \quad [\text{MeV/fm}^3], \tag{4.5}$$

the entropy density is

$$s(T, n_i) = -\left.\frac{\partial f}{\partial T}\right|_{n_i} \quad [\text{fm}^{-3}], \tag{4.6}$$

where the entropy is defined as

$$S(T, V, N_i) = V s(T, n_i) = -\left.\frac{\partial F}{\partial T}\right|_{V, N_i} \quad [\quad], \tag{4.7}$$

[2]Note that in the chosen domain thermal equilibrium corresponds to constant temperature, mechanical equilibrium to constant pressure, and chemical equilibrium to constant chemical potential.
[3]Free energy includes rest-mass contributions of the particles.

and the chemical potential of a particle i is

$$\mu_i = \frac{\partial F}{\partial N_i}\Big|_{T,V,N_j,j\neq i} = \frac{\partial f}{\partial n_i}\Big|_{T,n_j,j\neq i} \quad \text{[MeV]}. \tag{4.8}$$

The pressure p can be calculated by

$$p = \frac{\partial F}{\partial V}\Big|_{T,N_i} = n_B^2 \frac{\partial (f/n_B)}{\partial n_B}\Big|_{T,Y_q} = \sum_i \mu_i n_i - f \quad \text{[MeV/fm}^3\text{]}, \tag{4.9}$$

where $n_B = N_B/V$ is the baryon number density and $Y_q = n_q/n_B$ the charge fraction of the strongly interacting particles. For a system constrained by charge neutrality and with only electrons as charged leptons, $Y_q = Y_e$ holds.

By using Legendre transformations, the free energy can be transformed into the other thermodynamic potentials which are listed below for the sake of completeness. The internal energy is defined as

$$E = E(S, V, N_i) = F + TS \quad \text{[MeV]}, \tag{4.10}$$

the free enthalpy or Gibbs potential

$$G = G(T, p, N_i) = F + pV = \sum_i \mu_i N_i \quad \text{[MeV]}, \tag{4.11}$$

the enthalpy

$$H = H(S, p, N_i) = E + pV \quad \text{[MeV]}, \tag{4.12}$$

and the grand canonical potential

$$\Omega = \Omega(T, V, \mu_i) = F - \sum_i \mu_i N_i = -pV \quad \text{[MeV]}. \tag{4.13}$$

The analogous densities of E, G, H, and Ω are $e = E/V$, $g = G/V$, $h = H/V$, and $\omega = \Omega/V$, all in units of [MeV/fm^3].

As mentioned above an equation of state can only be applied if the corresponding system is considered in thermodynamic equilibrium. While thermal and mechanical equilibrium (with the variables T and p) are usually achieved quickly in astrophysical simulations, the chemical equilibrium is the more critical. The condition to assume an equation of state is in chemical equilibrium is that the corresponding reactions happen on a significantly shorter timescale than the hydrodynamic evolution of the system. This is mostly the case if the system is in the so-called nuclear statistical equilibrium (NSE) which is reached if temperatures reach values of $T \geq 0.5$ MeV [102]. This condition provides us also with the information where the equation of state is not valid anymore, e.g. in the outer regions of core-collapse supernovae or in explosive nucleosythesis. There, a nuclear reaction network would have to be used

to follow the time evolution of the matter in chemical equilibrium. The chemical potential for every particle i is given by

$$\mu_i = B_i\mu_B + Q_i\mu_q + L_i^e\mu_{le} + S_i\mu_s \tag{4.14}$$

with baryon number B_i, the charge number Q_i, electronic lepton number L_i^e, and the strangeness number S_i and their corresponding chemical potentials μ_B, μ_q, μ_{le}, and μ_s. In NSE, Eq. 4.14 reduces for each nucleus a with neutron number N_a and proton number Z_a to

$$\mu_a = (N_a + Z_a)\mu_B + Z_a\mu_q \equiv N_a\mu_n + Z_a\mu_p. \tag{4.15}$$

Weak interactions can in general not be considered in equilibrium. Their timescales can exceed the dynamical timescale of the considered astrophysical object. In the case of core-collapse supernovae, which is especially relevant for this work, weak equilibrium can only be obtained at high densities above 10^{-3} fm^3. Even there, neutrinos do not have to be in thermal or chemical equilibrium. This is the reason why in supernova codes neutrinos are generally treated in separate routines using a transport approach (see Sec. 8.4).

In almost all astrophysical scenarios, the length scales of the system can be considered as infinitely large compared to the ones used in the microscopic models in the equations of state. This implies that the thermodynamic limit is reached and hence electric charge neutrality is necessary. Elsewise, strong electric fields might occur. The local condition for charge neutrality is

$$n_Q = \sum_i Q_i n_i = 0. \tag{4.16}$$

Since Eq. 4.16 implies that n_Q is not an independent thermodynamic degree of freedom, often a hadronic charge density is introduced

$$n_q = \sum_j Q_j n_j, \tag{4.17}$$

where the sum only considers the hadrons (and possibly quarks if present). If the only leptons present are electrons Eq. 4.17 reduces to $n_q = n_e$.

4.1.2 Requirements on the thermodynamic variables and on the matter composition for a general purpose EOS

When constructing a general purpose equation of state, it should only depend on the temperature T, the total baryon number density n_B and the total hadronic charge density n_q. Often, instead of n_q the corresponding charge fraction $Y_q = n_q/n_B$ is

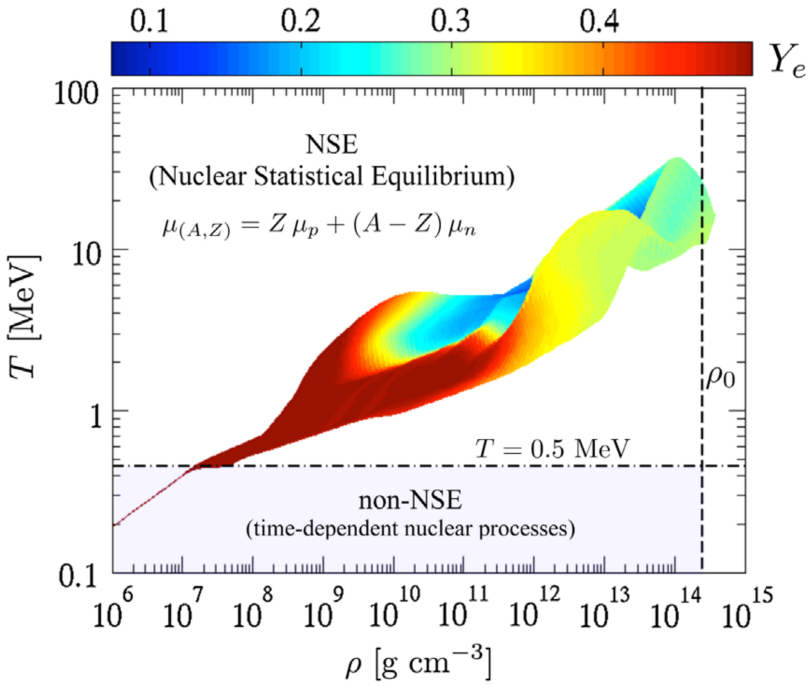

Fig. 4.1: Reprinted figure with permission from [153], copyright 2017 by the American Physical Society. Shown are the temperatures in MeV (left scale) and densities (lower scale the baryon number density in fm^{-3} and the upper scale the baryon density in g/cm^3). The Y_e fraction is indicated by the color coding.

used. In the following, the ranges of n_B, T and Y_e which should be considered in a general purpose equation of state are discussed.

Baryon number density n_B: From the observation of the 2 $M_\odot$ neutron stars (see [56, 11, 70]) it can be deduced that the baryon number densities in neutron stars can be as high as 10 times the nuclear saturation density $n_B^{\text{sat}} \approx 0.16$. While densities in core-collapse supernovae are generally lower, black hole formation due to a failed supernova can lead to even higher densities [192, 152, 94, 163] even though they will only last for less than a millisecond. While low density matter is almost irrelevant for neutron stars (few centimeters on the surface) it is important for core-collapse supernovae and neutron star mergers since in these cases ejecta are of interest. In such regions full thermodynamic equilibrium is not always fulfilled. For this reason an external nuclear network has to be applied to consider the time-dependent nuclear reactions. This is especially relevant to calculate the burning processes which contribute to the explosion energy.

Temperature T: A general purpose equation of state has to cover a huge temperature range. The lower limit is set by neutron stars. A new born neutron star cools extremely fast to temperatures below 1 MeV. This is small on the scale of nuclear energy and can hence be considered as zero in almost all models. In core-collapse supernova simulations temperatures between less than one MeV up to several tens of

quantity	range
temperature T	0 MeV $\leq T <$ 150 MeV
baryon number density n_B	10^{-11} fm$^{-3} < n_B < 10$ fm^{-3}
electron fraction Y_e	$0 < Y_e < 0.6$

Tab. 4.1: Table adapted from Oertel et al. [153]. Listed are the suggested ranges of temperature T, baryon number density n_B, and the electron fraction Y_e a general purpose equation of state should cover. If these ranges are described, a general purpose equation of state should be able to describe events as core-collapse supernovae and their products neutron stars, as well as neutron star mergers and eventually the onset of black hole formations.

MeV appear. In case of a failed supernova and the subsequent collapse into a black hole, temperatures above 100 MeV can appear (see e.g. [152]). Such scenarios set the upper boundary of the temperature scale for a general purpose equation of state. A general purpose equation of state should therefore cover the temperature range $0 \lesssim T \lesssim 150$ MeV.

Electron fraction Y_e: A general purpose equation of state has to be able to describe the whole range of Y_e during the simulation of a core-collapse supernova. While in the progenitor the electron fraction is $Y_e \approx 0.5$, Y_e decreases during the collapse due to electron captures. Matter becomes more and more neutron rich until the lowest limit of Y_e is reached. Initially, this lower limit for Y_e in the protoneutron star is set by the chemical equilibrium with trapped neutrinos where the total lepton fraction $Y_l = Y_e + Y_\nu$ is constant (see [65]). In the late stage, when the neutron star cools down, Y_e can reach values close to zero. Values of $Y_e > 0.5$ can be reached in parts of the supernova ejecta, corresponding to proton rich matter.

Figure 4.1 shows the temperatures, densities and electron fractions reached during a one-dimensional core-collapse supernova simulation using the 15 $M_\odot$ progenitor of Woosley and Weaver [212] (figure taken from [65]). It illustrates the above described ranges of n_B, T and Y_e. In Tab. 4.1 the ranges of T, n_B, and Y_e to be covered by each general purpose equation of state are summarized (table published in [153]).

Besides the requirements on thermodynamic variables that have to be covered by a general purpose equation of state, similar demands arise with respect to particle degrees of freedom. The composition of matter that can occur is very diverse and therefore “the wish” list for the equation of state long:

- To describe the surface layer, outer crust, and inner crust of cold neutron stars, ^{56}Fe ions (at the surface immersed in a sea of electrons) as well as heavy nuclei should be present (for detailed discussion of the composition of the neutron star crusts see [41]).

- At low densities and finite temperatures, a plasma consisting of a mixture of nuclei, nucleons, and electrons has to be described.
- To simulate shock-heated matter in core-collapse supernovae, light nuclear clusters, such as α particles, deuterons, tritons, and nucleons should be considered.
- The dissolution of nuclei at densities just below the saturation point (or high enough temperatures) into strongly interacting nuclear matter and electrons has to be described accurately.
- At even higher densities and temperatures, mesons such as pions can appear but also exotic matter such as hyperons or kaons can be present.
- In the highest density/temperature regime quark matter is possible to appear and therefore might also have to be considered.
- Besides the regular particles also some of their antiparticles should be considered.

Which of these ingredients are included into the equation of state and how depends on the underlying theoretical models and available experimental and observational data.

4.1.3 Characterization of nuclear matter properties in EOSs

To fit an equation of state to experimental and observational constraints, its nuclear parameters should be reduced to a meaningful set of parameters. Properties of nuclear matter can be compared well at the so-called saturation density $n_B^{\rm sat}$: At this density the symmetries of the strong interaction cause uniform nuclear matter at $T = 0$ to reach the state with the largest binding energy per nucleon. At this density, neutrons and protons are present in equal concentration[4]. At $T = 0$, the energy per nucleon E can be defined as a function of the baryon number density n_B and the so-called asymmetry α. The (isospin) asymmetry α describes the composition of the nuclear matter and is defined as

$$\alpha = \frac{n_n - n_p}{n_n + n_p} = 1 - 2Y_p \tag{4.18}$$

where n_n and n_p are the number densities of the neutrons and protons, respectively. $Y_p = n_p/n_B$ is the proton number fraction. The asymmetry α vanishes for symmetric matter where $Y_p = 0.5$. Using α, the energy per nucleon E can be expanded around symmetric matter at the saturation point $n_B^{\rm sat}$

$$E(n_B, \alpha) = E_0(n_B) + E_{\rm sym}(n_B)\alpha^2 + \mathcal{O}(\alpha^4) \quad \text{[MeV]}., \tag{4.19}$$

[4]For the exact equality of the number of protons and neutrons at saturation point, the mass difference between protons and neutrons has to be neglected.

where the energy per nucleon of symmetric matter reads as

$$E_0(n_B) = m_{\rm nuc} - B_{\rm sat} + \frac{1}{2}Kx^2 + \frac{1}{6}Qx^3 + \dots \quad \text{[MeV]}. \tag{4.20}$$

and the symmetry energy as

$$E_{\rm sym}(n_B) = J + Lx + \frac{1}{2}K_{\rm sym}x^2 + \dots \qquad \text{[MeV]}. \tag{4.21}$$

In general, the symmetry energy is defined as

$$E_{\rm sym}(n_B) = \frac{1}{2}\frac{\partial^2 E(n_B,\alpha)}{\partial \alpha^2}\bigg|_{a=0} \quad \text{[MeV]}. \tag{4.22}$$

Usually an expansion up to the quadratic term, as shown in Eq. 4.21, is sufficient. In Eq. 4.20 and 4.21, the variable x is defined as

$$x = \frac{1}{3}\left(\frac{n_B - n_B^{\rm sat}}{n_B^{\rm sat}}\right), \tag{4.23}$$

and can be considered as an expansion parameter of the baryon number density n_B close to the saturation density $n_B^{\rm sat}$. The coefficients $n_B^{\rm sat}$ and $B_{\rm sat}$, K, Q, J, L, $K_{\rm sym}$ [MeV], $\dots$ are used to characterize the equation of state and are discussed in more detail below. It is clear that these parameters do no describe all features of an equation of state, but they are especially relevant at densities close to the saturation density at $T = 0$ and close to symmetric nuclear matter. However, extrapolation from these values based on a polynomial expansion are dangerous and have to be thoroughly tested.

- The *saturation density of symmetric nuclear matter* $n_B^{\rm sat}$ can be defined more precisely by the condition that the pressure p vanishes

  $$p = n_B^2 \frac{dE(n_B,0)}{dn_B}\bigg|_{n_B=n_B^{\rm sat}} = 0 \quad \text{[MeV / fm}^3\text{]} \tag{4.24}$$

  and the energy per baryon is minimal. Typical values are commonly in the range 0.15 fm^{-3} $< n_B^{\rm sat} <$ 0.17 fm^{-3} [53].

- $B_{\rm sat}$ is the *binding energy of symmetric nuclear matter at saturation*. Ranges are usually 15.6 MeV $< B_{\rm sat} <$ 16.2 MeV [53].

- K [MeV] is defined as the *incompressibility of bulk nuclear matter*. It is defined by

  $$K = 9n_B^2 \frac{\partial^2 E(n_B,0)}{\partial n_B^2}\bigg|_{n_B=n_B^{\rm sat}} = 9n_B \frac{\partial p/n_B}{\partial n_B}\bigg|_{n_B=n_B^{\rm sat}} \quad \text{[MeV]}. \tag{4.25}$$

It quantifies the curvature of the binding energy per baryon with respect to the density variation at saturation. In [165] it is mentioned that the consensus for a good value of K given by nuclear experiments is given by $K = 240 \pm 10$ MeV.

- The parameter Q is the so-called *skewness coefficient of bulk nuclear matter*. It is defined as

$$Q = 27 n_B^3 \frac{\partial^3 E(n_B, 0)}{\partial n_B^3}\bigg|_{n_B = n_B^{\mathrm{sat}}} = 27 n_B^2 \frac{\partial^2 p/n_B}{\partial n_B^2}\bigg|_{n_B = n_B^{\mathrm{sat}}} - 6K \quad \text{[MeV]} \tag{4.26}$$

  Q in combination with K describes the surface properties of nuclei (e.g. surface tension to surface thickness).

- J is the *symmetry energy at saturation*. It is defined by

$$J = E_{\mathrm{sym}}(n_B^{\mathrm{sat}}) \quad \text{[MeV]}. \tag{4.27}$$

  J mainly defines the isospin dependence of the binding energy of nuclei and is therefore important to predict masses of exotic nuclei far off the valley of stability in the chart of nuclei. Typical values of J are shown in Fig. 4.2a. For more detailed information see [153].

- L is the *symmetry energy slope coefficient* which is given by

$$L = 3 n_B \frac{dE_{\mathrm{sym}}(n_B)}{dn_B}\bigg|_{n_B = n_B^{\mathrm{sat}}} \quad \text{[MeV]}. \tag{4.28}$$

  L shows the density dependence of the neutron matter equation of state close to the saturation density. It is strongly related to the neutron skin thickness of heavy nuclei. Typical values of L are shown in Fig. 4.2b. For more detailed information see [153].

- K_{sym} is the so-called *symmetry incompressibility* and is given by

$$K_{\mathrm{sym}} = 9 n_B^2 \frac{d^2 E_{\mathrm{sym}}(n_B)}{dn_B^2}\bigg|_{n_B = n_B^{\mathrm{sat}}} \quad \text{[MeV]}. \tag{4.29}$$

  In [53] typical values between -500 MeV $< K_{\mathrm{sym}} < 100$ MeV are mentioned.

4.1.4 Experimental and observational constraints on the EOS

In [153], a well-written and compact overview about the different experiments and their influence on determining the parameters n_B^{sat} and B_{sat}, K, Q, J, L, K_{sym} [MeV], ... is provided. In the following, a summary of the different methods listed in [153] is given. For more detailed information and an extensive list of references, the reader is encouraged to contact [153] for further reading. The parameters

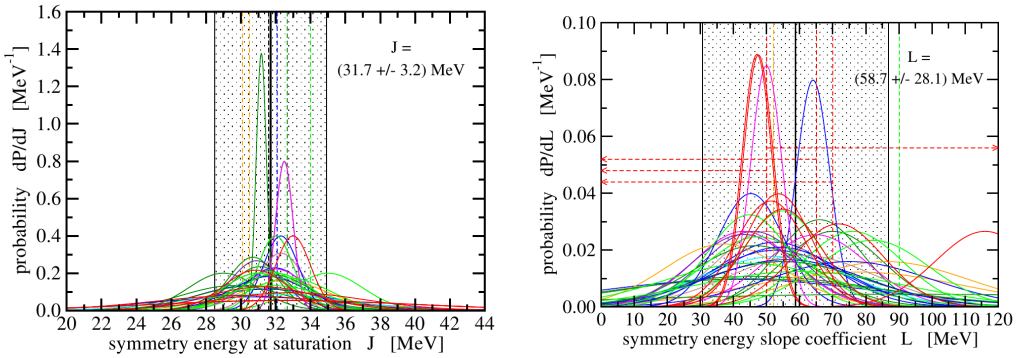

(a) **(b)**

Fig. 4.2: Reprinted figure with permission from [153]. The left panel shows a summary of the probability distribution of the symmetry energy J at saturation density, the right panel a summary of the probability distribution of the symmetry energy slope parameter L.

introduced in Sec. 4.1.3 can be constrained by experimental and observational data. Generally, we can differ three different categories (as listed in [153]):

1. *Terrestrial laboratory measurements of nuclear properties and reactions:*

   Nuclear masses (see e.g. [13, 14]) *and density distributions* (see e.g. [10]) provide the most basic constraints on the equation of state parameters listed in Sec. 4.1.3. Nuclear matter parameters can be obtained through extrapolation of the data to high mass numbers. Information on the saturation density $n_B^{\rm sat}$, the binding energy at saturation point $B_{\rm sat}$ and constraints on the symmetry energy $E_{\rm sym}$ is obtained. Indirectly, information on J and L can be extracted as well.

   Collective excitations of finite nuclei (so-called *nuclear resonances*) provide crucial information about isoscalar and isovector properties of the nucleon-nucleon interaction. This includes data from *giant monopole resonances* (to constrain the nuclear incompressibility K), *giant dipole resonances* (i.a. the symmetry energy $E_{\rm sym}$ can be constrained at $n_B = 0.1$ fm^{-3} to 23.3 MeV $< E_{\rm sym}(0.1{\rm fm}^{-3}) <$ 24.9 MeV [200], and the measurement of the *electric dipole polarizability* α_D (see e.g. [197]) which used to constrain L.

   Heavy, neutron-rich nuclei develop a neutron skin with thickness $\Delta r_{np} = \sqrt{\langle r_n^2\rangle} - \sqrt{\langle r_p^2\rangle}$ with $\sqrt{\langle r_i\rangle}$ $(i = n, p)$ the root-mean-square radii of the neutrons and protons, respectively. To determine the neutron skin thickness, the neutron radii of nuclei have to be measured.

   Heavy-ion collider experiments provide important information of warm/hot, strongly interacting matter. In such collider experiments densities of several times nuclear saturation densities and temperatures of several tenths of MeV can be obtained for a short period of time. Even though these values are very

similar to the values that can appear in supernovae, there are fundamental differences between matter in heavy-ion colliders and supernovae: Generally, matter in heavy-ion colliders is more isospin symmetric, while matter in supernovae can be more asymmetric (low proton fraction, high neutron fraction). Moreover, the fireball in heavy-ion collisions is finite size only, with a fixed number of nucleons which do not have to be in thermal equilibrium. As a consequence the maximum mass number of nuclear clusters is limited in such experiments. Contrariwise, matter in supernovae can be considered as in an infinite system and has therefore to be charge neutral. The net charge in heavy-ion collisions is fixed by the initial charge of the two colliding nuclei. Additionally, due to the high kinetic energies Coulomb energies are usually neglected in heavy-ions collisions. Another difference are the characteristic timescales: While in heavy-ion collisions, timescales of typically a few fm/c are reached and thus no equilibrium with respect to weak interactions is obtained, in neutron stars full equilibrium is obtained. This is also important for the strangeness changing reactions, which can be assumed to be in equilibrium in compact stars while in heavy-ions collisions the net strangeness is zero. From heavy-ion collisions a lot of information can be extracted e.g. constraints for the incompressibility K using information from kaon production (see e.g. [83]), isospin dynamics, the density dependence of the symmetry energy energy at moderate to high densities and multifragmentation reactions. The observation of light nuclei in heavy-ion collisions also provides important information to constrain the equation of state. For example the chemical equilibrium constant can be measured [169]. Figure 4.3 shows the comparison of the equilibrium constant of the α-particle obtained in the experiment (black diamonds) with different supernova equation of states (colored symbols) [92, 153]. Certain equations of state do clearly not lie within the grey error band of the experimental data.

2. *Theoretical ab-initio calculations:*

   In case of pure neutron star matter, its simple isospin structure simplifies the nuclear interaction Hamiltonian significantly. This allows *ab-initio calculations* which are more complex to perform in the case of asymmetric matter. Using different many-body techniques with well-calibrated interactions, calculations for a large range of densities are available. For an extensive review see [75]. Such calculations can serve as important constraints for the equation of states.

3. *Observations in astronomy*

   Neutron star masses set a strong constraint on the equation of state. Each equation of state should be able to support the masses of the most massive observed neutron stars. Two very precise measurements of neutron stars with masses of $2\ \mathrm{M}_\odot$ which are part of neutron-star-white-dwarf systems set the

strongest constraints: In 2010, a neutron star with the mass of (1.928 ± 0.017) $M_\odot$ [70] has been measured by a method based on the Shapiro delay [56]. In 2013, a second very precise measurement of a neutron star with the mass of (2.01 ± 0.4) $M_\odot$ has been measured [11]. In this case the orbital data was combined with the well-known structure model of the white dwarf in the binary system. There are indications of even more massive neutron stars (e.g. black widow and redback system [205, 173, 111]), but these measurements are more model dependent and do not reach the same precision (and hence reliability) as the two first mentioned measurements.

Measuring the *mass and radius of the same compact object* would be the ultimate observation to constrain the equation of state. For example in [186] it is discussed how a precise measurement of a low-mass neutron star might be translated into a constraint for a certain combination of K and L. Since radius measurements are done in an even more indirect way than mass measurements they are even more model dependent. To list a few possible sources of systematic error: distance to the source, composition of the atmosphere, residual accretion in binaries, brightness variation over the surface, interstellar extinction and the uncertainty considering rotation in case of sources with unknown rotation frequencies (for more detailed information see [144, 166]). Isolated neutron stars, quiescent X-ray transients, bursting neutron stars and rotation powered millisecond pulsars are the type of sources from which radii can be extracted currently. Future high precision astronomy, gravitational wave signals of neutron star mergers and the possible observation of gravitational redshift at the neutron star surface might provide better constraints on the radius.

Measuring the *cooling of neutron stars* gives a direct insight to the composition of a neutron star. Neutron star cooling depends directly on the composition of a neutron star and therefore determines the neutrino emission and the heat transport. Currently, the direct observation of the cooling of the neutron star in Cassiopeia A [88] seems to be promising to give a direct insight into the neutrons star composition.

Another constraint on the equation of state can be set by the measured rotation rates. However, the currently measured maximum frequency of 716 Hz does not set a significant limit on the equation of state [81]. This might change if even higher rotation rates would be measured.

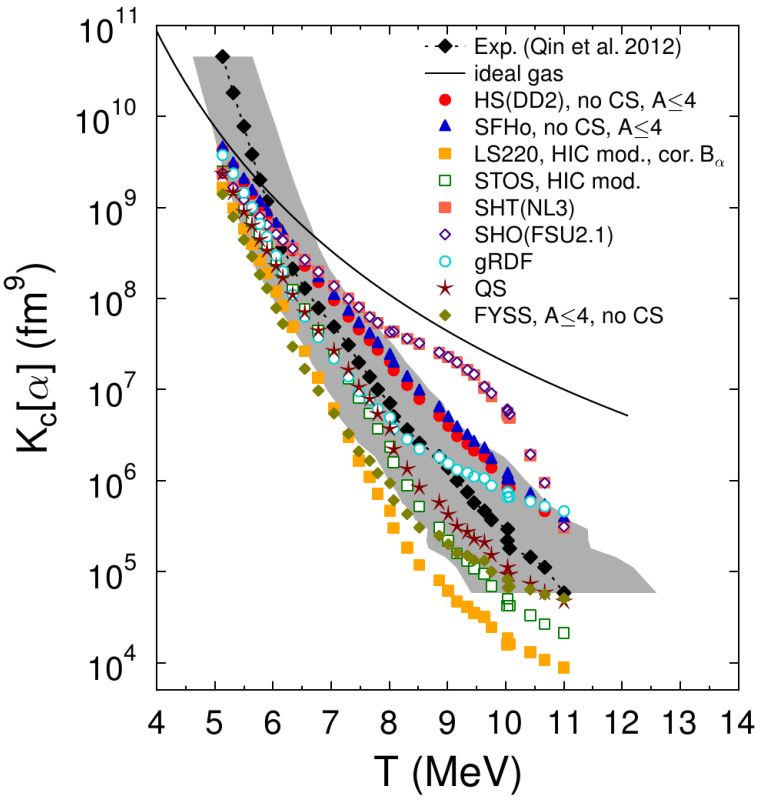

Fig. 4.3: Reprinted figure with permission from [153]. Shown are the equilibrium constants of α-particles obtained in heavy-ion collision experiments (black diamonds) as well as predictions from a selection of supernova equations of state and other models which were adapted to the experimental conditions as far as possible.

4.2 Hadronic equation of state

In this section all the relevant hadronic supernova equation of state models used in this work are listed and briefly described. We follow closely [153] when describing the different equations of state and extend the discussion where needed.

4.2.1 LS220

The equation of state by Lattimer and Swesty [125] is widely used in astrophysics. Even though not explicitly used in this work, it is briefly summarized here for the sake of completeness and later comparison with HS(DD2). In LS(220) nucleons, α-particles, and heavy nuclei in the single nucleus approximation are considered as degrees of freedom. The heavy nuclei are described with a medium-dependent liquid-drop model and for the nucleons a non-relativistic Fermic-Dirac statistics is applied. Additionally, a simplified momentum-independent nucleon-nucleon interaction is used. This results in constant nucleon masses which are identical to the used vacuum masses. To describe the interactions between the gas of nucleons, the α-particles and the heavy nuclei an excluded volume mechanism is used. α-particles are treated in a simplified way assuming they are hard spheres of the volume $V_\alpha = 24$ fm^3 that form an ideal Boltzmann gas. Excited states are neglected. Non-spherical nuclei and bubble phases can be formed as density increases and before nuclei completely dissolve into homogeneous nuclear matter. Such deformation is described by modifying the Coulomb and surface energies of the nuclei. A Maxwell construction is applied to describe the phase transition to bulk nuclear matter. LS(220) EOS has an incompressibility of $K = 220$ MeV. The maximum mass for cold neutron stars is 2.06 $M_\odot$.

4.2.2 STOS

The STOS EOS has been developed by Shen et al. in [183, 184, 182]. As in LS(220) the degrees of freedom are neutrons, protons, α-particles and one heavy nucleus in the single nucleus approximation. To describe the interactions of the nucleons a relativistic mean-field model with nonlinear meson self-interactions is used with the parameterization of TM1 [189]. Once again, α-particles are described as an ideal Boltzmann gas with excluded volume corrections while excited states are neglected. The properties of the single heavy nucleus are described *"by Wigner-Seitz cell calculations within the Thomas-Fermi approximation for parametrized density distributions of nucleons and α-particles"* [153]. As an additional simplification the translational energy and entropy contribution of heavy nuclei is not taken into account. The maximum mass for cold neutron stars is 2.23 $M_\odot$.

EOS	n_B^{sat} [fm^{-3}]	E_{sat} [MeV]	K [MeV]	Q [MeV]	J [MeV]	L [MeV]
LS(220)	0.1550	16.00	220	-411	28.61	73.82
STOS	0.1452	16.26	281	-285	36.89	110.79
HS(DD2)	0.1491	16.02	243	169	31.67	55.04

Tab. 4.2: Nuclear matter matter properties of the discussed hadronic supernova equation of state models.

4.2.3 HSDD2

The HS(DD2) EOS [96, 69] is a supernova equation of state available at finite temperature and variable proton fraction and density in the form of a table. As baryonic particle degrees of freedom, nucleons, and nuclei are considered. HS(DD2) describes matter as a chemical mixture of nuclei and unbound nucleons in nuclear statistical equilibrium (NSE). The interactions of the nucleons are described with density-dependent relativistic mean-field theory (DD2) which uses experimental nucleon masses as an input [204]. Several thousand nuclei are considered, including light ones and are treated as Maxwell-Boltzmann particles. Their binding energies are either determined by data from experimental measurements [13] or from various theoretical nuclear structure calculations (see [146, 122]). The formation of nuclei at subsaturation densities is considered in a statistical description employing experimentally measured binding energies and excluded-volume corrections [96]. Since in the HS(DD2) EOS the description of heavy nuclei is based on experimental data, it implicitly includes the correct shell effects of nuclei in vacuum. The HS(DD2) EOS is in good agreement with experimental constraints for the symmetry energy [89], theoretical constraints for the neutron matter equation of state [69], and cluster formation in low-energy heavy-ion collisions [92]. HS(DD2) EOS has a rather high maximum mass for cold neutron stars of 2.42 $M_\odot$.

Table 4.2 summarizes the equation of state parameters of LS(220), STOS and HS(DD2). In Fig. 4.4 the values of the slope parameter of the symmetry energy L and the value of the symmetry energy J at the saturation point shown in Tab. 4.2 are plotted. STOS EOS which is based on TM1 clearly lies outside the experimental constraints which are indicated in grey color. LS(220) also lies only at the left outer boundary of the weaker constraint area. We can conclude that the HS(DD2) EOS is a “state-of-the-art” supernova equation of state which is in best agreement with many experimental constraints.

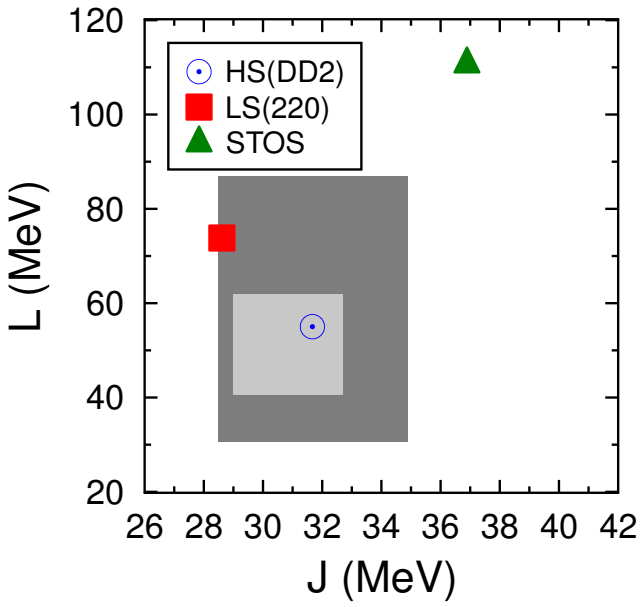

Fig. 4.4: Plotted are the slope parameter of the symmetry energy L against the value of the symmetry energy J at the saturation point for several equations of state: LS(220), STOS, and HS(DD2). The area shaded in dark grey indicates the constraints shown in Fig. 4.2. The area shaded in light grey indicates the stronger constraints given by [126].

4.2.4 BHB$\Lambda\phi$

Temperature and densities in core-collapse supernovae can reach values where the description of matter in terms of nucleons, electrons and nuclei is no longer sufficient. Hyperons represent an additional degree of freedom which can be considered in the hadronic EOS. Their appearance generally leads to a softening of the equation of state and therefore to a lower maximum mass. Often it is hard to even meet the 2 $M_\odot$ constraint. This problem is known under the name "hyperon puzzle"; see, e.g., [136, 45]. However, several hyperonic neutron star equations of state exist which have sufficiently high maximum masses by including repulsive hyperon interactions. An alternative solution to this puzzle is a phase transition to quark matter at low densities, which takes place before the appearance of hyperons; see [179, 218, 45].

The only existing supernova equation of state that considers hyperons and strictly fulfills the 2.01 $M_\odot$ neutron star constraint of [11] is the BHB$\Lambda\phi$ EOS [18]. It represents an extension of HS(DD2) where the Λ hyperon has been added as a particle degree of freedom within the density-dependent relativistic mean-field framework. Otherwise, the underlying models of HS(DD2) and BHB$\Lambda\phi$ are identical, e.g., regarding the nucleon interactions or the description of nuclei. Other hyperons than the Λ are not considered in BHB$\Lambda\phi$. The justification of this simplification is that the experimental data for the interactions of the other hyperons are even more uncertain than they are for the Λ (especially ΛN and $\Lambda\Lambda$ interactions are best

constraint from experiments), and that often the Λ is found to be the most important hyperon regarding the neutron star EOS. To reach the 2 $M_\odot$ constraint repulsive hyperon-hyperon interactions have been included in the BHB$\Lambda\phi$ EOS via the strange ϕ meson. The resulting maximum mass for cold, β-equilibrated matter is 2.11 $M_\odot$, and thus directly compatible with the measurement of [11]. This means BHB$\Lambda\phi$ does not show a hyperon puzzle.

4.2.5 Application of HS(DD2) and BHB$\Lambda\phi$ in neutron stars

In this work, we use the HS(DD2) and BHB$\Lambda\phi$ EOSs in beta equilibrium and at $T = 0.1$ MeV. A temperature of 0.1 MeV is negligibly small in comparison to typical Fermi energies in neutron stars, and thus a sufficient approximation for $T = 0$. Note that the inner and outer crust is included self-consistently in HS(DD2) and BHB$\Lambda\phi$, i.e., we have a unified EOS description for the entire neutron star. These equation of state tables have been kindly provided by PD M. Hempel.

4.3 Quark equation of state

In 1984, Witten proposed the concept of absolutely stable quark matter [209] (see also earlier works, e.g. [103, 72]). The main idea is that hadronic matter is only a metastable state of matter while strange quark matter is considered as the true ground state since its energy per baryon is lower than the one of ^{54}Fe. This hypothesis leads to the conclusion that the existence of so-called "strange stars" (stars which only consist of absolutely stable strange quark matter) is possible. In the same year as Witten published his hypothesis, Farhi and Jaffe investigated Witten's theory by using a Fermi-gas model to establish conditions under which strange matter in bulk is absolutely stable [63].

By "bulk quark matter", Farhi and Jaffe define a cluster of quark matter large enough that surface effects are negligible and electrons (respectively positrons) are bound in the bulk. It is supposed that strange quark matter is the true ground state of the strong interaction at zero temperature and pressure. In order for this to be true the energy per baryon E/A has to be smaller than the one of a nucleon with mass $M_N = 939$ MeV. If E/A is between 930 and 939 MeV, it is possible for strange matter to decay by emission of nuclei accompanied by weak interactions to stay in flavor equilibrium. If E/A is less than 930 MeV, in principle a nucleus can lower its energy by simply converting approximately one third of its quarks into strange quarks. However, this is not very likely since a very high-order weak interaction would be required. The rate up to forth order (which is considered here) remains for all practical purposes zero. Since ordinary nuclei consist of nucleons and not of pure (u,d) quark matter, E/A of non-strange (u,d) quark matter has to exceed the lowest energy per baryon found in a nuclei, which is 930 MeV in iron. Nevertheless, this is not restrictive enough for non-strange quark matter: For large, but still finite A it

is believed that its E/A is less than for $A \to \infty$ (which is the "bulk matter case"). On the other hand, strange quark matter behaves the opposite: Its E/A decreases with A. Therefore, in the case of non-strange quark matter a Δ (which describes the difference between the E/A of non-strange quark matter in bulk matter and for $A \approx 250$, ~ 4 MeV here) has to be added to the value of iron $930 + \Delta$ MeV (for detailed explanation, see [63]).

In this work we do not assume that strange quark matter is absolutely stable. At high densities and/or temperatures it is possible that hadronic matter can change its state into a phase of deconfined quarks and gluons, with restored chiral symmetry. In this regime, quarks and gluons can move as free and almost non-interacting particles due to the deconfinement and the asymptotic freedom (bag model assumption). Quarks obtain mass due to chiral symmetry restoration; up and down quarks only of the order of a few MeV while the strange quark obtains a mass of around $m_s \approx 100$ MeV [65]. In the following, we introduce the models by which we describe quark matter in core-collapse supernovae and hybrid stars in this work. We start the discussion of our models in Sec. 4.3.1 and Sec. 4.3.2 which can be applied for hybrid stars at $T = 0$ and β-equilibrium. In Sec. 4.3.3, we finally describe a thermodynamic bag model which is later used to describe quark matter in our core-collapse supernova simulations.

4.3.1 CSS model

A very simple, phenomenological model for quark matter was introduced by Alford et al. in [7]. Due to its simplicity it is well suited for systematic investigation of phase-transition properties in hybrid stars. The model describes the quark phase by the constant speed of sound (CSS) EOS :

$$\epsilon_{\mathrm{CSS}}(p) = c_{\mathrm{QM}}^{-2}(p - p_0) \, , \tag{4.30}$$

where c_{QM} is the density-independent speed of sound, p the pressure, and p_0 the pressure where $\epsilon_{\mathrm{CSS}} = 0$. Two values for c_{QM} are of special interest: $c^2_{\mathrm{QM}} = 1/3$ which corresponds to non- or weakly interacting, massless quarks and $c^2_{\mathrm{QM}} = 1$ which is the maximum value to be still consistent with special relativity. Later in this work, the main discussion is based on $c^2_{\mathrm{QM}} = 1/3$, which is typical for many quark EOSs and also in agreement with other, more sophisticated models (e.g., [6, 20]).

4.3.2 Bag model (for $T = 0$ and β-equilibrium)

The CSS EOS is not a very common equation of state for the description of quark matter. Furthermore, as it only represents a parametrization of thermodynamic quantities, it does not contain any composition or temperature dependence. Both aspects are important for the application in core-collapse supernova simulations simulations which we are aiming at in this work.

A commonly used and easy-to-handle model which provides this information is the so-called thermodynamic bag model, which is described in more detail in the following. The most prominent bag model is the one developed by Chodos et al. in 1974 [46], known as the "MIT bag model". Bag models are generally easy to handle and able to reproduce hadron properties well (see e.g. [46, 55, 58]). Their application to describe bulk quark matter is also fairly popular. The main idea of quark bag models can be summarized as follows: It is assumed that the true vacuum of QCD is a medium which refuses the intrusion of quarks and confines them with in a sphere, respectively "bag". This bag is a color neutral hadron. The pressure on the hadron exerted by the QCD vacuum is considered in the bag models by the phenomenological bag constant B. The pressure B onto the bag is opposed by the motion of the quarks in it. Quarks are assumed to move asymptotically free within the bag.

Farhi and Jaffe considered three-flavor (u, d, s) quark matter in beta equilibrium at zero temperature with a negative external bag pressure B acting on quark matter [63]. Matter is assumed to be in equilibrium regarding the following reactions:

$$\begin{aligned} d &\leftrightarrow u + e + \bar{\nu_e} \ , \\ s &\leftrightarrow u + e + \bar{\nu_e} \ , \\ s + u &\leftrightarrow u + d \ . \end{aligned} \tag{4.31}$$

In cold neutron stars where no neutrinos are present the chemical potentials thus fulfill the relation:

$$\mu_d = \mu_s = \mu_u + \mu_e \ . \tag{4.32}$$

The pressure p_i depending on the chemical potential μ_i for each species $i = u, d, s, e$ is easily calculated since the quarks are treated as noninteracting Fermi gases:

$$\begin{aligned} p_i \ = \ & \frac{1}{6}\frac{g}{4\pi^2}\left[\mu_i(\mu_i^2 - m_i^2)^{1/2}(\mu_i^2 - \frac{5}{2}m_i^2)\right. \\ & \left. + \frac{3}{2}m_i^4 \ln\left(\frac{(\mu_i^2 - m_i^2)^{1/2} + \mu_i}{m_i}\right)\right] \ . \end{aligned} \tag{4.33}$$

The degeneracy factor g is $g = 2_{\rm spin}$ for electrons and $g = 6 = 2_{\rm spin} \times 3_{\rm color}$ for quarks. The pressures for each species, assuming the masses for u and d quarks as well as electrons are negligible, are:

$$\begin{aligned} p_u^{\rm non-int} &= \frac{\mu_u^4}{4\pi^2} \,, \\ p_d^{\rm non-int} &= \frac{\mu_d^4}{4\pi^2} \,, \\ p_e^{\rm non-int} &= \frac{\mu_e^4}{12\pi^2} \,, \\ p_s^{\rm non-int} &= \frac{1}{4\pi^2}\left[\mu_s(\mu_s^2 - m_s^2)^{1/2}(\mu_s^2 - \frac{5}{2}m_s^2)\right. \\ &\quad \left. + \frac{3}{2}m_s^4 \ln\left(\frac{(\mu_s^2 - m_s^2)^{1/2} + \mu_s}{m_s}\right)\right] \,. \end{aligned} \tag{4.34}$$

The total pressure is the sum of the particle pressures with the bag constant subtracted:

$$p_{\rm tot} = \sum_i p_i^{\rm non-int} - B \,. \tag{4.35}$$

By using the number density for each species n_i, which can be obtained from the thermodynamic relation

$$n_i = \frac{\partial p_{\rm tot}}{\partial \mu_i} \,, \tag{4.36}$$

the charge neutrality condition can be expressed as

$$\frac{2}{3}n_u - \frac{1}{3}n_d - \frac{1}{3}n_s - n_e = 0 \,. \tag{4.37}$$

Equations (4.37) and (4.32) leave only one independent chemical potential. Using the $T = 0$ thermodynamic relation

$$\epsilon_{\rm tot} = -p_{\rm tot} + \sum_i \mu_i n_i \tag{4.38}$$

and Eq. (4.35), the total energy density can be written as

$$\epsilon_{\rm tot} = \sum_i (-p_i^{\rm non-int} + \mu_i n_i) + B \tag{4.39}$$

$$= \sum_i \epsilon_i^{\rm non-int} + B \,. \tag{4.40}$$

To include interactions, often a phenomenological parametrization is used. Here, we apply the model of [65] for $T = 0$:

$$p^{\rm QM} = \sum_i p_i^{\rm non-int} - B - \sum_{j=u,d,s} \frac{2\alpha_s}{\pi}\frac{\mu_j^4}{4\pi^2}, \tag{4.41}$$

where α_s accounts for strong interaction corrections. The model presented in [65] is similar to the ones from Alford et al. [4] and Weissenborn et al. [208]. Both use an interaction correction proportional to μ^4 (where μ denotes the quark chemical potential) similar to the α_s term in Eq. 4.41. In fact, Weissenborn's model is equivalent to Eq. 4.41 for $m_s = 0$, and in this case the proportionality factor a_4 of the μ^4-term can be identified as $a_4 = 1 - 2\alpha_s/\pi$. Alford's quark EOS is a generic power-series ansatz, which includes an additional $a_2\mu^2$ term. This term can be interpreted to be related to color superconductivity by using $a_2 = m_s^2 - 4\Delta^2$, where Δ represents the pairing gap [3, 4]. Another quark model suitable for astrophysical application is vBag, which was introduced in [115, 116]. It contains vector interactions and a medium-dependent bag pressure, which is based on the assumption of simultaneous deconfinement and chiral symmetry restoration. It would be interesting to compare vBag with the quark equations of state used in the present study in the future.

An important case is where u, d, and s quarks are massless. It follows $\mu_u = \mu_d = \mu_s = \mu$, and $\mu_e = 0$, and $n_u = n_d = n_s$ and $n_e = 0$, i.e., quarks maintain charge neutrality by themselves and there are no electrons in the quark phase. This allows us to compare the CSS EOS with the bag model of Eq. 4.41 in the limit of $m_s = 0$ and beta equilibrium. Therefore Eq. 4.30 has to be reformulated. Together with Eq. 4.38, Eq. 4.30 leads to

$$p^{\mathrm{CSS}} = \frac{c_{\mathrm{QM}}^2}{1 + c_{\mathrm{QM}}^2} \left(\frac{p_0}{c_{\mathrm{QM}}^2} + \mu n \right) , \tag{4.42}$$

where $n = n_u + n_d + n_s$. n depends on μ due to the relation $n = \partial p / \partial \mu$, which can be inserted in Eq. 4.42. Separating the variables and integrating over the respective boundaries leads to

$$p^{\mathrm{CSS}}(\mu) = \frac{c_{\mathrm{QM}}^2}{1 + c_{\mathrm{QM}}^2} p_0 \left[\left(\frac{\mu}{\mu_0} \right)^{\frac{1+c_{\mathrm{QM}}^2}{c_{\mathrm{QM}}^2}} + \frac{1}{c_{\mathrm{QM}}^2} \right] . \tag{4.43}$$

It is interesting to note that another constant μ_0 appears. The reason is that the $\epsilon(p)$-relation of Eq. 4.30 does not represent a thermodynamic potential. For given $\Delta\epsilon$ and p_{trans} (both quantities will be introduced in Sec. 4.4), which fix p_0 by Eq. 4.58, μ_0 can be fixed as well by inverting Eq. 4.43 and using the condition of chemical equilibrium at the phase transition point,

$$\mu^{\mathrm{CSS}}(p_{\mathrm{trans}}) = \frac{1}{3} \mu_B^{\mathrm{hadronic}}(p_{\mathrm{trans}}) , \tag{4.44}$$

which gives

$$\mu_0 = \frac{1}{3} \mu_B^{\mathrm{hadronic}}(p_{\mathrm{trans}}) \left(\frac{1 + c_{\mathrm{QM}}^2}{c_{\mathrm{QM}}^2} \frac{p_{\mathrm{trans}}}{p_0} - \frac{1}{c_{\mathrm{QM}}^2} \right)^{-\frac{c_{\mathrm{QM}}^2}{1+c_{\mathrm{QM}}^2}} . \tag{4.45}$$

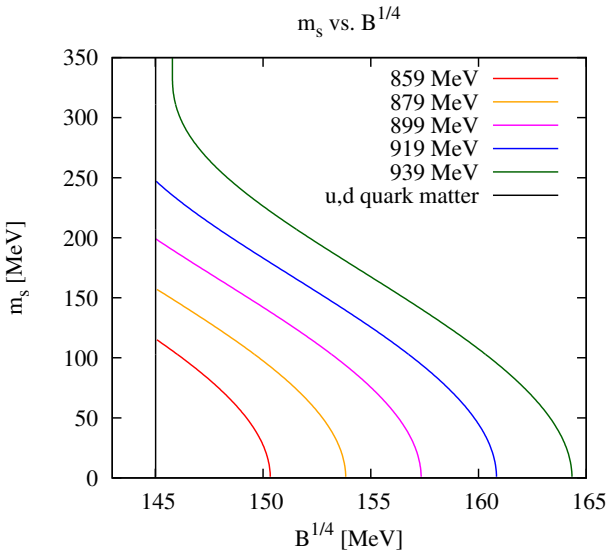

Fig. 4.5: Contour lines of fixed energy per baryon dependent on the strange quark mass m_s and the bag constant $B^{1/4}$. The black vertical line on the left indicates the minimum bag constant for which nonstrange $u-d$ quark matter is unbound.

The schematic form of Eq. 4.43 was already given in the appendix of [7]. However, in [7] chemical equilibrium was not considered explicitly, as it is done above.

Comparing the bag model description of Eq. 4.41 with the $p(\mu)$ formulation of the CSS EOS (Eq. (4.43), it is obvious that these two formulations are equivalent when $c^2_{\rm QM} = 1/3$. The identifications of the μ^4-dependent and μ-independent terms in the CSS and bag equations of state lead to

$$\begin{aligned} \alpha_s &= \frac{\pi}{2} - \frac{\pi^3}{6}\frac{p_0}{\mu_0^4} \\ B &= -\frac{3}{4}p_0 \, . \end{aligned} \tag{4.46}$$

Since we do not assume absolutely stable quark matter the bag constant B has to be chosen such that the previously described conditions for absolutely stable quark matter are not fulfilled. Figure 4.5 shows the contour lines of the non-interacting bag model for fixed energy per baryon dependent on the strange quark mass m_s and the bag constant $B^{1/4}$. As we will learn below a strange-quark mass of $m_s = 100$ MeV is a reasonable value. From Fig. 4.5 it is clear that in order to not fulfill the conditions for absolutely stable quark matter ($E/A < 939$ MeV), the bag constant should be chosen $B^{1/4} \gtrsim 161$ MeV in the non-interacting case. If strong interaction corrections are included this lower limit of $B^{1/4}$ is shifted to smaller values since the one-gluon-exchange effects inside hadrons are of repulsive nature.

4.3.3 Bag model for supernova EOS

In this section, we discuss the general case of the model of Farhi and Jaffe [63] described in Sec. 4.3.2. We use the model presented in [174, 65] and follow closely the discussion of [65].

As in the $T = 0$ and β-equilibrium, within the more general bag model the pressure p^Q, energy density ϵ^Q, entropy density s^Q and baryon number density n_B^Q can be expressed as follows:

$$p^Q = \sum_i p_i - B \tag{4.47}$$

$$\epsilon^Q = \sum_i \epsilon_i + B \tag{4.48}$$

$$s^Q = \sum_i s_i \tag{4.49}$$

$$n_B^Q = \frac{1}{3}\sum_i n_i \quad . \tag{4.50}$$

The summation index i runs over all present quark flavors. In the case of a non-interacting bag model, quarks can be treated as non-interacting fermions. The individual components can be calculated solving the corresponding Fermi integrals for a given temperature T, quark chemical potential μ_i, and quark mass m_i:

$$p_i^{\mathrm{non-int}}(m_i, T, \mu_i) = \frac{1}{3}\frac{g_i}{2\pi^2}\int_0^\infty k^2 dk\; k\frac{\partial E_i(k)}{\partial k} \times [f(k,\mu_i) + f(k,-\mu_i)] \tag{4.51}$$

$$\epsilon_i^{\mathrm{non-int}}(m_i, T, \mu_i) = \frac{g_i}{2\pi^2}\int_0^\infty E_i(k)k^2 dk \times [f(k,\mu_i) + f(k,-\mu_i)] \tag{4.52}$$

$$\begin{aligned} s_i^{\mathrm{non-int}}(m_i, T, \mu_i) = \frac{g_i}{2\pi^2}\int_0^\infty k^2 dk[&-f(k,\mu_i)\ln f(k,\mu_i) \\ &- (1-f(k,\mu_i))\ln(1-f(k,\mu_i)) \\ &- f(k,-\mu_i)\ln(f(k,-\mu_i)) \\ &- (1-f(k,-\mu_i))\ln(1-f(k,-\mu_i))] \end{aligned} \tag{4.53}$$

$$n_i^{\mathrm{non-int}}(m_i, T, \mu_i) = \frac{g_i}{2\pi^2}\int_0^\infty k^2 dk \times [f(k,\mu_i) + f(k,-\mu_i)]. \tag{4.54}$$

The degeneracy factor g_i consists of the number of degrees of freedom and is in the case of the considered quark matter $g_i = 2_{\mathrm{spin}} \times 3_{\mathrm{color}} = 6$. The functions $f(k, \pm\mu_i)$ are the Fermi distributions with momentum k, the quark Fermi energy $E_i(k) = \sqrt{m_i^2 + k^2}$ and the chemical potentials for particles $(+\mu_i)$ and the antiparticles $(-\mu_i)$:

$$f(k, \pm\mu_i) = \frac{1}{e^{\frac{(E_i(k)\mp\mu_i)}{T}} + 1}. \tag{4.55}$$

This model can be extended to include interactions of quarks. One way is to additionally consider first-order corrections for the strong interaction with a strong-interaction constant α_s as for example done in [63]. In this work, we use the same extension as described in [65]. In the case of massless quarks an analytical expression for the thermodynamic potentials at finite temperature and finite strong-interaction constant α_s can be derived. Therefore in [65] the pressure for massive quarks of flavor i is assumed to be:

$$\begin{aligned} p_i(m_i, T, \mu_i, \alpha_s) &= p_i(m_i, T, \mu_i, 0) + [p_i(0, T, \mu_i, \alpha_s] - p_i(0, T, \mu_i, 0)] \\ &= p_i(m_i, T, \mu_i, 0) - \left[\frac{7}{60} T^4 \pi^2 \frac{50\alpha_s}{21\pi} + \frac{2\alpha_s}{\pi} \left(\frac{1}{2} T^2 \mu_i^2 + \frac{\mu_i^4}{4\pi^2} \right) \right] \end{aligned} \tag{4.56}$$

$p_i(m_i, T, \mu_i, 0)$ corresponds to Eq. 4.51 and can be numerically solved. From Eq. 4.56, similar expressions for ϵ_i, s_i and n_i can be derived. This procedure is only applied to strange quarks. In this work, we choose a strange quark mass of $m_s = 100$ MeV which is in accordance with the range $m_s \sim 70 - 130$ MeV and the weighted average of $105^{+1.5}_{-1.3}$ of Amsler et al. [9]. Up and down quarks are treated as massless since their masses are only of the order of a few MeV. Heavier quark flavors are not included in our model since they are to heavy to appear in conditions of core-collapse supernovae and neutron stars.

4.4 Hybrid EOS

In this section, we describe how hybrid equations of state[5] are constructed in the present work. In Sec. 4.4.1 the model for cold hybrid stars is introduced which will be later used in the parameter scan for a systematic investigation of the phase-transition parameters. In Sec. 4.4.2 the concepts of constructing a hybrid supernova equation of state are introduced. These concepts are later used to construct the new hybrid supernova equation of state "BASQUARK" (see Chapter 6).

4.4.1 Hybrid neutron star EOS

Matter in cold hybrid stars is described under the condition $T = 0$ and is assumed to be in β-equilibrium. Alford et al. introduced in Ref. [7] a simple model to describe hybrid stars in a systematic way. We closely follow this modeling, except for one difference: Alford et al. used the rather soft HLPS and the rather stiff NL3 EOS for the hadronic part in [7] (respectively BHF and DBHF in [5]), to illustrate its impact on the hybrid star configurations. Instead, we apply HS(DD2) (respectively BHB$\Lambda\phi$ to study the effect of hyperons) which has a "stiffness" somewhere in between the

[5] We define hybrid equations of state as equations of state that contain both, hadronic and quark matter.

equations of state used by Alford et al.. The quark phase is described by the constant speed of sound (CSS) EOS as in Ref. [7]. Both phases are connected by the means of a Maxwell construction [7]. This means that local charge neutrality is assumed implicitly. It implies pressure, temperature and baryon chemical equilibrium at the transition point and no phase coexistence region is present in compact stars. In fact, previous parameter scans did not consider chemical equilibrium explicitly, which we will discuss further in Sec. 5.5. Pressure equilibrium at the transition pressure p_{trans} can be formulated as $p^{\mathrm{hadronic}} = p^{\mathrm{quark}} = p_{\mathrm{trans}}$. A direct consequence of the Maxwell construction is the appearance of a discontinuity in the energy density $\Delta\epsilon = \epsilon^{\mathrm{quark}} - \epsilon^{\mathrm{hadronic}}$ at p_{trans}. For a deconfinement transition from hadronic to quark matter one has $n_B^{\mathrm{quark}} > n_B^{\mathrm{hadronic}}$ (with the baryon number density n_B) and therefore also $\epsilon^{\mathrm{quark}} > \epsilon^{\mathrm{hadronic}}$.

The phase transition and the quark EOS depend on three variables: the transition pressure p_{trans}, the speed of sound in quark matter c_{QM} and the value of the discontinuity in the energy density $\Delta\epsilon$. In the present work we fix the speed of sound to $c^2_{\mathrm{QM}} = 1/3$ and $c^2_{\mathrm{QM}} = 1$ while p_{trans} and $\Delta\epsilon$ are varied systematically. The final form of the equation of state is written as

$$\epsilon(p) = \begin{cases} \epsilon^{\mathrm{hadronic}}(p) & p \leq p_{\mathrm{trans}} \\ \epsilon^{\mathrm{hadronic}}(p_{\mathrm{trans}}) + & \\ \Delta\epsilon + c_{\mathrm{QM}}^{-2}(p - p_{\mathrm{trans}}) & p > p_{\mathrm{trans}} \ . \end{cases} \tag{4.57}$$

This means that p_0 in Eq. (4.30) is fixed by the pressure and energy density of quark matter at the transition point, p_{trans} and $\epsilon_{\mathrm{CSS}}(p_{\mathrm{trans}}) = \epsilon_{\mathrm{trans}} + \Delta\epsilon$, with $\epsilon_{\mathrm{trans}} = \epsilon^{\mathrm{hadronic}}(p_{\mathrm{trans}})$, leading to

$$p_0 = p_{\mathrm{trans}} - c^2_{\mathrm{QM}}(\epsilon_{\mathrm{trans}} + \Delta\epsilon). \tag{4.58}$$

4.4.2 Hybrid supernova EOS

We construct an equation of state from the pure hadronic phase described by the HS(DD2) EOS to the quark phase described by the thermodynamic bag model explained in Sec. 4.3.3. The construction of the phase transition is done applying the Gibbs approach described in [78, 65]. This section closely follows these references.

In a Gibbs phase transition, conservation laws are globally fulfilled and the pressure within the mixed phase is a smooth function of the density. This allows a phase coexistence of hadron and quark matter in the phase transition region. Like the Maxwell phase transition, the Gibbs phase transition is of first order. In this work, finite-size effects and Coulomb contributions are neglected and the phases are treated

in the thermodynamic limit[6]. We define k as a globally conserved quantity. The corresponding chemical potentials are equal in the hadron and the quark phases. The conditions in the phase coexistence region, considering thermal and mechanical equilibrium of hadronic and quark matter, are

$$T^{\mathrm{hadronic}} \equiv T^{\mathrm{quark}} \tag{4.59}$$

$$\mu_k^{\mathrm{hadronic}} \equiv \mu_k^{\mathrm{quark}} \tag{4.60}$$

$$p^{\mathrm{hadronic}} \equiv p^{\mathrm{quark}} \ . \tag{4.61}$$

In the hadronic and the quark phase, the pressures p^{hadronic} and p^{quark} are sums over all available particles, including electrons and neutrinos. The conditions where quark matter sets in are generally at high temperatures and densities. This corresponds to regimes where neutrinos are still fully trapped. At a given lepton fraction Y_L, neutrinos are in weak equilibrium with nuclear matter, electrons, and positrons (see e.g. [187, 157]). Due to the equality of the chemical potentials of electrons and neutrinos in the Gibbs approach, their contribution in other thermodynamic quantities, like the pressure in Eq. 4.61, cancels as a consequence. In [91] it was shown that if an equation of state is provided for given temperature T, proton fraction Y_p, and baryon density n_B, neutrino contributions do not have to be taken into account when constructing a Gibbs or a Maxwell phase transition.

The equilibrium conditions where deconfinement takes place can be expressed as

$$p \leftrightarrow 2u + d \tag{4.62}$$

$$n \leftrightarrow 2d + u \ . \tag{4.63}$$

These conditions can be used to express the corresponding relations for the up and down quarks:

$$\mu_u = \frac{2}{3}\mu_p - \frac{1}{3}\mu_n \tag{4.64}$$

$$\mu_d = \frac{2}{3}\mu_n - \frac{1}{3}\mu_p \tag{4.65}$$

Weak reactions which produce strangeness (e.g. kaon decays [9]) happen on a shorter timescale (10^{-6}s) while the dynamical timescales in core-collapse supernova simulations are on the order of 10^{-3}s. Such reactions should be equilibrated in nuclear matter. As a consequence, strangeness has either to be already present in nuclear matter through hyperons (as e.g. in BHB$\Lambda\phi$) or has to be produced by a series of weak interactions in the quark phase. The reaction in the quark phase can be expressed as

$$u + d \leftrightarrow u + s \tag{4.66}$$

[6]Note that without neglecting the finite-size effects and Coulomb contributions, structures similar to the know pasta phases in hadronic matter can appear (spheres, rods, plans, ...).

which leads to

$$\mu_s = \mu_d \tag{4.67}$$

for the chemical potential of the strange quark. To characterize the mixed phase, the fraction of quark matter χ is introduced:

$$\chi = \frac{V^{\text{quark}}}{V^{\text{hadronic}} + V^{\text{quark}}}, \tag{4.68}$$

with the volume fractions for hadronic and quark matter V^{hadronic} and V^{quark}, respectively. Using χ the phase transition region and the pure hadronic and quark phase can be expressed as

$$\chi = 0 \text{ hadronic phase} , \tag{4.69}$$

$$0 < \chi < 1 \text{ mixed phase} , \tag{4.70}$$

$$\chi = 1 \text{ quark phase} . \tag{4.71}$$

In the mixed phase ($0 < \chi < 1$), the baryon number density n_B, the energy density ϵ, and the entropy density s can be calculated as a combination of the hadron and quark contributions:

$$n_B = (1-\chi) n_B^{\text{hadronic}} + \chi n_B^{\text{quark}} , \tag{4.72}$$

$$\epsilon = (1-\chi) \epsilon^{\text{hadronic}} + \chi \epsilon^{\text{quark}} , \tag{4.73}$$

$$s = (1-\chi) s^{\text{hadronic}} + \chi s^{\text{quark}} . \tag{4.74}$$

The proton fraction Y_p is a global quantity within the Gibbs approach. This leads to the following relation

$$Y_p n_B = (1-\chi) Y_c^{\text{hadronic}} n_B^{\text{hadronic}} + \chi Y_c^{\text{quark}} n_B^{\text{quark}} . \tag{4.75}$$

In Eq. 4.75 the charge fraction for hadronic matter is denoted by $Y_c^{\text{hadronic}} = n_p / n_B^{\text{hadronic}}$ and for quark matter $Y_c^{\text{quark}} = n_c^{\text{quark}} / n_B^{\text{quark}}$. n_c^{quark} can be calculated using the relation

$$n_c^{\text{quark}} = \frac{2n_u - n_d - n_s}{3} . \tag{4.76}$$

Start and end of the phase transition are chosen in such a way that in case of $T = 0$ and β-equilibrium the phase transition region is close to the the parameters p_{trans} and $\Delta\epsilon$ which are evaluated in Sec. 5.

Sagert et al. and Fischer et al. [65, 174, 175] generated several hybrid supernova equations of state in their papers. Here, we use the same quark interactions as applied in some of these equations of state. Similar quark-hadron hybrid supernova equations of state have also been generated by Nakazato et al. [149, 150]. They did not consider corrections from strong interactions, and therefore obtain maximum masses only below 2 $M_\odot$. Table 4.3 gives an overview of the already published

Name	$B^{1/4}$ (MeV)	α_s	$M_{\max}$ ($M_\odot$)	Explosion	Reference
B162	162	0	1.56	Yes	[174, 65]
B165	165	0	1.50	Yes	[174, 65]
B155	155	0.3	1.67	Yes	[65]
B139	139	0.7	2.04	No	[175, 67]
B145	145	0.7	1.97	No	[175]
B209	209	0	1.80	No	[149, 150]
B162	162	0	1.54	Yes	[150]
B184	184	0	1.36	No	[150]

Tab. 4.3: Overview of existing hybrid supernova equations of state and their tests in spherically symmetric core-collapse supernova simulations simulations. All models employ $m_s = 100$ MeV.

hybrid supernova equations of state. In all of them, STOS [183, 184, 182] was used for the hadronic part (see Sec. 4.2.2).

5 A Systematic Analysis of Cold Hybrid Stars

> *Schreiben ist gut, Denken ist besser. Klugheit ist gut, Geduld ist besser.*
>
> — **Hermann Hesse**
> Siddhartha

In this chapter we present the method and results of our so-called *parameter scan* which represents a systematic variation of the phase-transition parameters in hybrid stars and the calculated mass-radius relations. The results written in Sec. 5.2-5.6 have been published in [87] while Sec. 5.7 contains new additional data.

In order to systematically analyze hybrid stars in regard to the maximum mass constraint we use the scheme proposed by Alford et al. [7], applying a simplified, but representative quark equation of state. Four different subclasses of hybrid stars were introduced in [7] according to the stability of hybrid stars at the onset of quark matter and/or the existence of a third family[1] (see discussion in Chapter 3). In a subsequent work [5], a more detailed analysis was presented and different hadronic equation of states were applied. Zacchi et al. [216, 217] used the approach of Alford et al. for comparison of the results obtained with a newly developed SU(3) quark equation of state. A special emphasis was put on the occurrence of twin stars, which are pairs of compact stars at equal masses. For the hadronic equation of state, they used the relativistic mean-field model DD2 [204] as we do in the present study. Alford's classification was also applied in a number of other works [32, 172, 6, 8], varying the hadronic and/or quark equations of state. Similar parameter scans for quark matter properties were done in [208, 218], where, however, only the maximum mass but not the type of hybrid star was investigated. In this work, the motivation to use the parameter scan is different: One of the main motivations is to gather more insights about the parameter space describing the quark matter equation of state and the resulting QCD phase transition in the context of core-collapse supernovae.

[1] Remember: In the mass-radius (M-R) relation, first family stars are white dwarfs while second family stars are neutron stars. After a phase of instability a third stable branch can build up, which consists of hybrid stars [77, 178].

5.1 Numerical setup

In this section we describe the code setup used in the parameter scan. Two pieces of information are especially relevant when modeling a hybrid star: its maximum mass and the type of hybrid star. To calculate a single compact star, the Tolman-Oppenheimer-Volkoff (TOV) equations (Eq. 3.2 and Eq. 3.3) have to be solved for a given central density (see Sec. 3.2 for more details).

To solve the TOV equations, we developed a sophisticated TOV solver. It is based on the solver described in [86]. To achieve a good converging and stable code, the TOV equations are solved using a 4th-order Runge-Kutta scheme. Using this scheme, the overall accumulated error using a stepsize h is of order $\mathcal{O}(h^4)$ (see e.g. [168, 59] for detailed discussion). An initial value problem of the form

$$y'(x) = f(x, y) \qquad \text{with} \qquad y(x_0) = y_0 \ , \tag{5.1}$$

is solved numerically. During each step, four intermediate sub-steps are calculated

$$\begin{aligned} f_0 &= f(x_0, y_0) \\ f_1 &= f(x_0 + \frac{h}{2}, y_0 + \frac{h}{2} f_0) \\ f_2 &= f(x_0 + \frac{h}{2}, y_0 + \frac{h}{2} f_1) \\ f_3 &= f(x_0 + h, y_0 + f_2) \ , \end{aligned} \tag{5.2}$$

which are then combined to the solution

$$y(x_0 + h) = y(x_0) + \frac{h}{6}(f_0 + 2f_1 + 2f_2 + f_3) \ . \tag{5.3}$$

As shown in [86], this scheme achieves good convergence in actual simulations. The maximum mass configuration with fixed transition pressure p_{trans} and discontinuity in the energy-density $\Delta\epsilon$ is obtained from the mass-radius relation, where the central density of the hybrid stars is systematically varied. The detection of the maximum mass configuration is handled automatically. To achieve better performance, the integration step size of the solver is adjusted automatically when varying the central density, assuring that the results fulfill the wished precision. Our TOV solver is able to automatically classify the calculated mass-radius relations into the four hybrid star cases as defined by Alford et al. [7]. Additionally, a feature to detect and consider multiple phase transitions in the TOV calculations is implemented.

To systematically investigate hybrid stars, the phase-transition parameters p_{trans} and $\Delta\epsilon$ have to be varied. Hence, p_{trans} and $\Delta\epsilon$ are handled as input parameters in our TOV solver. The variation of p_{trans} and $\Delta\epsilon$ is done via an external routine. This procedure allows us to run a parameter scan on a small cluster in an embarrassingly parallel way: On each CPU a TOV solver with one input combination of p_{trans} and

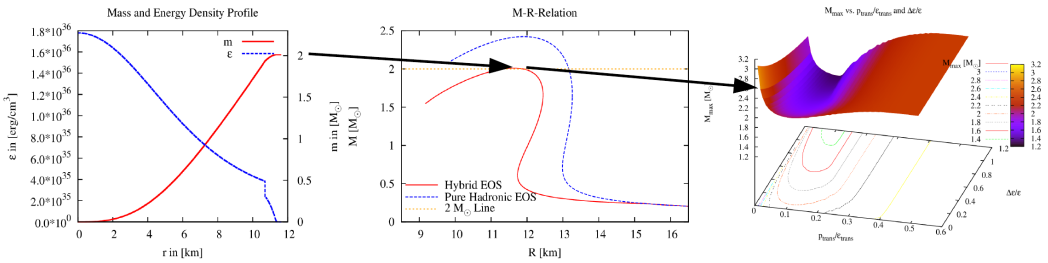

Fig. 5.1: Series of operations executed in a parameter scan: For each combination of a given central density, transition pressure p_{trans} and discontinuity in the energy density $\Delta\epsilon$ the TOV equations are solved to obtain its structure (left panel). To obtain the maximum mass configuration the central pressure has to varied (panel in the middle). When also varying the phase transition parameters p_{trans} and $\Delta\epsilon$ a three-dimensional mass distribution as a function of these two parameters is obtained (right panel).

$\Delta\epsilon$ is executed. This allows us to calculate several thousands of calculations on the order of a few hours. As a result a three-dimensional surface plot of the maximum mass as a function of these two parameters is obtained. Figure 5.1 summarizes this series of operations executed in a parameter scan.

5.2 Parameter scan

In [87], we considered 80 variations of each p_{trans} and $\Delta\epsilon$, varying p_{trans} from 1 MeV/fm^3 ($n_B \approx 0.1$ fm^{-3}) to 800 MeV/fm^3 ($n_B \approx 1.02$ fm^{-3}) while using HS(DD2) EOS. p_{trans} also fixes $\epsilon_{\mathrm{trans}}$, resulting in values $p_{\mathrm{trans}}/\epsilon_{\mathrm{trans}} = [0.01, 0.55]$. $\Delta\epsilon/\epsilon_{\mathrm{trans}}$ is varied within the range $[0, 1.3]$. In Sec. 5.4 we will also present an extended parameter scan for HS(DD2), covering the range of $p_{\mathrm{trans}}/\epsilon_{\mathrm{trans}} = [0.01, 0.55]$ and $\Delta\epsilon/\epsilon_{\mathrm{trans}} = [0, 3]$. For BHB$\Lambda\phi$ p_{trans} is varied from 1 MeV/fm^3 to 640 MeV/fm^3, covering the range of $p_{\mathrm{trans}}/\epsilon_{\mathrm{trans}} = [0.01, 0.41]$, while $\Delta\epsilon/\epsilon_{\mathrm{trans}}$ is varied from $[0, 1.3]$.

Figure 5.2 shows contour lines of the maximum mass for our considered range of parameters. The most important contour line is the 2 $M_\odot$ mass line, since all equations of state have to be able to support this mass. Such heavy compact stars can be reached at $p_{\mathrm{trans}}/\epsilon_{\mathrm{trans}} \gtrsim 0.22$ (case 1) and $p_{\mathrm{trans}}/\epsilon_{\mathrm{trans}} \lesssim 0.02$ (case 2) for any $\Delta\epsilon/\epsilon_{\mathrm{trans}}$. For $0.02 \lesssim p_{\mathrm{trans}}/\epsilon_{\mathrm{trans}} \lesssim 0.22$, $\Delta\epsilon/\epsilon_{\mathrm{trans}}$ (case 3) is limited to low values to be compatible with the observational constraint. In case 1, the hadronic phase is dominant and a mass of 2 $M_\odot$ is reached already in the hadronic branch. The higher $p_{\mathrm{trans}}/\epsilon_{\mathrm{trans}}$ gets, the later the quark phase sets in. At high values of $p_{\mathrm{trans}}/\epsilon_{\mathrm{trans}}$, hybrid stars consist almost only of hadronic matter. For $p_{\mathrm{trans}}/\epsilon_{\mathrm{trans}} > 0.47$, eventually the transition pressure is above the central pressure of the heaviest stable hadronic star. For low $p_{\mathrm{trans}}/\epsilon_{\mathrm{trans}}$ (case 2), one obtains an almost pure quark star with only a thin hadronic layer on top. At the lowest p_{trans}

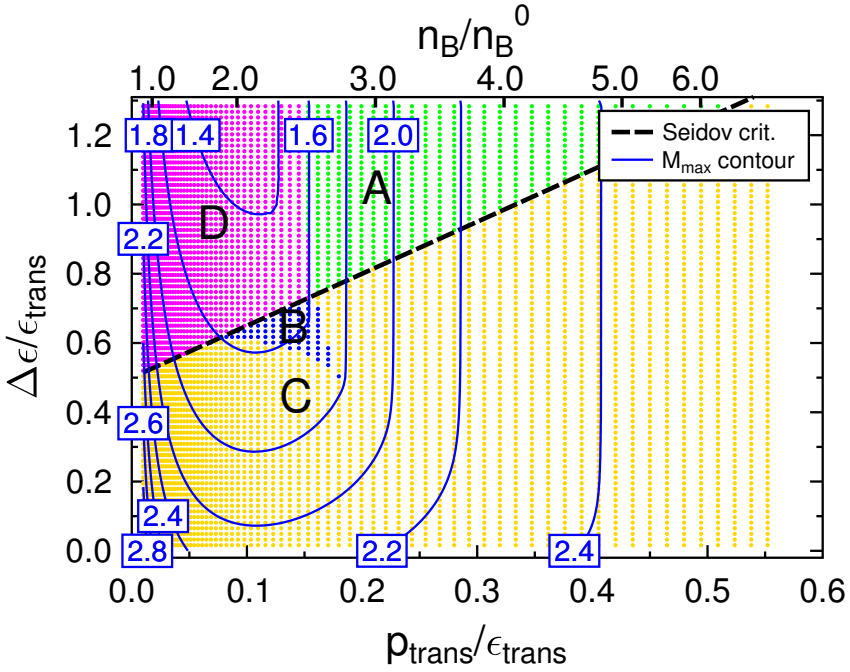

Fig. 5.2: Calculated hybrid star configurations, colored to distinguish the four cases A (absent), B (both), C (connected) and D (disconnected). The lines in blue show the maximum mass contours for 1.4, 1.6, 1.8, 2.0, 2.2, 2.4, 2.6, and 2.8 $M_\odot$. The thick black dashed line shows the analytic criterion from Seidov [180], above which neutron stars are unstable at the onset of quark matter. Published in [87].

and $\Delta\epsilon$, extremely high maximum masses of over 3 $M_\odot$ can be reached, well above the maximum mass of HS(DD2).

The dots in Fig. 5.2 represent all the parameter configurations that have been calculated. The color coding classifies the resulting M-R relations according to the four cases of Alford et al. The straight black diagonal line represents the analytical constraint derived by Seidov in 1971 [180]: $\Delta\epsilon_{\rm crit}/\epsilon_{\rm trans} = 1/2 + 3/2 \cdot p_{\rm trans}/\epsilon_{\rm trans}$. If $\Delta\epsilon$ is below $\Delta\epsilon_{\rm crit}$, hybrid stars are stable at the onset of quark matter. Above the Seidov line, cases A (green) and D (magenta) are found, below cases C (yellow) and B (blue). Apparently, $p_{\rm trans}$ has to be chosen low enough, to obtain a disconnected third family branch. Interesting cases for supernova simulations are in the small region on the left side of the two solar mass line and above the Seidov line. There, hybrid stars with a third family branch and maximum masses above 2 $M_\odot$ are found. Furthermore, they correspond to low onset densities of the phase transition between 1 and 2 n_B^0 (with n_B^0 denoting the nuclear saturation density) which is required to reach quark matter in a core-collapse supernova simulation, at least for low- and intermediate-mass progenitors, see [66]. Note that such low transition densities are compatible with heavy-ion collision experiments, where matter is more symmetric and strangeness is not in equilibrium, which shifts the phase transition to much higher densities [65].

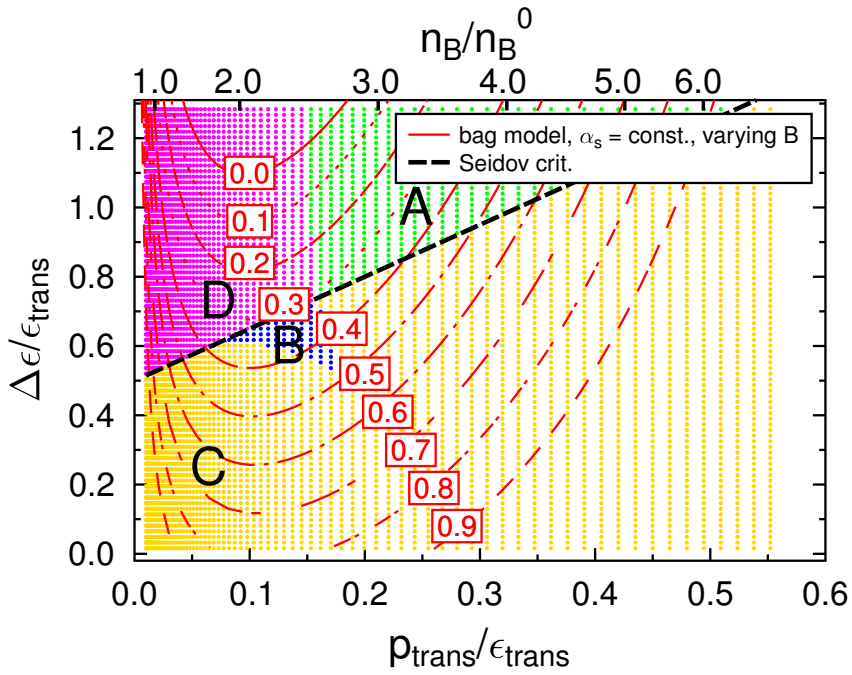

Fig. 5.3: Similar to Fig. 5.2, but with red lines showing the solutions of the bag model from Eq. (4.41) for varying B with increasing values from left to right, different values of α_s (as indicated in the figure), and $m_s = 0$. Published in [87].

In [5], Alford and Han showed results of a similar parameter scan done also for the CSS EOS with $c_s^2 = 1/3$, but with the stiff DBHF EOS and the soft BHF EOS for the hadronic phase, and in [7] for the HLPS and NL3 hadronic EOSs. The general distribution of the cases found here is the same as in [7] and [5]. The 2 $M_\odot$ curve from Fig. 5.2 behaves in a similar way as the 1.95 $M_\odot$ line of DBHF in Fig. 5 of [5]. Considering these two references, our results seem to be consistent with Alford et al. We can state here, that for $c^2_{\mathrm{QM}} = 1/3$, the hadronic phase has little impact on the distribution of the hybrid stars in the $p_{\mathrm{trans}}/\epsilon_{\mathrm{trans}}$ vs $\Delta\epsilon/\epsilon_{\mathrm{trans}}$ plot.

5.3 Comparing the quark EOS models

As discussed in Sec. 4.3.2, the CSS EOS is not a very common equation of state for the description of quark matter. However, it was shown that for the case $m_s = 0$ and the use of a strong interaction parameter α_s the commonly used bag model is transferable into the CSS model. Figure 5.3 shows a comparison of the CSS EOS and the bag EOS used for the description of quark matter. By varying the bag constant B from lower to higher values (left to right on the red curves) as well as the α_s parameter (increasing α_s leads to a downward shift of the curves), the whole parameter space of the CSS model can be reproduced.

More realistic models of quark matter often employ a finite strange quark mass. A typical value is $m_s = 100$ MeV, which is, as mentioned by Fischer et al. in [65] in accordance with the range $m_s \sim 70 - 130$ MeV and the weighted average of

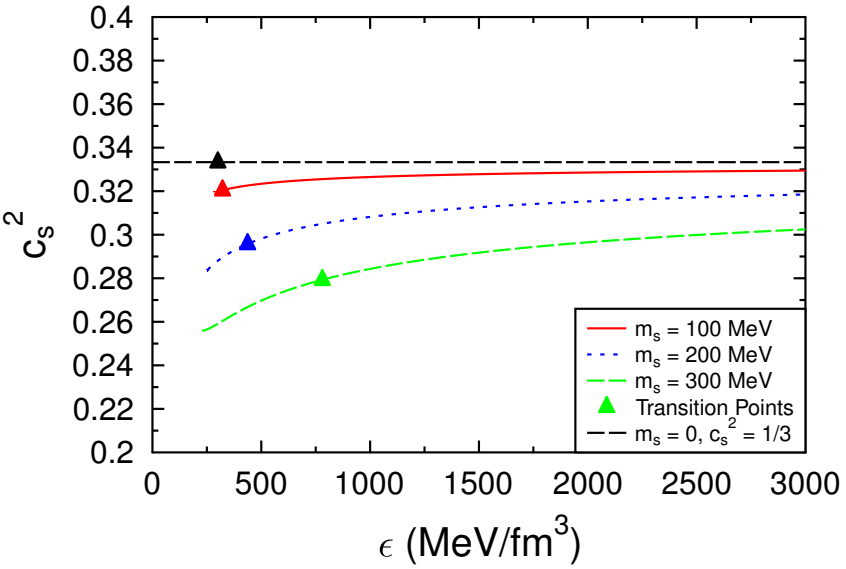

Fig. 5.4: Dependency of the speed of sound on the energy density for four different values of m_s (0, 100, 200 and 300 MeV), $B^{1/4} = 155$ MeV and $\alpha_s = 0.3$. The phase-transition points are indicated with triangles. Published in [87].

$105^{+1.5}_{-1.3}$ MeV of Amsler et al. [9]. Figure 5.4 shows the influence of a finite m_s on the speed of sound squared c_s^2. With increasing m_s, the speed of sound deviates significantly from the value of $c_s^2 = 1/3$, corresponding to $m_s = 0$ MeV. However, for $m_s = 100$ MeV the deviations are still small. The energy densities $\epsilon_{\text{trans}} + \Delta\epsilon$ at the phase transition from hadronic to quark matter are indicated in Fig. 5.4 by triangles. For $m_s = 200$ and 300 MeV, the strongly deviating part at the beginning is not of importance, since the phase transition happens at higher energy densities. As visible in the figure, if the value of the strange quark mass is larger than 100 MeV, it shifts the phase transition to higher densities, but for $m_s = 100$ MeV the effect is still small. As a conclusion we can state that with a finite m_s the one-to-one correspondence between the CSS model and the bag model is not true anymore, but nevertheless the models are still comparable. We have checked that at least for $m_s = 100$ MeV the induced differences in the M-R relation are small. Only for detailed comparisons, the exact M-R relations have to be calculated with the strange quark mass taken into account.

5.4 Restricting the bag model parameter space

As summarized in Table 4.3 in Sec. 4.4.2, so far only hybrid equations of state that have maximum masses below 2 $M_\odot$ were found to lead to explosions in spherically symmetric core-collapse supernova simulations. In particular, the models B139 and B145, which both have QCD interaction terms and support maximum masses around 2 $M_\odot$, did not lead to explosions. Currently, these are the only two available supernova equations of state that include quark matter and support maximum

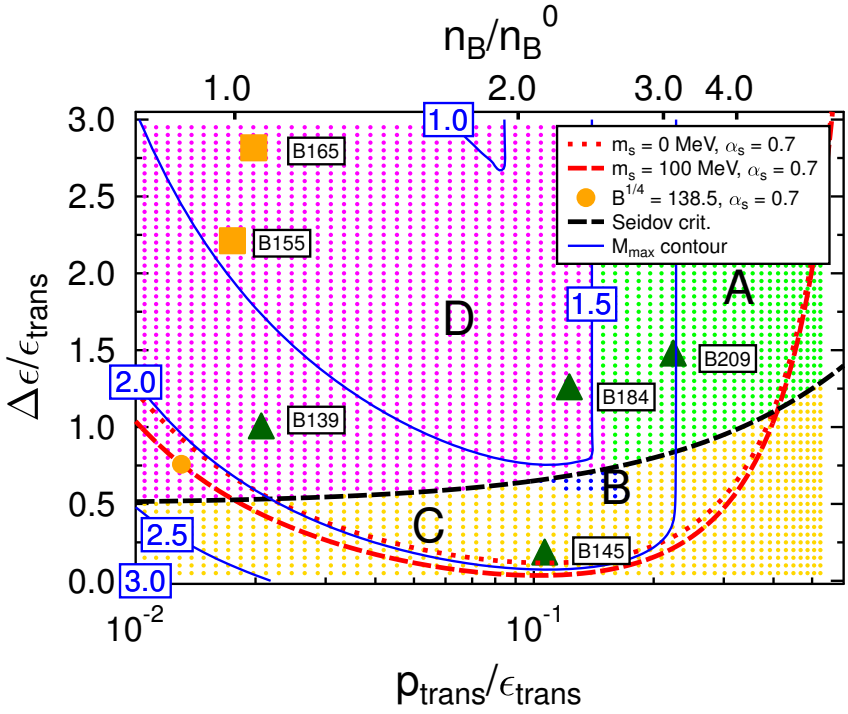

Fig. 5.5: Parameter scan extended to higher $\Delta\epsilon/\epsilon_{\mathrm{trans}}$ and logarithmic scale for $p_{\mathrm{trans}}/\epsilon_{\mathrm{trans}}$. Additionally, the phase transition parameters of the hybrid equations of state of Table 4.3 are plotted with yellow squares (explosions found) and green triangles (no explosions found). Note that the hadronic part of these equations of state is based on STOS, whereas the results in the figure (maximum mass and classification) are based on HS(DD2), for details see the main text. Marked with a yellow circle is an example case whose M-R relation is shown in Fig. 5.6. Published in [87].

neutron stars masses above 2 $M_\odot$. Note that so far only very few progenitors have been tested in core-collapse supernova simulations of this scenario. A systematic progenitor exploration is still missing, even for the few existing hybrid supernova equations of state.

In the following, we use the properties of the existing hybrid supernova equations of state listed in Table 4.3 to identify interesting regions of the quark matter parameter space which could be favorable for core-collapse supernova explosions. In these equations of state STOS is used for the description of hadronic matter and Gibbs' conditions for phase equilibrium are applied. For the present parameter scan HS(DD2) and Maxwell's conditions are used instead, which complicates the comparison. For the aspects we are mostly interested in the parameters $p_{\mathrm{trans}}/\epsilon_{\mathrm{trans}}$ and $\Delta\epsilon/\epsilon_{\mathrm{trans}}$ are more relevant than the bag model parameters: the former have a physical meaning independent on the particular hadronic equations of state that is used, as, for example, they determine whether or not hybrid stars are stable at the onset of quark matter (cases A and D vs B and C). Therefore we calculate these parameters for the STOS EOS and the given bag model parameters m_s, B, and α_s. As the only difference to the original hybrid equations of state of Table 4.3, we have to assume local instead of global charge neutrality to achieve the desired Maxwell transition at

constant pressure. The results are shown by green triangles and yellow squares in Fig. 5.5. Four of the seven configurations did not lie in the original parameter space used in Fig. 5.2. For this reason, we expanded the parameter space to $\Delta\epsilon/\epsilon_{\rm trans}$ up to 3. Now only B162, with $\Delta\epsilon/\epsilon_{\rm trans} \approx 6.1$ and $p_{\rm trans}/\epsilon_{\rm trans} \approx 0.005$ lies outside the parameter range considered in the figure. We are also using a logarithmic scale for $p_{\rm trans}/\epsilon_{\rm trans}$ to achieve a clearer presentation of the data. Note that the maximum mass contour lines and Alford classification are still calculated for the HS(DD2) EOS (as before) so that they are different from the values given in Table 4.3, due to the procedure described above.

The exploding equations of state B155 and B165 have values just slightly above $p_{\rm trans}/\epsilon_{\rm trans} = 0.01$. B139 has a comparable value of $p_{\rm trans}/\epsilon_{\rm trans}$ to the ones from B155 and B165, but differs in the energy discontinuity $\Delta\epsilon$ which is smaller. B145 seems to be rather different: the phase transition happens at very high $p_{\rm trans}/\epsilon_{\rm trans}$ and low $\Delta\epsilon/\epsilon_{\rm trans}$. B184 and B209 have similar $p_{\rm trans}/\epsilon_{\rm trans}$ but higher $\Delta\epsilon/\epsilon_{\rm trans}$. These results indicate that a high $\Delta\epsilon/\epsilon_{\rm trans}$ and low $p_{\rm trans}/\epsilon_{\rm trans}$ are more favorable for obtaining explosions. Interestingly, these are the conditions that result in a disconnected third family. This confirms our expectations presented in the introduction (see Sec. 3.3.2) and is in agreement with [95], that supernova explosions induced by a QCD phase transition are related to the existence of a third family. Note that B139 has a disconnected third family but did not explode, indicating that a *pronounced* third family is favorable for explosions. It has to be emphasized that the inclusion of the existing hybrid equation of state in Fig. 5.5 can only serve as a weak guideline regarding the explodability, because in the simulations a different hadronic equation of state STOS is used, and global instead of local charge neutrality is assumed.

As already discussed in Sec. 5.2, the 2 $M_\odot$ line in Fig. 5.5 excludes a lot of potential parameter combinations for new supernova equations of state. Only the "disconnected" cases D in the lower left corner, which have a sufficiently high maximum mass, are left as interesting candidates. The other parameter regions with $M_{\rm max} > 2\ M_\odot$ have either a very low $\Delta\epsilon/\epsilon_{\rm trans}$ or a very high $p_{\rm trans}/\epsilon_{\rm trans}$, and in any case do not lead to a third family of compact stars. These results nicely illustrate the tension between high maximum masses and the possibility of core-collapse supernova explosions induced by a strong phase transition, but there is still an interesting parameter region remaining.

Next we discuss the implications for the bag model formulation of the quark equation of state. Choosing $\alpha_s = 0.7$ leads to configurations that lie almost on top of the 2 $M_\odot$ line in the lower left corner, as can be seen by the red dotted line in Fig. 5.5. We consider this as a lower boundary for α_s to choose. Higher values of α_s are allowed, too, but are constrained to be above the Seidov line if one requires a third family. Considering a finite strange quark mass of $m_s = 100$ MeV shifts the $\alpha_s = 0.7$ line slightly to lower $\Delta\epsilon_{\rm trans}$ values, as can be seen by comparing with the red dashed

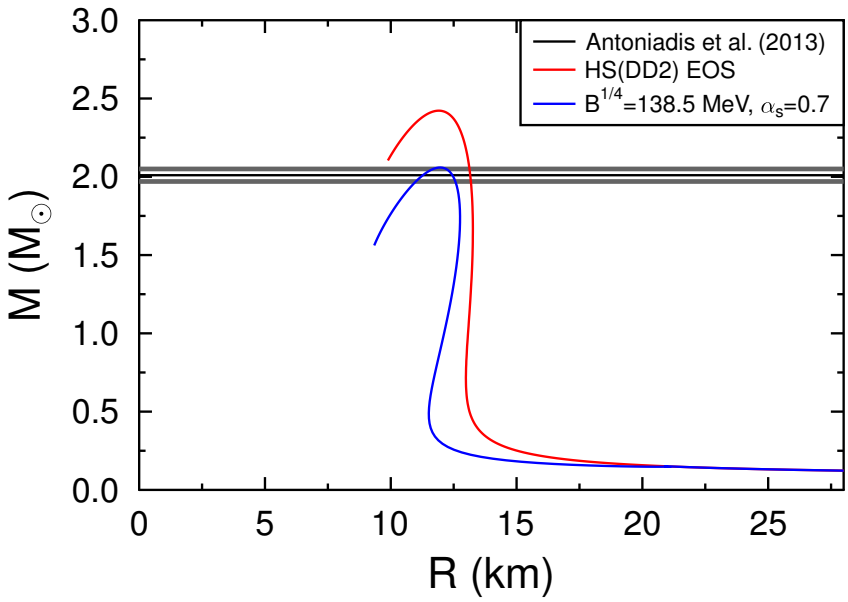

Fig. 5.6: M-R relation of an example hybrid equation of state which might be interesting for core-collapse supernovae. The quark matter parameters are $m_s = 100$ MeV, $\alpha_s = 0.7$, and $B^{1/4} = 138.5$ MeV. Published in [87].

line. However, cases with same bag constants B and interaction parameters α_s, but different strange quark masses m_s, can lead to big differences in $\Delta\epsilon/\epsilon_{\rm trans}$ and $\epsilon_{\rm trans}/p_{\rm trans}$ values, which is not visible in the figure.

As an example of what a possible hybrid star configuration might look like, we chose the configuration $m_s = 100$ MeV, $\alpha_s = 0.7$, and $B^{1/4} = 138.5$ MeV. The phase transition properties are shown in Fig. 5.5 by the yellow circle and the mass-radius relation is shown in Fig. 5.6. The values of the phase transition parameters are $p_{\rm trans}/\epsilon_{\rm trans} = 0.013$ and $\Delta\epsilon/\epsilon_{\rm trans}$=0.76. The maximum mass configuration has $M_{\rm max} = 2.05$ M$_\odot$ with $R = 11.98$ km. For 1.4 M$_\odot$ the hybrid equation of state leads to a somewhat smaller radius of 12.64 km than HS(DD2) with 13.22 km. The onset of quark matter in the M-R curve takes place around 22 km, corresponding to a density of 0.127 fm^{-3} which is close to n_B^0. Note again, that such a low onset density in neutron stars is not in disagreement with heavy-ion collision experiments. For the conditions in heavy-ion collisions (isospin symmetric matter with zero net strangeness), the onset density at $T = 0$ shifts to much higher values: for the example case to 0.962 fm^{-3}.

It is important to point out that the third-family feature of the example case is so weak, that it is almost not visible in Fig. 5.6. Also for the other cases B and C with stable hybrid stars we found that the characterizing features often are very weak, and look very different than the prime examples of Fig. 3.1 discussed in Sec. 3.3.1. However, in [95] it was shown that finite entropies as they occur in the protoneutron star in a core-collapse supernova can significantly enhance the third-family features so that they become very pronounced (see discussion in Sec. 3.3.2).

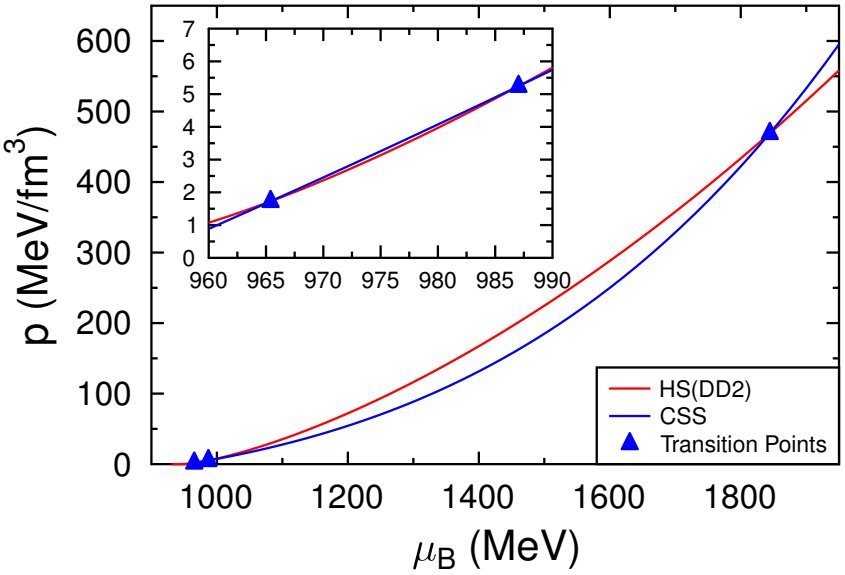

Fig. 5.7: Example case with three phase transitions. The inlay shows a zoom-in of the first two phase transitions. Published in [87].

5.5 Reconfinement and stability of quark matter

In the model used in Sec. 5.2, by construction there is always just one (deconfinement) phase transition, which goes from hadronic to quark matter. Figure 5.2 shows that in this case masses well above 2 $M_\odot$ and even above the maximum mass of the hadronic HS(DD2) EOS are possible. However, the $p(\mu_B)$ relation of the CSS EOS derived in Eq. 4.43 reveals that more than a single phase transition can happen. Multiple phase transitions were also found for other hybrid equations of state; see, e.g., [123, 218, 42, 26]. Figure 5.7 shows an example where three phase transitions occur. The phase transition in the original setup of the parameter scan, where the $p(\mu_B)$-relation is not considered, is the one most to the left, with values $p_{\text{trans}}/\epsilon_{\text{trans}} \simeq 0.014$ and $\Delta\epsilon/\epsilon_{\text{trans}} = 0.2$. For higher chemical potentials, by construction the CSS quark EOS is always used. From the selected values of p_{trans} and $\Delta\epsilon$ and the condition for chemical equilibrium at the transition point (see Eq. 4.44), the $p(\mu_B)$ relation of the CSS EOS is uniquely fixed. By using this relation as shown in Fig. 5.7, it turns out that quark matter is not the true ground state for chemical potentials between approximately 987 and 1844 MeV. Instead, at 987 MeV a reconfinement transition from quark to hadronic matter takes place, and another deconfinement transition around 1844 MeV. We abbreviate such a series of phase transitions as HQHQ. The original setup is forced to have only one phase transition and the other(s) are ignored. Strictly speaking, this leads to thermodynamically unstable solutions (violating the second law of thermodynamics), which, however, can be justified by making additional assumptions. We give a more elaborate assessment of reconfinement and multiple phase transitions at the end of this section.

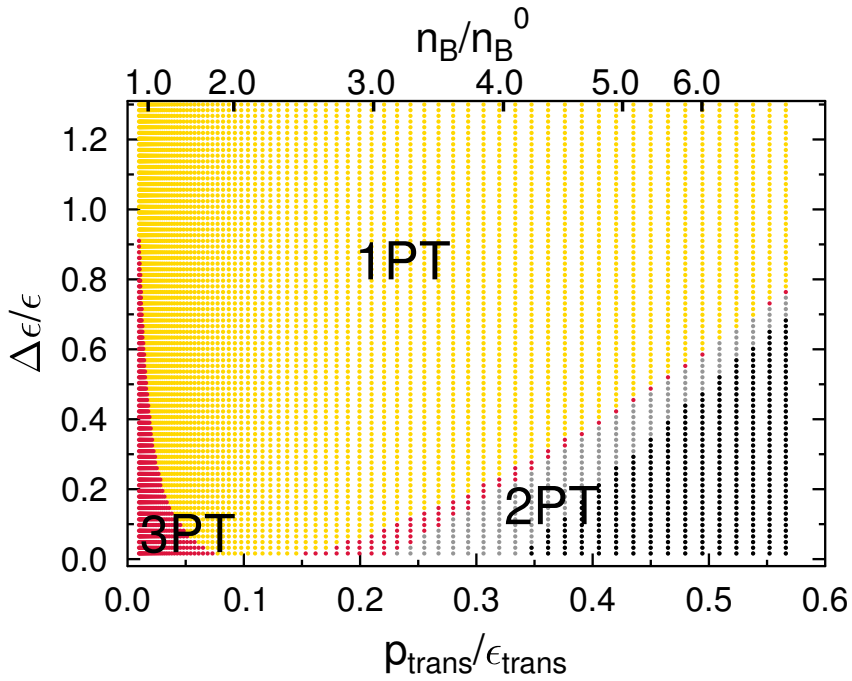

Fig. 5.8: This figure shows the number of phase transitions that occur for given $\Delta\epsilon$ and p_{trans}. The yellow dots represent cases with one phase transition (HQ), red dots with three phase transitions (HQHQ), and grey dots with two phase transitions (QHQ), where quark matter is absolutely stable. The black dots represent QHQ cases, where even negative energy densities occur. Published in [87].

Considering the parameter range of Fig. 5.2, we find that there are one, two, or three phase transitions possible, as shown in Fig. 5.8. The yellow dots in Fig. 5.8 represent the cases where only one phase transition happens. It occurs from hadronic to quark matter (HQ transition) and therefore does not differ from the transition points chosen manually in the original parameter scan. The red dots correspond to cases with three phase transitions (HQHQ), as discussed for Fig. 5.7. The grey dots describe cases with two phase transitions (QHQ). They differ from the first two, since quark matter exists also at the lowest densities. At intermediate densities reconfinement happens, a phase with hadronic matter appears, which disappears again in a deconfinement transition at higher densities. The resulting compact stars of QHQ cannot be considered as hybrid stars in a classical sense, but more as quark stars with a thin hadronic shell somewhere in their interior. In fact, as quark matter is the ground state at lowest densities, this case corresponds to absolutely stable strange quark matter. The black dots represent unphysical cases, where, on top of that, quark matter even has negative energy densities. For these reasons we will not consider the QHQ cases as viable models for the supernova equation of state in our hybrid star analysis.

Figure 5.9 shows the parameter scan taking multiple phase transitions into account. In addition to the color coding used in Fig. 5.2, which distinguishes the type of hybrid star, A, B, C, and D, red dots show cases with a reconfinement transition

(HQHQ), and the grey dots cases of QHQ where strange quark matter is absolutely stable. For such cases with multiple phase transitions, the hybrid-star classification of Alford cannot be applied.

The maximum mass contour lines up to 2 $M_\odot$ and slightly above lie completely in the HQ area. Therefore, they correspond exactly to the ones shown in Fig. 5.2. This is also true for the regions of hybrid star cases A and B. Imposing strict thermodynamic stability has a strong effect on the maximum masses in the other regions, which would have been cases D or C otherwise. With strict thermodynamic stability masses above the maximum mass of the HS(DD2) EOS are not possible anymore in the lower left corner. For example, for the phase transition parameters which are used in Fig. 5.7 ($p_{\mathrm{trans}}/\epsilon_{\mathrm{trans}} \simeq 0.014$ and $\Delta\epsilon/\epsilon_{\mathrm{trans}} = 0.2$) and which are situated in the three phase transition region, the maximum mass changes from 2.53 $M_\odot$ (HQ) to 2.42 $M_\odot$ (HQHQ). QHQ phase transitions on the other hand, with the additional occurrence of quark matter at low densities taken into account, lead to an increased maximum mass above the one of HS(DD2). This is due to the dominance of quark matter in these compact stars, which in fact are almost pure quark stars. The triangular region in the lower right without points represents the unphysical cases where negative energy densities would occur, for which the M-R relations are not calculated. Finally we note that the phase transition parameters extracted for the hybrid equations of state of Table 4.3, and which are shown in Fig. 5.5, do not lead to the problem of reconfinement, at least not for the HS(DD2) hadronic equation of state employed in the present study. The same is true for the phase transition parameters belonging to the example of Fig. 5.6.

Chamel et al. also discussed the possibility of multiple phase transitions for a few example equations of state [42]. They observed the same behavior as discussed above in the HQHQ case: a first phase transition to quark matter, then another one back to hadronic matter, and finally a last one to quark matter with increasing pressure is observed. It is also mentioned that the appearance of quark deconfinement in the strictly thermodynamically stable setup always leads to a lowering of the maximum mass. In contrast, if only one phase transition is enforced, the maximum mass can be increased, as we observe too.

Similar results were obtained by Zdunik and Haensel [218]. They showed that the reconversion of quark matter back to hadronic matter limits the size of the quark core in their hybrid stars. The resulting maximum mass of the hybrid star has almost the same value as the neutron star consisting of pure hadronic matter when thermodynamic stability is taken into account. Only by ignoring reconfinement can an increased maximum mass be obtained.

The occurrence of reconfinement and multiple phase transitions should probably not be taken as a physically realistic scenario, but rather as artifacts of the equation of state models. The purpose of our investigation is just to show for which phase

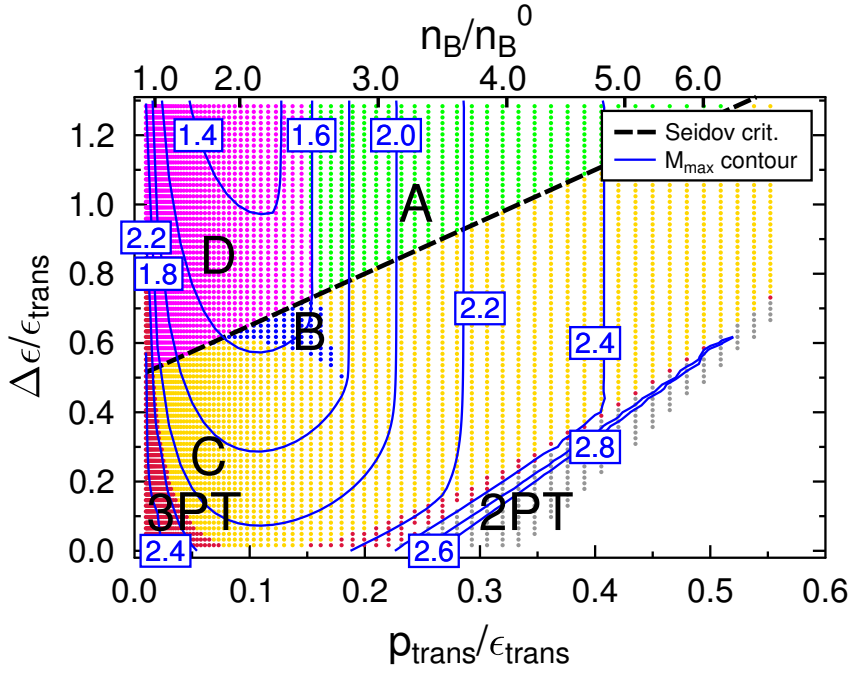

Fig. 5.9: Results for the parameter scan taking into account the occurrence of multiple phase transitions. Red dots show parameter combinations resulting in three phase transitions (HQHQ), grey in two phase transitions (QHQ) and absolutely stable strange quark matter. The other points have only one phase transition (HQ), for which the Alford classification (A, B, C, or D) can be done. The empty triangular region in the lower right corner corresponds to unphysical equations of state with negative energy density, for which the M-R relation has not been calculated. Published in [87].

transition parameters they occur. If several phase transitions are present, this could be taken as an indication that the quark equation of state parameters are unrealistic. One can also argue that the hadronic equation of state is not appropriate at high densities and neither is the quark equation of state at low densities, if one uses a two-phase approach as in the present study; see also [218, 26]. The hadronic equation of state model does not account for chiral symmetry restoration and deconfinement, whereas the quark equation of state model usually does not account for confinement and the saturation properties of nuclear matter. In [218, 26] it was discussed that the problem of reconfinement could be cured by taking into account the finite size of baryons in the hadronic equation of state. From this perspective it is acceptable to enforce just one phase transition and ignore the others as is done in the original parameter scans of Fig. 5.2 and [7, 216, 216, 217, 32, 172, 6].

5.6 Hyperons

With increasing density, hyperons such as Λ's and Ξ^-'s can appear. To investigate their effect on the maximum mass of hybrid stars, Fig. 5.10 shows a parameter scan using the BHB$\Lambda\phi$ EOS (see Sec. 4.2.4) for the hadronic part. We remind the

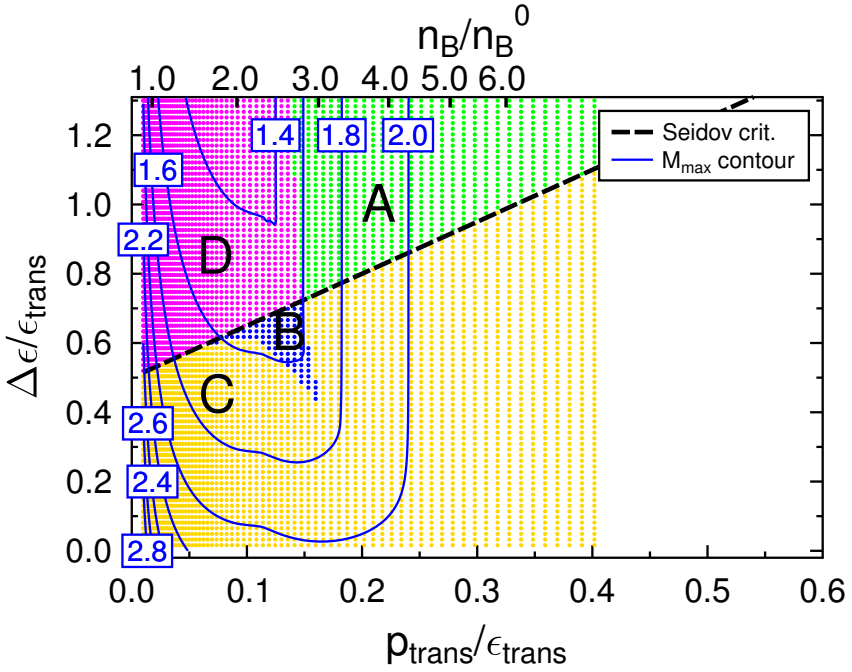

Fig. 5.10: As in Fig. 5.2, but including hyperons by using the BHB$\Lambda\phi$ EOS instead of HS(DD2). Published in [87].

reader that BHB$\Lambda\phi$ is an extension of HS(DD2) where only Λ hyperons have been added. Thus it is identical to HS(DD2) at low densities and temperatures. For BHB$\Lambda\phi$ we calculate hybrid stars only up to $p_{\rm trans}/\epsilon_{\rm trans} \approx 0.4$, which is the highest value available in this EOS table. Comparing Fig. 5.10 with the previous parameter scan using the nucleonic HS(DD2) EOS shown in Fig. 5.2, we find no qualitative difference in the distribution of the four different hybrid star cases. Since the Λ hyperons appear at around $p/\epsilon = 0.11$ a slight kink in the maximum mass contour lines is visible there. For phase transitions at lower pressures, the results of Fig. 5.10 are identical to those of Fig. 5.2 because hyperons are not yet present. At higher phase transition pressures, the maximum masses are generally reduced due to the presence of hyperons in the hadronic part of the hybrid star. For $p_{\rm trans}/\epsilon_{\rm trans} > 0.34$, the phase transition pressure is above the central pressure of the heaviest stable hadronic star, so that quark matter does not appear in stable compact stars and the results are identical to the purely hadronic calculations. We remark that the part of the parameter space we are interested in (case D at low transition pressures), and also our example hybrid equation of state used in Fig. 5.6, is not affected from the presence of hyperons.

As discussed in Sec. 5.5 for HS(DD2), strict thermodynamic stability can lead to the appearance of multiple phase transitions. In Fig. 5.11 we repeat the parameter scan for BHB$\Lambda\phi$ but this time taking into account strict thermodynamic stability. As in Fig. 5.9 one, two and three phase transitions are possible. The red dots indicate again the cases with three phase transitions (HQHQ). At low $\Delta\epsilon/\epsilon_{\rm trans}$, the region of three phase transitions expands up to $p_{\rm trans}/\epsilon_{\rm trans} = 0.125$ and appears again at

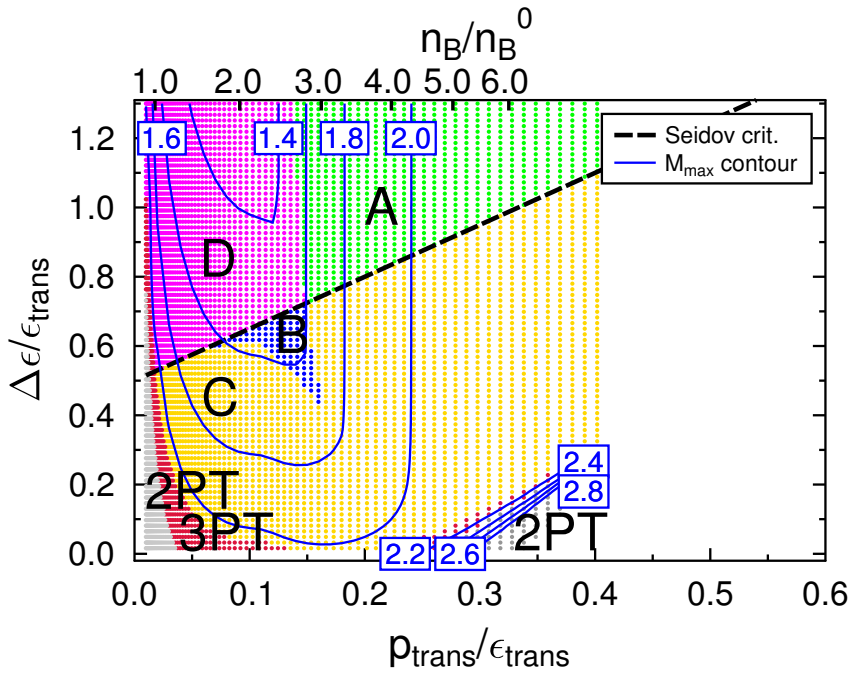

Fig. 5.11: As in Fig. 5.9, but including hyperons by using the BHB$\Lambda\phi$ EOS instead of HS(DD2). Published in [87].

around $p_{\rm trans}/\epsilon_{\rm trans} = 0.22$. Compared to Fig. 5.9, this region is shifted to slightly higher values of $p_{\rm trans}/\epsilon_{\rm trans}$. The cases with two phase transitions, represented by grey dots, appear in two regions: at high $p_{\rm trans}/\epsilon_{\rm trans}$, these cases are of the same type as in Fig. 5.9 (QHQ). These quark stars show again masses well above the maximum mass of the BHB$\Lambda\phi$ EOS. When using the BHB$\Lambda\phi$ EOS, an additional two phase transition region appears at low $p_{\rm trans}/\epsilon_{\rm trans}$. Whereas with the HS(DD2) EOS, this region was populated by HQHQ cases, now only an HQH sequence of phase transitions happens. At high densities, the hadronic equation of state including hyperons remains favored over quark matter. The maximum masses of these cases are still below the maximum mass of the BHB$\Lambda\phi$ EOS, as we observed for the strictly thermodynamically stable parameter scan for the HS(DD2) EOS. This is similar to the results of [218]. Without considering reconfinement, it was found that the phase transition to quark matter can resolve the hyperon puzzle; i.e., it can increase the too low maximum mass of a hyperonic equation of state to sufficiently high values. If reconfinement is permitted, the maximum mass of the hybrid equation of state remains very similar or becomes lower than the one of the hadronic equation of state.

5.7 Case $c^2_{\rm QM} = 1$

To investigate the effect of an increased speed of sound in quark matter, we set $c_{\rm QM}$ to the maximum value still consistent with special relativity; $c^2_{\rm QM} = 1$. Figure 5.12

shows the same set up as presented in Fig. 5.9, but with the adjusted value of the speed of sound for quark matter to $c^2_{\mathrm{QM}} = 1$.

The contour lines of the maximum masses in Fig. 5.12 show an overall increase of the maximum masses when using $c^2_{\mathrm{QM}} = 1$ compared to the ones shown in Fig. 5.9 where $c^2_{\mathrm{QM}} = 1/3$ was used. Especially, the significantly higher values at moderate to low $p_{\mathrm{trans}}/\epsilon_{\mathrm{trans}}$ are striking. The important 2 $\mathrm{M}_\odot$ line is only present in the upper left quarter of the plot. The number of parameter combinations excluded by the 2 $\mathrm{M}_\odot$ constraint has decreased tremendously. The highest masses are reached again at low $p_{\mathrm{trans}}/\epsilon_{\mathrm{trans}}$ and compared to the $c^2_{\mathrm{QM}} = 1/3$ calculations even higher masses are possible. At the lowest $p_{\mathrm{trans}}/\epsilon_{\mathrm{trans}}$ and $\Delta\epsilon/\epsilon_{\mathrm{trans}}$ masses (lower left corner), masses above 4.8 $\mathrm{M}_\odot$ are occurring. Such high mass hybrid star configurations consist of almost only quark matter and only a very thin layer of hadronic matter on top. They are only possible due to the additional stiffening of the quark equation of state due to the extreme c_{QM}.

Interesting to note is the effect of a high c_{QM} on the distribution of the four hybrid star cases, especially on the region containing third family cases: The case D region is extended to higher $p_{\mathrm{trans}}/\epsilon_{\mathrm{trans}}$. Cases D are now also possible at transition densities above 3 n_B/n_B^0. Due to the overall higher masses in the parameter scan, more cases D fulfill the 2 $\mathrm{M}_\odot$ constraint compared to the $c^2_{\mathrm{QM}} = 1/3$ parameter scan. The case B region is expanded as well, not only to higher $p_{\mathrm{trans}}/\epsilon_{\mathrm{trans}}$ but also to smaller $\Delta\epsilon/\epsilon_{\mathrm{trans}}$. In the corner of the case B region values of $p_{\mathrm{trans}}/\epsilon_{\mathrm{trans}} = 0.29$ and $\Delta\epsilon/\epsilon_{\mathrm{trans}} = 0.31$ are reached. With the exception of a small region at around 3 n_B/n_B^0 close to the Seidov line, all cases B fulfill the 2 $\mathrm{M}_\odot$ constraint. This is remarkable since with a speed of sound of $c^2_{\mathrm{QM}} = 1/3$, this constraint could not be met at all. Considering the expansion of the case D and B regions, using $c^2_{\mathrm{QM}} = 1$ leads to a notably bigger amount of options for third family configurations that fulfill the 2 $\mathrm{M}_\odot$ constraint. Regarding the construction of a possible new supernova equation of state this increases the possible remarkably. Even though $c^2_{\mathrm{QM}} = 1$ is probably an overestimated value, an increased speed of sound above $c^2_{\mathrm{QM}} = 1/3$ for sure leads to interesting new options worth to consider in a more detailed analysis.

Considering strict thermodynamic stability leads again to the appearance of multiple phase transitions (see Fig. 5.13). Whereas with $c^2_{\mathrm{QM}} = 1/3$ one (HQ), two (QHQ) and three phase transitions (HQHQ) are possible, using $c^2_{\mathrm{QM}} = 1$ only one and two phase transition cases appear. These two phase transition cases are of a different kind than the previously observed ones: After a phase transition from hadronic to quark matter a second phase transition happens back from quark to hadronic matter (HQH). After this second phase transition no transition back to quark matter is possible anymore what makes hadronic matter the favored state of matter at high densities. This is quite surprising since it is generally assumed that quark matter is the preferred state of matter at high densities. More than half of all the parameter

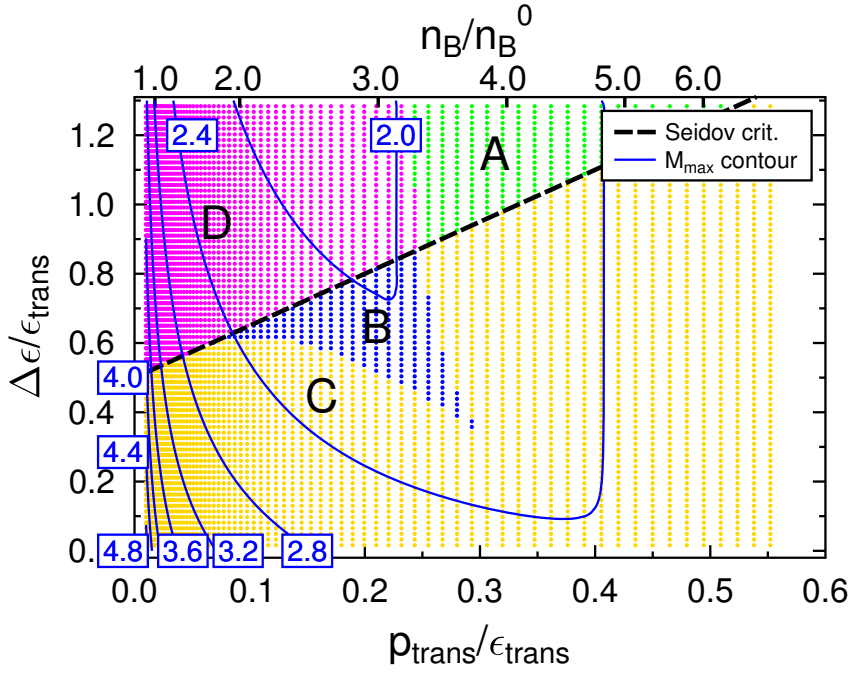

Fig. 5.12: As in Fig. 5.9, but with the maximum value for the speed of sound in quark matter of $c^2_{\rm QM} = 1$.

configurations in the considered parameter space are affected by multiple phase transitions. The region spreads from the lowest $p_{\rm trans}/\epsilon_{\rm trans}$ (and all $\Delta\epsilon/\epsilon_{\rm trans}$) to the highest $p_{\rm trans}/\epsilon_{\rm trans}$ (and $\Delta\epsilon/\epsilon_{\rm trans}$ up to $\Delta\epsilon/\epsilon_{\rm trans} = 0.36$).

The appearance of multiple phase transitions generally leads to a lowering of the maximum masses compared to the cases with only one phase transition and maximum masses above the one of the purely hadronic HS(DD2) EOS. While at low $\Delta\epsilon/\epsilon_{\rm trans}$ the maximum masses are similar or below the maximum mass of the HS(DD2) EOS at high $\Delta\epsilon/\epsilon_{\rm trans}$ masses above the maximum mass of the HS(DD2) EOS are possible. Figure 5.14 shows an example M-R curve corresponding to the values $p_{\rm trans}/\epsilon_{\rm trans} = 0.018$ and $\Delta\epsilon/\epsilon_{\rm trans} = 1.27$. In an M-R curve like Fig. 5.14, the central pressure of the plotted configurations increases from the right to the left in the curve (large to small radii except for the cases where multiple mass configurations are possible at the same radius). The two magenta crosses in Fig. 5.14 indicate the positions where the phase transitions first occur. To the right of the phase transition at $M = 0.23$ $\rm M_\odot$ and $R = 15.60$ km, neutron stars consist only of hadronic matter. In between the two crosses (second phase transition takes place at $M = 2.60$ $\rm M_\odot$ and $R = 12.30$ km), quark matter is present in the core of the neutron stars. It is clearly visible that the second phase transition at the larger neutron star mass happens to be only slightly below the maximum mass configuration. If the phase transition would happen at merely higher transition pressures this case would turn into a one phase transition case (HQ). We can conclude that such high-mass cases are only possible due to a pronounced quark region which contributes significantly to the total mass.

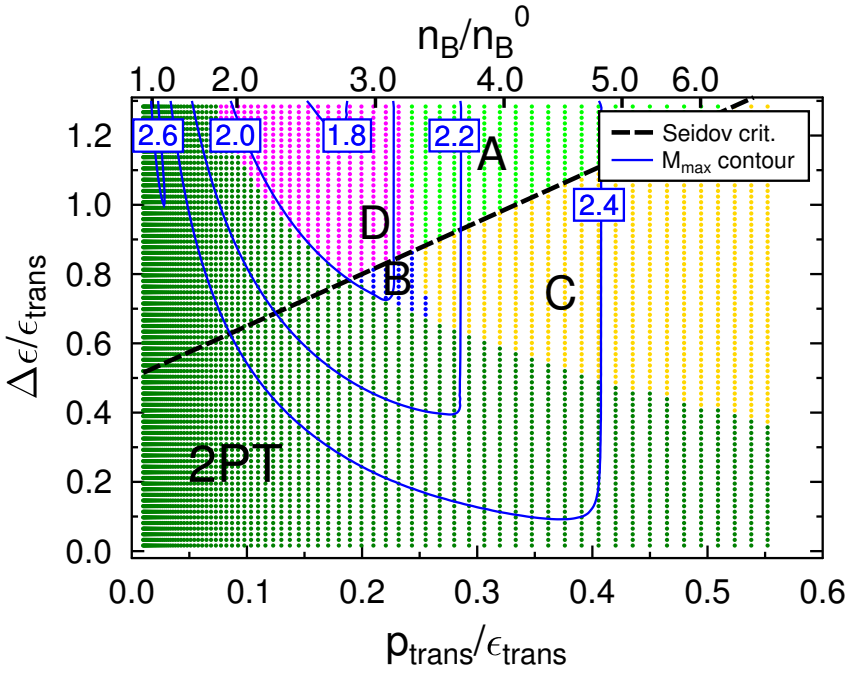

Fig. 5.13: As in Fig. 5.12 but imposing strict thermodynamic stability. This leads again to the appearance of multiple phase transitions. The dark green dots mark the two phase transition cases (HQH) which do not appear in the case of $c^2_{\mathrm{QM}} = 1/3$.

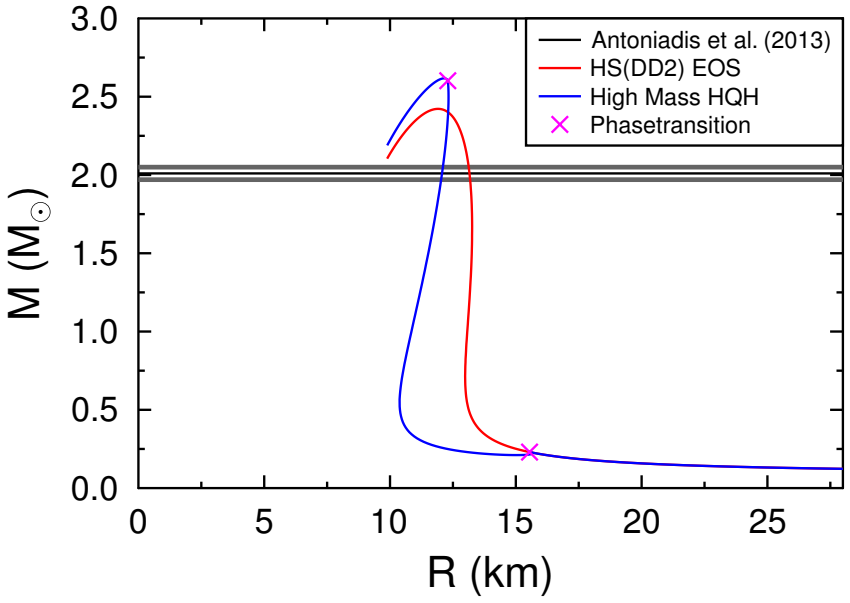

Fig. 5.14: M-R relation of a two phase transition case where the maximum mass exceeds the maximum mass of the HS(DD2) EOS. The phase transition parameters are $p_{\mathrm{trans}}/\epsilon_{\mathrm{trans}} = 0.018$ and $\Delta\epsilon/\epsilon_{\mathrm{trans}} = 1.27$. Indicated with magenta crosses are the positions where the phase transitions first occur.

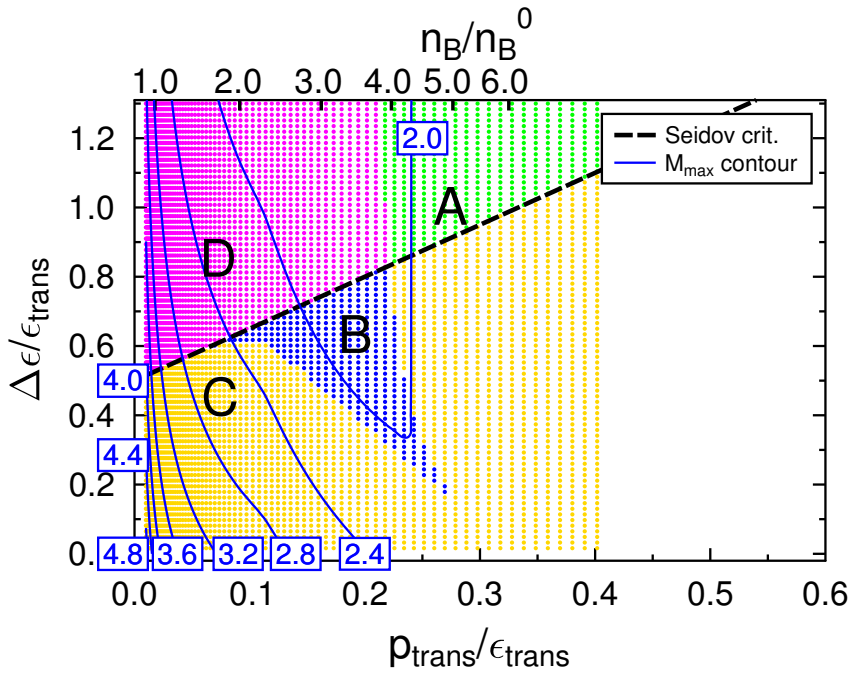

Fig. 5.15: As in Fig. 5.12, but including hyperons by using the BHB$\Lambda\phi$ EOS instead of HS(DD2) EOS.

Only few of the third family cases which do meet the 2 $M_\odot$ constraint are not affected by the appearance of multiple phase transitions: a narrow band of cases D left and right of the 2 $M_\odot$ line and a small region of cases B right of the 2 $M_\odot$ line are left. As a consequence, finding an example case with a low transition pressure, as it was done using $c^2_{\mathrm{QM}} = 1/3$, is excluded.

Figure 5.15 shows a parameter scan including hyperons using BHB$\Lambda\phi$ using $c^2_{\mathrm{QM}} = 1$. Again, the higher speed of sound leads to an increase of the maximum masses. Especially, at moderate to low $p_{\mathrm{trans}}/\epsilon_{\mathrm{trans}}$, the mass contour lines very high maximum masses. Compared to Fig. 5.12 the 2 $M_\odot$ line expands to lower $\Delta\epsilon/\epsilon_{\mathrm{trans}}$ which excludes more parameter combinations compared to the calculations using the HS(DD2) EOS. In this region the transition pressures allow the appearance of hyperons and consequently the equation of state differs from the purely hadronic HS(DD2) EOS. The regions including third family cases expand to higher $p_{\mathrm{trans}}/\epsilon_{\mathrm{trans}}$ compared to the HS(DD2) calculations. The tail of the cases B even expands to values of $p_{\mathrm{trans}}/\epsilon_{\mathrm{trans}} = 0.27$ and $\Delta\epsilon/\epsilon_{\mathrm{trans}} = 0.18$. For both cases B and D, it is possible to find parameter configurations which meet the 2 $M_\odot$ constraint. In contrast to Fig. 5.12 it is not possible to find cases D that fulfill the 2 $M_\odot$ constraint right of the 2 $M_\odot$ contour line. However, since hyperons occur at $p/\epsilon = 0.11$ it is possible to find parameter configurations of cases B and D where at the transition point to quark matter hyperons are present in the hadronic phase. This is not feasible with a speed of sound of $c^2_{\mathrm{QM}} = 1/3$.

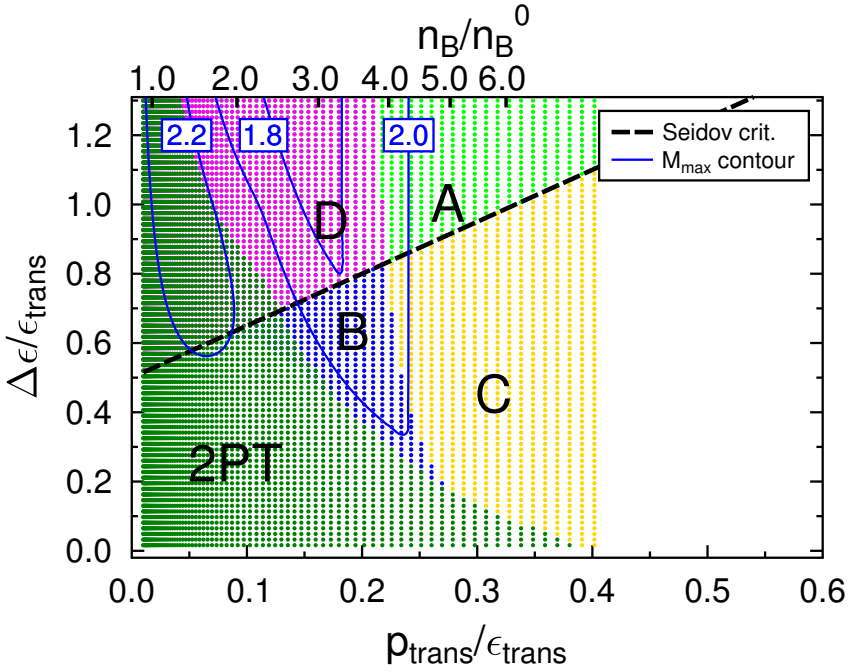

Fig. 5.16: As in Fig. 5.13, but including hyperons by using the BHB$\Lambda\phi$ EOS instead of HS(DD2) EOS.

Figure 5.16 shows the results for BHB$\Lambda\phi$ with $c^2_{\rm QM} = 1$ using a thermodynamically consistent treatment of the phase transitions. Again, multiple phase transitions in the form of the two phase transition case (HQH) appear. Similar to Fig. 5.13, the appearance of multiple phase transitions leads to a lowering of the maximum mass at moderate to low $p_{\rm trans}/\epsilon_{\rm trans}$. As in the HS(DD2) calculations, massive hybrid stars with masses above the maximum mass of the hadronic equation of state (BHB$\Lambda\phi$) are possible at low $p_{\rm trans}/\epsilon_{\rm trans}$ and high $\Delta\epsilon/\epsilon_{\rm trans}$. The two phase transition region spreads over almost the whole $p_{\rm trans}/\epsilon_{\rm trans}$ range except for the largest treated values. At moderate to high $p_{\rm trans}/\epsilon_{\rm trans}$ the two phase transition region does not expand to $\Delta\epsilon/\epsilon_{\rm trans}$ values as high as reached in Fig. 5.13. At low $p_{\rm trans}/\epsilon_{\rm trans}$ values the whole $\Delta\epsilon/\epsilon_{\rm trans}$ range consists of two phase transition cases.

Interestingly, using BHB$\Lambda\phi$ more third family cases which do meet the 2 $M_\odot$ constraint and are not affected by the appearance of multiple phase transitions. Hence, the reconfinement problem is less severe when using hyperons and $c^2_{\rm QM} = 1$. A continuous band spreading through the case D and B area is found left and below the 2 $M_\odot$ contour line. It is considerably wider than the one found using the HS(DD2) EOS in Fig. 5.13. Since lower $p_{\rm trans}/\epsilon_{\rm trans}$ are generally allowed compared to the by reconfinement unaffected HS(DD2) EOS cases, it might be more interesting to construct a new hybrid supernova equation of state using BHB$\Lambda\phi$ than using only HS(DD2). As mentioned for the HS(DD2) calculations the $c^2_{\rm QM} = 1$ value is probably an overestimation. Nevertheless, constructing a new hybrid supernova equation of state using BHB$\Lambda\phi$ at $c^2_{\rm QM} > 1/3$ is an interesting option.

6 BASQUARK - A New Hybrid Supernova Equation of State

> *Dass ich erkenne, was die Welt im Innersten zusammenhält.*
>
> **— aus Goethe's Faust**

In this chapter, the new hybrid supernova equation of state BASQUARK is presented. In the first section the setup of BASQUARK is discussed in detail. The second section deals with the implementation of BASQUARK into the spherical supernova code AGILE-BOLTZTRAN.

6.1 BASQUARK

Based on the parameter configuration presented in Chapter 5, Matthias Hempel calculated the new hybrid supernova equation of state called BASQUARK. In the following a short summary over the main characteristics is given:

As in the parameter scan (see Chapter 5), the hadronic phase is described by the state-of-the-art supernova equation of state HS(DD2) [90]. The quark phase is described by the bag model (see Sec. 4.3.3) using a bag constant of $B^{1/4} = 138.5$ MeV, a strong-interaction constant $\alpha_s = 0.7$, and a strange-quark mass $m_s = 100$ MeV. The design of the phase transition is based on our best guess parameters obtained in Sec. 5.4: $p_{\rm trans}/\epsilon_{\rm trans} = 0.013$ and $\Delta\epsilon/\epsilon_{\rm trans} = 0.76$. In BASQUARK local charge neutrality is assumed. Since we do not assume beta equilibrium as a condition for our new supernova equation of state, we have to apply a Gibb's phase transition construction. This phase transition transforms in the neutron star limit ($T = 0$ and beta equilibrium) back to a Maxwell phase transition. BASQUARK uses the same mesh structure in temperature T, electron fraction Y_e and baryon number density n_B as HS(DD2):

- **Temperature T:** 81 temperature entries are available which can be calculated by: $T = 0.1 \cdot 10^{0.04(i-1)}$ MeV with $i = 1, \ldots, 81$. The mesh considers the range 0.1 MeV $\leq T \leq 158.5$ MeV.
- **Electron Fraction Y_e:** 60 electron fraction entries are available and can be calculated by $Y_e = j \cdot 0.01$ with $j = 1, \ldots, 60$. The mesh in Y_e considers the range $0.01 \leq Y_e \leq 0.6$.

- **Baryon Number Density n_B:** 326 baryon number density entries are available. They can be calculated by $n_B = 10^{-12} \cdot 10^{0.04(k-1)}$ fm^{-3} with $k = 1, \ldots, 326$. The mesh considers values in the range of 10^{-12} fm$^{-3} \leq n_B \leq 10$ fm^{-3}.

Additionally to the BASQUARK-EOS table, a table containing the mass fraction of the quarks corresponding to the entries of BASQUARK is provided. This table can be used for detailed analysis of the quark fractions in core-collapse supernova simulations.

As previously mentioned, every constructed equation of state must fulfill the 2 M$_\odot$ constraint [56, 11]. In Fig. 6.1 the dashed magenta line shows the M-R curve of BASQUARK in beta equilibrium and at temperature $T = 0.1$ MeV[1]. The blue line shows the original example case obtained in the parameter scan in Sec. 5.4. As shown in Fig. 6.1, there is a very good agreement between the M-R curves of BASQUARK and the example case. The maximum mass configuration of BASQUARK has $M_{\max} = 2.05$ M$_\odot$ with a radius of $R_{M_{\max}}$ = 11.99 km and thus meets the 2 M$_\odot$ constraint. For 1.4 M$_\odot$ the hybrid equation of state leads to a somewhat smaller radius of 12.63 km than HS(DD2) (red line) with 13.22 km. The yellow 1 σ and orange 2 σ area indicate the observational radius constraints from Steiner et al. [188]. The M-R curve of BASQUARK does cross the observational constraints between 1 and 1.3 M$_\odot$. For higher masses the BASQUARK EOS is still close to the 2 σ area. The onset of quark matter is marked by the point where the BASQUARK curve parts from the HS(DD2) M-R curve. As mentioned previously, the parameter set of BASQUARK is classified as a case D in Alford's classification scheme [7]. However, it is important to point out that the third-family feature of BASQUARK is so weak that it is almost not visible in Fig. 6.1.

6.2 Testing BASQUARK with AGILE-BOLTZTRAN

Initial tests with the new BASQUARK EOS are done in spherical symmetry using the general-relativistic AGILE-BOLTZTRAN code with three-flavor Boltzman neutrino transport, developed by Liebendörfer et al. [130].

We aim to compare our results with the ones obtained by Sagert et al. [174] and Fischer et al. [65] who first showed the QCD phase-transition induced supernova mechanism and discussed it in detail. In both papers, AGILE-BOLTZTRAN was used for the simulations performed. In a first simulation of BASQUARK in AGILE-BOLTZTRAN, we use the 15 M$_\odot$ progenitor from Woosley et al. [214]. Both references [174, 65] use this progenitor amongst others, hence it provides a good opportunity to compare it with these simulations. We setup our simulation including the innermost 2.03 M$_\odot$ of the progenitor in the computational domain and distribute it over 140 grid zones. Three neutrino flavors are treated (ν_e, $\bar{\nu}_e$ and $\nu_{\mu,\tau}$,$\bar{\nu}_{\mu,\tau}$) using two propagation angles.

[1] Note, a temperature of 0.1 MeV is negligibly small in comparison to typical Fermi energies in neutron stars. Hence, it is a sufficient approximation for ideally $T = 0$ MeV.

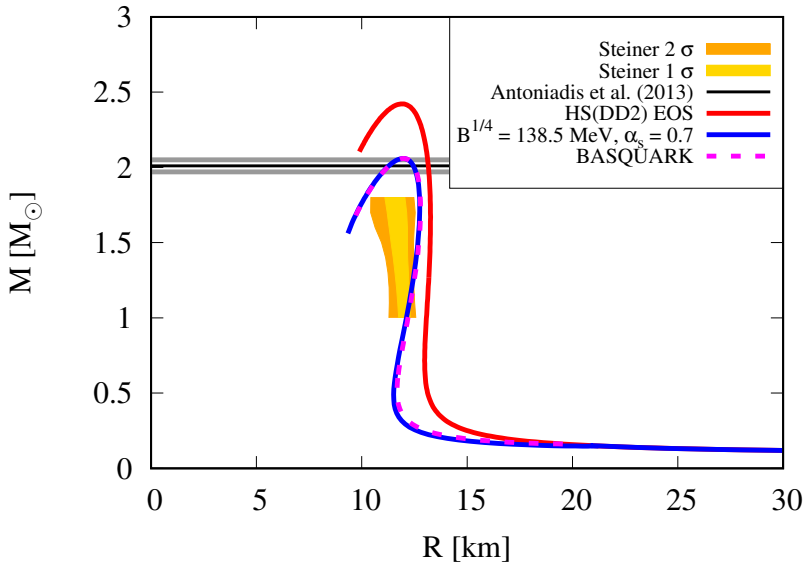

Fig. 6.1: M-R relation of BASQUARK (dashed magenta) and HS(DD2) (red) in beta-equilibrium and at $T = 0.1$ MeV. The blue line shows the M-R relation of the example case presented in Sec. 5.4 with the quark parameters in BASQUARK are $m_s = 100$ MeV, $\alpha_s = 0.7$, and $B^{1/4} = 138.5$ MeV.

In the following, we discuss the results obtained in our simulation in detail. We follow the discussion in [65] and compare our results to the ones present therein.

6.2.1 Appearance of quark matter and dynamic evolution

Figure 6.2 shows the evolution of the central density ρ_c with time. This figure provides a good overview over different stages of the post-bounce evolution and shall serve as guideline for the subsequent discussion. A brief summary over the key events happening in the simulation: After 293 ms simulation time, the simulation reaches bounce where the central density reaches $\rho_{\mathrm{bounce}} = 3.48 \cdot 10^{14}$ g/cm^3. Up to 357 ms post bounce, no quark matter is present and therefore the results of the simulation with BASQUARK correspond to the a run executed with the pure-hadronic HS(DD2) EOS. At $t_{\mathrm{pb}} = 501$ ms, the protoneutron starts to collapse. During this so-called "second collapse" ρ_c increases up to $\rho_c = 6.85 \cdot 10^{14}$ g/cm^3 ($t_{\mathrm{pb}} = 504.6$ ms). After the second collapse ρ_c stabilizes before decreasing due to the explosion, as we will see below. The oscillations at around 800 ms post bounce are probably of numerical origin. They might be an effect of an insufficient treatment of the neutrinos in context of quark matter. As in the simulations of [174] and [65] we assumed in our calculations that neutrinos only appear in optically thick regimes and are therefore in thermal and chemical equilibrium. For this reason, the results are assumed to be independent of the precise value of the quark-neutrino interaction rates, and the hadronic weak-interaction rates (e.g. [29]) are used in the quark phase to derive the hadron chemical potentials from the quark chemical potentials so

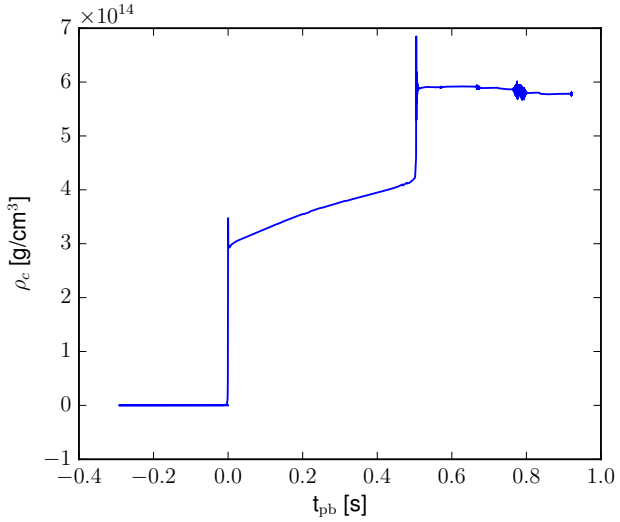

Fig. 6.2: Evolution of central density ρ_c of BASQUARK with time for the 15 $M_\odot$ progenitor.

that weak equilibrium is obtained (see [174]). It is questionable if this assumption also hold after the second collapse and for sure needs further investigation.

Figure 6.3 shows a selection of hydrodynamical quantities in their radial profile at three different times; at bounce (blue), $t_{\mathrm{pb}} = 101.72$ ms (green), and $t_{\mathrm{pb}} = 403.2$ ms (brown). Quark matter can only be obtained, if the central density and the temperatures are sufficiently high and the electron fraction low enough. In our simulation using BASQUARK, the conditions for quark matter at bounce were not given while the simulations of [65] already showed quark matter at this stage. At $t_{\mathrm{pb}} = 101.72$ ms the shock has stalled. The temperatures behind the shock have risen and the electron fraction has been lowered. Still, the conditions for the appearance of quark matter are not met. After another ~ 250 ms of mass accretion onto the protoneutron star, at $t_{\mathrm{pb}} = 357$ ms the conditions finally favor the appearance of quark matter. This leads to another interesting difference between our simulations and [174, 65]: In our simulation, quark matter appears first off center while in [174, 65] quark matter always appeared the center of the protoneutron star first: Figure 6.4 shows the detailed radial profiles of the quark mass fraction at different times post bounce. Quark matter first appears at around 0.5 $M_\odot$ and spreads faster outwards to higher masses and more slowly to lower masses. Only after the second collapse happened quark matter appears in the center of the protoneutron star. At $t_{\mathrm{pb}} = 921.54$ ms, there is a mixed phase from the center to ~ 0.73 $M_\odot$, followed by a layer of pure quark matter up to ~ 0.9 $M_\odot$. Up to 1.28 $M_\odot$, the quark mass fraction lies still above 0.95 followed by a strong decrease up to 1.55 $M_\odot$ where no quark matter is present anymore.

The appearance of quark matter has serious implications on the dynamics of the protoneutron star. As mentioned above quark matter first appears at $t_{\mathrm{pb}} = 357$ ms. During approximately 150 ms the quark mass increases gradually until the last

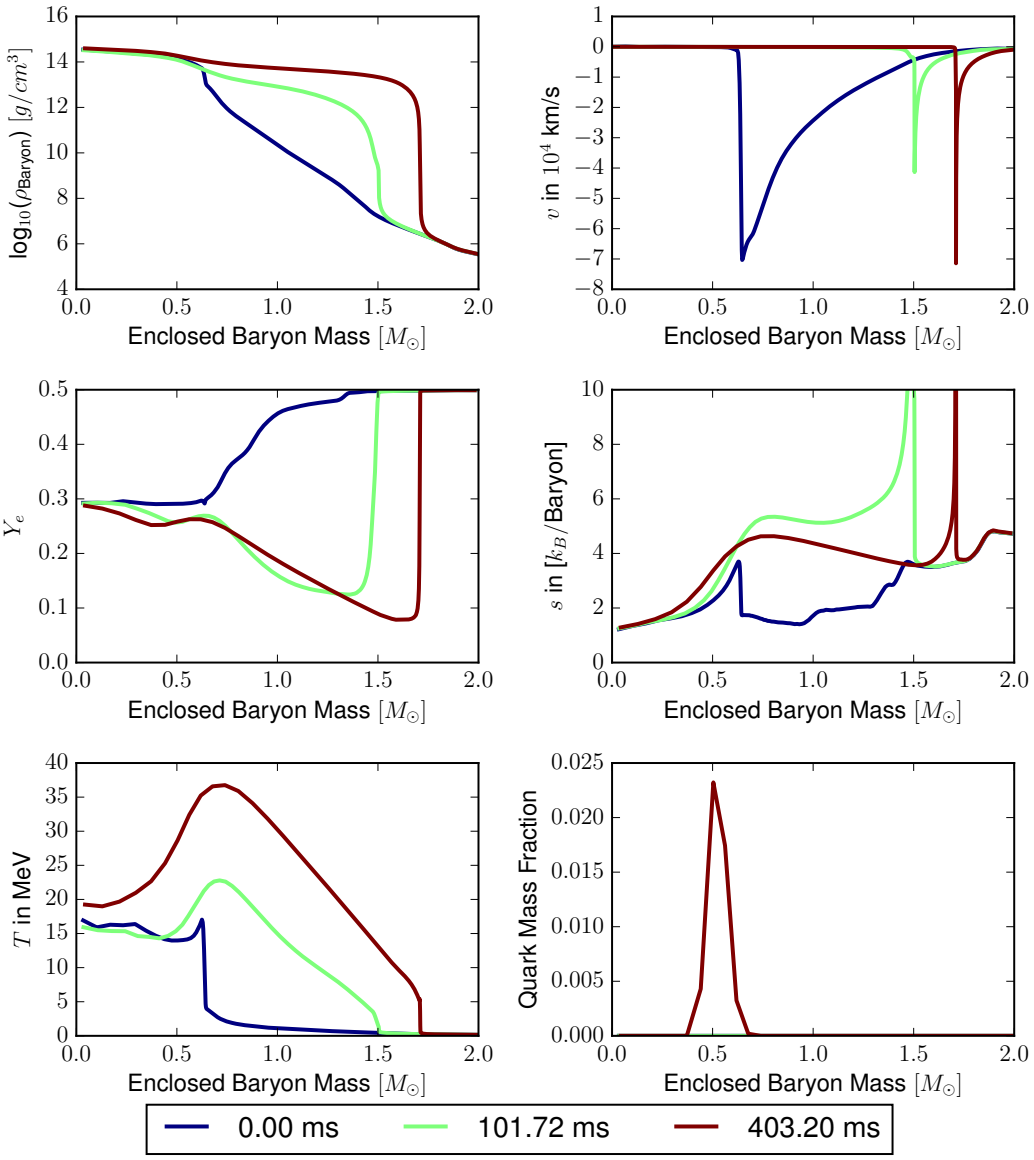

Fig. 6.3: Radial profiles of selected hydrodynamical quantities for the 15 $M_\odot$ progenitor at three different times; at bounce (blue), $t_{\rm pb} = 101,72$ ms (green), and $t_{\rm pb} = 403.2$ ms (brown).

stable configuration of the current protoneutron star is reached at $t_{\rm pb} = 501.51$ ms. Ultimately, the protoneutron star starts to collapse. The softening of the equation of state due to the appearance of the hadron-quark mixed phase leads to a sudden contraction of the protoneutron star. Figure 6.5 shows a series of hydrodynamical profiles from the start of the second collapse until the protoneutron star stabilizes again. In Fig. 6.5a the radial coordinate is the integrated mass while in Fig. 6.5b the logarithm of the radius is used. The velocity profiles in the upper right panel of Fig. 6.5b show the sudden contraction of the protoneutron star. The density in the central region and temperature increase considerably within a few milliseconds. This change in thermodynamic conditions leads a lower electron fraction Y_e due to a

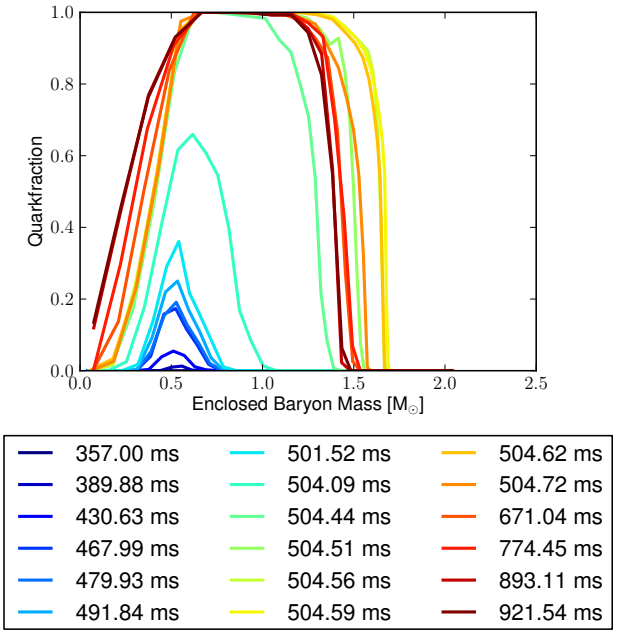

Fig. 6.4: Radial profiles of quark mass fraction at different times post bounce.

readjustment of the weak equilibrium. The biggest changes in the profiles of these three quantities are found in the region where density increases by about one order of magnitude from 10^{14} to 10^{15} g/cm^3. The collapse is adiabatic as the entropies stay constant in the collapse region (see entropy panel in Fig. 6.5a). The higher densities and temperatures as well as the lower electron fraction are now sufficient conditions to turn a large fraction of the hadronic matter into quark matter. While the maximum central densities are reached (see second peak in the central density curve in Fig. 6.2) we can also see a short overshoot of the quark matter fraction up to almost 1.7 $M_\odot$ in Fig. 6.5a. When the inner core stabilizes afterwards, the quark matter fraction also stabilizes at around 1.5 $M_\odot$. This feature is not mentioned in [65] but should also be found in their simulations. The rise of the quark matter fraction to 1, which corresponds to a pure quark phase, leads to stiffening of the equation of state. As a result, the collapse of the protoneutron star stops and a second hydrodynamic shock forms at the outer boarder of the hadron-quark mixed phase. Since the velocities of the outer infalling parts are supersonic, the outer parts get no information about the central stiffening of the core and the formed shock wave. Initially this shock front is a pure accretion front without any matter outflow. Density and temperature increase at the shock front due to the infalling matter as seen in Fig. 6.5b. The thermal pressure behind the shock front is increasing. When the densities of the infalling matter become lower, the second shock can finally detach from the core surface. The shock changes its nature from an accretion shock to a dynamic, accelerating, outwards-propagating shock wave. The shock further accelerates due to the strong drop in densities on the order of several orders of magnitude outside the protoneutron star surface. As in [174, 65], we find velocities

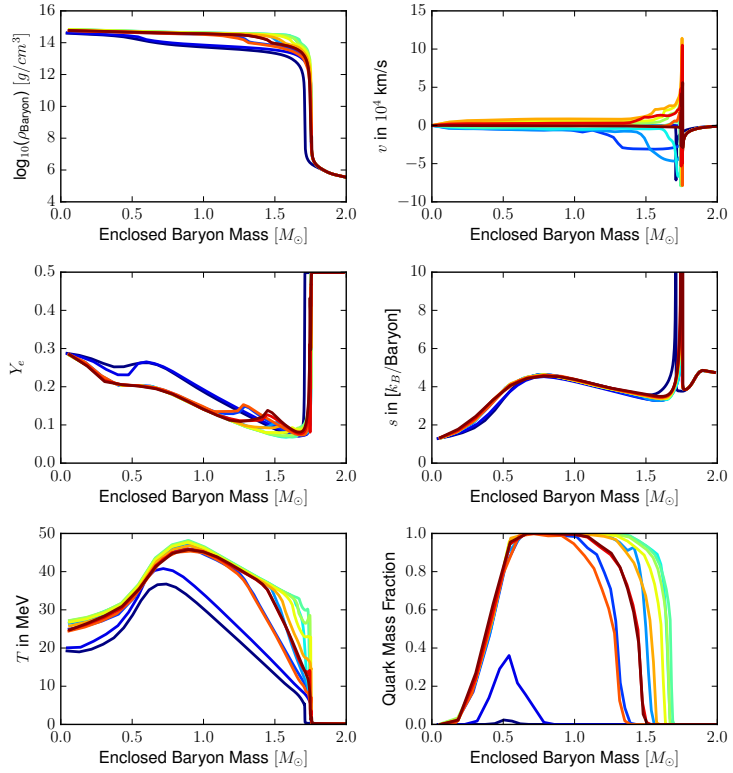

(a)

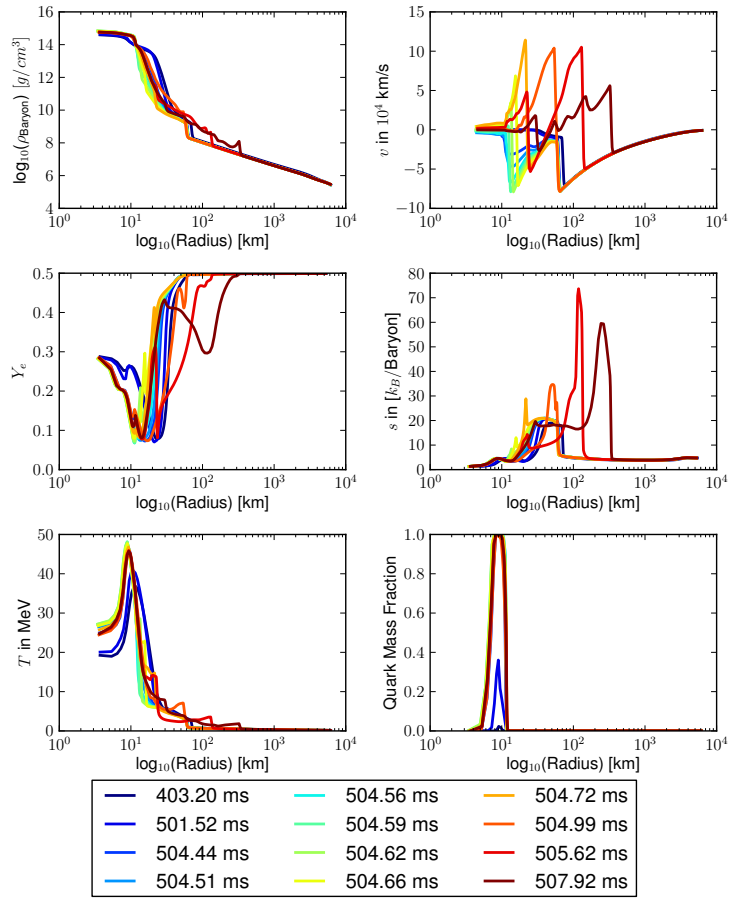

(b)

Fig. 6.5: As in Fig. 6.3, a selection of hydrodynamical quantities in their radial profile during the second collapse and shortly after.

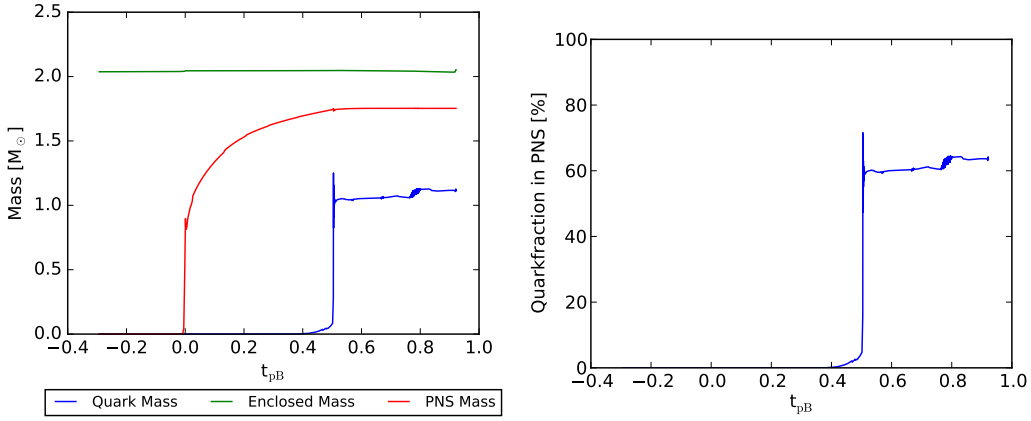

(a) (b)

Fig. 6.6: In the left panel, the green line represents the total mass included in the computational domain, the red line the total rest mass of the protoneutron star ($\rho > 10^{12}$ g/cm^3), and the blue line shows the total mass of the quark matter. The right panel shows the percentage of quark matter compared to the total protoneutronstar mass.

above 10^5 km/s for this outwards moving shock wave. Fischer et al. [65] give additional information on the nature of the shock wave: Since the infalling matter onto the shock wave is *"already dissociated and composed of only free nucleons and nuclei"* (no heavy nuclei infall in contrast to the first formed shock wave at bounce), *"the shock does not loose energy during the initial propagation. Even more, during the initial shock expansion neutrino heating still deposits energy behind the shock wave"*[65]. At $t_{\mathrm{pb}} = 504.99$ ms the second shock wave merges with the standing accretion front produced at bounce. The energy of the second shock wave is high enough to continue its outward propagation with velocities still above 10^5 km/s. In Fig. 6.5b, the profile of $t_{\mathrm{pb}} = 505.62$ ms shows an additional newly formed shock wave at around 11 km. This shock wave is formed due to oscillations of the protoneutron star which happen right after the second collapse. Such oscillations might become a source of gravitational waves in multi-dimensional simulations. The small shock waves later merge with the outwards moving shock wave. This is easily visible in form of the bumps in the velocity profile at $t_{\mathrm{pb}} = 505.62$ ms behind the sharp shock front. Fischer et al. [65] also find oscillations of the central densities in their simulations. However, it is not explicitly mentioned that these oscillations lead to delayed, weaker shock waves which are sent into the strong shock front, even though it is visible for example in their Fig. 12. Since the expanding shock wave is including more and more mass, it slows down with bigger radii but still has high positive velocities up to several thousand kilometers of radii. We therefore consider our model to be exploded.

In Fig. 6.6 more detailed information about the total accumulated quark fraction is shown: The green line in Fig. 6.6a represents the total mass included in the computational domain and remains constant. The red line represents the rest mass

Prog. [$M_\odot$]	EOS	$t_{\rm pb}$ [ms]	ρ_c [10^{14}g/cm^3]	T_c [MeV]	Y_e
15	B162	172	7.523	17.15	0.170
15	B165	275	7.586	16.25	0.187
15	B155α_s0.3	308	5.511	17.67	0.197
15	BASQUARK	501.5	4.226	20.06	0.290

Tab. 6.1: Selected central quantities of the protoneutron star at the onset of the second collapse. The first three rows represent the values given in Tab. 2 in [65]. The forth row represents the simulation with BASQUARK.

of the protoneutron star. As a density criterion for the protoneutron star we use $\rho > 10^{12}$ g/cm^3. The protoneutron star is formed at bounce and its mass is constantly increased due to accretion up to the second collapse. As soon as the second shock wave detaches from the protoneutron star surface, its mass stays almost constant for the rest of the simulation time. The remaining neutron star has a total baryon rest mass of 1.75 $M_\odot$. This neutron star mass is about 0.1 $M_\odot$ higher than the ones obtained with the hybrid equation of state in [174, 65]. Such a high mass neutron star might be interesting as a candidate for the high mass observations of [56, 11]. If such a neutron star would be born in a binary system, its mass could likely be increased up to two solar masses by mass accretion. The blue line represents the total quark mass in the computational domain. After the second collapse, where for a short period up to 1.25 $M_\odot$ of quarks are present in the protoneutron star, the total mass of quark matter is around 1.05 $M_\odot$. This corresponds to roughly 60% of the total mass of the protoneutron star! In the later evolution this value rises up to even 63% of the total protoneutron-star mass.

To compare BASQUARK with the other hybrid equations of state of [174, 65], we list the information given there in Tab. 6.1 and 6.2, and add our obtained results. In [174, 65] a different hadronic equation of state (Shen et al. [183]) compared to BASQUARK has been used. While in [174, 65] several equations of state with the same hadronic model but different parameters for the quark model could be compared amongst each other, we are now comparing our model which has a different hadronic model and different quark parameters to them. We highlight the main differences in the following:
Comparing the post bounce times where the second collapse sets in, we find that BASQUARK collapses almost 200 ms later than B155α_s0.3. The central density at collapse is $1.285 \cdot 10^{14}$ g/cm^3 smaller than the value of B155α_s0.3. On the other hand, the central temperature is almost 3 MeV above the highest temperatures of the other models. The central Y_e is also higher than the other values. The differences are due to an overlap of the effects of using a different hadronic equation of state and a quark model with a smaller bag constant and larger strong-interaction correction.

Prog. [$M_\odot$]	EOS	$M_{\rm NS}$ [$M_\odot$]	$E_{\rm expl}$ [10^{51} erg]	$t_{\rm col}$ [ms]	$\rho_{\rm max}$ [10^{15}g/cm^3]
15	B162	1.608	0.420	175.07	1.487
15	B165	1.641	BH	277.10	15.362
15	B155α_s0.3	1.674	0.458	312.99	1.342
15	BASQUARK	1.753	?	504.62	0.684

Tab. 6.2: Obtained neutron star mass $M_{\rm NS}$, explosion energy $E_{\rm expl}$, time where the second collapse reached its maximum central density $t_{\rm col}$, and the maximum central density $\rho_{\rm max}$. The arrangement of the models is the same as in Tab. 6.1. Model B165 did not explode but collapsed into a black hole (BH).

Additionally, we remember the reader at this point that the phase transition in BASQUARK is modeled under the assumption of local charge neutrality while in the equations of state by Sagert et al. the conservation laws are fulfilled globally. Once more it should be mentioned at this point that with BASQUARK quark matter appears off-centered initially while with the other equations of state quark matter appears first in the center of the protoneutron star.

In Tab. 6.2 some general features about the second collapse and the succeeding explosion are summarized. Compared to the other equations of state, we do only get about half the value of the peak central density $\rho_{\rm max}$. However, the time between the onset of the collapse and the peak central density is for all models in the range between 3 and 4 ms (see [65],except for model B155α_s0.3 which collapses into a black hole). This collapse feature is very robust and does not vary a lot. Unfortunately, we were not yet able to calculate the explosion energy for our model. However, we should be able to do this in the near future. As mentioned above, when using BASQUARK the remaining neutron star has a baryon mass of 1.753 $M_\odot$. It is 0.08 - 0.15 $M_\odot$ heavier than the ones obtained with the other mentioned models.

6.2.2 Neutrino signal

In the following we discuss the neutrino signal produced in our simulation. The discussion is, as above, based on the information given in [174, 65].

Figure 6.7 shows the neutrino signal produced for BASQUARK in our AGILE-BOLTZTRAN run. The blue line represents the luminosity of ν_e, the dashed green line the luminosity of $\bar{\nu}_e$, and the straight red respectively the dashed cyan line the ν_μ/ν_τ respectively their anti-neutrino luminosities.
Shortly after bounce there is a strong peak in the ν_e luminosity which has a peak value of $L_{\nu_e} = 1.805 \cdot 10^{53}$ erg/s at 37 ms post bounce. This burst is produced by the strong deleptonization processes occurring at bounce. $\bar{\nu}_e$'s are only produced post bounce: In the post-bounce phase, a reduced degeneracy allows charged current

reactions as well as pair processes for positrons as well. At around $t_{\rm pb} = 100$ ms, the $\bar{\nu}_e$ luminosity almost converged with the ν_e luminosity. μ/τ neutrinos are also solely produced after bounce in pair-processes.

Two processes determine the neutrino luminosities in this post-bounce phase: The mass accretion and the neutrino diffusion at the neutrino spheres. The small maximum in the ν_e and $\bar{\nu}_e$ signal at around $t_{\rm pb} = 180$ ms is caused by the initially stronger mass accretion. In the ν_μ/ν_τ luminosities we do not find such a peak in the signal. Up to $t_{\rm pb} = 357$ ms, no quark matter is present and the neutrino luminosities therefore correspond to the ones of the purely hadronic HS(DD2) EOS.
On its way to the neutrino sphere, the second shock wave passes regions with low Y_e produced by the first shock wave. This region consists of formerly dissociated matter which is now reheated by the second shock wave. The high temperatures of the passing shock wave allow the creation of new electron-positron pairs. Their creation is succeeded by positron captures on neutrons which then lead to higher Y_e. This is visible as the small peak in the low Y_e region (see Fig. 6.5). As soon as the shock wave passes the protoneutron-star surface, the velocities change to positive values. Not shown here (but in [65], Fig. 15) is that the degeneracy in front of the shock wave is reduced while it is increased right after the shock wave compared to the unshocked state. This leads to smaller Y_e in front of the shock wave and larger Y_e right behind the shock wave. We find this behavior in the Y_e plot in Fig. 6.5.
At $t_{\rm pb} = 537.9$ ms respectively $t_{\rm pb} = 540.7$ ms we find second peaks in the ν_e and $\bar{\nu}_e$ respectively ν_μ/ν_τ luminosity signal in Fig. 6.7. The peaks are not found in simulations with pure hadronic matter. They are a consequence of the appearance of quark matter in the center of the protoneutron star which causes a collapse of it and the formation of a second shock wave. As soon as the second shock wave passes the neutrino sphere a second neutrino burst is released. The peaks in the $\bar{\nu}_e$ and the and ν_μ/ν_τ signal are more pronounced than the ν_e peak. This can be explained by the production of electron-positron pairs what is favored due to the high temperatures occurring at the shock front. Since most positrons are captured by neutrons there is a pronounced peak in the $\bar{\nu}_e$ luminosity as a direct consequence. Additionally, electron-positron annihilation is possible producing neutrino anti-neutrino pairs which explain the other peaks. The values of the luminosity peaks are: $L_{\nu_e} = 4.13 \cdot 10^{52}$ erg/s, $L_{\bar{\nu}_e} = 5.44 \cdot 10^{52}$ erg/s, $L_{\nu_\mu/\nu_\tau} = 2.55 \cdot 10^{52}$ erg/s, and $L_{\bar{\nu}_\mu/\bar{\nu}_\tau} = 2.58 \cdot 10^{52}$ erg/s.

Our results are in good qualitative agreement with the results of [174, 65]. The peak values of the luminosities are generally lower than in [174, 65]. This is due to the different microphysical input of the hadronic equation of state (already the bounce luminosity peak of BASQUARK is less than half as intense as the one obtained with the Shen EOS) as well as the different values for the phase transition and the quark model. However, measuring a multi-flavor neutrino signal (see e.g. Dasgupta et al. [54] for some estimation on the Super-Kamiokande and the IceCube detectors)

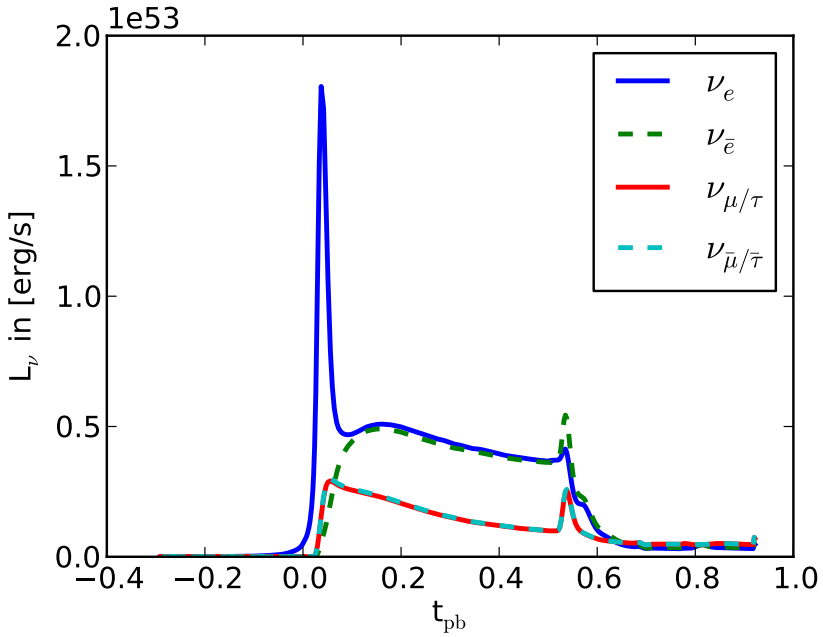

Fig. 6.7: Neutrino luminosities for the different treated neutrino flavors using the 15 $M_\odot$ progenitor and BASQUARK EOS.

might give some serious constraints on the equation of state used. Especially the information on the delay of the second neutrino burst and its order of magnitude contains a lot of information on the hadronic and the quark equation of state: In case the hadronic equation of state is determined and the progenitor star of the event is known, the conditions for hadron-quark phase transition could be determined.

Ideally, the information from several observables are combined in a so-called *multi-messenger* approach: The measurement of the neutrino signal, the gravitational waves, the electromagnetic signature etc. would provide detailed information of the processes inside a core-collapse supernova. With this information we would have critical information to model matter at extreme conditions.

7 Conclusions I

> *What 's done is done.*
>
> **— William Shakespeare**
> Macbeth

The main objective of the first part of this thesis was to systematically explore the hadron-quark phase transition of cold hybrid stars in order to generate a new hybrid supernova equation of state. All of the currently existing hybrid supernova equations of state employ STOS for the description of hadronic matter. STOS is known to have an unrealistically high symmetry energy. Furthermore, only two of all the existing hybrid supernova equations of state using STOS are compatible with the 2 $M_\odot$ constraint. Here, we choose HS(DD2) to describe the hadronic matter which has good nuclear matter properties. Quark matter is described by a constant speed of sound (CSS) equation of state with $c_s^2 = 1/3$, first. The two equations of state were combined to a new hybrid equation of state. By systematically varying the phase-transition pressure and the energy-density discontinuity, we performed a parameter scan as introduced by Alford et al. [7]. In addition to analyzing the maximum mass, we also applied Alford's classification scheme, resulting in four different types of hybrid stars. Overall, the results look similar as in [7] where different hadronic equations of state were used: we find the same qualitative distribution of the four hybrid star categories.

We showed that the simple CSS parametrization for quark matter is equivalent to the thermodynamic bag model with $m_s = 0$ and an additional term from strong interactions that scales with μ^4. This identification is quite important for our purposes, as the CSS parametrization does not provide a temperature and composition dependence required for core-collapse supernova simulations. $m_s = 0$ is not considered as the most realistic value. For this reason, often $m_s = 100$ MeV is used instead. A finite strange quark mass induces a nonconstant speed of sound. Therefore, the one-to-one correspondence between the CSS and the thermodynamic bag model equations of state does not hold anymore. It also changes the resulting phase-transition parameters $p_{\mathrm{trans}}/\epsilon_{\mathrm{trans}}$ and $\Delta\epsilon/\epsilon_{\mathrm{trans}}$. However, we showed that for $m_s = 100$ MeV the speed of sound shows only little deviation from the fixed value $c_s^2 = 1/3$.

In order to get insights about the quark matter parameter regions which are favorable for core-collapse supernova explosions, we calculated $p_{\mathrm{trans}}/\epsilon_{\mathrm{trans}}$ and $\Delta\epsilon/\epsilon_{\mathrm{trans}}$ of the already existing hybrid equations of state from Sagert et al. and Nakazato et al., and added this information to the results of our parameter scan. The equations of

state that showed explosions in one-dimensional core-collapse supernova simulations are all situated in the parameter region that shows a disconnected third family of compact stars. This supports our initial considerations that third-family features might play an important role in the core-collapse supernova explosion mechanism induced by the QCD phase transition; see also [93] for further details.

Regarding the question whether this mechanism can still work despite the 2 $M_\odot$ constraint, the results do not look very promising at first. To form a third family in cold compact stars, phase transition densities below 2.5 n_B^0 are required. On the other hand, to reach sufficiently high maximum masses, the energy density discontinuity has to be rather low, meaning that the phase transition is rather weak and the third family is not very pronounced. As a consequence, only a small parameter region remains where one has third families and a maximum masses above 2 $M_\odot$. From this region we presented the M-R relation of a new hybrid supernova equation of state, employing the bag model parameters $\alpha_s = 0.7$ and $B^{1/4} = 138.5$ MeV. The energy density discontinuity of our example case is lower than the one of B139 which was not (yet) found to explode. However, we want to emphasize again that the existing hybrid equations of state have been tested only for very few progenitor models. It is not excluded that even a slightly more pessimistic equation of state could still trigger explosions for other progenitors. The effects of the hadronic equation of state and of local vs. global charge neutrality for the phase transition also remain to be studied.

Considering hyperons in the hadronic equation of state, using the BHB$\Lambda\phi$ EOS, did not show a qualitative difference in the distribution of the four Alford cases. Again, only a small parameter region remained which might be interesting for future supernova equation of state candidates. Since the transition pressures in this region lie below the pressure where hyperons appear, our proposed example case for a new hybrid supernova equation of state is affected by the presence of hyperons.

In an another section we discussed the problem of reconfinement. Using the assumption of chemical equilibrium at the transition point, the pressure relation $p(\mu_B)$, depending on the baryon chemical potential, of the CSS EOS can be derived. The $p(\mu_B)$ relation revealed that multiple phase transitions appear in our considered range of the parameter scan. Three cases were identified: one (hadron-quark, HQ); two (quark-hadron-quark, QHQ); or three (hadron-quark-hadron-quark, HQHQ) phase transitions. The second case corresponds to a special form of absolutely stable strange quark matter and in the third case, a spurious reconfinement and subsequent second deconfinement transitions occur. Low $p_{\rm trans}$ and small $\Delta\epsilon$ (in regions which otherwise belong to cases C and D) lead to HQHQ phase transitions, whereas high $p_{\rm trans}$ and low $\Delta\epsilon$ (in regions which otherwise belong to case C) lead to QHQ phase transitions. For BHB$\Lambda\phi$ an additional two-phase-transition case (hadron-quark-hadron, HQH) at low transition pressures is present. In Sec. 5.5 we discussed

different options on how to interpret and deal with reconfinement. If it occurs in a density region where one of the two equations of state is not reliable any more, it is justified to ignore it. Otherwise it might point to a region of the quark matter parameter space which is not realistic and should be avoided.

Without considering multiple phase transitions, i.e. ignoring thermodynamic stability in a strict sense, we found that the hybrid stars can have a maximum mass above the ones of the purely hadronic equations of state HS(DD2) and BHB$\Lambda\phi$. Conversely, if strict thermodynamic stability is taken into account, this is not possible unless one has absolutely stable quark matter. Masuda et al. [140, 141] constructed a crossover phase change by an interpolation between the hadronic and the quark equation of state instead of using the usual Maxwell or Gibbs construction. In this procedure, which represents a "manual" manipulation of the equation of state, the maximum mass can be increased. One can conclude that without further assumptions the inclusion of quark matter (using $c_s^2 = 1/3$) generally leads to a reduction of the maximum mass. Only by making use of additional assumptions (e.g. crossover or suppression of reconfinement) the maximum mass can be increased. It would be interesting to further explore the role of multiple phase transitions for other hadronic equations of state in the context of the hyperon puzzle (similarly as in [218]), especially as HS(DD2), and to a smaller extent also BHB$\Lambda\phi$, are particularly stiff equations of state at high densities.

Works such as [7, 5, 27, 172] have shown that an increase of c_s^2 above $1/3$ leads to stronger third-family features in the M-R relation and generally higher maximum masses. A speed of sound above $c_s^2 = 1/3$, can be realized, e.g. by introducing vector interactions; see [21, 217, 172, 115, 116]. To investigate this effect in our calculations, we set the speed of sound to the largest value still consistent with special relativity; $c_s^2 = 1$. Indeed, our calculations for HS(DD2) and BHB$\Lambda\phi$ show a general increase of the maximum masses. The number of parameter combinations excluded by the 2 $M_\odot$ neutron star constraint is reduced tremendously. The third family regions (case B and D) are expanded to higher $p_{\rm trans}/\epsilon_{\rm trans}$ and the case B region also to lower $\Delta\epsilon/\epsilon_{\rm trans}$, compared to the $c_s^2 = 1/3$ results. Hence, significantly more third-family configurations that consider the 2 $M_\odot$ neutron star constraint are found, what makes this scenario interesting for possible candidates for future hybrid supernova equation of state that might induce an explosion.
Considering hyperons in the hadronic equation of state leads to a slightly more restrictive scenario than without them: More third family cases are excluded by the 2 $M_\odot$ constraint. Compared to the calculations with $c_s^2 = 1/3$ it is possible to find parameter configurations where hyperons are already present at the onset of the phase transition to quark matter. This is not the case with a speed of sound of $c_s^2 = 1/3$.

The consideration of thermodynamic stability in a strict sense again leads to multiple phase transitions. Two cases were identified: Besides the one phase-transition HQ, a new two phase transition case (hadron-quark-hadron, HQH) was found. The occurrence of the latter case, HQH, affects the majority of the phase-transition configurations when using HS(DD2). Only a small number of possible supernova equation of state candidates with a third-family feature is not affected. In case of BHB$\Lambda\phi$, the situation is more optimistic and significantly more configurations are still possible. Therefore, we can conclude that it might be very interesting to use BHB$\Lambda\phi$ in case of $c_s^2 > 1/3$ to enlarge the number of possibilities where the chosen phase transition configuration is not affected by multiple phase transitions. While the consideration of thermodynamic consistent stability is expected to result in lowering the maximum mass below the maximum mass of the hadronic equation of state using $c_s^2 = 1$, we still found cases where masses above are possible. A closer analysis of the M-R curves revealed that such cases are only possible due to the huge quark fraction in the neutron star. The large c_s^2 allows the maximum mass to be increased.

The detailed analysis of the hadron-quark phase transition in cold hybrid stars lead to a best-guess configuration for a possible new hybrid supernova equation of state. Based on these values, we constructed the new hybrid supernova equation of state BASQUARK and tested it in the spherical supernova code AGILE-BOLTZTRAN. Our simulation using BASQUARK and a 15 $M_\odot$ progenitor shows an explosion which confirms the choice of our parameters. BASQUARK represents the first hybrid supernova equation of state that fulfills the 2 $M_\odot$ neutron star constraint and triggers the QCD phase transition explosion mechanism. The explosion shows qualitatively the same features as discussed in [174, 65]. However, while in [174, 65] quark matter appeared at core-bounce in the center, we find quark matter to appear off-center sever hundred milliseconds post bounce before spreading to the center. At the end of our simulation, a heavy neutron star with a mass of ~ 1.75 $M_\odot$ is born consisting of around 60 % quark matter. So far, a detailed discussion of the equation of state properties is missing. This will be done in the near future and will contribute to a better understanding of the simulation results.

We conclude that in case of $c_s^2 = 1/3$, suitable parameters for alternative new hybrid supernova equation of state have to be searched for in a strongly restricted region of $\Delta\epsilon$ and p_{trans}, where a maximum mass of 2 $M_\odot$ is obtained and a third-family feature is found. Additionally, the possibility of multiple phase transitions also has to be considered. Considering $c_s^2 > 1/3$, the possible parameter space is enlarged. Additionally, the influence of extra interaction parameters such as a_2 might be analyzed. It would also be interesting to compare with the high-density limit of perturbative QCD [120, 119]. BASQUARK is a new supernova equation of state constructed on the basis of the parameters from the determined example case which shows an explosion for the 15 $M_\odot$ progenitor. In the near future it has

to be systematically tested using other progenitors to investigate the effects of the phase transition. Still an open question is the behavior of hybrid equations of state in multidimensional simulations, i.e. if and how the QCD phase transition explosion mechanism is still working. A first step towards the answer of this question is done in the following chapters.

8 ELEPHANT - An Efficient 3D Core-Collapse Supernova Code

> *Success is not final, failure is not fatal, it is the courage to continue that counts.*
>
> — **Winston Churchill**

In this chapter we give an overview over the code ELEPHANT (Elegant and Efficient Parallel Hydrodynamics with Approximate Neutrino Transport) used to simulate the innermost region of a core-collapse supernovae in three dimensions. ELEPHANT was developed within the Basel group under the leadership of M. Liebendörfer (see e.g. [113, 129, 132, 135, 177, 112]).

8.1 Overview

The ELEPHANT code actually is a combination of several codes. It consists of a central 3D computational domain which is embedded in a larger spherically symmetric computational domain. In the 3D computational domain, the magnetohydrodynamical equations are solved using the explicit hydrodynamics code FISH (Fast and Simple Ideal magneto-Hydrodynamics) [113]. During the collapse phase, the neutrino electron scattering is effectively taken into account using the parametrized deleptonization scheme developed by Liebendörfer et al. [129]. The neutrino transport in the post-bounce phase is solved using the IDSA (Isotropic Diffusion Source Approximation) [135, 22]. A leakage scheme [162] is used to take the energy loss caused by μ/τ-neutrinos into account. Gravity is solved using a poisson solver and general-relativistic corrections are considered using a modified gravitational potential following Marek et al. [138]. The evolution of the outer layers of the progenitor (and therefore also providing the boundary conditions of the 3D computational domain) is handled by the spherically symmetric code AGILE-IDSA [131, 135]. Figure 8.1 summarizes schematically the described code setup.

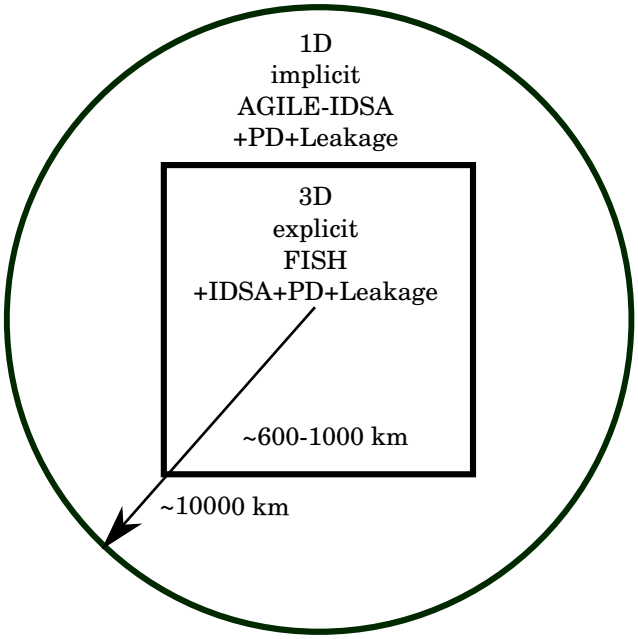

Fig. 8.1: Schematic representation of the code set-up used in the ELEPHANT code. The inner domain of the collapsing star is described in full-3D while the outer layers are described only in spherical symmetry.

8.2 Ideal magnetohydrodynamics

Matter in astrophysical scenarios such as core-collapse supernovae can be described as magnetized fluids. The fluid description is valid when

$$\Lambda \ll L \,, \tag{8.1}$$

holds, where Λ is the collisional mean free path of the involved particles and L a scale over which the distribution function varies significantly [147]. The conditions of Eq. 8.1 are generally met in a core-collapse supernova and therefore the concept of a fluid element can be introduced. The size of the discrete fluid element should be large compared to Λ but still small compared to L. The amount of particles in such a fluid element is large and therefore it is possible to define mean physical quantities such as e.g. density and velocity for the fluid element.

The forces between particles have to be of a short-range nature [147]. Since gravity is a long-range force it has to be included as an external macroscopic force.
A magnetized fluid can be described by the theoretical framework of the so-called *magnetohydrodynamics* (MHD) (see e.g. [118, 106]). It is sufficient to describe the core-collapse supernova matter by the equations of the *ideal magnetohydrodynamics* [118]: In this approach, all dissipative processes are neglected and no viscosity and conductivity[1] are assumed.

[1]The resistivity of the fluid is so small that the it can be treated as a perfect conductor.

8.2.1 Magnetohydrodynamical equations

The three-dimensional conservation equations (including gravitational source terms) which are solved in the hydrodynamical part of ELEPHANT read as follows:

$$\frac{\partial \rho}{\partial t} + \frac{\partial}{\partial x_j}(\rho v_j) = 0 \,, \tag{8.2}$$

$$\frac{\partial}{\partial t} + \frac{\partial}{\partial x_j}(\rho v_i v_j + b_i + b_j + p\delta_{ij}) = \rho \frac{\partial \phi}{\partial x_i} \,, \tag{8.3}$$

$$\frac{\partial E}{\partial t} + \frac{\partial}{\partial x_j}[(E+p)v_j] = -\rho v_i \frac{\partial \phi}{\partial x_i} \,, \tag{8.4}$$

$$\frac{\partial}{\partial t}(\rho Y_e) + \frac{\partial}{\partial x_j}(\rho Y_e v_j) = 0 \,, \tag{8.5}$$

$$\frac{\partial}{\partial t}(\rho Y_\nu^t) + \frac{\partial}{\partial x_j}(\rho Y_\nu^t v_j) = 0 \,, \tag{8.6}$$

$$\frac{\partial}{\partial t}\left[(\rho Z_\nu^t)^{\frac{3}{4}}\right] + \frac{\partial}{\partial x_j}\left[(\rho Z_\nu^t)^{\frac{3}{4}} v_j\right] = 0 \,, \tag{8.7}$$

$$\frac{\partial}{\partial x_i}\left(\frac{\partial \phi}{\partial x_i}\right) = 4\pi G \rho \,. \tag{8.8}$$

The magnetic field is additionally included in the hydrodynamics part by the operator split evolution of the a magnetic field $B_i = \sqrt{4\pi} b_i$,

$$\frac{\partial \mathbf{b}}{\partial t} - \nabla \times (\mathbf{v} \times \mathbf{b}) = 0 \,. \tag{8.9}$$

In Eq. 8.2 - 8.9, t denotes time, x_i the spatial coordinate, ρ the baryonic mass density, v_i the velocity, Y_e the electron fraction, and ϕ the gravitational potential. Temperature T is indirectly considered by the specific internal energy $e(\rho, T, Y_e)$ in the total energy $E = \rho e + \rho v^2/2$. The pressure $p(\rho, T, Y_e)$ and the specific internal energy $e(\rho, T, Y_e)$ are provided via the equation of state. Equations 8.2, 8.3, 8.4, and 8.9, are the ideal MHD equations which conserve the divergence of the magnetic field, so that the divergence-free condition, $\nabla \cdot \mathbf{b} = 0$, remains true. The ideal MHD equations are complemented by Eq. 8.5 for the Y_e evolution. The trapped electron neutrino fraction Y_ν^t and a multiple of the neutrino energies $(\rho Z_\nu^t)^{\frac{3}{4}}$[2], where Z_ν represents the mean neutrino specific energy, are considered in Eq. 8.6 and 8.7 as part of the IDSA. G is the gravitational constant.

8.2.2 Implementation

Providing a detailed description of how Eq. 8.2 to Eq. 8.9 are implemented in the code is beyond the scope of this work, as they are thoroughly described in [113, 112, 177]. In the following the methods are coarsely outlined and we refer to more detailed sources that the reader can examine in case of interest.

[2]Note that the power $3/4$ is introduced to achieve a conservative formulation of the evolution of ρZ_ν^t.

The general numerical framework of ELEPHANT is based on the FISH code [113, 112, 177] which is, in turn, based on the algorithm of Pen et al. [160]. In FISH, the fluid MHD equations (Eq. 8.2,8.3 and 8.4) are rewritten in a very compact form using a vector of conserved variables $\mathbf{u}$ and three flux vectors $\mathbf{F}$, $\mathbf{G}$ and $\mathbf{H}$ for the x, y, and z directions, and vector $\mathbf{S}$ of source terms:

$$\frac{\partial \mathbf{u}}{\partial t} + \frac{\partial \mathbf{F}}{\partial x} + \frac{\partial \mathbf{G}}{\partial y} + \frac{\partial \mathbf{H}}{\partial z} = \mathbf{S} \; . \tag{8.10}$$

The vector with the conserved fluid variables is defined as

$$\mathbf{u} = \begin{bmatrix} \rho \\ \rho v_x \\ \rho v_y \\ \rho v_z \\ E \end{bmatrix} \; . \tag{8.11}$$

The fluxes are given by

$$\mathbf{F} = \begin{bmatrix} \rho v_x \\ \rho v_x + P - b_x^2 \\ \rho v_x v_y - b_x b_y \\ \rho v_x v_z - b_x b_z \\ (E+P) v_x - b_x \mathbf{b} \cdot \mathbf{v} \end{bmatrix} \tag{8.12}$$

$$\mathbf{G} = \begin{bmatrix} \rho v_y \\ \rho v_y v_y - b_y b_x \\ \rho v_y^2 + P - b_y^2 \\ \rho v_y v_z - b_y b_z \\ (E+P) v_y - b_y \mathbf{b} \cdot \mathbf{v} \end{bmatrix} \tag{8.13}$$

$$\mathbf{H} = \begin{bmatrix} \rho v_z \\ \rho v_z v_x - b_z b_x \\ \rho v_z v_y - b_z b_y \\ \rho v_z^2 + P - b_z^2 \\ (E+P) v_z - b_z \mathbf{b} \cdot \mathbf{v} \end{bmatrix} \; . \tag{8.14}$$

The source term takes into account only gravity and is defined as

$$\mathbf{S} = \begin{bmatrix} 0 \\ \rho \partial \phi / \partial x \\ \rho \partial \phi / \partial y \\ \rho \partial \phi / \partial z \\ \rho \mathbf{v} \cdot \nabla \phi \end{bmatrix} \; . \tag{8.15}$$

In FISH, Eq. 8.10 is solved using a finite volume method (details e.g. in [168]) and applying operator splitting [113]. The full discussion of the numerical solution can be found in [113, 112, 177]. In the following, just a few short comments on the solution of Eq. 8.10:

To solve Eq. 8.10 it is decomposed into an homogeneous and an inhomogeneous equation:

$$\frac{\partial \mathbf{u}}{\partial t} + \frac{\partial \mathbf{F}}{\partial x} + \frac{\partial \mathbf{G}}{\partial y} + \frac{\partial \mathbf{H}}{\partial z} = 0 \tag{8.16}$$

$$\frac{\mathrm{d}\mathbf{u}}{\mathrm{d}t} = \mathbf{S}\,. \tag{8.17}$$

Equation 8.16 is solved while keeping the magnetic field constant and interpolating it between the cells. Additionally, the gravitational source terms are neglected during this step. Equation 8.17 is solved assuming that the gravitational potential is given and constant in time for the current iteration. The induction equation (Eq. 8.9) is evaluated separately while keeping quantities, other than the magnetic field, constant. To fulfill the physical constraint $\nabla \cdot b = 0$, in FISH the so-called *constrained transport* method of Evans & Hawley [62] is applied.

To couple the IDSA to the hydrodynamics the vectors $\mathbf{u}$, $\mathbf{F}$, $\mathbf{G}$ and $\mathbf{H}$ can be simply expanded to:

$$\mathbf{u} = \begin{bmatrix} \rho \\ \rho v_x \\ \rho v_y \\ \rho v_z \\ E \\ \rho Y_e \\ \rho Y_\nu^t \\ (\rho Z_\nu^t)^{\frac{3}{4}} \end{bmatrix}, \tag{8.18}$$

$$\mathbf{F} = \begin{bmatrix} \rho v_x \\ \rho v_x + P - b_x^2 \\ \rho v_x v_y - b_x b_y \\ \rho v_x v_z - b_x b_z \\ (E+P)v_x - b_x \mathbf{b}\cdot\mathbf{v} \\ v_x \rho Y_e \\ v_x \rho Y_\nu^t \\ v_x (\rho Z_\nu^t)^{\frac{3}{4}} \end{bmatrix}, \tag{8.19}$$

and $\mathbf{G}$ and $\mathbf{H}$ are expanded in the same way as $\mathbf{F}$ following the same strategy.

8.3 Treatment of general relativity

In ELEPHANT gravity is considered via the Poisson equation

$$\nabla^2\phi = 4\pi G\rho \ . \tag{8.20}$$

The Poisson equation is an non-homogeneous, elliptic partial-differential equation of second order, while the MHD equations are of hyperbolic nature. Whereas the MHD equations propagate the physical information only at a finite speed in the Poisson equation information is propagated instantaneously[3]. This means that, in the case of the MHD equations, communication takes only place between the treated cell and its immediate neighbors. In the case of the elliptical Poisson equation, the whole information of the entire domain must be available.

In ELEPHANT it is possible to choose between four options to calculate gravity: We can choose between a 1D and a 3D treatment of gravitiy in either a pure Newtonian approach or with relativistic corrections. In the following, we give a brief overview over the available options:

- The purely **Newtonian spherically symmetric** Poisson equation reads as follows:

$$\frac{1}{r^2}\frac{\partial}{\partial r}\left(r^2\frac{\partial\phi}{\partial r}\right) = 4\pi G\rho(r) \tag{8.21}$$

  $\rho(r)$ is obtained from the spherically averaged 3D data. Equation 8.21 is easily integrable and it is computationally not expensive. The one dimensional approach is a good approximation for non- or slowly rotating stars, as long as centrifugal forces do not produce strong deformations. However, it has been shown in spherical symmetric core-collapse supernova simulations that considering full GR results in more compact core radii, smaller shock radii, and different neutrino luminosities and and rms energies of each occurring flavor during the shock reheating epoch [30, 133]. GR should therefore not be neglected in core-collapse supernova simulations.

- Due to the mentioned differences between the full general relativistic potential and the Newtonian potential, ELEPHANT includes an **approximation to the radial general relativistic effects**. To mimic the general relativistic effects, the Newtonian ϕ is replaced by an effective potential ϕ_{eff} according to [138, 112]:

$$\phi_{\text{eff}} = \int_r^\infty \frac{G}{r^2}\left(M_{\text{eff}} + \frac{4\pi r^3}{c^2}(p+p_\nu)\right)\frac{1}{\Gamma^2}\left(\frac{\rho c^2+\rho e+p}{\rho c^2}\right)\mathrm{d}r \ , \tag{8.22}$$

[3]The equation is non-causal which means the propagation speed of the physical information is not restricted by the speed of light

where p is the gas pressure, ρ the rest mass density, e the internal energy density, and p_ν the neutrino pressure. The potential is theoretically motivated by the TOV solution for spherical general relativistic stars in hydrostatic equilibrium (see e.g. [181]). For the effective mass M_{eff}, "case A" of [138, 112] is implemented

$$M_{\text{eff}} = \int_0^\infty 4\pi \left(\rho + \frac{\rho e}{c^2} + \frac{E_\nu}{c^2}\right) \Gamma r^2 \mathrm{d}r \ , \tag{8.23}$$

with E_ν representing the neutrino energy density. The metric function Γ is given by

$$\Gamma(r) = \sqrt{1 + \frac{v_r^2}{c^2} + \frac{2GM_{\text{eff}}}{c^2 r}} \ , \tag{8.24}$$

where v_r is the radial fluid velocity.

- In core-collapse supernovae non-spherical effects, such as e.g. convection, play an important role. Thus, the Poisson equation (Eq. 8.9) has to be solved in three dimensions. The **Poisson equation in 3D Cartesian coordinates** reads

$$\nabla^2 \phi(x,y,z) = \left(\frac{\partial^2}{\partial x^2}, \frac{\partial^2}{\partial y^2}, \frac{\partial^2}{\partial z^2}\right) \phi(x,y,z) = 4\pi G \rho(x,y,z). \tag{8.25}$$

  To solve the Poisson equation efficiently, ELEPHANT uses the HYPRE library[4] which is a highly scalable multi-grid solver.

- An effective potential for multi-dimensional flows can be designed according to [138]

$$\phi_{\text{eff}}(x,y,z) = \phi(x,y,z) - \bar{\phi}(r) + \bar{\phi}_{\text{eff}}(r) \ , \tag{8.26}$$

  where $\phi(x,y,z)$ is the 3D Newtonian potential, $\bar{\phi}$ the monopole term of the Newtonian potential, and $\bar{\phi}_{\text{eff}}$ refers to Eq. 8.22. However, in $\bar{\phi}$ and $\bar{\phi}_{\text{eff}}$ the quantities $\rho, e, P, v, E,$ and p_ν are replaced by the spherically averaged 3D quantities.

8.4 Neutrino interactions and transport

The inclusion of neutrino physics into core-collapse supernova simulations is a crucial ingredient. During the evolution of the collapse and the post-bounce stage, the vast majority of the released binding energy is converted into neutrinos of all species. The neutrino interactions play an essential role during the deleptonization of the protoneutron star and in the subsequent explosion dynamics. Ideally, neutrino transport should be treated using the full Boltzmann equation to describe the neutrino distributions and their temporal evolution (see e.g. [143]). The Boltzmann equation describes the time t evolution of the particle distribution function $f(x,v,t)$

[4] For the latest releases of the HYPRE suite please see: `http://computation.llnl.gov/projects/hypre-scalable-linear-solvers-multigrid-methods`.

with x as the position and v as the velocity. According to [143], the classical Boltzmann equation in Cartesian coordinates is

$$\left(\frac{\partial f}{\partial t}\right) + v^i \left(\frac{\partial f}{\partial x^i}\right) + a^i \left(\frac{\partial f}{\partial v^i}\right) = \left(\frac{Df}{Dx^i}\right)_{coll} . \tag{8.27}$$

Equation 8.27 describes, in its most general form, a 7-dimensional problem: time and the 6-dimensional neutrino phase space (3 spatial coordinates, neutrino energy and two angular degrees of freedom). The numerical solution of this equation results thus in a very computationally demanding calculation that lies in the sustained exascale, being nowadays out of reach for current computational resources/infrastructures. The Boltzmann transport has been routinely implemented in 1-dimensional simulations (see e.g. [133, 130]) and there have also been approaches to solve the Boltzmann equation in full 3D (see [191]). Nevertheless, using todays supercomputer it is still not possible to effectively implement the solution of the Boltzmann equation in 3-dimensions without making big trade-offs on other quantities such as the spatial resolution.

A common set of neutrino interactions used in 1D core-collapse supernova simulations with Boltzmann transport (see e.g. [65]) is listed below.

$$e^- + p \rightleftarrows n + \nu_e \tag{8.28}$$
$$e^+ + n \rightleftarrows p + \bar{\nu_e} \tag{8.29}$$
$$e^- + \langle A, Z\rangle \rightleftarrows \langle A, Z-1\rangle + \nu_e \tag{8.30}$$
$$\nu + N \rightleftarrows \nu' + N \tag{8.31}$$
$$\nu + \langle A, Z\rangle \rightleftarrows \nu' + \langle A, Z\rangle \tag{8.32}$$
$$\nu + e^{\pm} \rightleftarrows \nu' + e^{\pm} \tag{8.33}$$
$$e^- + e^+ \rightleftarrows \nu + \bar{\nu} \tag{8.34}$$
$$N + N \rightleftarrows N + N + \nu + \bar{\nu} \tag{8.35}$$
$$\nu_e + \bar{\nu}_e \rightleftarrows \nu_{\mu/\tau} + \bar{\nu}_{\mu/\tau} \tag{8.36}$$

The key of the denoted variables is as follows: e^- = electrons, e^+ = positrons, n = free neutrons, p = free protons, N = free neutrons or protons, $\langle A, Z\rangle$ = nuclei with mass number A and charge number Z, ν = any type of neutrinos and $\bar{\nu}$ the respective antineutrino. For a detailed discussion of these interactions see e.g. [29] and an illustrative summary see [177]. It has to be noted at this stage that ELEPHANT does not consider all of these rates, but only a selection: the IDSA currently includes reactions 8.28, 8.29, 8.31, 8.32, and the μ/τ-leakage reaction 8.36. Reactions 8.30 and 8.32 are still based on the old Bruenn rates [29].

8.4.1 Parametrized deleptonization

As mentioned in Chapter 1, the stellar collapse proceeds by an imbalance between self-gravitating forces of the inner core and its fluid pressure. While baryons contribute the dominant part to the gravitational mass of the stellar core, the degenerate electron gas represents the dominant contribution to the pressure. The electron fraction Y_e is, therefore, the most important quantity for the stability of the inner core and its further evolution. During the collapse, the electron fraction evolves by electron capture on nuclei (Eq. 8.30) and electron captures on protons (Eq. 8.28). These reactions lead to a reduction of the electron fraction Y_e. These electron captures during the collapse are called **deleptonization**. The collapse halts when matter in the core reaches nuclear density. Compressibility is reduced due to strong interactions and leads to the core bounce. This generates an outward traveling pressure wave which turns into a shock wave as it reaches the sonic point at the edge of the collapsing inner core. The location of this transition determines the size of the inner core.

The correct treatment of the deleptonization is therefore crucial for the correct description of the collapse phase in core-collapse supernovae. As mentioned above, full Boltzmann transport is generally too computationally expensive for multi-dimensional applications. For this reason, in ELEPHANT, the so-called parametrized deleptonization scheme is applied [129]. It is a simple and efficient scheme which relies on a Y_e vs. ρ parametrization. As described in [129], the deleptonization scheme uses the idea that, during the collapse, the $Y_e(\rho, t)$ profiles depend only weakly on time in spherical simulations with full Boltzmann transport. For this reason it is possible to replace the computationally expensive calculation of $Y_e(\rho, t)$ by a linear interpolation in the logarithmic density of a time-dependent tabulated template of Y_e at the time of bounce, $\bar{Y}_e(\rho) = Y_e(\rho, t = t_b)$, using the interpolation formula provided in [129]. It is important to fit the Y_e as accurately as possible at the time of bounce, since at that point the final size of the inner core is determined. Pan et al. [159] also found that the level of electron deleptonization during the collapse can have dramatic effects on the post-bounce evolution.

The implementation of an electron fraction along the fitted $\bar{Y}_e(\rho)$ is achieved by

$$\frac{\delta Y_e}{\delta t} = \frac{\min\{0, \bar{Y}_e(\rho(t + \delta t)) - Y_e(t)\}}{\delta t} \,, \tag{8.37}$$

where the variation is taken at the same fluid element. The minimum function guarantees that the electron fraction monotonically decreases even in the case of transient instances in which the parametrized $\bar{Y}_e$ is larger than the actual Y_e.

The electron captures during the collapse are not only changing the electron fraction Y_e, but also affect the matter entropy and the neutrino stress. Depending on the matter density and the energy of the produced neutrinos, three cases are possible:

Case 1: the neutrinos directly escape, case 2: they thermalize and then escape, case 3: they are trapped for a longer timescale than the dynamical timescale. Entropy has to be modified for case 2, the neutrino pressure and the neutrino stress in all cases. The corresponding formulas can be found in [129].

As soon as bounce is reached, the parametrized deleptonization scheme is turned off and the neutrino physics has to be treated with a different scheme to appropriately treat the later evolution as the parametrized deleptonization scheme cannot describe the neutrino burst.

8.4.2 IDSA

In ELEPHANT, the neutrino transport equation used in the post-bounce phase is approximated by the IDSA (Isotropic Diffusion Source Approximation) [135]. The IDSA is considered a spectral method. We will follow the explanations therein closely in the following.

The main idea is to decompose the distribution function f_ν of a given neutrino species ν into an isotropic distribution function of trapped neutrinos f_ν^t and a distribution function of streaming particles f_ν^s, depending if the local zone is opaque or transparent for neutrinos. The total distribution function is then the sum of the trapped and the streaming distribution functions $f_\nu = f_\nu^t + f_\nu^s$. It is assumed that these two components evolve separately. Using a linear operator D describing the particle propagation, the transport equation can be written as

$$D(f_\nu = f_\nu^t + f_\nu^s) = C_\nu \ . \tag{8.38}$$

$C_\nu = C_\nu^t + C_\nu^s$, represents a suitable decomposition of the collision integral according to the coupling to trapped (C_ν^t) or streaming (C_ν^s) particle components. The transport equation Eq. 8.38 can then be split in two equations:

$$D(f_\nu^t) = C_\nu^t - \Sigma_\nu \ , \tag{8.39}$$

$$D(f_\nu^s) = C_\nu^s + \Sigma_\nu. \tag{8.40}$$

Σ_ν represents an additional (coupling) source term which converts trapped particles into streaming particles and vice versa. It can be determined approximately by the requirement that a temporal change of f_ν^t in Eq. 8.39 has to reproduce the diffusion limit in the limit of small free mean paths. In [135], Σ_ν is therefore named the "diffusion source".

The full derivation for the expression of the neutrino distribution function can be found in [135]. A strict mathematical discussion of the IDSA has been done in [22] including the discussion of all limiting cases. Below, a short review on the actual implementation in ELEPHANT is provided closely following [158]. Based on the

trapped neutrino fraction Y_ν^t and the trapped mean neutrino specific energy Z_ν^t the neutrino distribution function f_ν^t is constructed first, assuming an equilibrium spectrum for the trapped component. With this information, the diffusion equation

$$\frac{\partial f_\nu^t}{c\partial t} = j_\nu - (j_\nu + \chi_\nu) f_\nu^t - \Sigma_\nu \tag{8.41}$$

can be solved in three dimensions with the diffusion source

$$\Sigma_\nu = \min\left\{\max\left[\alpha_\nu + (j_\nu + \chi_\nu)\frac{1}{2}\int f_\nu^s \mathrm{d}\mu, 0\right], j_\nu\right\}; \ , \tag{8.42}$$

where the non-local scalar is

$$\alpha_\nu = \nabla \cdot \left(\frac{-1}{3(j_\nu + \chi_\nu + \phi_\nu)} \nabla f_\nu^t\right) \ . \tag{8.43}$$

The angular integral of the streaming neutrinos $\frac{1}{2}\int f_\nu^s \mathrm{d}\mu$,[5] is provided based on the value from the previous time step. In Eq. 8.41 - 8.43, j_ν represents the spectral neutrino emissivity, χ_ν the neutrino absorptivity, and ϕ_ν includes the isoenergetic scattering in the mean free path (see e.g. [29]). The non-local diffusion term α_ν (Eq. 8.43) is evaluated using an *explicit* finite differencing scheme. All other variables are local. In each zone of the computational domain, they are iterated towards convergence using an *implicit* Newton-Raphson scheme. Equation 8.41 also determines the net interaction rates $s_\nu = j_\nu - (j_\nu + \chi_\nu)(f_\nu^t + j_\nu^s)$ between matter and radiation particles. These rates in turn determine the updates of the electron fraction Y_e and the specific energy e

$$s_\nu = \frac{\partial f_\nu^t}{c\partial t} + \Sigma_\nu - (j_\nu + \chi_\nu)\frac{1}{2}\int f_\nu^s \mathrm{d}\mu \ , \tag{8.44}$$

$$\frac{\partial Y_e}{c\partial t} = -\frac{m_b}{\rho}\frac{4\pi c}{(hc)^3}\int (s_{\nu_e} - s_{\bar{\nu}_e}) E^2 \mathrm{d}E \ , \tag{8.45}$$

$$\frac{\partial e}{c\partial t} = -\frac{m_b}{\rho}\frac{4\pi c}{(hc)^3}\int (s_{\nu_e} + s_{\bar{\nu}_e}) E^3 \mathrm{d}E \ , \tag{8.46}$$

where m_b is the baryon mass, c the speed of light and h the Planck constant. The change in the electron fraction Y_e (Eq. 8.45) and the specific internal energy e (Eq. 8.46) are then fed back into j_ν, χ_ν and ϕ_ν and adjusted until convergence is reached.

In [135], for the streaming part a stationary-state solution is assumed and observer corrections are neglected. Using these assumptions, the integration of the net rate over a sphere with radius R gives a useful approximation for the neutrino number luminosity $4\pi R^2 q_\nu$ at the surface of the sphere. The streaming neutrino flux reads then

$$q_\nu = \frac{1}{4\pi R^2}\int_0^R \left(\frac{1}{2}\int [-(j_\nu + \chi_\nu] f_\nu^s + \sigma_\nu] \mathrm{d}\mu\right) 4\pi r^2 \mathrm{d}r \ . \tag{8.47}$$

[5] μ is the momentum space spanned by the angle cosine.

The spectral neutrino density can then be derived from the neutrino flux by an analytically estimated flux factor $F(E)$ and reads

$$\frac{1}{2}\int f_\nu^s \mathrm{d}\mu = \frac{q_\nu}{F(E)} \,, \tag{8.48}$$

where the estimated flux factor is defined as

$$F(E) = 1 + \sqrt{1 - \left(\frac{R_\nu(E)}{\max(r, R_\nu(E))}\right)^2} \,, \tag{8.49}$$

with R_ν being the radius of the monochromatic last scattering sphere (also called the neutrino sphere) that depends on the particle energy E. The spectral neutrino density from Eq. 8.47 enters the diffusion equation (Eq. 8.41) in the next time step.

Using the solution of Eq. 8.41, the trapped neutrino fraction Y_ν^t and the trapped mean neutrino specific energy Z_ν^t are updated by integrating the spectral f_ν^t over the energy E:

$$\frac{\partial Y_\nu^t}{\partial t} = \frac{m_b}{\rho}\frac{4\pi c}{(hc)^3}\int \frac{\partial f_\nu^t}{\partial t} E^2 \mathrm{d}E \,, \tag{8.50}$$

$$\frac{\partial Z_\nu^t}{\partial t} = \frac{m_b}{\rho}\frac{4\pi c}{(hc)^3}\int \frac{\partial f_\nu^t}{\partial t} E^3 \mathrm{d}E \,, \tag{8.51}$$

$$\frac{\partial \mathbf{v}}{\partial t} = -\frac{1}{\rho}\nabla\left(\frac{\rho Z_\nu^t}{3m_b}\right) \,. \tag{8.52}$$

Equation 8.52 describes the contribution of the neutrino pressure on the matter which leads to an extra momentum.

Finally, it has to be noted that ELEPHANT includes the crucial compressional heating of the trapped neutrino gas in Eq. 8.7, which in the original Boltzmann equation is an $\mathcal{O}(v/c)$ observer correction. This correction is important to fulfill the hydrodynamical limit.

In the future, the IDSA could be upgraded including neutrino-electron scattering. This would make the parametrized deleptonization redundant since the collapse could also be treated with the IDSA self consistently. However, it would also make the computations more computationally demanding. Furthermore, the scheme could be applied to μ/τ neutrinos whose spectrum is significantly determined by non-isoenergetic scattering.

8.4.3 μ/τ-Leakage

Since μ/τ neutrinos (and their respective anti-particles) are not handled within the IDSA but still play an important role by their effect on the compactness of the protoneutron star, they are treated separately. The role of such neutrinos is primarily

to cool the neutron star. They do not interact with the outer accreting layers after their emission from the neutrino surface. In ELEPHANT, the energy loss caused by the μ/τ neutrinos during the collapse and the post-bounce phase is treated using a so-called spectral μ/τ leakage scheme which is similar to the one used in [162, 161]. The following description closely follows [161].

In the used leakage, μ and τ neutrinos (and their antineutrinos) are treated as a collective species which only act as a source of cooling. Due to the neutral current reactions, it is assumed that for this type of neutrinos always the same amount of neutrinos and antineutrinos are produced. The leakage includes the pair production which is supposed to be the main source of neutrinos

$$e^+ + e^- \rightarrow \nu_{\mu,\tau} + \bar{\nu}_{\mu,\tau} \ . \tag{8.53}$$

The production rates are calculated using the interpolating formulas from Itoh et al. [104]. These formulas give directly the production rate R_{prod} using the thermodynamic conditions specified by matter density ρ, temperature T, and electron fraction Y_e,

$$(\rho, T, Y_e) \rightarrow R_{\mathrm{prod}} \ . \tag{8.54}$$

At every point of the grid, the effective emission rate is calculated using a smooth interpolation between the local production rate and the diffusion rate. The latter is determined by assuming the μ/τ neutrinos to be an ideal Fermi gas with zero chemical potential. The diffusion time scale, used to determine the diffusion, can be found in [161, 162].

8.5 Equation of state

To be able to solve the set of equations (Eq. 8.2 - 8.9), an equation of state has to provide the pressure as well as other quantities as a function of the density ρ, temperature T or entropy s, and the electron fraction Y_e.

Elephant has two built-in interfaces to read tabulated equations of state, such as described in Sec. 4.2. The first interface supports the format for the equations from Lattimer and Swesty [125]. The second interface supports the new format "HS" from the equation of states developed by Matthias Hempel and collaborators[6] e.g. the HS(DD2) EOS [96, 69]. In this second part of the work, we focus on the HS(DD2) EOS (see Sec. 4.2.3) and BASQUARK (see Sec. 4.2.4) which both have the new format. Presently, an extension to the regions not fulfilling the nuclear statistical equilibrium (NSE) is missing in ELEPHANT.

[6] Equations of state calculated by Matthias Hempel using another standardized format are available at `http://phys-merger.physik.unibas.ch/~hempel/`

8.6 Elephant upgrades to support quark matter simulations

To consider quark matter in ELEPHANT two important upgrades had to be done compared to the standard version:

- **Two independent equations of state:** As mentioned above, ELEPHANT consists of a central 3D hydro code and the 1D AGILE-IDSA code which runs in the background treating the outer layers and providing the outer boundary conditions of the 3D domain. In the standard version, both domains use the same equation of state. This treatment leads to a problem when using a hybrid supernova equation of state: due to the spherical nature of the AGILE-IDSA it is possible that a collapse of the protoneutron star and an eventual explosion occurs before this happens in the 3D domain. Since AGILE-IDSA is providing the boundary conditions of the 3D domain, this is fatal! As soon as the shock wave in AGILE-IDSA reaches the region from which the boundary of the 3D domain is updated the boundary is not treated correctly anymore. High entropy material from the shock is fed into the boundary of the 3D domain which is consequently falling onto the protoneutron star in the central 3D domain leading to a prompt explosion.

  To avoid this problem we run AGILE-IDSA with a purely hadronic equation of state. Using a hadronic equation of state ultimately leads to a black hole formation in 1D, but this happens significantly later than the second collapse would take place in case of using a hybrid equation of state. In this second part of this work, we want to implement BASQUARK into ELEPHANT. As mentioned in Sec. 6 the hadronic part of BASQUARK is described by the HS(DD2) EOS. We therefore use the BASQUARK EOS in the 3D domain and implement the HS(DD2) EOS in AGILE-IDSA. The boundary conditions should still be treated correctly since the appearance of quark matter happens in the central protoneutron star. Since this information cannot go beyond the standing accretion front the boundary conditions are not influenced.

- **Quark routines:** In the next chapters, we will need the information about the quark matter fraction distribution. The quark matter fraction is calculated and stored during the simulation to be available for later post processing. This is done by an additionally implemented “quark routine”. The quark mass fraction is interpolated from a separate table additionally to the normal BASQUARK table using density ρ, electron fraction Y_e and temperature T as an input.

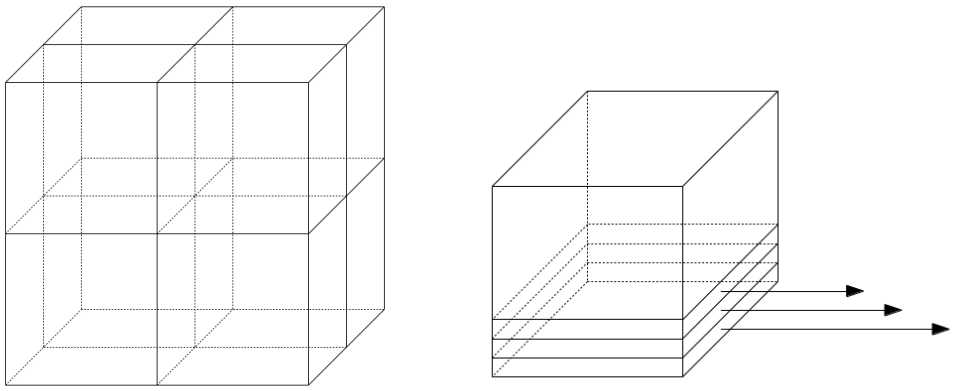

(a) (b)

Fig. 8.2: Illustration of the domain decomposition used in ELEPHANT. The left panel shows for instance the decomposition of the 3D computational domain into 8 blocks. Each of these blocks is assigned to one distributed memory MPI-task. The magnetohydrodynamical equations of each block are then solved efficiently using additional shared memory OpenMP parallelization. The right panel shows the treatment of the IDSA: an example block is decomposed into further sheets which are sent to the GPU where OpenACC is used for further parallelization.

8.7 Code set-up and parallelization

As mentioned above in Sec. 8.1, ELEPHANT consists of a central 3D computational domain which is embedded in a larger spherical computational domain. The 3D computational domain usually consists of $\sim 600^3$ cells with a resolution of $1-2$ km. Since such a problem size can not be handled with a single CPU anymore therefore the code is parallelized. The strategy is a domain composition, dividing the whole 3D computational domain into n rectangular blocks of dimension $n_x \cdot n_y \cdot n_z$ (see Fig 8.2a). Each of these blocks is assigned to one MPI-task [71, 80] with distributed memory and is enclosed by buffer zones to ensure that that the largest stencil are supported in the boundary zones. Each MPI-task uses additionally shared memory OpenMP parallelization [52, 44] to solve the magnetohydrodynamical equations. The solver for the 3D diffusion equation in the IDSA uses the same domain decomposition and MPI-tasks. For further parallelization the block is sliced into sheets. The operations on the sheets can either be parallelized by OpenMP or be sent to a GPU using OpenACC [154]. To ensure efficient data transfer, the zones of a block are swept from bottom to top sending one sheet after the other (illustrative representation given in Fig. 8.2b). Using the OpenACC version, a speed-up of a factor of two can be achieved compared to the version using OpenMP. To handle the input / output operations efficiently and ensure portability and scalability ELEPHANT uses the HDF5 library [198].

Figure 8.3 shows information about the scaling behavior of ELEPHANT on the Cray XC30 named Piz Daint at CSCS in Lugano. Only lately, in November/December 2016,

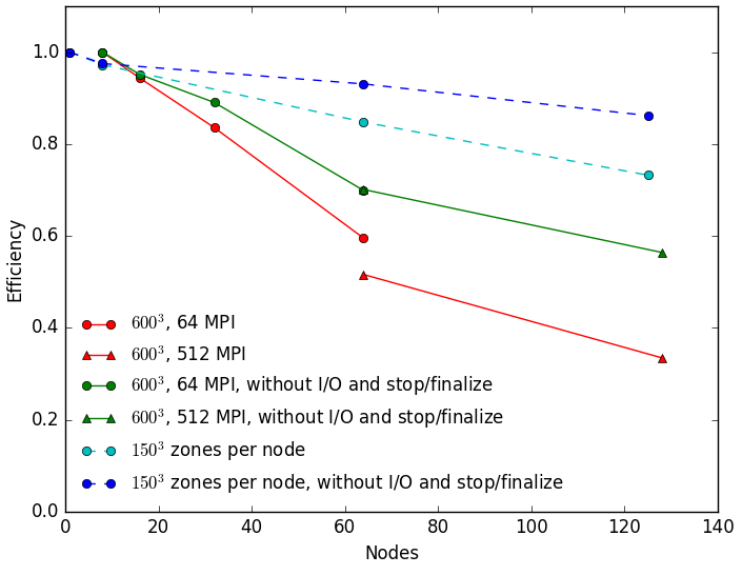

Fig. 8.3: Scaling behavior of ELEPHANT on the XC30 (name Piz Daint) at Swiss National Supercomputing Center (CSCS) showing the efficiency against the number of used nodes. The timing is done post-bounce using 10 hydro steps. The solid lines show the strong scaling behavior of ELEPHANT using a problem size of 600^3 cells and are gauged to 8 nodes. The two colors indicate if the poorly-scaling writing and stopping routines are considered or not. The dashed lines in blue represent the weak scaling behavior of ELEPHANT with increasing problem size varying from 150^3 to 750^3 cells.

Piz Daint has been upgraded to an Cray XC50/XC40 hybrid machine and a scaling analysis should now be redone on the new machine. For our analysis we restart the simulation shortly post bounce using a purely hadronic equation of state. The solid lines in red and green in Fig. 8.3 show the strong scaling of a fixed problem size of 600^3 cells using 1 km resolution which corresponds to a representative production-size model. We split the domain in 64 and 512 MPI-tasks which results in 1 to 8 MPI-tasks per node. The GPU accelerator is also enabled. Since the problem size does not fit on 1 node anymore, we start our analysis on 8 nodes (the efficiency is therefore normalized to 8 nodes). The timing is done for 10 hydro steps. The straight line in red shows the scaling behavior of ELEPHANT. ELEPHANT does not show a good scaling behavior at all. However, we realized that determining the timing of ELEPHANT using only 10 hydro steps differs from the actual production behavior: The 1D writing routine and the finalization ("comm_mpistop") do scale poorly and contribute strongly to the overall time. Since these two routines only play a minor role during an actual production run, we subtracted their time from the overall timing. This corrects our results closer to the actual behavior found in a production run. The result is shown by the solid green line. Based on the efficiency shown in Fig. 8.3, we can conclude that a run with the size of 600^3 cells can be efficiently done on 64 nodes. The dashed lines in blue (with and without the correction of the two poorly scaling routines) shows the weak scaling of ELEPHANT increasing the overall problem size. We investigated 150^3 zones on 1 node, 300^3 zones on 8 nodes, 600^3 zones on 64 nodes and 750^3 zones on 128 nodes. This setup corresponds to always 150^3 zones per node. We gauged the timing results from the problems with size of $300^3, 600^3$ and 750^3 cells to the one with 150^3 cells on one node. We find that it is possible to enlarge the computational domain or the resolution without sacrificing efficiency.

9 Restarting a 3D Core-Collapse Supernova Simulation from a Spherical Profile

> *"Everything must be made as simple as possible. But not simpler."*
>
> **— Albert Einstein**

This chapter deals with the newly developed *spherical restart method*. As we will see in the following chapter, this method has proven to be extremely useful when testing BASQUARK in ELEPHANT. In this chapter the method is discussed in detail and tested, using the purely hadronic equation of state HS(DD2) to exclude possible artifacts from quark matter in the discussion.

9.1 Motivation

Simulating core-collapse supernovae in three spatial dimensions is a computationally very demanding task. As mentioned previously, our code ELEPHANT provides us a useful and efficient tool to simulate the core-collapse and the following evolution of the innermost few hundred kilometers of the star. Since the ultimate goal of this second part of this work is to simulate quark matter and its effects in three-dimensional core-collapse supernova calculations, simulation times up to several hundreds of milliseconds post bounce have to be reached. This is computationally very expensive. A small example shall illustrate the time consumption: Even "low resolution" simulations, with 2 km resolution in our central 3D computational domain, calculates only 35 ms of physical time per 18 hours batch of wall-clock time (run on 27 nodes on the Cray XC30 "Piz Daint" at CSCS) in the post-bounce phase. To get to ~ 500 ms post-bounce, where one could expect quark matter, around 15 to 16 batches have to be used. Depending on the occupancy of "Piz Daint", each one of these batches can have a queuing time of around three days on average which leaves us with more than a month to get to the relevant post-bounce time. Furthermore, since ELEPHANT was never run with a hybrid supernova equation of state before we completely lack of any experience. Therefore, to test ELEPHANT in this scenario, a new tool has to be developed to overcome the mentioned long-term simulation times and be able to set up test cases without wasting vast amount of computational resources. Besides the expected long simulation times, we are completely unaware

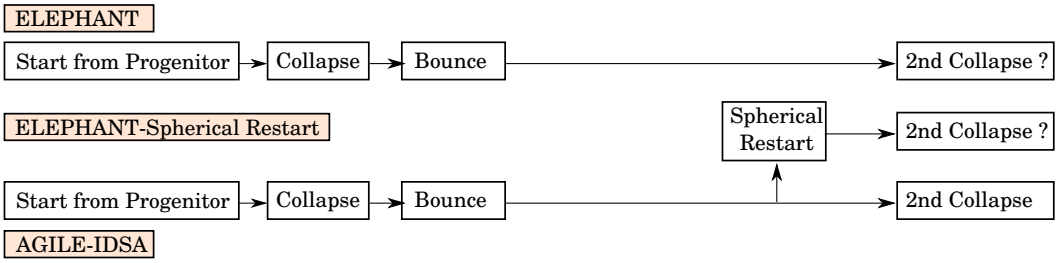

Fig. 9.1: Diagram illustrating the method of a spherical restart in ELEPHANT.

at this stage of what spatial resolution is needed to correctly treat quark matter in the core of the protoneutron star. Resolution might become especially important in the case of a collapse of the protoneutron star. The ability to test resolution at late post-bounce time is therefore another crucial requirement for future flagship calculations.

Simulating core-collapse supernovae in spherical symmetry is computationally much less demanding than a full 3D simulation. Using the time-implicit AGILE-IDSA code (see Liebendörfer et al. [131, 135]), a simulation can be run up to several hundreds of milliseconds post-bounce within a few hours, using one single CPU on a simple desktop computer. Since AGILE-IDSA is also run in the background of ELEPHANT, providing the boundary conditions of the 3D domain, in principle it should be possible to map any 1D AGILE-IDSA profile into ELEPHANT and restart from there. This is what we call the *spherical restart method*. Figure 9.1 illustrates the discussed idea of a spherical restart.

9.2 Method and implementation

The spherical restart method can coarsely be divided into two parts: The initial remapping of the spherical profiles into the 3D domain of ELEPHANT and the subsequent relaxation of ELEPHANT.

9.2.1 Remapping

The spherical profile is extracted from a standard AGILE-IDSA run[1] at the desired time post-bounce. The profile should not be chosen during the collapse too close to core bounce. This is motivated by the fact that ELEPHANT shows problems when trying to restart (from a three-dimensional restart file) during the collapse and bounce in full ab-initio runs. Mapping a one-dimensional profile from an external AGILE-IDSA run into ELEPHANT is done in the following steps (also see Fig. 9.2):

[1] In the following, we will use the term *standard AGILE-IDSA* for an AGILE-IDSA run that is run separately and is independent of the ELEPHANT calculations.

1. In a first step the profile from the standard AGILE-IDSA run is read in and the data transferred into the background AGILE-IDSA of ELEPHANT. The read-in quantities are: Rest mass $m_{\rm rest}$, radius r, velocity v, gravitational mass $m_{\rm grav}$, density ρ, temperature T, electron fraction Y_e, the lapse function α, electron-neutrino fraction Y_ν and its anti-neutrino fraction $Y_{\bar{\nu}}$, and the neutrino mean specific energy Z_ν respectively the anti-neutrino mean specific energy $Z_{\bar{\nu}}$. With an equation of state call using the variables ρ, T, and Y_e , the quantities pressure p, specific energy e, entropy per baryon s, and the speed of sound c_s are determined. In AGILE-IDSA these variables are defined either on the cell-edges (*a-grid* quantities) or on the cell-centers (*b-grid* quantities):

   - a-grid quantities are: $m_{\rm rest}$, r, v, and $m_{\rm grav}$.
   - b-grid quantities are all other quantities: ρ, T, Y_e, α, Y_ν, $Y_{\bar{\nu}}$, Z_ν, $Z_{\bar{\nu}}$, p, e, s, and c_s.

2. AGILE-IDSA uses an adaptive grid what causes the zones to be unequally spaced. ELEPHANT on the other hand uses an equally spaced 3D grid. For this reason, in a second step a remapping from the not-equally spaced AGILE-IDSA array to an equally spaced 1D dummy array is done. This dummy array has half the length of the 3D ELEPHANT domain and the same equal grid spacing. The remapping is done using an internal routine which maps the quantities $m_{\rm rest}$, s, Y_e, the derived relativistic factor Γ, Y_ν, $Y_{\bar{\nu}}$, Z_ν, $Z_{\bar{\nu}}$, and v in a conserved form to the new grid. This ensures that the conservation laws such as; mass, momentum, charge, and energy conservation, are fulfilled. The new dummy array does not differ between a-grid and b-grid values. All quantities are defined cell-centered. The reason for this restructuring is that in ELEPHANT all quantities are defined in a cell-centered manner. In case cell-edged values are needed for a calculation, these are calculated and stored only temporarily.

3. In a third step, the equally-gridded spherical data, stored in the dummy array, is mapped in the 3D domain. The values of the cells in the 3D domain are interpolated from the spherical data using an internal mapping routine. Again it is ensured that the conservation laws are fulfilled.

The routines to remap AGILE-IDSA values into ELEPHANT and vice versa have already been implemented in ELEPHANT since they are also crucial for a correct treatment of the boundary conditions. However, only using the remapping routines did not lead to successful spherical restarts as we will learn in the following chapters. Important new concepts and routines had to be developed.

9.2.2 Relaxation scheme

In AGILE-IDSA the innermost zone corresponds to a sphere. However, the b-grid quantities are only evolved at half of the radius of this innermost cell (cell b2 in

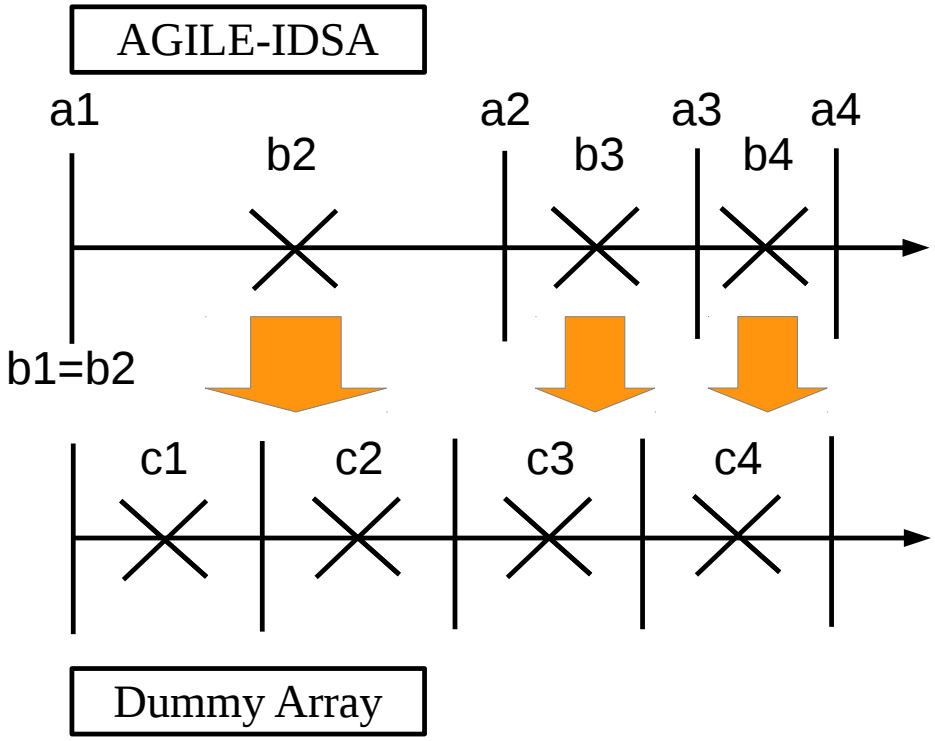

Fig. 9.2: Illustration of the remapping from the unequally spaced AGILE-IDSA grid to the equally spaced dummy grid which is then used to distribute the spherical data into the 3D domain of ELEPHANT. In AGILE-IDSA it is differed between quantities defined on the cell-edges a1, a2, a3, . . . (a-grid quantities) and such defined on the cell-centers b2, b3, b4, . . . (b-grid quantities). Please note that the centered values in the center b1 correspond to the values of the first cell center b2. b1 is not evolved separately in the code. In the equally spaced dummy array all quantities are defined cell-centered (c1, c2, c3, . . .).

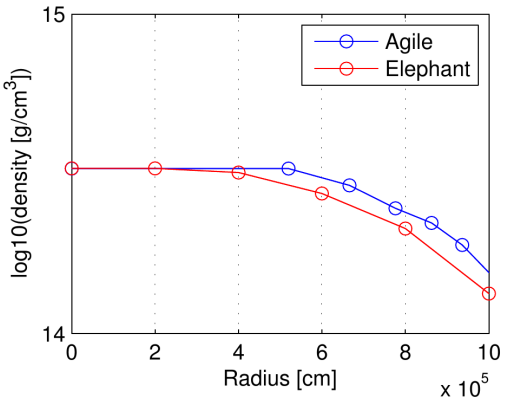

Fig. 9.3: Spherically averaged density profiles at the beginning of a spherical restart. The blue line represents the background AGILE-IDSA data while the red line shows the spherically averaged data of the 3D domain of ELEPHANT. The circles indicate the positions of the cells in the code. The offset between the blue line and the red line is due to the remapping of the zones under the condition of mass conservation.

Fig. 9.2). The values at zero radius correspond to the values of half of the radius (b1=b2 in Fig. 9.2). Additionally, the adaptive-grid algorithm in AGILE-IDSA usually chooses this innermost zone to have quite a large radial expansion on the order of several kilometers. Especially the large radial expansion of the central zone has a crucial impact on the evolution of the star during the relaxation.

Figure 9.3 shows the innermost region of the radial density profiles of ELEPHANT after mapping a typical standard AGILE-IDSA profile into it. The blue line shows the values of the AGILE-IDSA code in the background. In AGILE-IDSA the first zone (the cells are marked with circles) expands over almost 5 km due to the adaptive grid alignment. The red line represents the spherically averaged values of the 3D domain in ELEPHANT. In the plotted example a coarse resolution of 2 km is used in the 3D domain of ELEPHANT. The remapping shown in Fig. 9.3 is done i.a. requiring mass conservation. The central pressure in the two profiles remains the same. However, under the condition of i.a. mass conservation and the change from a non-equally spaced grid into an equally-spaced one leads to the consequence that the mapped profile in ELEPHANT is not identical to the original standard AGILE-IDSA profile [2]. Furthermore, this mapped spherical profile does not represent a hydrodynamical stable state in three dimensions. An obvious feater is e.g. the flat density profile of the innermost zones. This is an artifact of the large first zone the standard AGILE-IDSA which is mapped onto several zones of ELEPHANT. As a result, during the further evolution ELEPHANT tries to adjust its hydrodynamical state until a new stable state is found. Initial tests showed that this triggers strong artificial shock waves which lead to an explosion within a few milliseconds. To solve this problem, we developed a simple but efficient relaxation scheme.

[2] In Fig. 9.3 the red line is below the blue line. This is not always the case as at larger radii it can also be vice versa. See e.g. Fig. 9.6.

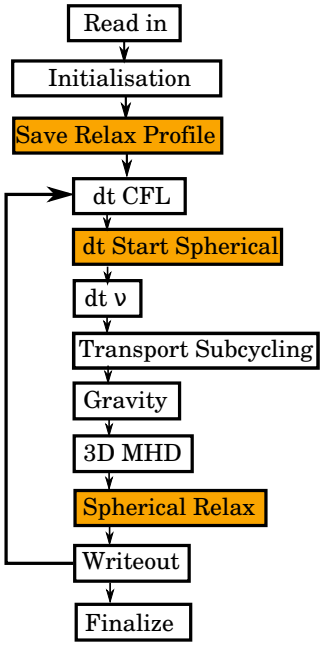

Fig. 9.4: Flow chart that illustrates the main calculation steps of the ELEPHANT code. The orange boxes indicate the positions where routines for the spherical restart are placed.

The principle is simple: We allow the mapped spherical model in ELEPHANT to adjust itself to a new three-dimensional hydrodynamical stable state while damping out all the artificial shock waves that might be triggered during this process. Figure 9.4 shows a flow chart illustrating the main calculation steps executed in the ELEPHANT code. The orange boxes indicate the routines needed for a successful spherical restart:

Save Relax Profile: After the read-in of the spherical data, the remapping into ELEPHANT, and the initialization of the routines in ELEPHANT, a "snapshot" of the initial velocity profile is saved into an array. For each cell in the three-dimensional domain we save a reference velocity

$$v_{\mathrm{ref}}(i,j,k) = max(c_{\mathrm{s}}(i,j,k,t_0) * a, v(i,j,k,t_0) * b) \ , \tag{9.1}$$

where the integers i, j, k indicate the cell indices, t_0 the time at the start of the spherical restart, c_{s} the local speed of sound, and v the velocity of the cell. a and b are real parameters to tune the influence of c_{s} and v, respectively.

dt Start Spherical: The actual damping mechanism takes place in the loop illustrated in Fig. 9.4. It is usually activated during the first 700 to 1000 iterations. During the first few iterations a very small time step dt_{man} is chosen[3], well below the usual time step dt_{CFL} determined by the CFL-condition [51]. In each iteration the time step is increased $dt_{\mathrm{man,new}} = 1.1 * dt_{\mathrm{man,old}}$ until it reaches the value of dt_{CFL}

[3] A typical value to start with is e.g. 1×10^{-7} s.

which will be used henceforth. This permits a smooth start of the spherical restart since the initially chosen time step dt_{CFL} would be too large and result in bigger perturbations.

Spherical Relax: The actual damping takes place after each 3D MHD step: The absolute value of the new velocity in each cell $|v(i,j,k)|$ at time t_{i} is calculated. If $|v(i,j,k,t_{\mathrm{i}})| > |v_{\mathrm{ref}}(i,j,k)|$ the value is reset to the initial reference value $|v(i,j,k,t_{\mathrm{i}})| = |v_{\mathrm{ref}}(i,j,k)|$. The idea behind this velocity criterion, dependent on v_{ref}, is that small changes in the velocity during the relaxation are allowed while big velocity changes (e.g. induced by artificial shocks) are damped back to the initially saved value of the velocity criterion. We take the absolute value of the velocities to allow both contracting and expanding adjustments. In the domain of the protoneutron star matter velocities v are very small. In this domain the speed of sound c_{s} is bigger than than the velocities v. Therefore the first argument of Eq. (9.1) determines v_{ref} in this regime. In the outer domain (outside of the protoneutron star), where matter falls in at supersonic velocities, the second argument of Eq. (9.1) determines v_{ref}. The parameters a and b control the strength of the damping. Two conditions apply: $b > 1$ (otherwise the in-falling matter would be slowed down) and $0 < a < 1$. Typical values are for example: $a = 0.2$ and $b = 1.2$. A more detailed analysis on the influence of the parameters a and b on the relaxation behavior is given below.
Using this scheme, small changes in the absolute values of the velocities are still allowed, but big changes will be damped. Since the criterion is only based on the absolute value of the velocity, changes in all spatial directions are still possible. This scheme allows the star to evolve into the new, hydrodynamically stable state without triggering an artificial explosion due to remapping artifacts.

9.3 Results

In this chapter, we provide a detailed analysis of our spherical restart method. We discuss in detail the different stages of a spherical restart. The results are compared to a full ELEPHANT simulation executed on Piz Daint. We use the following setup: As the progenitor we use the s15(W2007) model from Woosley and Heger [211] and for the equation of state we use HS(DD2) [90], see Sec. 4.2.3. The simulation uses an initial angular velocity of $\Omega = 0.3$ rad/s (applying a shellular velocity profile) and a magnetic field according to Heger, Woosley and Spruit [85]. The gravity uses an effective GR potential according to Marek et al. [138] (see Sec. 8.3). The parameterized deleptonization scheme [129] used during the collapse phase is fitted to the s15(2007) progenitor using the AGILE-BOLTZRAN code [130]. We simulate the 3D domain with 450^3 cubes with 2 km resolution, using 27 nodes with GPU enabled. For this analysis the simulation is run up to 248 ms post-bounce, which corresponds to 555 ms of total simulation time.

To create the spherical profiles with a standard AGILE-IDSA simulation (which are later mapped into ELEPHANT), we use the same setup regarding the progenitor, equation of state, and parametrized deleptonization values. Due to the one-dimensional nature of AGILE-IDSA, we cannot simulate the magnetic field and rotation. For this reason we do not consider rotation and magnetic fields when doing a spherical restart with ELEPHANT.

9.3.1 General features - time evolution of the central density

Figures 9.5a and 9.5b show the time evolution of the central density ρ_c of a full ELEPHANT run (red) (called ELEPHANT-full hereafter) and a standard AGILE-IDSA run (blue). The main reason for the large difference of the plotted central densities is due to the different treatment of the central zones. The flattening central density evolution of ELEPHANT is mostly due to the low resolution, as we have seen in other higher resolved runs that the evolution becomes not as flat. The red cross marks the used initial AGILE-IDSA profile at $t_{\rm pb} = 166$ ms which is mapped into ELEPHANT. The orange line shows the further evolution of ρ_c in ELEPHANT after the mapping (called ELEPHANT-SR hereafter).

As shown in Fig. 9.5, ρ_c of ELEPHANT-SR after the relaxation is generally higher than the corresponding values of ELEPHANT-full. This feature is mainly caused by the different collapse behavior of ELEPHANT and the standard AGILE-IDSA:
The reason for the different collapse behavior is found in the different grid treatment (spherical vs. 3D Cartesian gird), the different resolutions used, and the different treatment of the gravity (full-GR vs. effective potential). As a consequence, as seen in the ρ_c evolution at same simulation times in Fig. 9.5b, ELEPHANT collapses 28.85 ms earlier than standard AGILE-IDSA. The internal background AGILE-IDSA avoids this problem by using a feedback routine: Up to bounce after each hydro step the spherically averaged data of the 3D domain of ELEPHANT is copied into the background AGILE-IDSA domain. This assures the same collapse history (and therefore the same bounce time) and assures that the boundary conditions of the 3D domain are treated correctly. As we will see in Sec. 9.3.6, restarting from such a background AGILE-IDSA profile leads to an extremely good agreement in the spherically averaged profiles of ELEPHANT-full and ELEPHANT-SR. However, the standard AGILE-IDSA does not share the same prebounce history with ELEPHANT. As a consequence, the central density ρ_c of ELEPHANT-SR is different compared to the ELEPHANT-full profile when performing a spherical restart using such an AGILE-IDSA profile[4].

[4]Not shown here but important: The standard AGILE-IDSA has higher ρ_c in the postbounce phase compared to the background AGILE-IDSA. Starting with this higher ρ_c also leads to higher ρ_c in the ELEPHANT code.

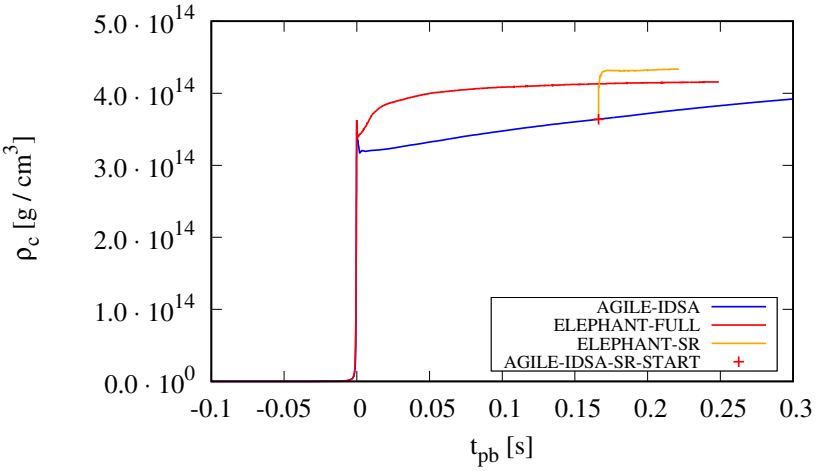

(a) Central density ρ_c vs. post-bounce time t_{pb}

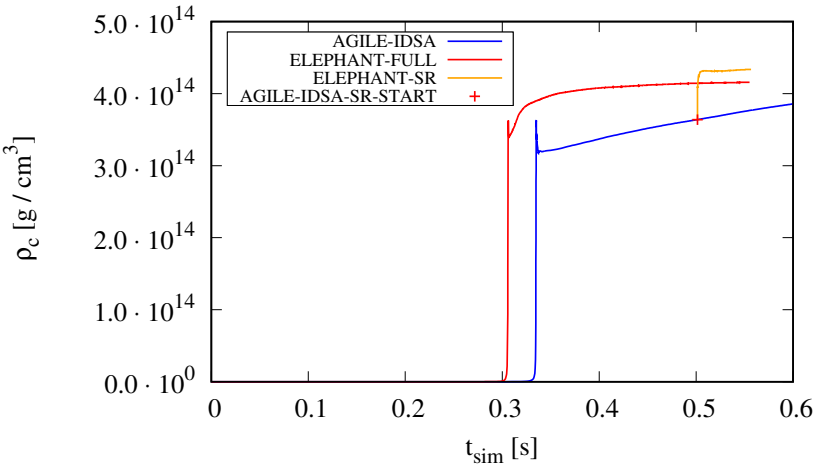

(b) Central density ρ_c vs. total simulation time t_{sim}

Fig. 9.5: Time evolution of the central density ρ_c. The red line shows a full ELEPHANT run using 2 km spatial resolution. The blue line shows the data of a standard AGILE-IDSA run which provides the data for a spherical restart. The red cross marks the profile used to perform a spherical restart in ELEPHANT and the orange line shows ρ_c evolution of the spherical restart.

In Fig. 9.5a the central densities are fixed to equal bounce times. This allows us to compare the evolution of the hydrodynamical quantities at same post-bounce times.

Figure 9.5 shall serve as a reference for discussion below. Observing the evolution of ρ_c with time gives a good overview in what stage of the relaxation and further evolution the spherically restarted run ELEPHANT-SR is.

9.3.2 Initial profiles - mapping properties

A spherical restart is initialized by mapping a one-dimensional standard AGILE-IDSA profile into ELEPHANT by using the mapping method described in Sec. 9.2.1. In our case the mapped initial profile is marked with a red cross in Fig. 9.5. Again, there are two ways of comparing the mapped data of ELEPHANT-SR to the ELEPHANT-full data: a comparison at same post-bounce times ($t_{\mathrm{pb}} = 166$ ms, see Fig. 9.6) or at same simulation times ($t_{\mathrm{sim}} = 501$ ms, see Fig. 9.7). We start our discussion using the profiles at the same post-bounce time and indicate later the differences to a comparison at equal simulation time.

Figure 9.6a shows the spherically averaged values of the density ρ, velocity v, electron fraction Y_e, and entropy per baryon s of ELEPHANT-SR in a radial profile (red dashed lines), as well as the values of the background AGILE-IDSA (blue dashed lines) after remapping. The mapped spherically averaged ELEPHANT-SR values lie close to the original AGILE-IDSA lines. Only small deviations are visible, e.g. in the velocity profile at the shock front. These are caused by the remapping discussed above. With an increased resolution such deviations can be reduced. The solid lines indicate the values of the ELEPHANT-full run. The solid blue lines represent the values of the background AGILE-IDSA and solid red lines the spherically averaged values of the 3D domain of ELEPHANT-full. It is obvious that in the ELEPHANT-full run the data of the background AGILE-IDSA and the data from the 3D domain do not coincide. This is mainly due to the different treatment of gravity in the background AGILE-IDSA (spherical and full-GR), the different resolution and grid structure, and the differences due to multidimensional effects in the 3D domain. To give an example: The shock front of ELEPHANT-full is at a about 20 km larger radius than the one of the background AGILE-IDSA which can be explained by the development of convection behind the shock region which only occurs in multidimensional simulations. The differences between the blue lines of the two background AGILE-IDSA profiles are due to the above mentioned different bounce times respectively different pre-bounce history.

Figure 9.6b shows the same quantities as Fig. 9.6a but plotted against the integrated mass. Again, we find rather small deviations between the initial 1D profiles and the spherically averaged 3D profiles of the restart. The mass representation does not resolve the region of the shock front, since the majority of the mass in the

computational domain is bound in the protoneutron star. However, we find that the mass is well conserved during the mapping process.

Visible in both Fig. 9.6a and Fig. 9.6b is the large difference in the central Y_e between AGILE-IDSA and ELEPHANT. It is a known problem of the current ELEPHANT code version that after bounce, the Y_e starts to lower what results in too low Y_e values in the post-bounce phase. Most likely this is a diffusion problem but no definite answer can be provided at this stage. Further investigations towards an answer of this problem are done currently.

Figure 9.7 shows the same data of ELEPHANT-SR but compared to ELEPHANT-full at same simulation time. Comparing the data at same simulation time means, that due to the earlier collapse of ELEPHANT-full compared to the standard AGILE-IDSA run, the post-bounce evolution of ELEPHANT-full is 28.85 ms later compared to the analysis at same post-bounce times. As a consequence, the shock front of ELEPHANT-full is at a slightly bigger radius in Fig. 9.7a. The surprisingly good agreement between the background AGILE-IDSA profiles in the ρ, v, and s panels is more a coincidence of the chosen restart time than a consistent feature that is also found at other simulation times.

The differences between Fig. 9.6 and Fig. 9.7 are rather small. Comparing the profiles at same simulation times does not reveal significant differences compared to the comparison at same post-bounce times. Hence, we will restrict the discussion in the following to same post-bounce times.

9.3.3 Relaxation I

After the initial mapping of the standard AGILE-IDSA profile into ELEPHANT, the 3D profile has to be relaxed into its new, hydrodynamically-stable 3D state. During the first 1000 hydro time steps, the damping mechanism described in Sec. 9.2.2 is applied. The upper two panels of Fig. 9.8 show the evolution of the central density ρ_c with time while using the damping mechanism. In the left panel time is plotted linearly while in the right panel a logarithmic scale is used to obtain a better representation of the data during the first iterations. The second row shows the corresponding total number of zones where the damping mechanism applies (using the same x-scales in the figures above). In this run we used $a = 0.2$ and $b = 1.2$. As mentioned in Sec. 9.2.2, the innermost zones of ELEPHANT-SR are fitted to the flat AGILE profile. Running the code, the central density is adjusting itself to higher ρ_c trying to reach the new hydrodynamically-stable state. Since this stable state is not reached within a few iterations the central density profile shows several humps until it converges to a constant ρ_c. The adjustment of ρ_c has serious implications on the dynamics of the star: it triggers pressure waves which move from the center outwards. On their way outwards, the pressure waves turn into shock waves which are then decelerated by the damping mechanism. The number of damped zones

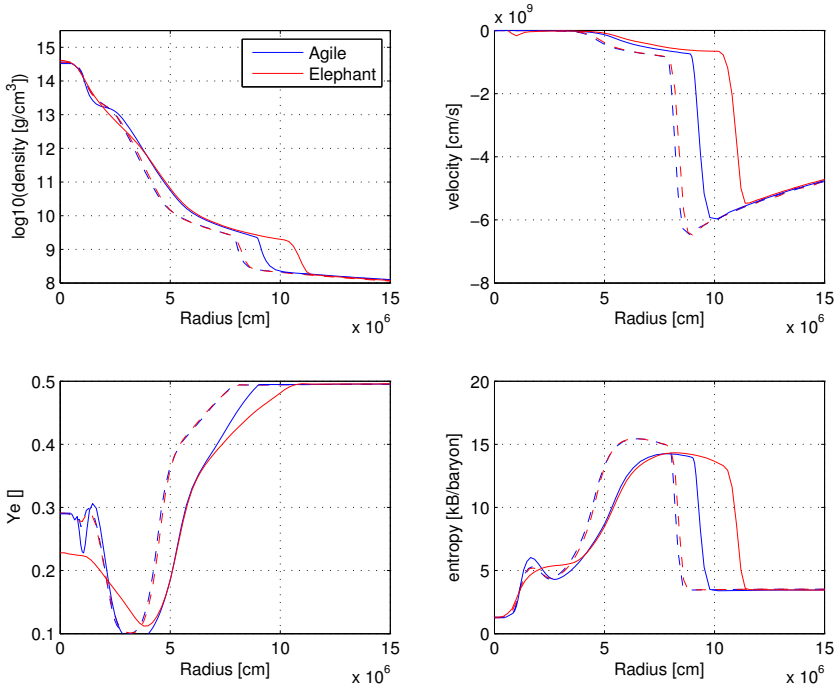

(a) Radial profiles of density ρ, velocity v, electron fraction Y_e, and entropy per baryon s plotted against the radius.

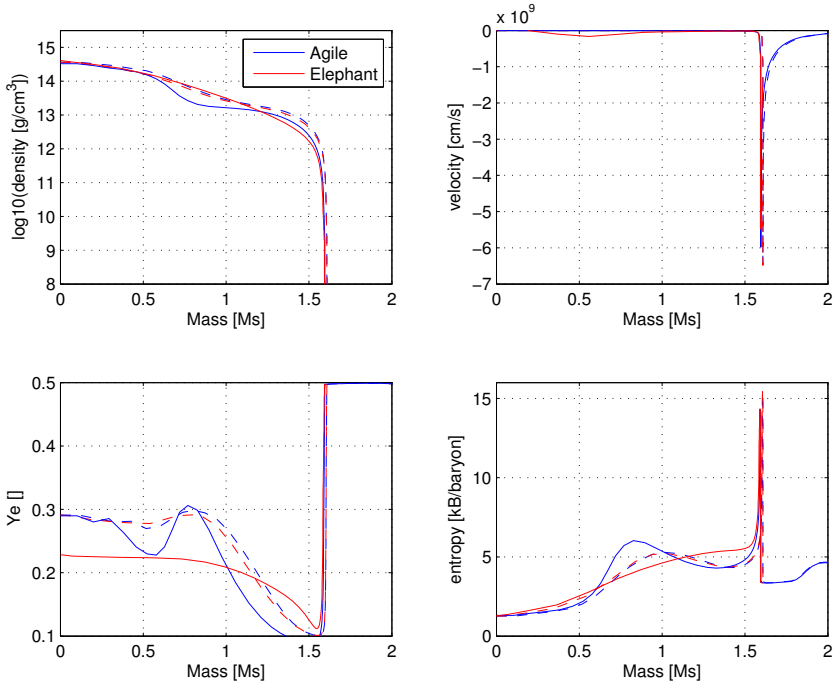

(b) Radial profiles of density ρ, velocity v, electron fraction Y_e, and entropy per baryon s plotted against the integrated mass.

Fig. 9.6: Profiles of typical hydrodynamical quantities after mapping a one-dimensional AGILE-IDSA profile into ELEPHANT. The red lines show the values in ELEPHANT while the blue lines show the values of the background AGILE-IDSA. The dashed lines show the ELEPHANT-SR, the solid lines ELEPHANT-full at same post-bounce time ($t_{\rm pb} = 166$ ms). Figure 9.3 shows a zoom-in of the ρ_c panel of Figure a).

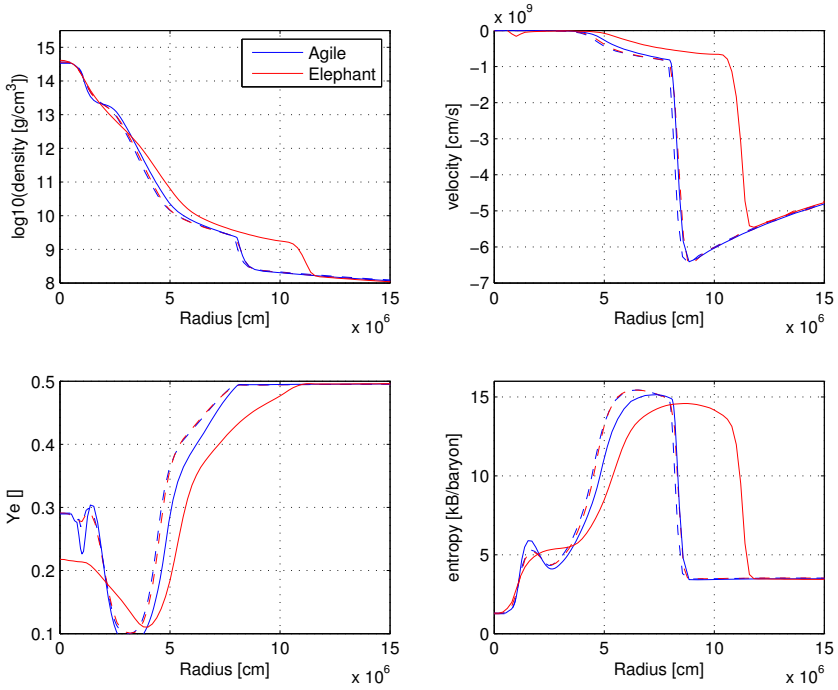

(a) Radial profiles of density ρ, velocity v, electron fraction Y_e, and entropy per baryon s plotted against the radius.

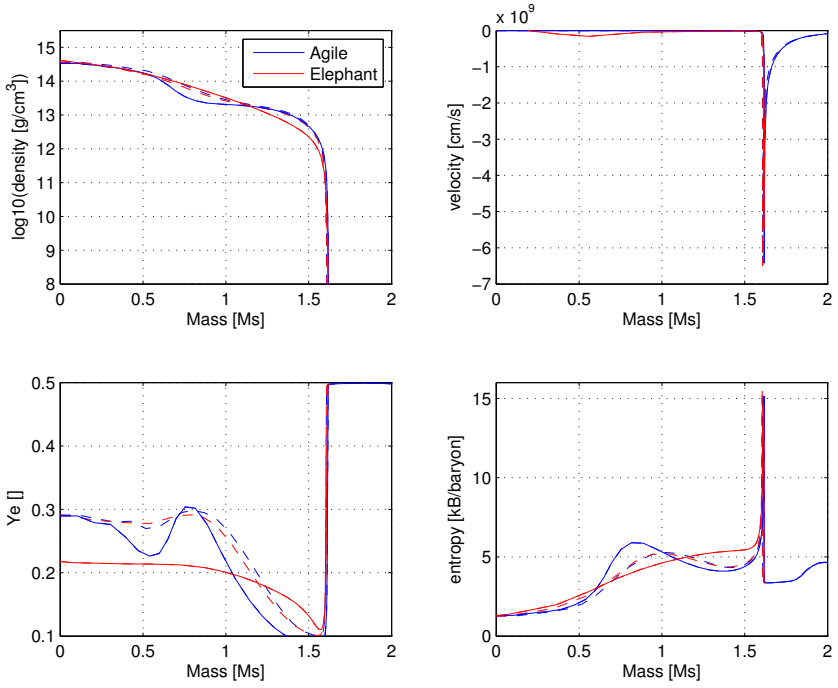

(b) Radial profiles of density ρ, velocity v, electron fraction Y_e, and entropy per baryon s plotted against the integrated mass.

Fig. 9.7: Profiles of typical hydrodynamical quantities after mapping a one-dimensional AGILE-IDSA profile into ELEPHANT. The red lines show the values in ELEPHANT while the blue lines show the values of the background AGILE-IDSA. The dashed lines show the ELEPHANT-SR, the solid lines ELEPHANT-full at same simulation time ($t_{\rm sim} = 501$ ms).

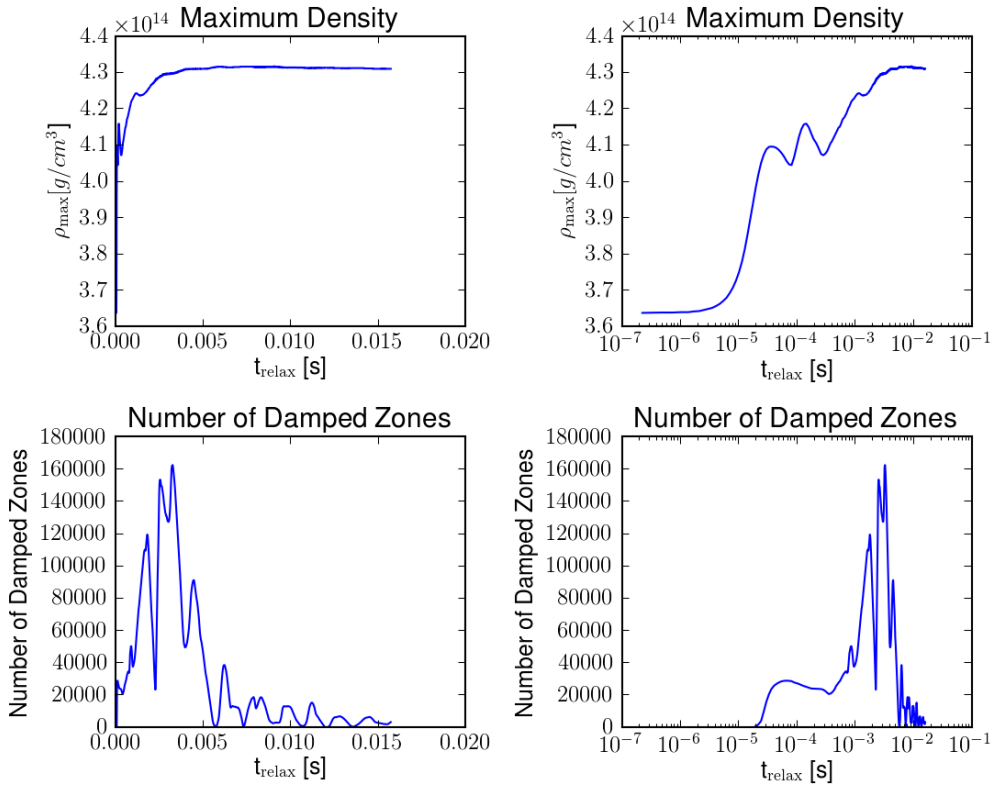

Fig. 9.8: The two upper panels show the evolution of central density ρ_c using a linear x-scale in the left panel and a logarithmic x-scale in the right panel. The second row shows the corresponding number of zones which are damped by the mechanism described in Sec. 9.2.2.

depends on the intensity of the damped shock wave and the position where the damping takes place. The more off-center the damping takes place the more cells are affected. The first intense shock waves are decelerated from the core region all the way to the standing accretion shock. Later, weaker shocks are only damped when reaching the standing accretion shock region since they are only sensitive to the velocity criterion that applies in this region.

Figure 9.9 shows the x-y plane slices of the 3D domain of ELEPHANT-SR at different relaxation times t_{relax}. The zones plotted in color are affected by the damping mechanism. The colors indicate the intensity of the damping $|v_{\mathrm{ref}}|/|v(i,j,k,t_i)|$. Values close to 1 represent a small damping (blue colors) while values down to 0.7 indicate a strong damping (green, yellow, and red colors). Figure 9.9a and 9.9b show slices at $t_{\mathrm{relax}} = 0.46$ ms and $t_{\mathrm{relax}} = 1.17$ ms which correspond to times before the number of zones peaks in Fig. 9.8. At this stage, strong shock waves are triggered in the central region of the protoneutron star. Strong damping takes place at the surface region of the protoneutron star. Figure 9.9c at $t_{\mathrm{relax}} = 2.99$ ms represents a profile which is placed in the peak region of the number of damped zones plot in Fig. 9.8. The shock waves travel outwards and are damped on their way towards

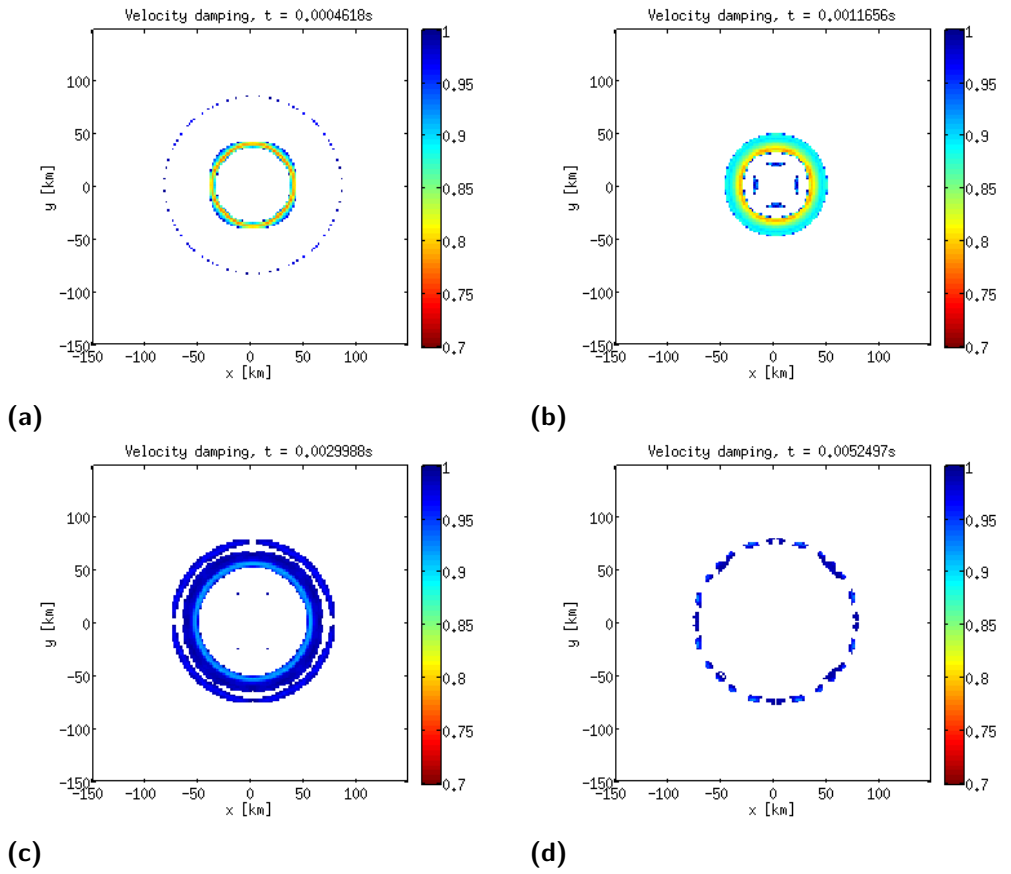

Fig. 9.9: x-y plane slice of the 3D domain of ELEPHANT-SR at different times t_{relax} showing the zones affected by the damping mechanism. The colors indicate the intensity of the damping $|v_{\mathrm{ref}}|/|v(i,j,k,t_i)|$: Blue corresponds to a weak damping while green, yellow, and red indicate a stronger damping. The white background indicates the regions not affected by the damping criterion.

the standing accretion front. In Fig. 9.9d at $t_{\mathrm{relax}} = 5.2497$ ms, the strongest shock waves have already been damped out. Weaker shock waves from the core region are still moving outwards and are damped in the region close to the standing accretion front.

After 10 to 15 ms, the time evolution of the central density has flattened and the number of damped zones has reduced to a vanishingly small number compared to the total number of cells of the computational domain (see Fig. 9.8). At this time, the damping mechanism can be switched off and the star can be evolved freely. Figure 9.10 shows the radial profiles after a relaxation time of $t_{\mathrm{relax}} = 13.48$ ms. From this time on, we run the code without the damping mechanism (see Sec. 9.3.4). In the following, we discuss the results of this first relaxation step in more detail.

The density profile in Fig. 9.10a shows a good agreement between ELEPHANT-SR and ELEPHANT-full down to densities of around $5 \cdot 10^{12}$ g/cm^3, respectively a radius of 25 km. Up to 25 km radius, we also find good agreement in the velocity and entropy profiles, only the electron fraction in the core region is well above the ELEPHANT-full

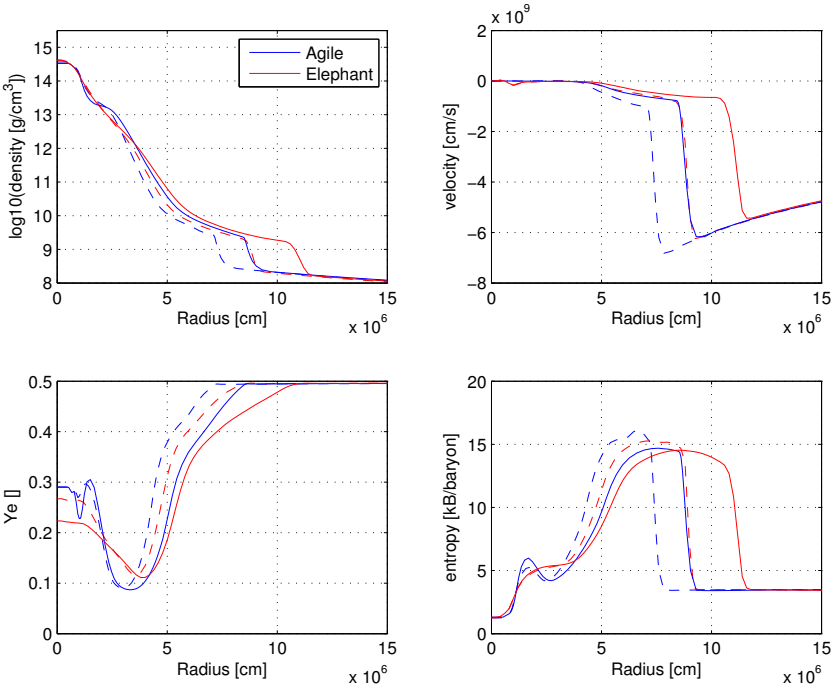

(a) Radial profiles of density ρ, velocity v, electron fraction Y_e, and entropy per baryon s plotted against the radius.

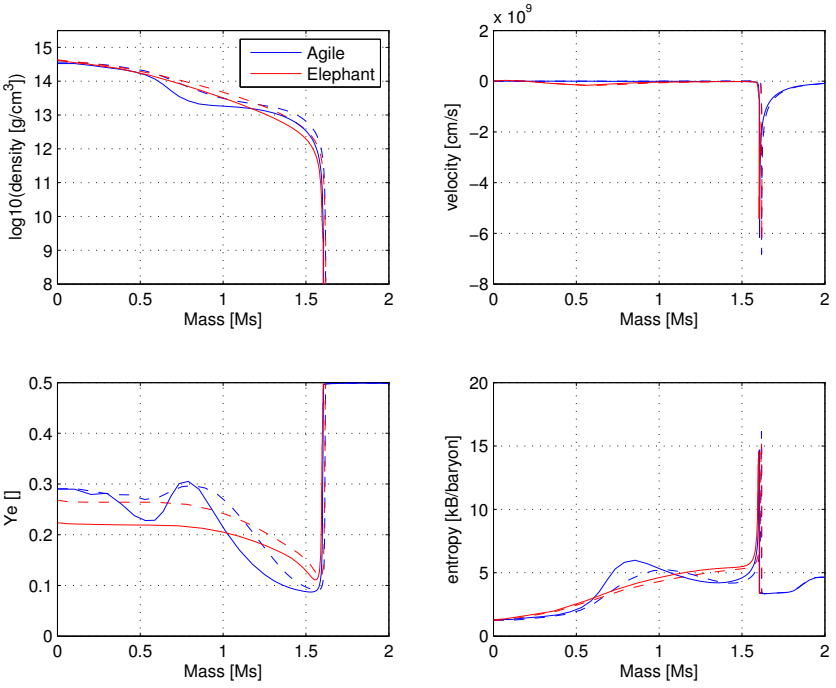

(b) Radial profiles of density ρ, velocity v, electron fraction Y_e, and entropy per baryon s plotted against the integrated mass.

Fig. 9.10: Profiles of typical hydrodynamical quantities after a relaxation time of $t_{\mathrm{relax}} = 13.48$ ms. The red lines show the values in ELEPHANT while the blue lines show the values of the background AGILE-IDSA. The dashed lines show the ELEPHANT-SR, the solid lines ELEPHANT-full at post-bounce time ($t_{\mathrm{pb}} = 179$ ms).

run. We can conclude that the dense part of the protoneutron star expanded into a new, hydrodynamical-stable configuration which is very similar to the one obtained by in the ELEPHANT-full run. In the region between 25 km and approximately 90 km (position of the standing accretion shock of ELEPHANT-SR), the profiles of ELEPHANT-SR moved towards the ELEPHANT-full profiles but did not converge yet. We still find a gap of roughly 25 km between the standing accretion front of ELEPHANT-SR and the one of ELEPHANT-full. This is due to the convection that is present in ELEPHANT-full but is still underdeveloped in ELEPHANT-SR. Examining the profiles depending on the integrated mass (shown in Fig. 9.10b) we also find convergence of the ELEPHANT-SR towards the ELEPHANT-full profiles. The density profile of ELEPHANT-SR shows a similar shape as the one of ELEPHANT-full but generally shows slightly higher densities. As mentioned above, this is an artifact of the initial profile of the standard AGILE-IDSA run which leads to a slightly more compact hydrodynamical-stable state compared to the ELEPHANT-full run.

Compared to Fig. 9.6b the humps in the Y_e and s profiles at around 0.8 $M_\odot$ have diminished in Fig. 9.10b in the Y_e panels. These humps in Fig. 9.6b were a relict of the core bounce. In spherical simulations this feature is mostly conserved due to the missing prompt convection which is occurring in multi-dimensional simulations. During this relaxation phase, we observe a similar prompt convection as known after core bounce. This results in a smoothed Y_e and s profile. Even tough the Y_e profile of ELEPHANT-SR has smoothed, it is still systematically higher than its counterpart of ELEPHANT-full. With the ongoing evolution this difference will shrink further. Again this is caused by the the suspected diffusive problem of the "too low Y_e problem" mention previously. Nevertheless, the agreements of the density, velocity, and entropy profiles are remarkably good.

9.3.4 Relaxation II

After the damping mechanism is turned off, the 3D domain of ELEPHANT-SR can evolve naturally. In the high-entropy regions around the protoneutron star convection starts to build up. This leads to a slight reduction of the central density since the developing convection expands the high-entropy region and pushes the shock front outwards (barely visible in Fig. 9.5). Later, the central density increases again due to the ongoing accretion. Figure 9.11 shows the volume-rendered entropy profile in 3D after a total run time of 55.1 ms since the beginning of the spherical restart. The purple sphere in the center represents the protoneutron star and the blue layer on the outside, the shock front. The brown to yellow colors represent the entropies between 14.5 and 17.9 k_B/baryon. It is clearly visible that between the protoneutron star surface and the shock front the entropy profile is not smooth anymore. Convection leads to mixing and the bubble-like features in Fig. 9.11. However, the overall profile still shows some spherical features (e.g. symmetry of bubbles, almost spherical shock

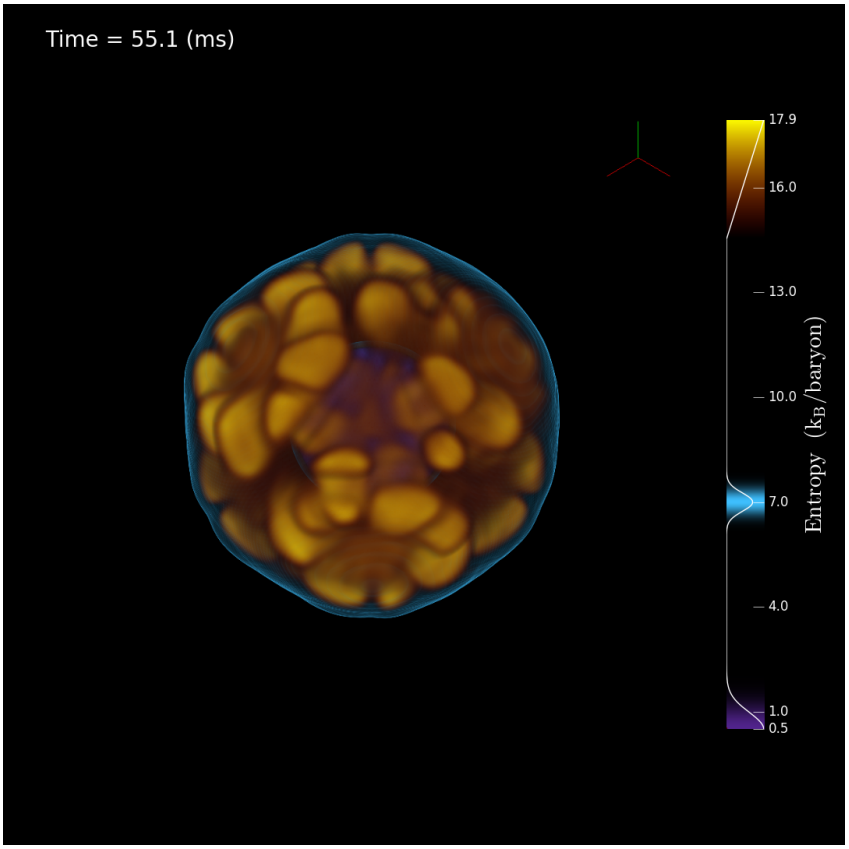

Fig. 9.11: Volume-rendered entropy profile of ELEPHANT-SR after 55.1 ms simulation time. The almost covered purple sphere in the center represents the protoneutronstar. The outer layer in blue represents the shock front. The surfaces with the colors from brown to yellow represent the entropy bubbles which are formed due to convection.

front). These spherical relict will diminish with time due to stronger convection and the ongoing mixing.

Figure 9.12 shows the profiles of ELEPHANT-SR and ELEPHANT-full at $t_{\mathrm{pb}} \sim 220$ ms (54 ms after the spherical restart). Comparing the radial profiles from Fig. 9.12a with the ones at the end of the first relaxation stage in Fig. 9.10, we find an even better agreement between the dashed red lines of ELEPHANT-SR and the solid red lines of ELEPHANT-full in all of the four subplots. The main reason for this improvement is the convection that pushes the shock front of ELEPHANT-SR to a larger radius, closer to the one from ELEPHANT-full. As shown in Fig. 9.12b the profiles of the inner part of ELEPHANT-SR do not converge significantly closer to the ones of ELEPHANT-full. The differences between the ELEPHANT profiles shown in Fig. 9.12b and Fig. 9.10b are rather small. The adjustment of the protoneutron star configuration took already place at during the “damping stage” of the spherical restart and does not change severely afterwards.

In summary we can state that the profiles of ELEPHANT-SR are well comparable to the profile of ELEPHANT-full after 55 ms of relaxation time.

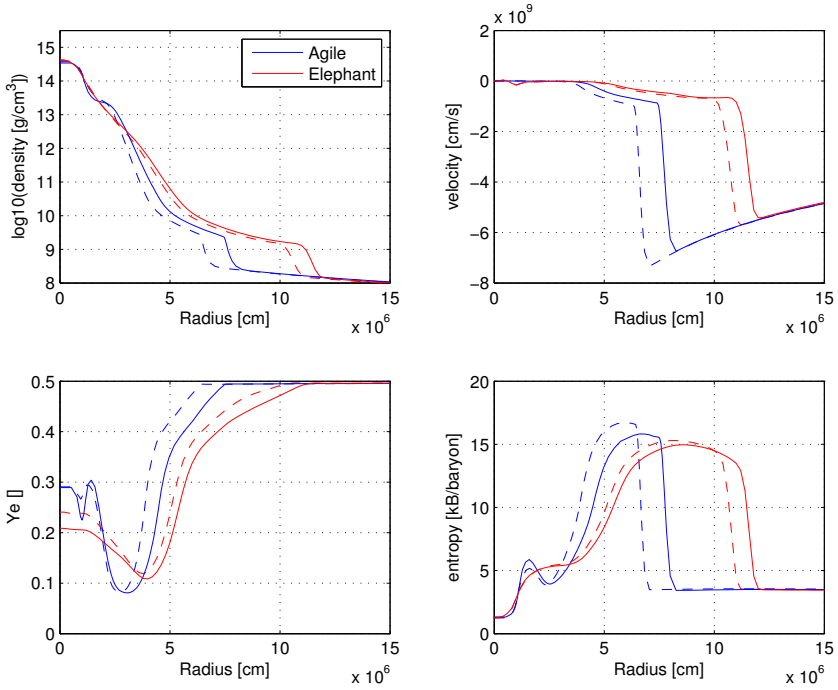

(a) Radial profiles of density ρ, velocity v, electron fraction Y_e, and entropy per baryon s plotted against the radius.

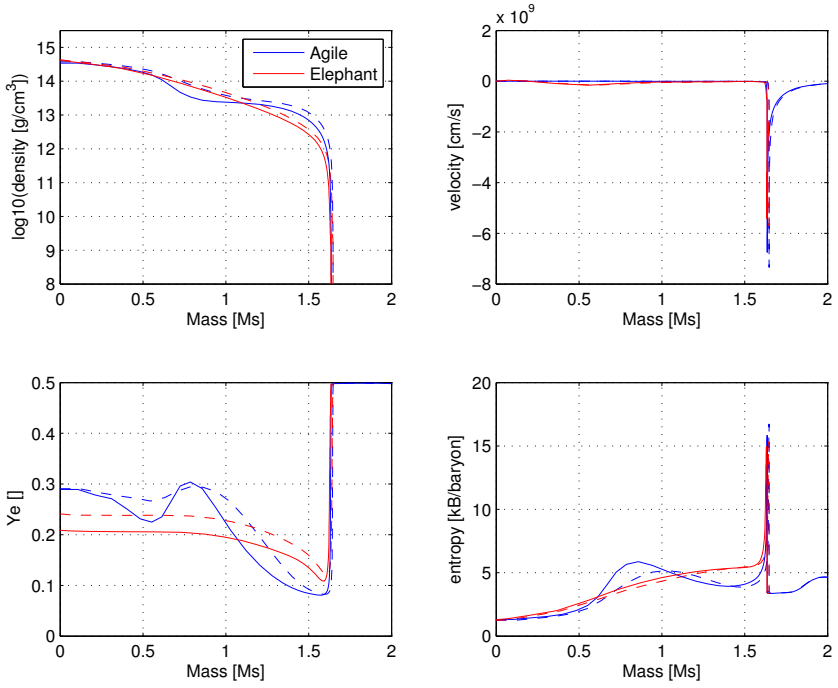

(b) Radial profiles of density ρ, velocity v, electron fraction Y_e, and entropy per baryon s plotted against the integrated mass.

Fig. 9.12: Profiles of typical hydrodynamical quantities after mapping a one-dimensional AGILE-IDSA profile into ELEPHANT. The red lines show the values in ELEPHANT while the blue lines show the values of the background AGILE-IDSA. The dashed lines show the ELEPHANT-SR, the solid lines ELEPHANT-full at same post-bounce time ($t_{\rm pb} = 220$ ms).

9.3.5 Variation of relaxation parameters

In the preceding discussion of the relaxation method the two free parameters of damping criterion (Eq. 9.1) were chosen as $a = 0.2$ and $b = 1.2$. In this short section other parameter combinations are tested and their effect on the damping mechanism is shown. From these results we are able to justify why our previously used values are in general a good choice.

In the following we focus our discussion on stronger damping values which might shorten the period where the damping mechanism is applied. We choose three additional combinations of a and b to illustrate possible effects on the damping mechanism: $a = 0.2$ and $b = 1.1$, $a = 0.1$ and $b = 1.2$, and $a = 0.1$ and $b = 1.1$. Figure 9.13 shows the same quantities as Fig. 9.8 but with the extra three sets of parameters. The initially discussed set of parameter ($a = 0.2$ and $b = 1.2$) is shown in brown color.

Case $a = 0.2$ and $b = 1.1$ is shown in yellow. Reducing b to lower values means setting a stronger constraint on the velocity criterion in Eq. 9.1. This criterion acts mainly in the low-density regions. The maximum density evolution shows almost the exact same behavior as case $a = 0.2$, $b = 1.2$. Considering the number-of-damped-zones plots (lower panels in Fig. 9.13), the same behavior as case $a = 0.2$, $b = 1.2$ is found but shifted to slightly higher numbers of damped zones. This is due to a stronger damping in the shock-front region where the velocity criterion acts dominantly. The peaks are at the same position since the speed-of-sound parameter a is left unchanged. Hence, the damping behavior in the central high-density regimes remains the same. The behavior of the maximum density of case $a = 0.2$ and $b = 1.1$ does not show differences to case $a = 0.2$, $b = 1.2$. The stable state seems to be reached at the same time.

Cases $a = 0.1$, $b = 1.2$ (cyan lines) and $a = 0.1$, $b = 1.1$ (dark-blue lines) both have a lower a-parameter value which corresponds to a stronger constraint on the speed-of-sound criterion in Eq. 9.1. In the maximum-density profiles a sightly smoother behavior is visible between approximately 1 and 5 ms compared to the simulations with $a = 0.2$. Especially the third bump of $\rho_{\max}$ is almost inexistent. The reason for this behavior is found in the stronger damping of the central region. Up to around 5 ms a similar trend of between the lines with $a = 0.1$ and $a = 0.2$ is found in the number of damped zones plots. Afterwards, the lines with $a = 0.1$ diverge significantly from the lines with $a = 0.2$. Figure 9.14 shows the ρ_c, v, Y_e, and s profiles of different ELEPHANT-SR and its background AGILE-IDSA at different relaxation times: The dashed lines correspond to the case $a = 0.1$, $b = 1.2$ at $t_{\mathrm{relax}} = 0$ ms, the solid lines to the same case but at $t_{\mathrm{relax}} = 15.66$ ms and the dotted lines to case $a = 0.2$, $b = 1.2$ at same $t_{\mathrm{relax}} = 15.66$ ms. In all of the four panels, case $a = 0.1$, $b = 1.2$ and $a = 0.2$, $b = 1.2$ at $t_{\mathrm{relax}} = 15.66$ ms have almost identical profiles up to approximately 50 km radius. This nice agreement corresponds

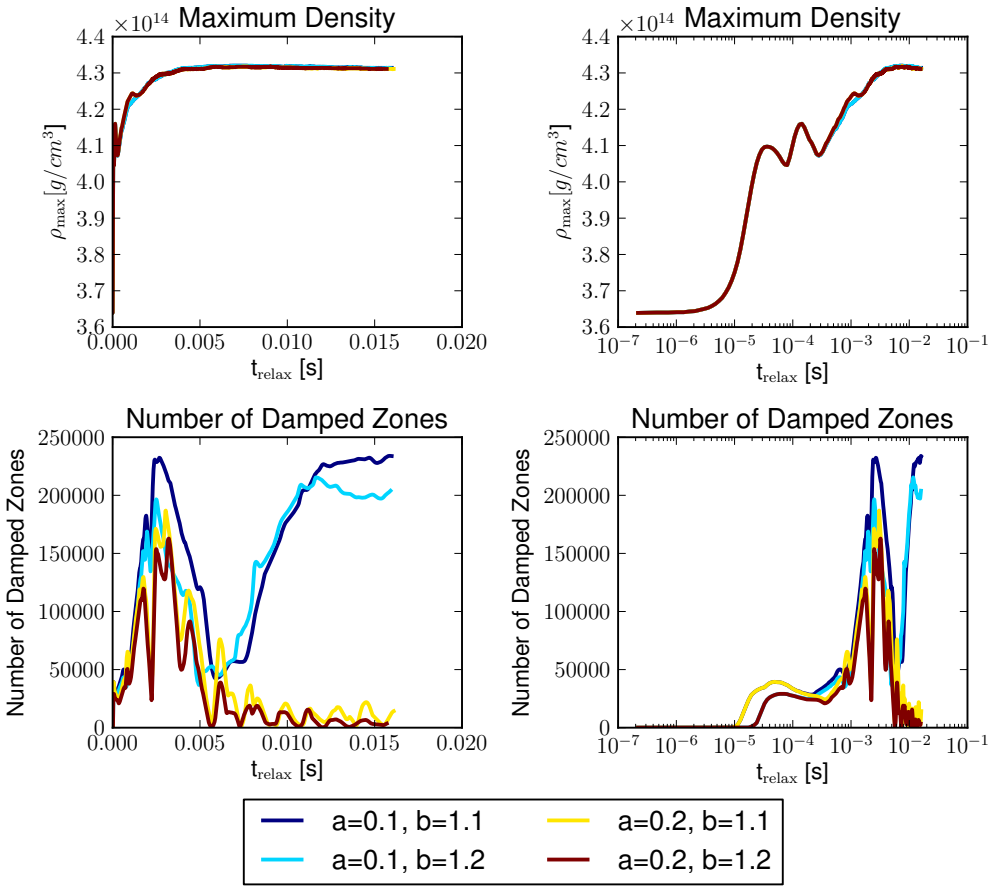

Fig. 9.13: As in Fig. 9.8, but for three additional combinations of a and b. The initial set used above ($a = 0.2$, $b = 1.2$) is shown in brown.

to densities above 10^{10} g/cm^3. In this region, both values of a are able to relax the protoneutron star efficiently that results in the good agreement. The situation changes at lower densities respectively in the region between roughly 60 and 80 km radius. Case $a = 0.2$, $b = 1.2$ was able to evolve the system in a correct manner: The shock front was pushed around 10 km further outwards while all of the four quantities did not indicate any inconsistencies. Contrarily, with a value of $a = 0.1$ the shock front is fixed at the same position as it was at the initial restart. The density is lowered as well as the velocity. The biggest difference is visible in the entropy profile where the high-entropy region has been lowered significantly. This behavior is clearly not physical. It is caused by a too intense damping: In this region the speed-of-sound criterion of Eq. 9.1 is still dominant and using $a = 0.1$ is too strict to allow this region evolve naturally. The region is damped too strong, the entropy reduces and the shock front can not evolve to the place it belongs. The continuous damping of this region causes the large number of damped zones in Fig. 9.13. This problem of "overdamping" could be solved by continuously changing a towards $a = 0.2$ after about 6 ms of relaxation.

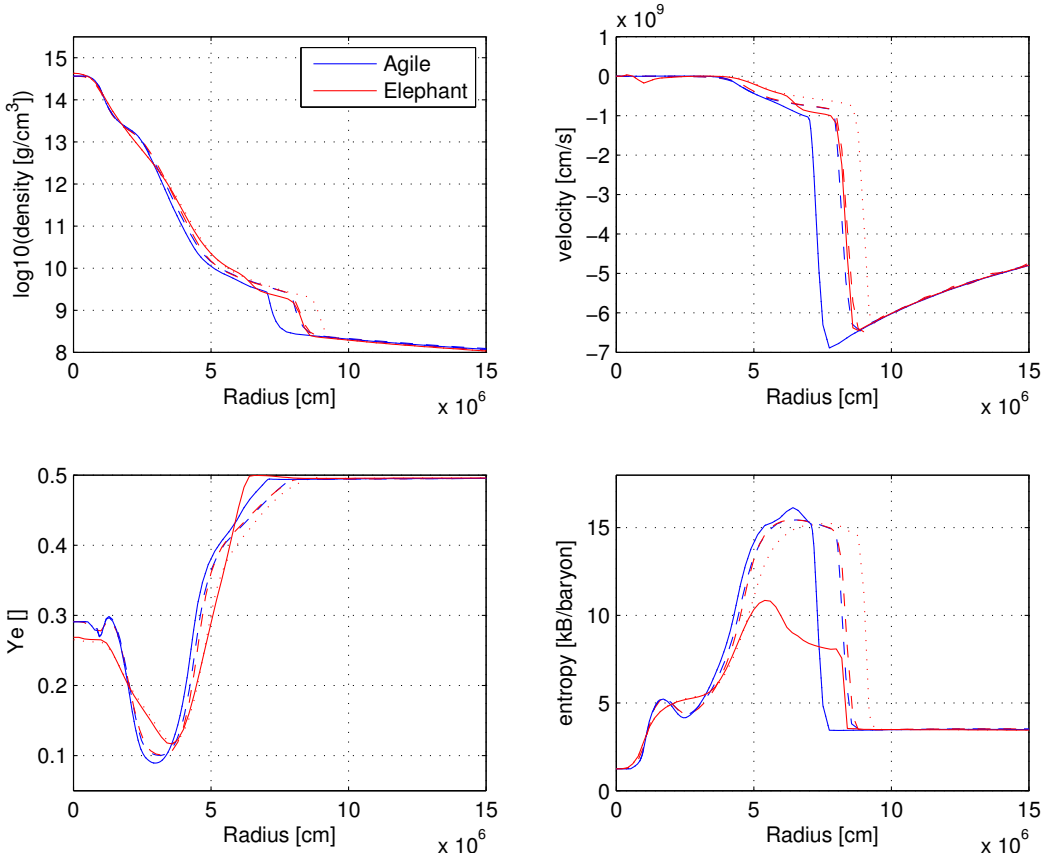

Fig. 9.14: Radial profiles (of the quantities ρ_c, v, Y_e and s) of the 3D-domain of ELEPHANT-SR for case $a = 0.1$, $b = 1.2$ at the moment of the spherical restart (red-dashed line) and after a relaxation time of $t_{relax} = 15.66$ ms (solid-red line). The red-doted line indicates the profiles of case $a = 0.2$, $b = 1.2$ at same t_{relax}. The blue lines represent the values of the background AGILE-IDSA.

In the case of $a > 0.2$ the damping in the high density regions is reduced which leads to stronger oscillations of the central density. Therefore stronger shock waves spread outwards. Applying bigger a's must therefore be accompanied by choosing smaller b's to compensate for the weaker damping in the central region. We can conclude that there is no advantage of choosing $a > 0.2$.

In summary we can state that our initial choice of the damping parameters $a = 0.2$ and $b = 1.2$ is a good choice. $a = 0.2$ shows a good damping of the high density part while still allowing to evolve the shock front. $a < 0.2$ is only applicable if after a certain initial period the values are changed to $a \approx 0.2$ to inhibit an "overdamping".

9.3.6 Restarting from the background AGILE-IDSA

Above, we discussed the method of a spherical restart from an external standard AGILE-IDSA run. This option allows for example to test the code at late post-bounce times that otherwise would have required weeks of computations. Another option is to directly restart ELEPHANT from a spherical profile extracted from the internal

background AGILE-IDSA. The advantage of this option is that the background AGILE-IDSA shares the same prebounce history as the 3D domain. The initial profile is again chosen at ~ 166 ms post bounce. ELEPHANT-SR is then relaxed for $t_{\rm relax} = 15.53$ ms and freely evolved for another 53.44 ms. Figure 9.15 shows the final ELEPHANT-SR profile ($t_{\rm pb} \approx 235$ ms) together with the corresponding ELEPHANT-full profile. The agreement in all the profiles respective quantities in both representations is remarkable. Using a background AGILE-IDSA profile for the remapping allows us to reproduce a spherically-averaged ELEPHANT-SR profile that is almost identical to the profile obtained in a ELEPHANT-full run. Only the Y_e profile has not converged to the ELEPHANT-full values and the shock-front is still at a few kilometers behind. It is expected that both quantities will converge to the ELEPHANT-full lines with further evolution.

This extremely good agreement between the spherically averaged profiles of an ELEPHANT-SR and an ELEPHANT-full run allows to draw some interesting conclusions: The post-bounce evolution of a spherical restart run is primarily dependent on the behavior of the simulation up to bounce. The background AGILE-IDSA and the standard AGILE IDSA used above have exactly the same setup. The only difference is the transfer of the spherically averaged 3D data into the background AGILE-IDSA up to bounce. It is clear that the detailed 3D profiles of the ELEPHANT-full and ELEPHANT-SR runs still show their differences due to their different history and possible spherical relict. Nevertheless, it is remarkable that using the spherical restart method we are able to obtain a on spherical average almost identical state in the post-bounce evolution without simulating the whole post-bounce evolution in a consistent 3D manner!

The good agreement between ELEPHANT-SR and ELEPHANT-full at the same resolution makes the spherical restart tool even more powerful: At any given time post-bounce we simply have to perform a spherical restart. After the relaxation and an evolution long enough to generate multi-dimensional fluid motion and wash out the spherical symmetry, the simulation is well comparable to a consistently performed simulation. The method can therefore be used to perform resolution studies and data analysis. In case of a hybrid supernova equation of state the method might be especially interesting for a high resolution study of an eventual second collapse. Of course, this method, imitating a fully consistent run, has its limitations: Since we do not yet consider rotation, the comparison are only valid if we compare an ELEPHANT-SR run to a non- or slowly-rotating ELEPHANT-full run. However, applying artificially and additional rotation profile to the ELEPHANT-SR run might help to even imitate rotation in a core-collapse supernovae! The lack of magnetic fields in an ELEPHANT-SR is another drawback of the method at the moment. By applying an artificial field configuration at the begin of the spherical restart, this might as well help to approach ELEPHANT-SR even closer ELEPHANT-full.

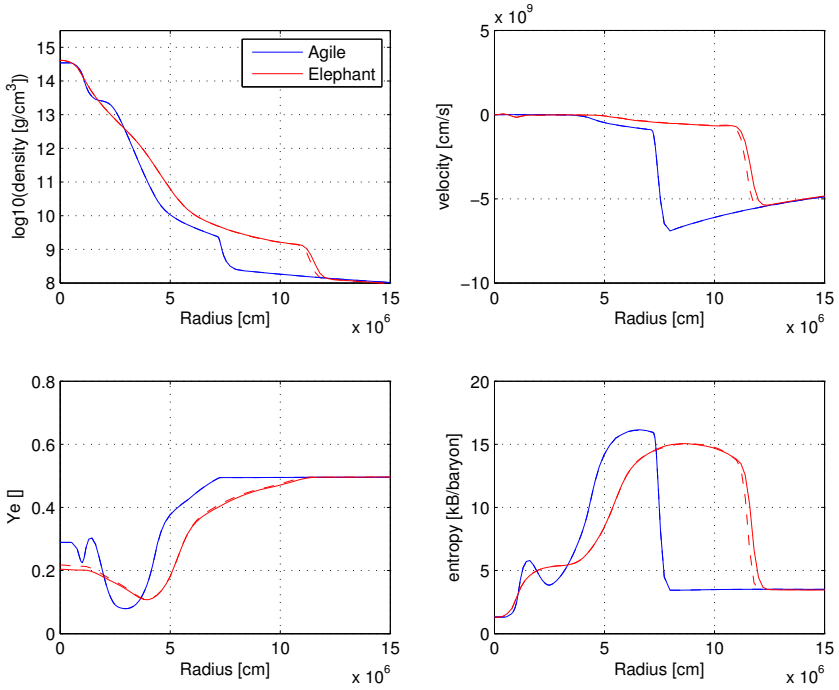

(a) Radial profiles of density ρ, velocity v, electron fraction Y_e, and entropy per baryon s plotted against the radius.

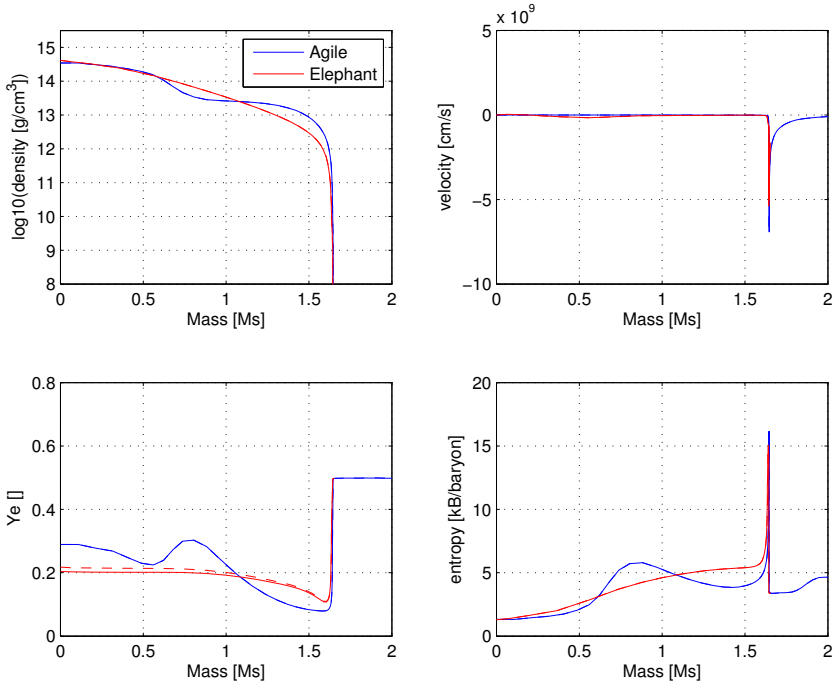

(b) Radial profiles of density ρ, velocity v, electron fraction Y_e, and entropy per baryon s plotted against the integrated mass.

Fig. 9.15: Profiles of typical hydrodynamical quantities after mapping a spherical background AGILE-IDSA profile into ELEPHANT. The red lines show the values in ELEPHANT while the blue lines show the values of the background AGILE-IDSA. The dashed lines show the ELEPHANT-SR, the solid lines ELEPHANT-full at same post-bounce time ($t_{\rm pb} = 235$ ms).

Summing up the discussion of this chapter: We can state that final differences between the ELEPHANT-SR profiles and the ELEPHANT-full profiles, at same post-bounce times, are mostly caused by the different pre-bounce history. The relaxation behavior of the spherical restart method itself is very robust.

10 Quark Matter in 3D Core-Collapse Supernova Simulations

> *Strength does not come from winning. Your struggles develop your strengths. When you go through hardships and decide not to surrender, that is strength.*
>
> **— Arnold Schwarzenegger**

This chapter deals with the application of BASQUARK in the 3D core-collapse supernova code ELEPHANT. This is the first time a hybrid supernova equation of state is applied in a 3D core-collapse supernova simulation. The aim is to investigate the influence of the appearance of quark matter on the explosion mechanism. One of the key questions to answer is whether a second collapse can also happen in 3D simulations. We split our discussion into two parts: Calculations simulating the collapse and a long part of the post-bounce phase (so-called "ab-initio" simulations) and simulations using the spherical-restart method to simulate a second collapse in the star in three dimensions with increased resolution. It has to be mentioned at this point that the following results where all produced within the last two months of my PhD studies. For this reason, the results are still preliminary and have to be handled with care.

10.1 Ab-initio calculations

In this section, we simulate BASQUARK in ELEPHANT ab-initio. We investigate two progenitor models with different masses: the 15 $M_\odot$ and the 40 $M_\odot$ models of [211] (called w15 and w40 progenitor below).

The 15 $M_\odot$ model has already been used to investigate BASQUARK in spherical symmetry using AGILE-BOLTZTRAN (see Sec. 6.2). The hadron-quark phase transition lead to a second-collapse of the protoneutron star which ultimately caused an explosion of the spherical model. It is therefore important to rerun this progenitor in a three-dimensional simulation to be able to investigate the effects of quark matter in three dimensions as well. Furthermore, the 15 $M_\odot$ model is interesting since other non-rotating (respectively slowly rotating) three-dimensional simulations showed explosions for this model using purely hadronic equations of state (see e.g. [128,

121, 109])[1]. It is therefore reasonable to expect that a neutrino-driven explosion happens before the conditions for a second collapse are reached.

For this reason we decided to run additionally a second simulation using a heavier 40 $M_\odot$ progenitor. Such a progenitor is expected to collapse into a black hole when using a purely hadronic equation of state [152, 190]. Using our hybrid supernova equation of state BASQUARK, we also find a second collapse succeeded by an explosion in spherical symmetry. As we will learn in Sec. 10.1.2, the elapsed time until the second collapse is shorter than in the 15 $M_\odot$ case. We expect this progenitor to explode in three dimensions with the QCD phase-transition mechanism, too. This case might be interesting to perform an analysis of the second collapse using the spherical restart method.

We run our simulations using ELEPHANT with the setup described in Sec. 8. Additionally, we use an initial angular velocity of $\Omega = 0.3$ rad/s, and an initial magnetic field with a $1.6 \cdot 10^6$ G poloidal and $5 \cdot 10^9$ G toroidal component, all implemented according to [85]. So far, our main simulation references are the performed spherical simulations which indicate that quark matter (and a possible second collapse) appears only at several hundred of milliseconds post-bounce time. Since we advance with our 3D simulations in completely unchartered waters, we start our analysis using a low spatial resolution of 2 km in a computational domain of 450^3 cells. The main benefit of the low resolution is that the computational costs are relatively low and our simulation proceeds with around 45 ms physical time per day per 18 hours batch wall-clock time during the post-bounce phase. This allows us to perform such a simulation within approximately two weeks. The drawback is of course the low spatial resolution itself: It is known that resolution has a crucial impact on the dynamics of a core-collapse supernova [170, 171]. In full awareness of this effect, we consider the following two runs as starting point for further, more detailed investigation.

[1] A broad variety of tested progenitors in 3D supernova simulations is still missing due to the tremendous amount of computational resources needed to perform a single simulation.

10.1.1 15 $M_\odot$ progenitor

To determine the effects of quark matter on the post-bounce evolution in comparison with a usual, purely hadronic simulation, we executed two runs using the w15 progenitor: one with the purely hadronic HS(DD2) EOS and one with the BASQUARK EOS.

Figure 10.1 shows the evolution of the central density ρ_c with time for the HS(DD2) EOS and the BASQUARK EOS using ELEPHANT (red and yellow lines). Additionally, the corresponding spherical simulations using standard AGILE-IDSA are plotted (magenta and blue lines). All runs are shifted to same bounce times for a better comparison. The ρ_c evolution shall serve as a guide line for the subsequent discussion of the post-bounce phase. The initial large differences in ρ_c after bounce, between ELEPHANT and AGILE-IDSA, are mainly due to large first zone of AGILE-IDSA and that the density of the first zone is considered as ρ_c (see also discussion in Sec. 9.2.2). The low resolution in the ELEPHANT runs causes the initial strong increase and the following strong flattening of the central density. In the purely hadronic HS(DD2) EOS run with ELEPHANT (red line), the ρ_c evolution continues very flat up to the end of the simulation. This is a result of the coarse resolution which has a strong effect on the evolution of the convection of the protoneutron star. The simulation finally indicates an explosion of the star: The post-bounce phase develops as known from a typical neutrino-driven mechanism; convection starts to build up (see e.g. the entropy profile shown in Fig. 10.4a) and the shock front expands to bigger radii. However, the explosion is ultimately not caused by the neutrino driven mechanism but by an excited protoneutron star which starts to oscillate in the center of the star. The occurring behavior of the protoneutron star is similar to the acoustic mechanism described by Burrows et al. in [35, 36]. We believe that this behavior is due to the coarse resolution and will not be reproduced with higher resolution. Without running a better resolved simulation, we can not provide a definite answer. For sure this subject needs a closer investigation.

The yellow line shows the evolution of the central density in ELEPHANT using the BASQUARK EOS. As long as the yellow and the red line superpose no, or a not significant amount, of quark matter is present in the protoneutron-star core. As soon as enough quark matter is present in the central part of the protoneutron star the central density starts to increase. Compared to the spherical simulation this happens at a significantly earlier time. Figure 10.2 shows the evolution of quark matter in the protoneutron star. Quark matter appears first at around $t_{\mathrm{pb}} = 63$ ms and increases gradually. At the end of the simulation, around 18 % of the protoneutron star consists of quark matter. The more quark matter is present in the core, the more the yellow ρ_c line in Fig. 10.1 departs from the red line. Another interesting property: Even though the quark fraction in the protoneutron star in three dimensions is higher

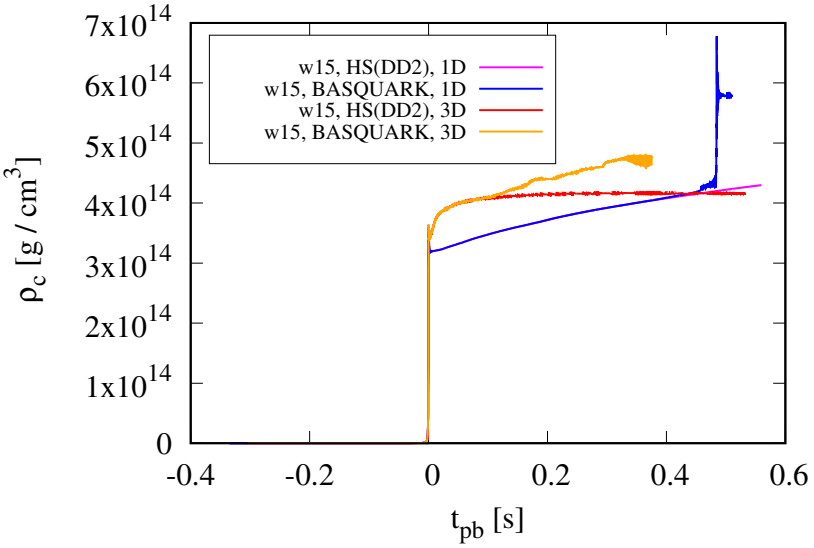

Fig. 10.1: Evolution of the central density ρ_c with time using the 15 $M_\odot$ progenitor of [211]. Shown are the results from the simulations in spherical symmetry using AGILE-IDSA for the HS(DD2) EOS (magenta) and the BASQUARK EOS (blue), as well as the corresponding simulations with ELEPHANT (red and yellow). All profiles are shifted to same bounce times.

than the spherical simulations discussed in Sec. 6.2 at same post-bounce times the protoneutron star does not collapse.

Figure 10.3 shows a selection of hydrodynamical quantities for different times post-bounce. The solid lines refer to the BASQUARK run while the dotted lines represent the HS(DD2) run. Up to $t_{\rm pb} = 100$ ms the radial profiles of BASQUARK and HS(DD2) are practically identical. The quark mass fraction at this time is too small to have an influence on the structure and dynamics. At 150 ms, a quark mass fraction of around 10 % is present in the center. The appearance of quark matter from the center outwards is different compared to the results gained in the spherical simulations, discussed in Sec. 6.2.1. In spherical symmetry quark matter appears off-center and only later spreads inwards. The lower Y_e and higher temperatures in the core region in ELEPHANT favor the appearance of quark matter. At $t_{\rm pb} = 250$ ms, respectively even better at $t_{\rm pb} = 300$ ms, clear differences between the two equation of state runs become visible in several profiles. The appearance of quark matter leads to a more compact protoneutron star. Figure 10.4c shows a typical picture of the quark core in the protoneutron star ($t_{\rm pb} = 300$ ms). Due to the low resolution, the quark core consists only of a few hundreds of zones. The structure of this quark core is clearly under resolved. The increase of the quark matter fraction leads to a decrease of the electron fraction Y_e in the center while in the outer boarder of the quark-mixed phase entropy s and temperature T increase. At $t_{\rm pb} = 300$ ms, the convectional zone expanded and shows higher entropies compared to the hadronic run. This is also

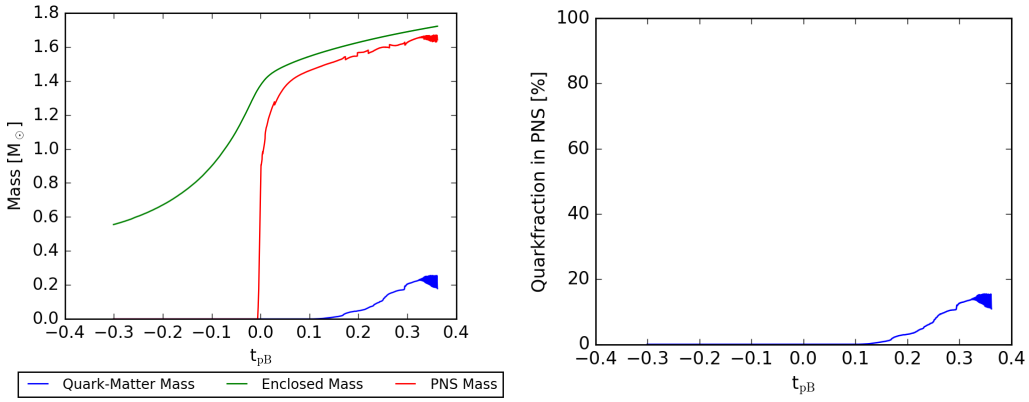

(a) **(b)**

Fig. 10.2: Same representation as in Fig. 6.6 but for ELEPHANT using the w15 progenitor and BASQUARK. In the left panel, the green line represents the total mass included in the computational domain, the red line the total rest mass of the protoneutron star ($\rho > 10^{12}$ g/cm^3), and the blue line shows the total mass of the quark matter. The right panel shows the percentage of quark matter compared to the total protoneutron star mass.

visible in the x-y plane entropy slices of ELEPHANT in Fig. 10.4a (HS(DD2) EOS) and Fig. 10.4b (BASQUARK EOS), respectively.

After $t_{\rm pb} = 300$ ms, the protoneutron star starts to oscillate what is well visible in the yellow ρ_c line in Fig. 10.1. Again, we find no obvious trigger for these oscillations. It is probable that they are caused by convection which stimulates the protoneutron star in the eigenfrequency. As mentioned above, the simulation using the HS(DD2) EOS also showed an explosion triggered by oscillations of the protoneutron star. Using the BASQUARK EOS, the oscillations set in at a significantly earlier time and lead to more pronounced oscillations of the central density. Quark matter seems to facilitate such oscillations. To be able to determine whether this behavior is of physical origin or just an effect of the low resolution, we will have to rerun this simulation using a higher resolution. Figure 10.5 shows a selection of velocity profiles between $t_{\rm pb} = 330$ ms and $t_{\rm pb} = 350$ ms. The dip in the velocity profile at approximately 10 km is due to the occurrence of quark matter and occurs at the beginning of the phase mixture. The figure clearly shows the oscillations in the outer layers of the protoneutron star which send shock waves outwards and push the standing accretion front to bigger radii (see also velocity profile in Fig. 10.3b).

Aside from these unexpected oscillations, no sign of a collapse of the protoneutron star is found. The overall evolution of the simulations seems to indicate that the explosion is powered by the neutrino driven mechanism. This assumption can only be confirmed when running the simulation using a higher resolution.

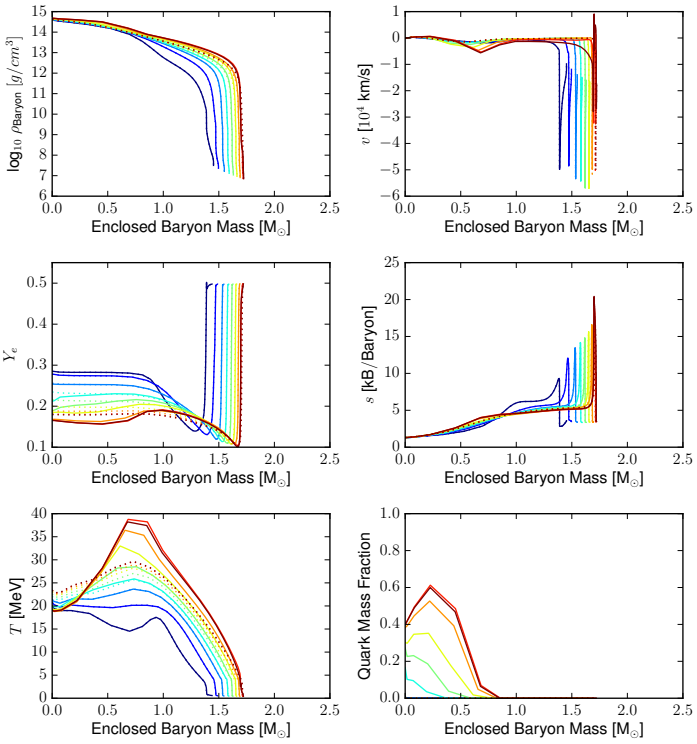

(a)

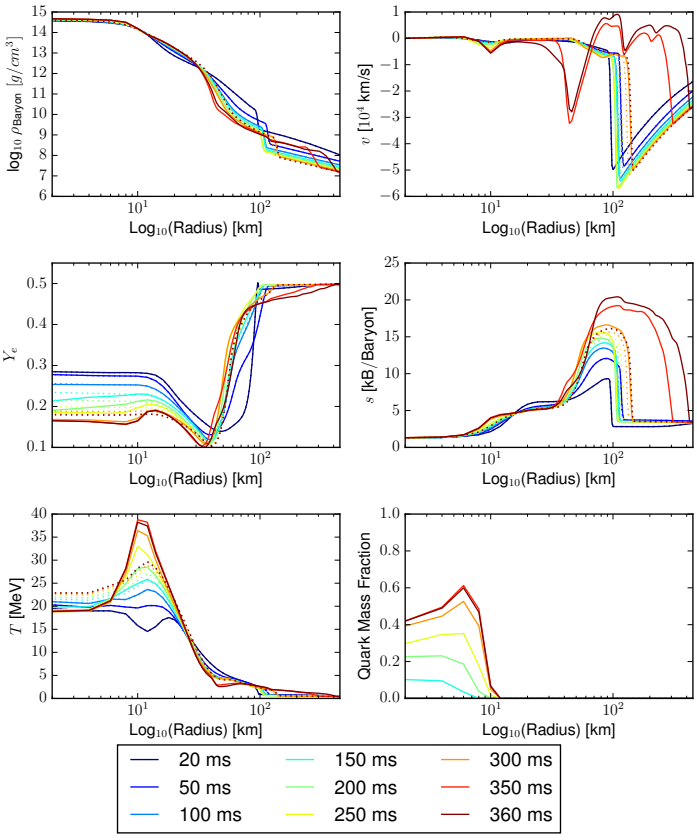

(b)

Fig. 10.3: Selection of hydrodynamical quantities in their radial profiles for selected post-bounce times using the 15 $M_\odot$ progenitor. The solid lines refer to the BASQUARK run while the dotted lines represent the HS(DD2) run.

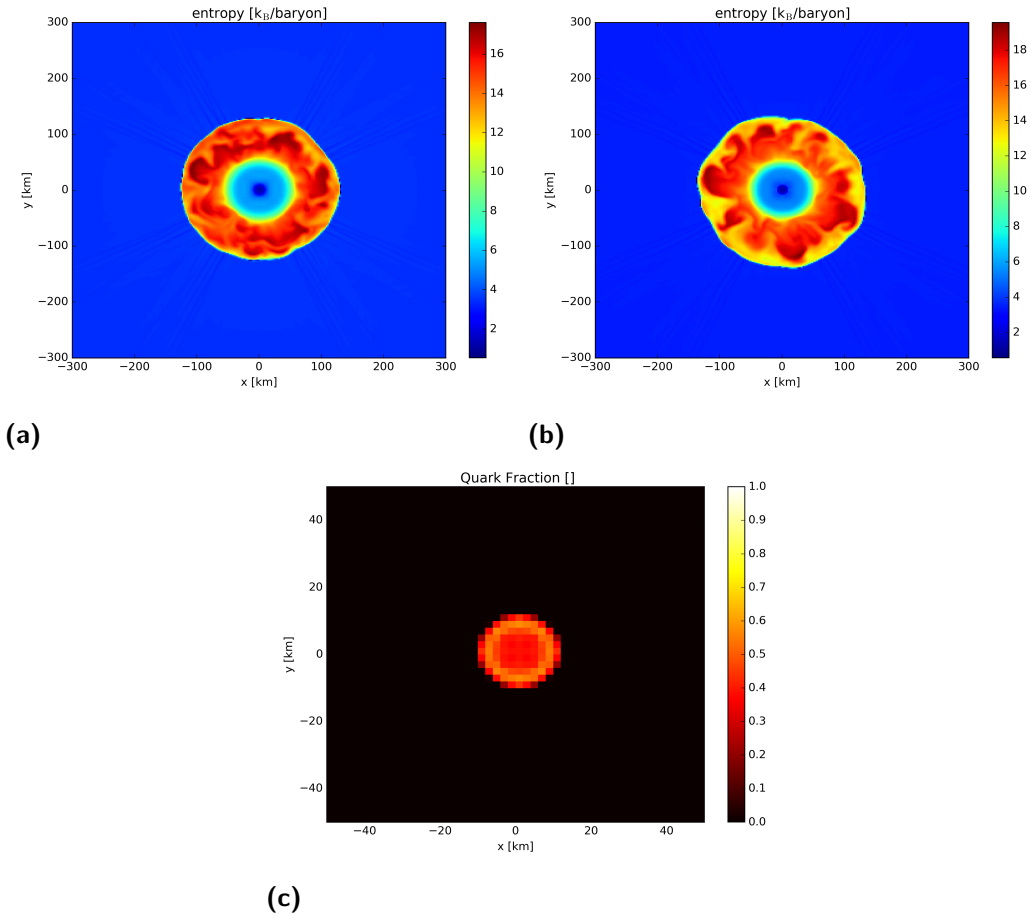

Fig. 10.4: Several snapshots of the x-y plane in ELEPHANT at $t_{\rm pb} = 300$ ms. Panel a) shows the entropy profile using the HS(DD2) EOS, panel b) the entropy profile using BASQUARK, and panel c) shows the quark mass fraction in the protoneutron star core when using the BASQUARK EOS.

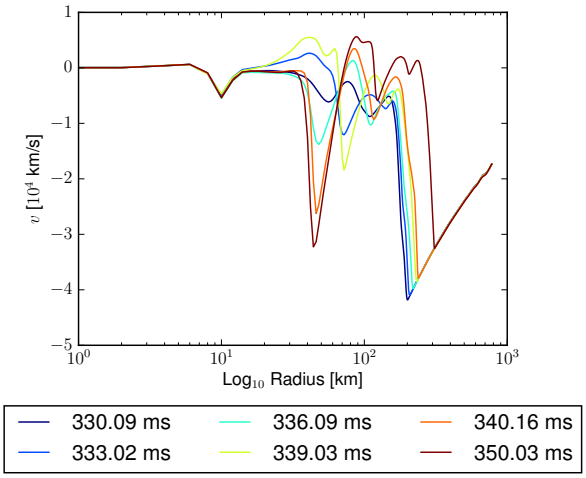

Fig. 10.5: A selection of velocity profiles that show the strong oscillations of the protoneutron star surface which ultimately lead to an explosion of the star.

10.1.2 40 $M_\odot$ progenitor

As for the 15 $M_\odot$ progenitor, two simulations were executed with ELEPHANT for the 40 $M_\odot$ progenitor (one with the HS(DD2) EOS and one with the BASQUARK EOS).

The BASQUARK run is restarted from the HS(DD2) run shortly after bounce where still no quark matter is present[2]. Figure 10.6 shows the evolution of the central density ρ_c for the HS(DD2) EOS and the BASQUARK EOS obtained with AGILE-IDSA (magenta and blue lines) and ELEPHANT (red and yellow lines) for the 40 $M_\odot$ progenitor of [211]. As initially mentioned in this chapter, the second collapse of the 40 $M_\odot$ progenitor in spherical symmetry happens more than 200 ms earlier than for the 15 $M_\odot$ progenitor. Further more, the peak maximum density at the second collapse is almost $2 \cdot 10^{14}$ g/cm^3 higher.

In our simulation with ELEPHANT using the hadronic equation of state, no explosion happened. The strong accretion hinders that the standing accretion shock front can expand to larger radii and the low resolution prevents the development of effective convection. The divergence between the central densities of the runs using the HS(DD2) EOS and the BASQUARK EOS is again due to the appearance of quark matter in the core of the protoneutron star. Using the BASQUARK EOS in ELEPHANT, quark matter already appears at around $t_{\rm pb} \sim 15$ ms. Figure 10.2 shows the amount of produced quark matter with time. Up to $t_{\rm pb} \sim 150$ ms, quark matter represents less than 10 % of the total mass of the protoneutron star. As for the 15 $M_\odot$ progenitor, we find strong oscillations in the central density, this time at around $t_{\rm pb} \sim 160$ ms. The situation seems to be different: Compared to the 15 $M_\odot$ progenitor, the oscillations do not appear gradually but start with a strong increase of ρ_c.

Figure 10.8 shows the same set of hydrodynamical quantities for several post-bounce times, as in Fig. 10.3. Again, the solid lines refer to the BASQUARK run while the dotted lines refer to the HS(DD2) run. Up to $t_{\rm pb} \sim 100$ ms almost no differences are visible between the profile lines of the HS(DD2) run and the BASQUARK run. Quark matter is present in the very inner core of the protoneutron star, but only with a quark mass fraction 0.1 or less. At $t_{\rm pb} \sim 120$ ms, respectively $t_{\rm pb} \sim 150$ ms, the differences between the HS(DD2) run and the BASQUARK run become more pronounced. Quark matter leads to a more compact protoneutron star which results in a standing accretion front at smaller radii. In the central part Y_e is again lowered due to the appearance of quark matter while entropy is slightly increased at ~ 10 km. Between 158 and 160 ms, the profiles change drastically.

[2]Remember that the hadronic part of the BASQUARK EOS is based on the HS(DD2) EOS and therefore the evolution of the simulation up to the point of the appearance of quark matter is identical.

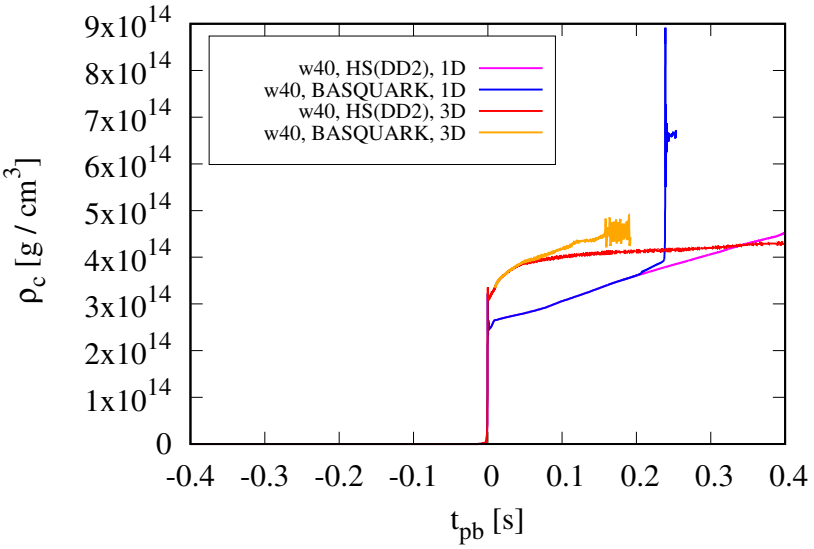

Fig. 10.6: As in Fig. 10.1, but for the 40 $M_\odot$ progenitor of [211].

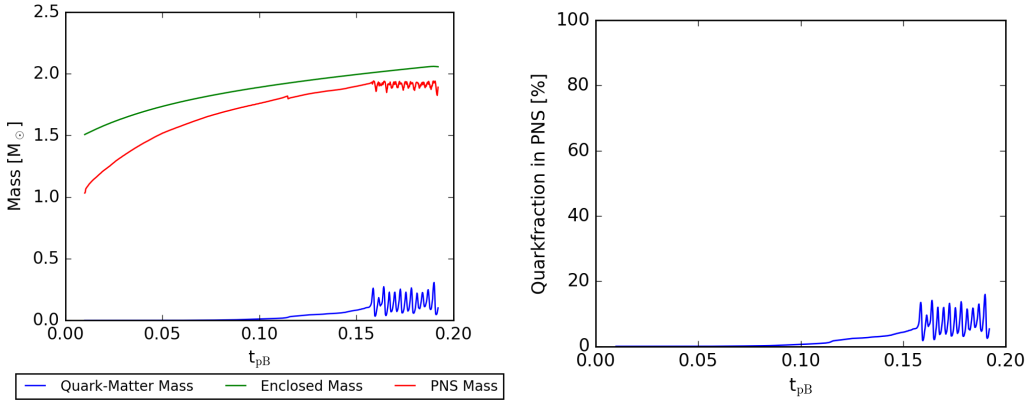

(a) **(b)**

Fig. 10.7: As in Fig. 10.2 but for the 40 $M_\odot$ progenitor.

Figure 10.9 shows the radial velocity profiles between 157 and 160 ms. Again, a negative velocity dip is visible at around 10 km (see discussion in Sec. 10.1.1). At $t_{\rm pb} = 157.97$ ms, negative velocities appear in the region between approximately 10 and 50 km which was stable before. At $t_{\rm pb} = 158.17$ ms, these negative values increase further until at $t_{\rm pb} = 158.17$ ms a new shock front starts to build out between 30 and 40 km. Afterwards, positive velocities start to appear which lead to an outward moving shock wave. At $t_{\rm pb} \sim 160$ ms, the shock wave merges with the standing accretion shock.

The sudden negative velocities and the building of a new shock front resemble the behavior of a second collapse observed in spherical symmetric simulations. However, a closer look at the profiles reveals that this is not a "proper collapse of the protoneutron star": Based on the knowledge of spherical simulations, the protoneutron star should collapse until the stiffening of the equation of state due to pure quark matter leads to an halt. At the boarder of the quark phase, the shock formation is expected. The shock detaches from the surface of the quark core, gains positive velocities, and ultimately merges with the standing accretion front. In the present ELEPHANT simulation, the negative infall velocities are by orders smaller than expected. Furthermore, the shock front does not form at the border of the quark mixed phase but a few tenths of kilometers further outside. The quark panels in Fig. 10.8 show that the quark matter fraction is increased during this process but pure quark matter is not obtained. As a result, the peak central densities are clearly too low. Summing up, we can state that although a beginning of a collapse of the protoneutron star is recognizable we are not able to identify this behavior as a "proper collapse" of the protoneutron star.

The resulting shock waves produced by this collapse-like behavior are not strong enough to trigger an explosion of the star. Moreover, this "collapsing" process stimulates the protoneutron star to oscillate in a monopole mode. This excitation finally leads to an explosion: New shock waves triggered from the surface of the protoneutron star merge at the accretion front and move the shock wave gradually outwards. This behavior can be observed in the profiles from $t_{\rm pb} = 170$ ms onwards.

At this point we assume that the insufficient resolution of this initial simulation to be the cause of failure of the suspected collapse of the protoneutron star. As described above in Sec. 10.1.1, the quark core in the center of the protoneutron star only consists of a few hundred simulation cells. This region, which is crucial in QCD phase-transition mechanism, is therefore completely underresolved and not able to describe the important physical processes. Additionally, since the time steps in ELEPHANT are controlled by the CFL-condition [51], also the time resolution is too coarse to describe the fast dynamics of a second collapse. Higher resolution is needed with no doubt; the only question is: to which extend?

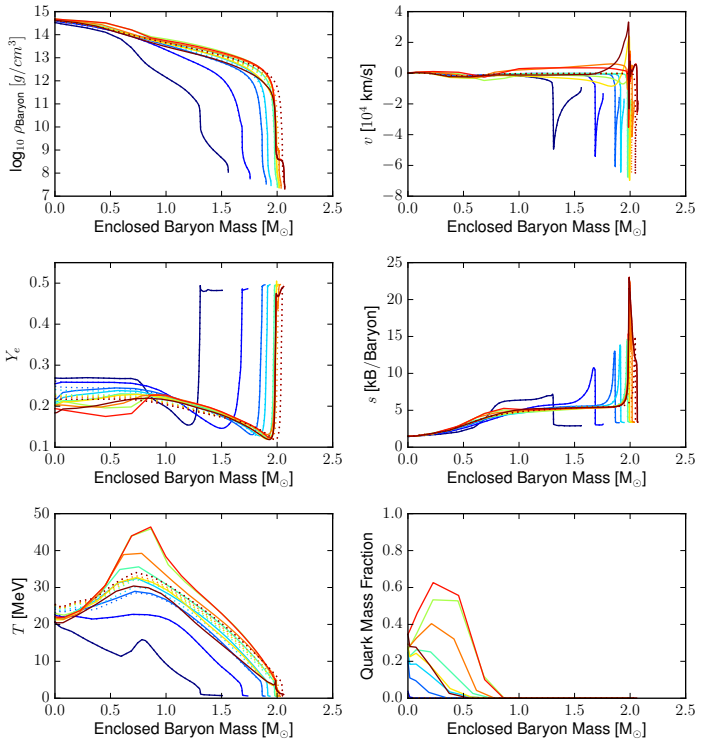

(a)

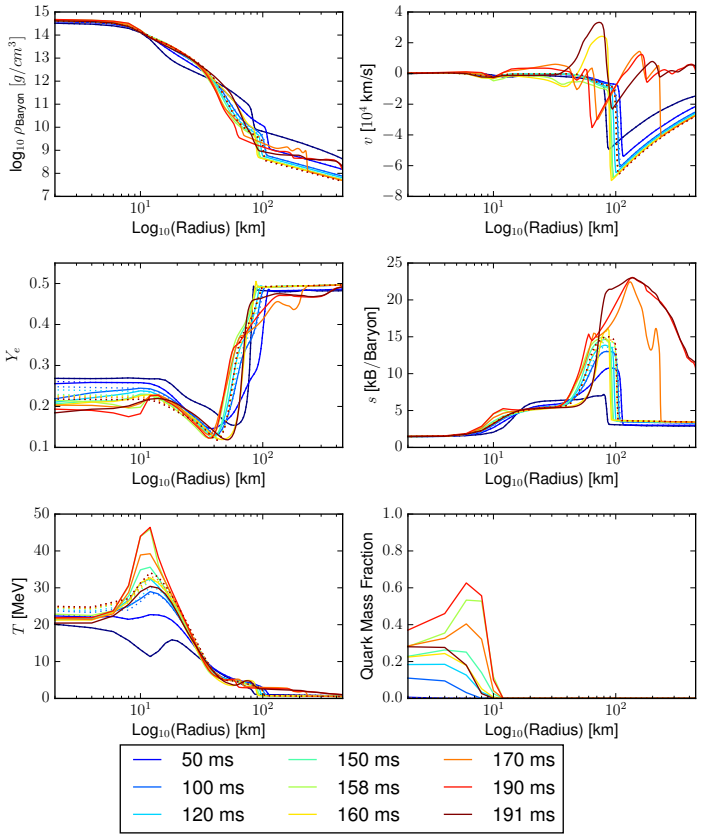

(b)

Fig. 10.8: Selection of hydrodynamical quantities in their radial profiles for selected post-bounce times using the w40 progenitor. The solid lines refer to the BASQUARK run while the dotted lines represent the HS(DD2) run.

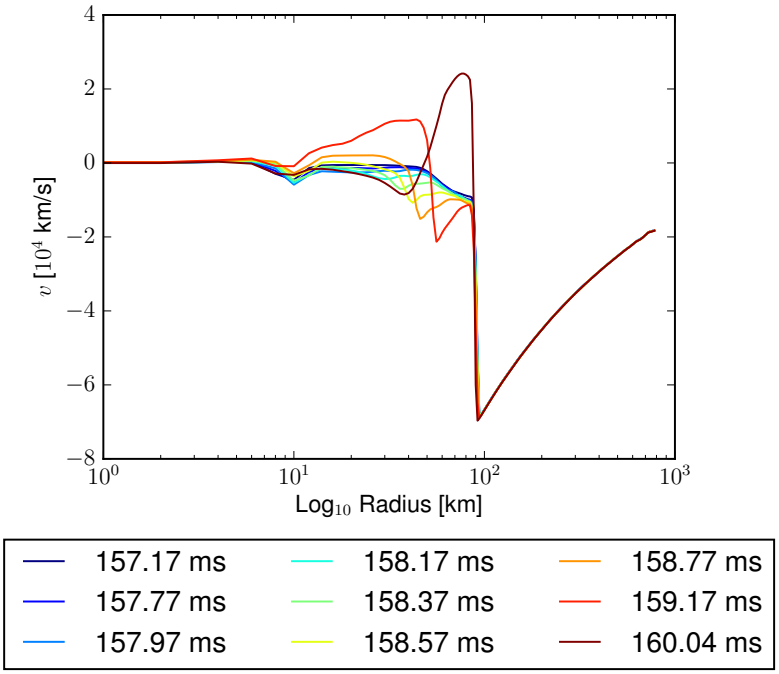

Fig. 10.9: Radial profiles of the velocity profiles at times between $t_{\rm pb} = 157$ and 160 ms. The profiles show the weak features of a second collapse behavior known from spherical simulations.

10.2 Spherical restart

In this section, we investigate the supposed collapse of the protoneutron star of the 40 $M_\odot$ progenitor using the spherical restart method. The spherical restart method has the advantage that the resolution can be increased arbitrarily when restarting from background AGILE-IDSA. Using this feature, this will help us to get an idea on the minimal requirements of resolution needed to simulate a possible second collapse in 3D core-collapse supernova. ELEPHANT can be restarted at the point of the suspected collapse without using a huge amount of computational resources. However, there are a few differences to ab-initio simulations which have to be kept in mind:

- **No rotation:** Compared to the full ab-initio runs, no rotation is considered when doing a spherical restart. So far, we do not know how rotation might effect a second collapse.
- **No magnetic fields:** Since we cannot reproduce the full evolution of the magnetic field found in ab-initio simulations, we do not consider magnetic fields in our spherical-restart runs.

Both of these assumptions move the conditions in the protoneutron star closer to the ones encountered in the one-dimensional case. In the following, we show the results for the initial two spherical restart simulations performed. We restart the simulation at $t_{\rm pb} = 148$ ms from a spherical profile of the background AGILE-IDSA in ELEPHANT.

10.2.1 Spherical restart using 2 km spatial resolution

We start our spherical restart investigation by using the same resolution as in the full ab-initio simulations discussed in Sec. 10.1.2. The computational domain consists of a box with 300^3 cells. This reduced box is still big enough to simulate the relevant part of the star, but saves quite some computational time. Even though we are aware that 2 km resolution leads to problems in the ab-initio simulations, we use it to investigate any fundamental differences between a simulated second collapse in full ab-initio simulation and the spherical restart simulation. Figure 10.10 shows the evolution of the central density ρ_c with time for the ab-initio simulation discussed in Sec. 10.1.2 (red line) and the simulation using the spherical restart method (yellow line). After the initial relaxation (first strong vertical increase of the yellow line), the ρ_c of the spherical restart approaches the values of the ab-initio simulation. The radial profiles of both simulations at $t_{\rm pb} = 156$ ms are shown in Fig. 10.11, a point close to the second collapse indicated with the blue cross in Fig. 10.10. The radial profiles show a remarkable good agreement between all hydrodynamical quantities. The good agreement agrees with the results shown in Sec. 9.3.6. Using the same resolution, our spherical restart tool seems to well reproduce the conditions found

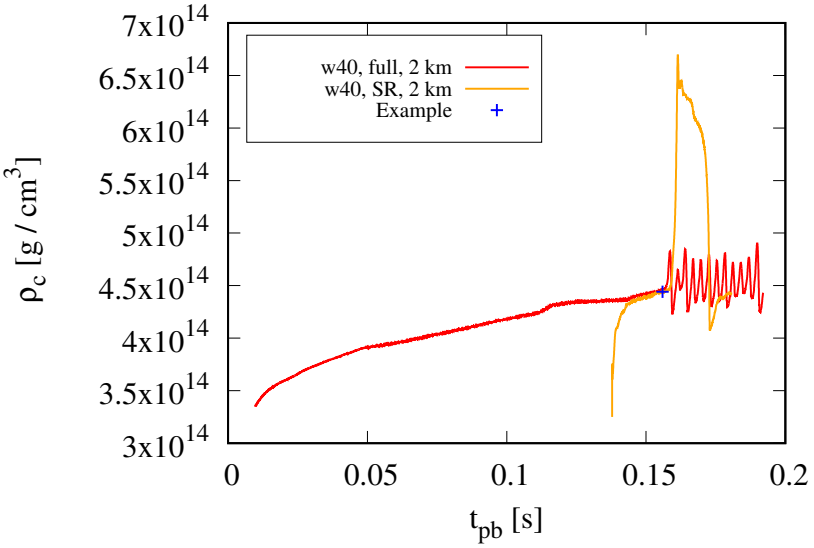

Fig. 10.10: Shown is the evolution of the central density ρ_c with time. The red line indicates the results obtained in the full ab-initio simulation with 2 km spatial resolution as discussed in Sec. 10.1.2. The yellow line represents the data obtained from a spherical restart simulation which is also performed using 2 km spatial resolution. The blue cross indicates the time where the profiles shown in Fig. 10.11 are compared.

in an ab-initio simulation, on spherical average. Since in the 40 $M_\odot$ case the shock front does not expand to large radii, the spherical restart method can even reproduce the shock front reasonably well.

A few milliseconds later after the snapshot shown in Fig. 10.11 a "collapse"[3] of the protoneutron star sets in at a density of approximately $\rho_c = 4.5 \cdot 10^{10}$ g/cm^3. As shown in Fig. 10.10, the ab-initio and the spherical restart simulation collapse almost simultaneously. This confirms that with the spherical restart method we are able to reproduce a very similar situation as found in the ab-initio simulation. The spherical restart run shows a more pronounced collapse feature. The central density rises to values up to $\sim 6.7 \cdot 10^{14}$ g/cm^3 at $t_{\rm pb} = 161.39$ ms. Figure 10.12 shows a selection of radial profiles of typical hydrodynamical quantities, beginning at the start of the collapse until a few milliseconds after the collapse. The velocity profiles clearly show the negative values during the collapse phase. Compared to the ab-initio run in Sec. 10.1.2, this feature is well pronounced. Still, the shock front forms at a surprisingly large radius, similar to the ab-initio run. Afterwards, the shock front detaches from the place of formation and moves towards the standing accretion front (positive velocities in the velocity profile). However, the shock wave is too weak to push the standing accretion front outwards. In the center of the protoneutron star densities are high enough to reach quark mass fractions up to 1. Based on our knowledge of the spherical simulations, we would expect such

[3] We will discuss the validity of the term for this simulation below.

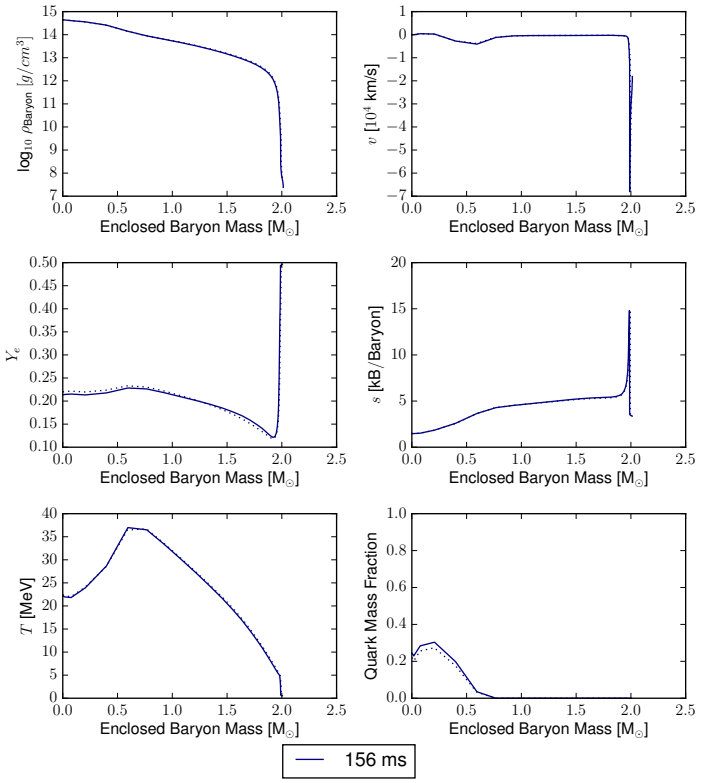

(a)

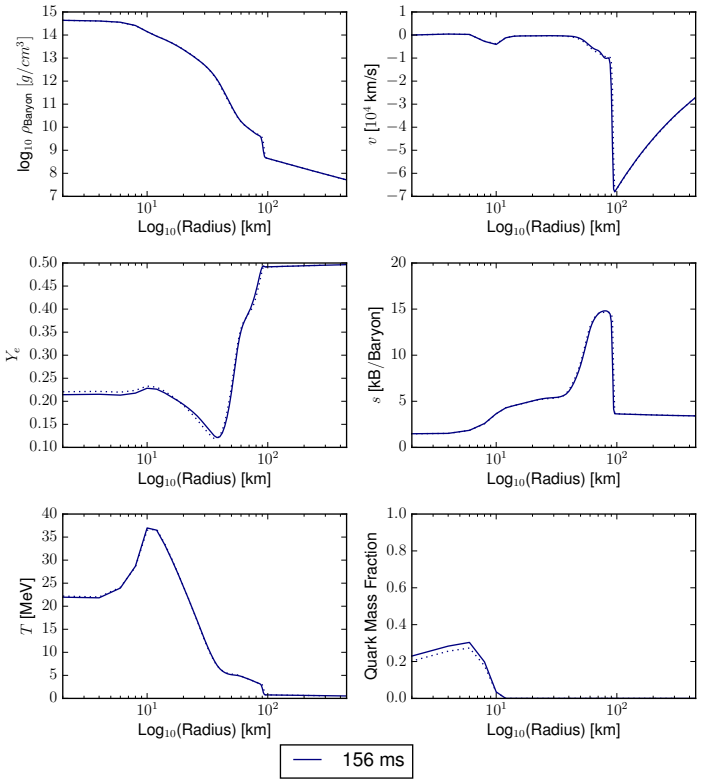

(b)

Fig. 10.11: Comparison of a selection of hydrodynamical quantities in their radial profiles at $t_{\rm pb} = 156$ ms (indicated with a blue cross in Fig. 10.10) of the ab-initio run (solid line) and the spherical restart run (dotted) line of a 40 $M_\odot$ progenitor with 2 km resolution. The profiles show a good agreement of the two simulations at the same post-bounce time.

high quark mass fraction. Compared to the full ab-initio calculation of the 40 $M_\odot$ progenitor, it is more reasonable to use the term "collapse" for the behavior found in this simulation. The central density profile shows a pronounced increase of ρ_c which allows to reach quark matter fractions of up to 1 in the core. Only the shock front is still formed at a too large radius.

At $\sim t_{\mathrm{pb}} = 171$ ms, we observe the start of a strange behavior of the protoneutron star (see the radial profiles of Fig. 10.13): The protoneutron star becomes unstable, best visible as the huge drop in the central density shown in Fig. 10.10, leading to an expansion and decompression. This results in positive velocities between the surface of the quark region and the standing accretion front. Matter of the outer part of the protoneutron star is pushed towards the standing accretion front, merges with it, and continues afterwards as an outwards moving shock front. During this process a lot of quark matter is reconverted back into hadronic matter, reducing the quark matter fraction from a maximum of 1 back to below 0.5. We consider this whole process as not physical, but more as a consequence of the poor resolution of the central protoneutron star. With a resolution of 2 km the code seems not able to support a hydrodynamical equilibrium after the second collapse. Most probably this can be explained by the fact that the strong gradients are not resolved well enough.

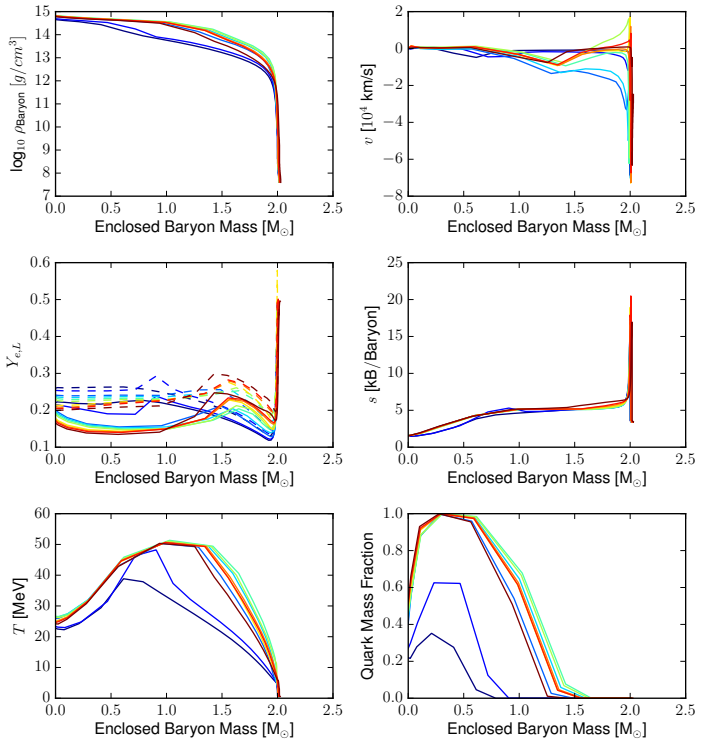

(a)

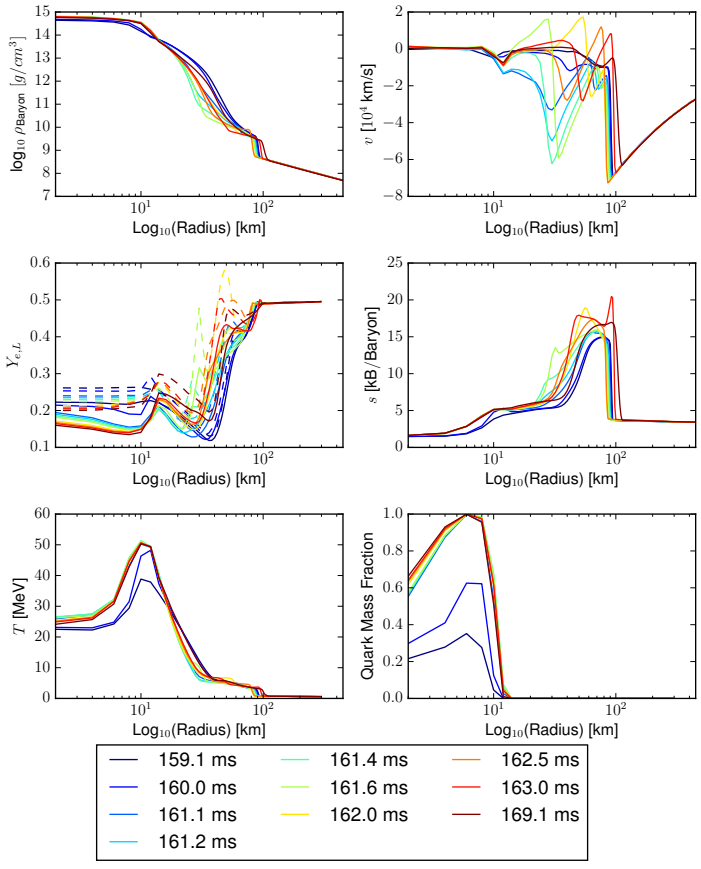

(b)

Fig. 10.12: Radial profiles of a selection of hydrodynamical quantities for the spherical restart model with 2 km spatial resolution during and shortly after the second collapse. In the $Y_{e,L}$ profiles, the dashed lines indicate Y_L and the solid lines Y_e.

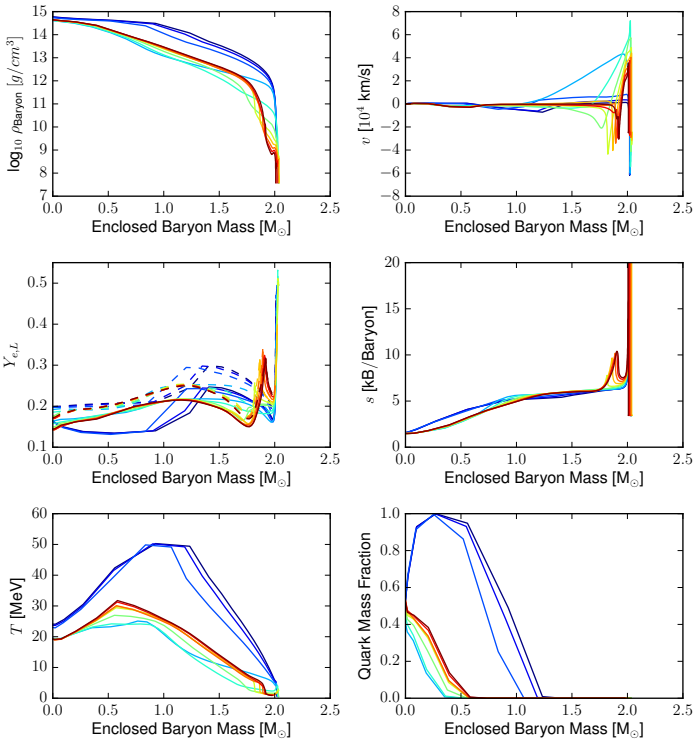

(a)

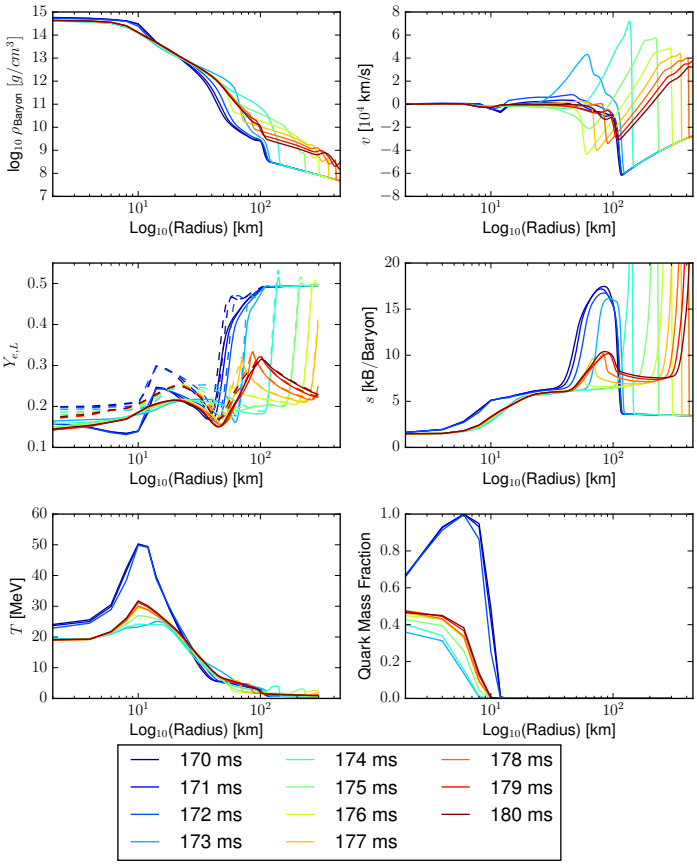

(b)

Fig. 10.13: As in Fig. 10.12, but for times from $t_{\rm pb} = 170$ ms onwards.

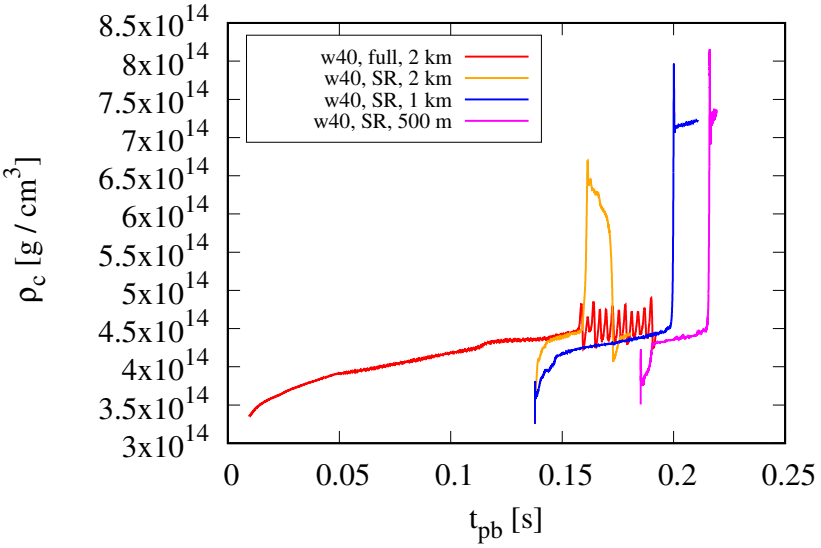

Fig. 10.14: Central densities of the spherical restart runs. The red line indicates the ab-initio run discussed in Sec. 10.1.2, the yellow line indicates the simulation with 2 km resolution discussed in Sec. 10.2.1, the blue line the simulation discussed in Sec. 10.2.2, and the magenta line the simulation discussed in Sec. 10.2.3.

10.2.2 Spherical restart using 1 km spatial resolution

In this section we discuss a spherical restart simulation using a 600^3 box with 1 km resolution. We restart the simulation at the same position as in Sec. 10.2.1.

Figure 10.14 shows the evolution of the central density of the simulation with 2 km spatial resolution (red line, ab-initio run as discussed in Sec. 10.1.2 and yellow line, as discussed in Sec. 10.2.1), the simulation using 1 km spatial resolution (blue line), and the simulation using 500 m resolution (magenta line) discussed in the succeeding section. Relaxing the system with 1 km resolution does not lead to the same hydrodynamical stable configuration as running with 2 km resolution. The central densities of the 1 km resolution run are clearly lower than the ones of the 2 km resolution run. This is due to the better resolved protoneutron star. Until sufficiently high densities for a second collapse are reached, the simulation has to be run for almost 50 ms. The second collapse sets in again at around $\sim 4.5 \cdot 10^{14}$ g/cm^3. During the second collapse, central density rises up to values of $\rho_c = 7.97 \cdot 10^{14}$ g/cm^3 what is significantly higher than using a resolution of 2 km. After the second collapse the protoneutron star seems to remain stable. The shape of the central density curve is now very similar to the spherically symmetric case, i.e. the shape expected from a collapse of the protoneutron star.

Figure 10.15 shows the radial profiles of a selection of hydrodynamical quantities during the second collapse. The second collapse starts to set in at around $t_{\rm pb} = 198.4$ ms. The velocity profiles show the large negative velocities of the in-falling matter of the outer protoneutron-star shells. At around $t_{\rm pb} = 200$ ms, a shock front forms close

to the outer boundary of the quark core which then detaches from the surface and moves outwards with high positive velocities (profiles from $t_{\mathrm{pb}} = 200.2$ ms onwards). With 1 km resolution, the shock seems to be formed at the position expected. The outward moving shock has enough energy to keep its positive velocities even after having merged with the standing accretion front. This is the behavior we expect the QCD phase-transition mechanism to show in a three-dimensional simulation, based on our knowledge of the spherical simulations.

Figure 10.16 shows entropy in the x-y plane of the 3D-ELEPHANT domain for several times before and after the collapse of the protoneutron star. Figure 10.16a shows the entropy profile just before the collapse. Even though small convections are visible around the protoneutron star, they are not strong enough to visibly deform the standing accretion front surface. The shock front remains almost spherical in shape. In Fig. 10.16b, the formation of the pressure wave is visible as a yellow ring in the low entropy part around the almost blue quark core. As soon as the detached shock front reaches the convectional high entropy region, a sharp, almost spherical shock front is visible, exhibiting high entropy values (see Fig. 10.16c and 10.16d). The shock front later merges with the standing accretion front (Fig. 10.16e) where entropies above 32 k_B/baryon are reached. The outwards moving shock then decouples from the high entropy "ring" (red colors) when moving away from the former standing accretion front region (Fig. 10.16f). While the spherically averaged profiles show similar features as known from the AGILE simulations, the 2D slices clearly show multi-dimensional effects: The irregular pattern inside the shock front seems to be caused by Rayleigh-Taylor instabilities. Additionally, it would be interesting to investigate the effects of the outwards moving second shock wave on a more perturbed standing accretion front. This might be achieved using a different progenitor, in a full ab-initio simulation, or an earlier spherical restart.

As visible in the quark mass fraction panel in Fig. 10.15, during the collapse of the protoneutron star the quark mass fraction rises significantly. The increased resolution helps to better model the different regions of the central core: While in the inner core a hadron-quark mixed phase with quark mass fraction of just below 0.5 is present, in the outer core the quark mass fraction rises towards 1 leaving a region of several kilometers with pure quark matter. In the subfigures of Fig. 10.17, the evolution of the quark mass fraction during the second collapse is shown in the x-y plane of ELEPHANT. In Fig. 10.17a the onset of the increasing of the quark mass fraction starts to be visible. The stronger increase along the grid axis is a numerical artifact. In Fig. 10.17b and Fig. 10.17c a ring with a large quark mass fraction is formed which also spreads inwards during the collapse. Again, the square shaped deformation of the red inner core in Fig. 10.17c is due to the grid nature of code. Such features could be prevented using a different, non-grid code setup, for example using a smooth particle hydrodynamics code such as SPHYNX [39]. Figure 10.17d shows the quark mass fraction distribution when it reached its maximum. This shape

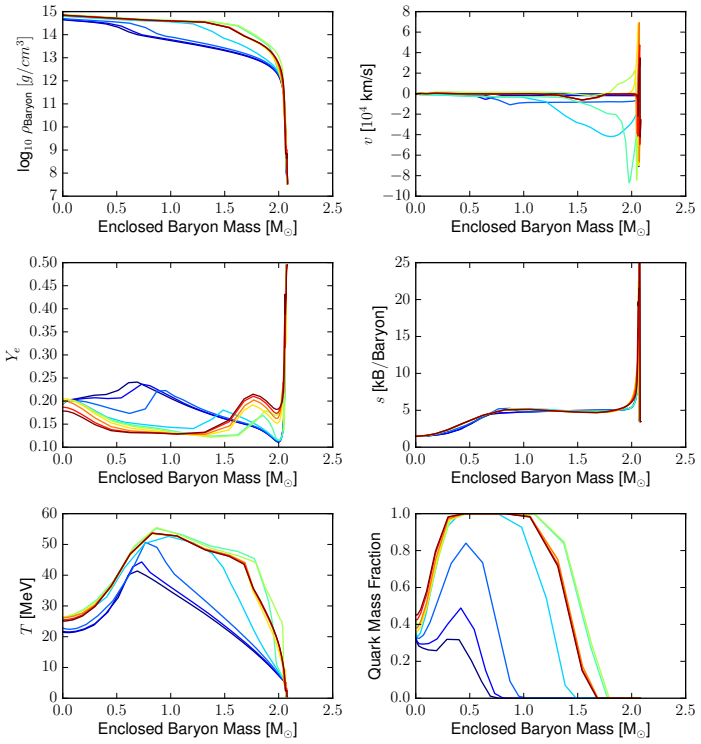

(a)

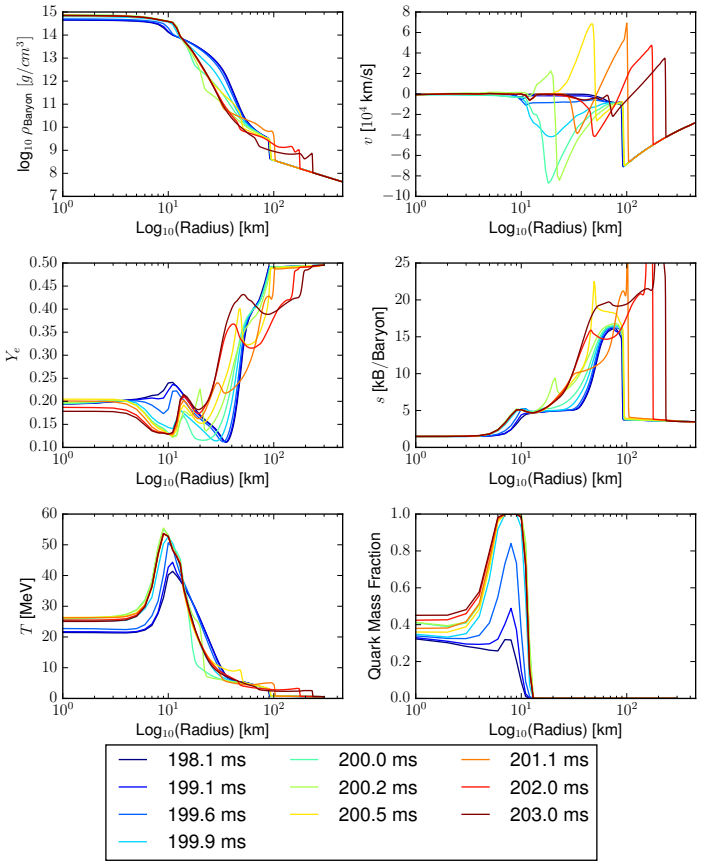

(b)

Fig. 10.15: Selection of hydrodynamical quantities in their radial profiles during and shortly after the second collapse.

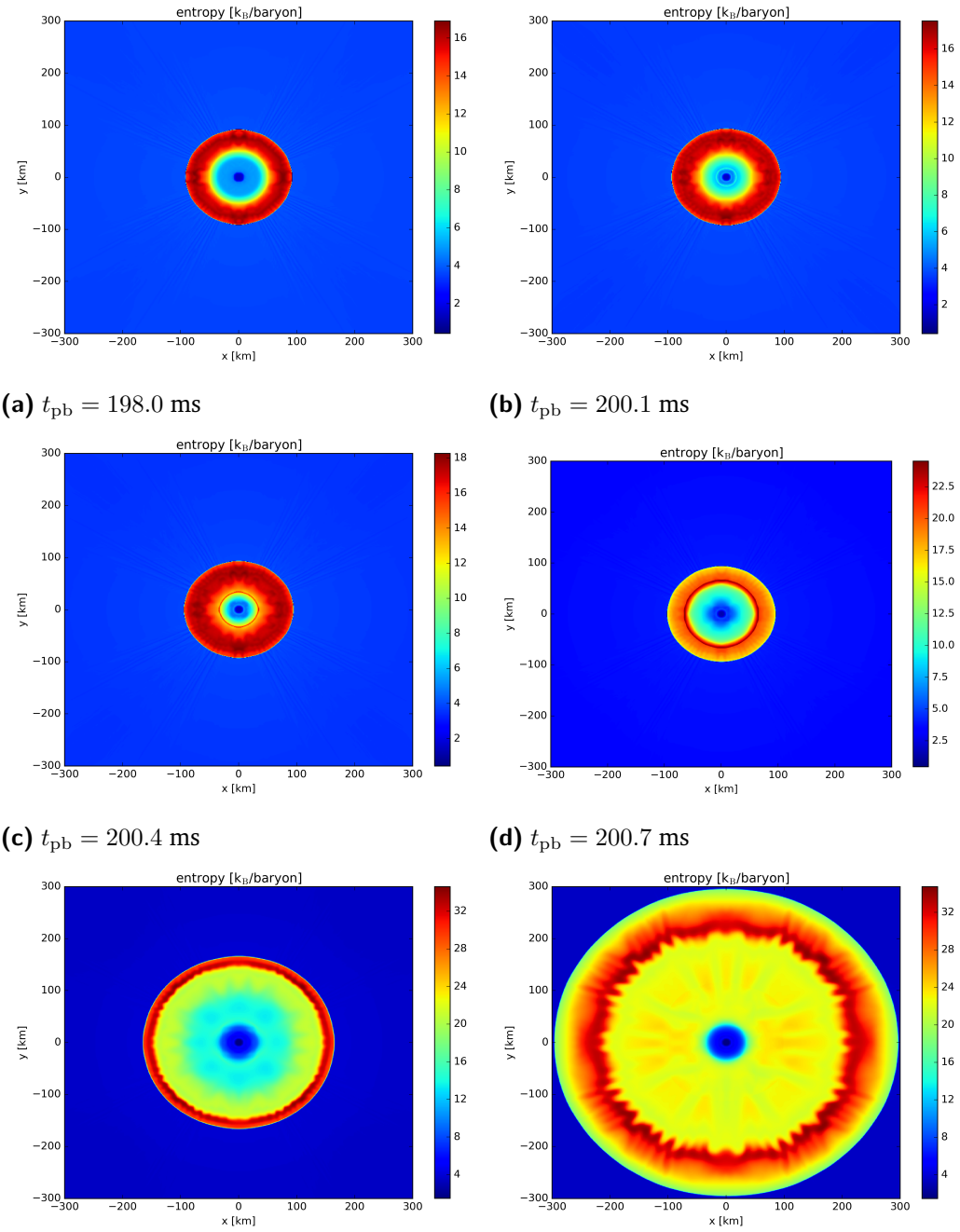

(a) $t_{\mathrm{pb}} = 198.0$ ms **(b)** $t_{\mathrm{pb}} = 200.1$ ms

(c) $t_{\mathrm{pb}} = 200.4$ ms **(d)** $t_{\mathrm{pb}} = 200.7$ ms

(e) $t_{\mathrm{pb}} = 201.8$ ms **(f)** $t_{\mathrm{pb}} = 204.6$ ms

Fig. 10.16: Snapshots of the entropy in the x-y plane of ELEPHANT at different times post bounce.

does not change significantly until the end of the simulation. In Fig. 10.18, the evolution of the total quark mass is plotted. The second collapse leads to an increase of quark matter from ~ 0.15 $M_\odot$ to ~ 1.22 $M_\odot$, which corresponds to almost 60 % of the total protoneutron star mass. This high quark mass fraction is in good agreement with spherical results as for example shown in Sec. 6.

As known from spherical simulations, the second collapse can release a vast amount of neutrinos. The integrated neutrino luminosities are shown in Fig. 10.19. During the second collapse, all neutrino types ($\nu_e, \bar{\nu}_e, \nu_{\mu/\tau}/\bar{\nu}_{\mu/\tau}$) show sharp peaks in their luminosity signals. The strongest feature is found in the μ/τ neutrino signal: The luminosity peaks at $L_{\mu/\tau} = 8.4 \cdot 10^{53}$ erg/s. The strong peak in the μ/τ neutrino signal is different to the 1D simulations and might be overestimated due to the applied leakage. Nevertheless, such a strong signal might be interesting as a possible observable for neutrino detection. Unfortunately, the anti-neutrino luminosities become negative after the second collapse. This might indicate a problem with the quark-neutrino rates (see discussion in Sec. 6.2.1) or a problem with the IDSA (or both). The IDSA neutrino treatment might run into problems in this scenario since it is constructed to trap neutrinos in optically thick regimes and release them in optically thin regimes. A collapse of the protoneutron star and the succeeding second shock wave might mess with the original order of the optical thickness and trouble the IDSA. In the near future, we have to check if the IDSA is still handling all the regimes in a correct manner.

10.2.3 Spherical restart using 500 m spatial resolution

In this section we discuss the spherical restart simulation using a 750^3 box with 500 m resolution. Since this setup requires 125 nodes on Piz Daint and advances only approximately 8 ms per day, the spherical restart is started at $t_{\mathrm{pb}} = 184.7$ ms.

In Fig. 10.14 the magenta line indicates the run with 500 m grid resolution. Again, the better resolution leads to lower central densities at same post-bounce times compared to the lower resolutions runs. After the relaxation the simulation runs for approximately 22 ms until the second collapse sets in at $\sim 4.5 \cdot 10^{14}$ g/cm^3. This density is consistent with the results obtained in the 2 km and 1 km grid-resolution runs. During the second collapse the central density rises up to values of $\rho_c = 8.06 \cdot 10^{14}$ g/cm^3. This value is only slightly ($0.09 \cdot 10^{14}$ g/cm^3) higher than the value of the 1 km run. After the second collapse the protoneutron star seems to remain stable. The central density increases after the second collapse due to fallback onto the protoneutron star. Unfortunately, we were not able to further investigate the evolution of the explosion i.e. the ρ_c evolution since the shock front passed the domain walls.

In Fig. 10.20 a selection of hydrodynamical quantities during the second collapse are shown. In general, the results are very similar to the 1 km results discussed

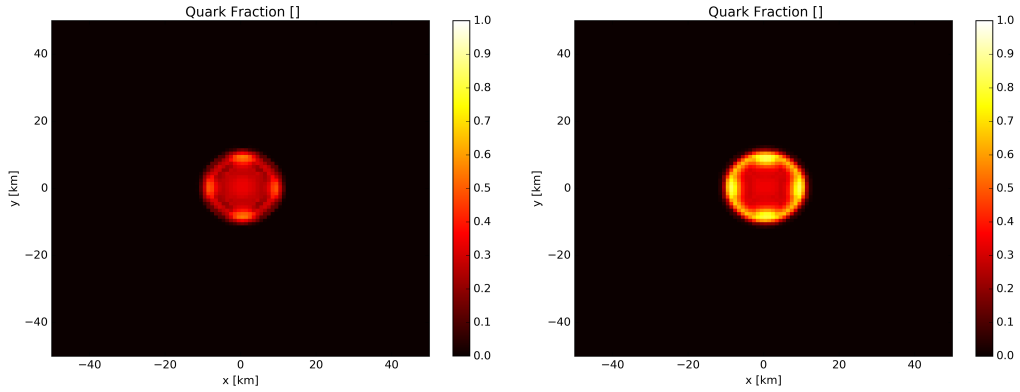

(a) $t_{\mathrm{pb}} = 198.0$ ms **(b)** $t_{\mathrm{pb}} = 199.4$ ms

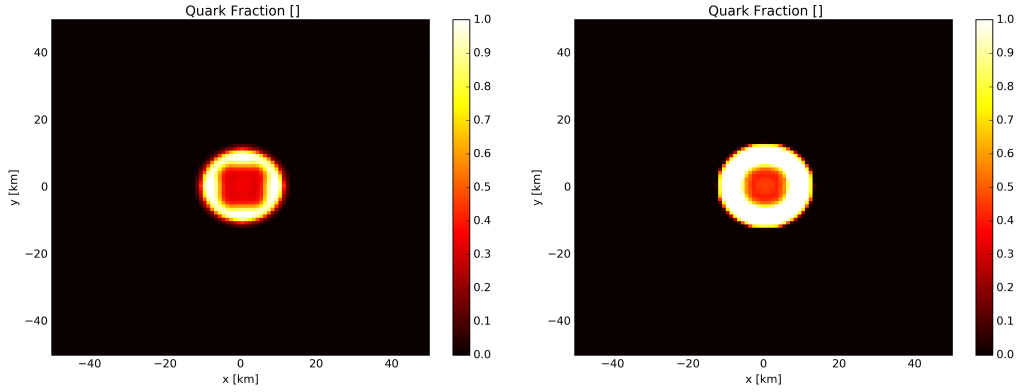

(c) $t_{\mathrm{pb}} = 199.6$ ms **(d)** $t_{\mathrm{pb}} = 200.1$ ms

Fig. 10.17: Snapshots of the quark mass fraction in the x-y plane of ELEPHANT at different times post bounce.

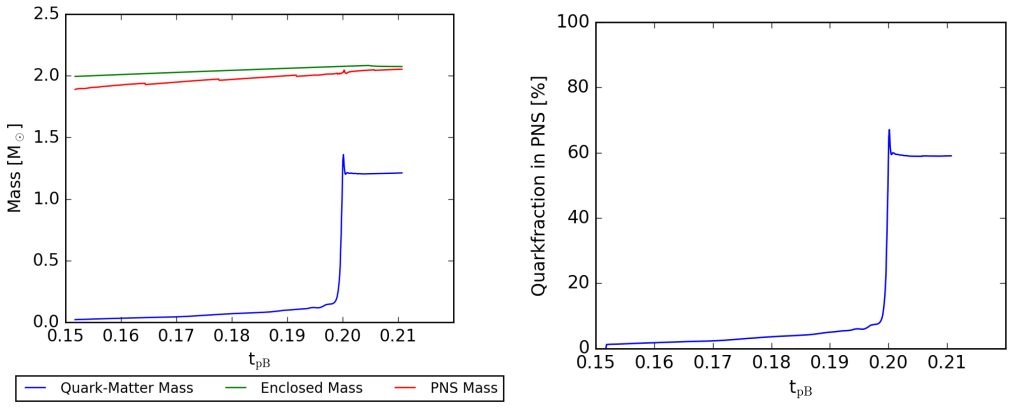

(a) **(b)**

Fig. 10.18: Evolution of the quark mass fraction with time as in Fig. 10.2.

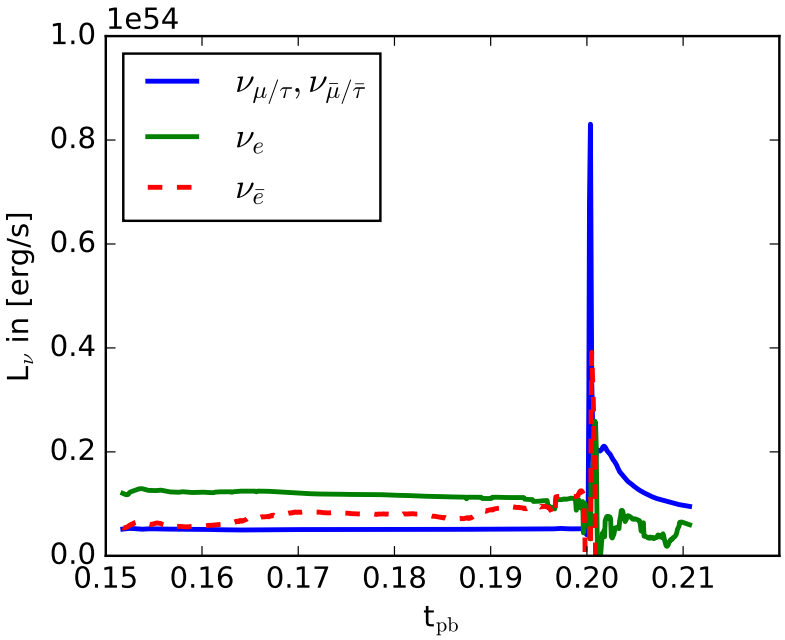

Fig. 10.19: Neutrino luminosities for the different treated neutrino flavors in the spherically restarted 40 $M_\odot$ simulation using 1 km grid resolution.

in Sec. 10.2.2 just shifted to later post-bounce times. The second collapse sets in at around $t_{\rm pb} = 214.2$ ms. Large negative velocities of the in-falling matter of the outer protoneutron-star shells are the consequence until at around $t_{\rm pb} = 215.6$ ms a shock front is formed at the outer boundary of the quark core. The position of the formation of the shock front coincides very well with the results obtained using 1 km resolution. When the shock detaches from the surface its velocity is again large enough to continue the expansion even after having merged with the standing accretion front.

In Fig. 10.21, several entropy slices in the x-y plane of the 3D-ELEPHANT domain are shown before and after the collapse of the protoneutron star. The figures show times where the second shock is at similar positions as shown in Fig. 10.16. Figure 10.21a shows the entropy profile close to the collapse of the protoneutron star. In Fig. 10.16a, using 1 km resolution, the convections was small, showed symmetric features, and did not visibly deform the standing accretion front. In Fig. 10.21a clear convection bubbles with entropies around or above 20 k_B/baryon appeared. These bubbles are strong enough to visibly deform the surface of the protoneutron star surface. Furthermore, the convection does not show any artifacts from the spherical restart but is more randomly distributed. The convectional features at the low-high entropy region at around 60 km radius is another property which could not be resolved using 1 km resolution. We can state that performing a spherical restart with 500 m grid resolution enhances the convection and leads to a more realistic convection pattern. Figure 10.21b shows the snapshot at a time where the newly formed pressure wave is visible in the central part of the protoneutron star. The (low

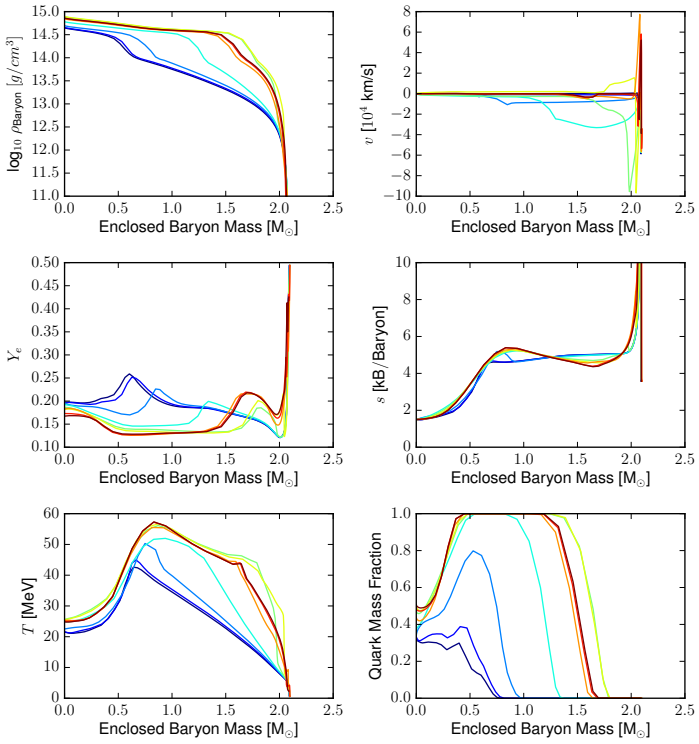

(a)

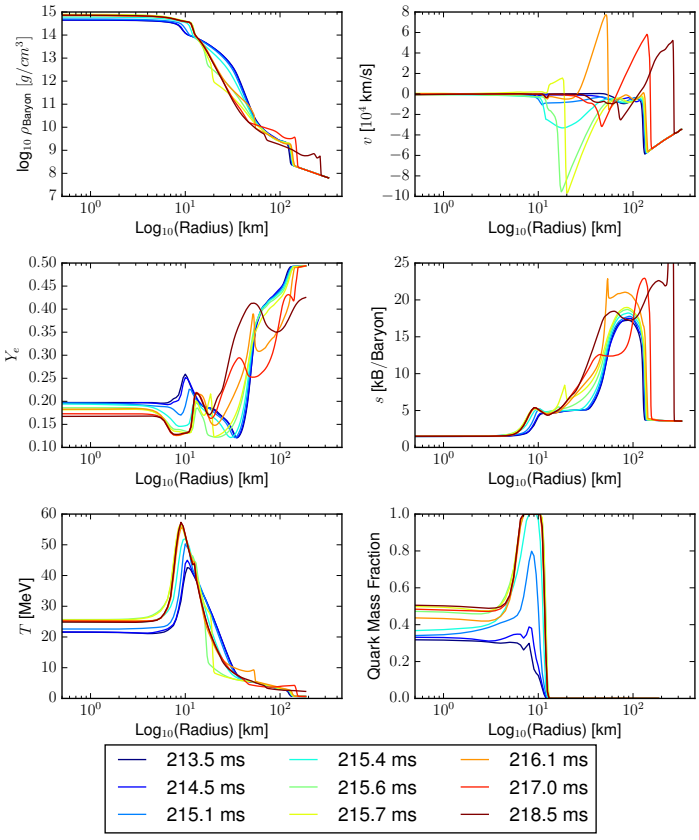

(b)

Fig. 10.20: Selection of hydrodynamical quantities in their radial profiles during and shortly after the second collapse using 500 m grid resolution.

entropy) core of the protoneutron star has collapsed to a quark core (dark blue in the center) and the pressure wave moves outwards (turquoise ring). In Fig. 10.21c the detached shock front has reached the high entropy region, now indicating increased entropies. The shock front is still almost spherical and the convectional features towards the lower entropy region shown in Fig. 10.21a and 10.21b are destroyed by it. The squarish feature of the central core (in blue) is due to its oscillation and is a consequence of the grid code. In Fig. 10.21d the shock front has moved deeper in the high entropy region. The shock front is gradually more distorted. In the back of the shock front new hydrodynamical instabilities become visible i.e. Rayleigh-Taylor instabilities. In Fig. 10.21e the second shock wave has merged with the standing accretion front. Entropies above 30 k_B/baryon are reached and the instabilities behind the shock front become even more pronounced. In contrast to the simulation with 1 km grid resolution the merged shock front does not show a spherical shape any more but more undulations on the surface to the unshocked region. This feature is even more enhanced in Fig. 10.21f. It would be very interesting to perform a spherical restart with this resolution at an earlier restart time to give the system even more time to develop convections and distort the standing accretion front. The effect of the second shock wave merging with a more strongly deformed standing accretion shock might lead to an even more non-spheric shock evolution, and therefore be even more realistic.

The quark mass fraction panels in Fig. 10.20 show similar results as shown in Fig. 10.15: The central core consists of a mixed phase of hadronic and quark matter with a quark mass fraction of 0.5 and below. With the better resolution this becomes also better visible in the quark matter panel in Fig. 10.20a. In the subfigures of Fig. 10.22, the quark mass fraction is shown in the x-y plane of ELEPHANT at several times during and after the second collapse. Figure 10.22a shows the profile before the second collapse. The higher quark fractions along the grid axis is again a numerical artifact. Figure 10.22b shows the profile shortly after the onset of the second collapse. The quark mass fractions increase and the protoneutron star is strongly deformed, due to the grid structure of the code. In Fig. 10.22c the majority of the protoneutron star mass has been transformed into quark matter, visible as the white ring. Again, the square shape in the center is an artifact. Finally, in Fig. 10.22d the core has reached its final state at the end of the simulation. The deformation of the inner part is gone since the core has stopped the strong oscillation caused by the collapse of the protoneutron star. The higher resolution shows now in more detail the interfaces between the different quark fractions regions. Figure 10.23 shows the evolution of the total quark matter. Again, the second collapse leads to an increase of the quark matter from around ~ 0.15 $M_\odot$ to ~ 1.3 $M_\odot$ which is slightly higher than the value obtained in the 1 km run. This corresponds to 65 % of the total protoneutron star mass.

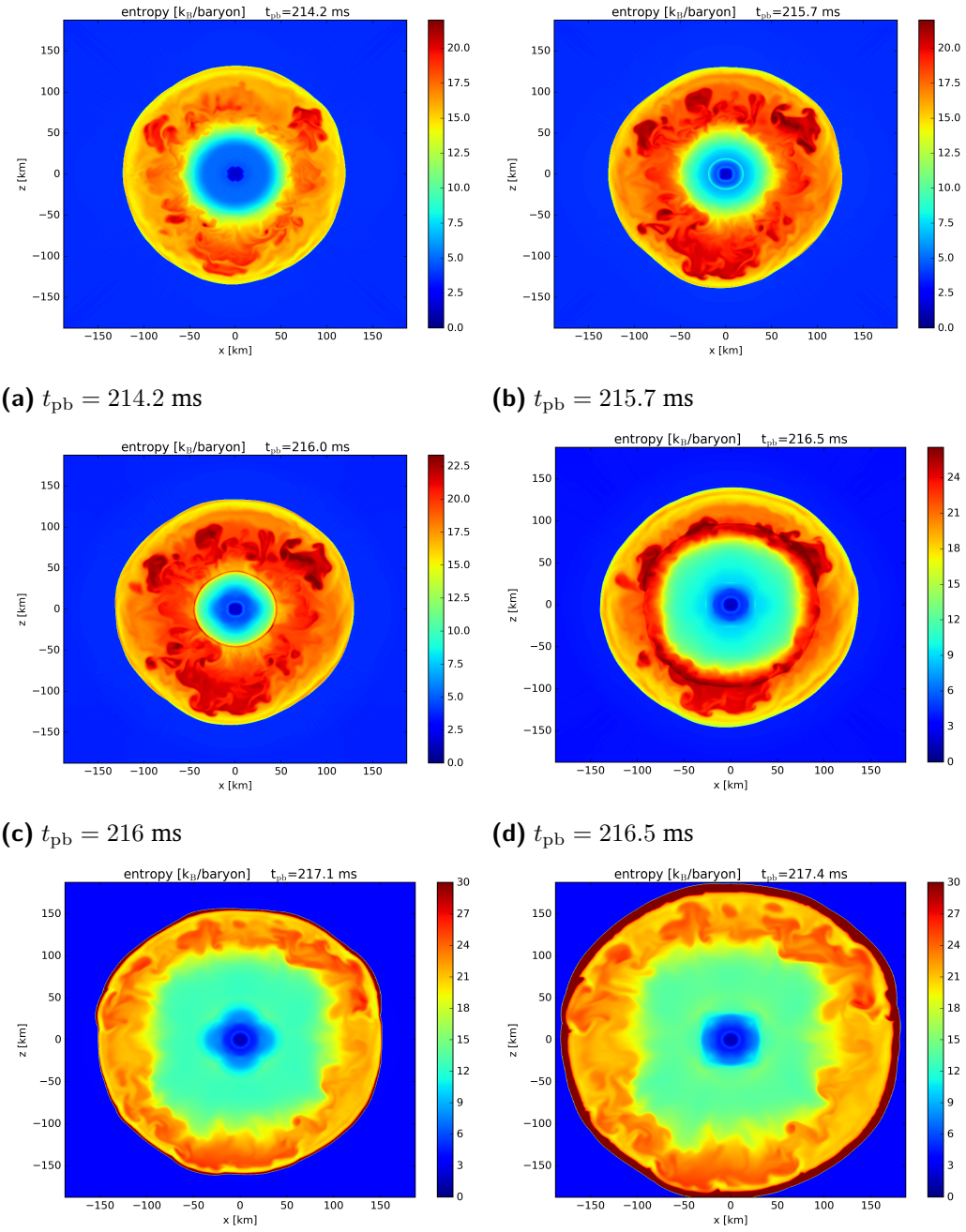

(a) $t_{\mathrm{pb}} = 214.2$ ms **(b)** $t_{\mathrm{pb}} = 215.7$ ms

(c) $t_{\mathrm{pb}} = 216$ ms **(d)** $t_{\mathrm{pb}} = 216.5$ ms

(e) $t_{\mathrm{pb}} = 217.1$ ms **(f)** $t_{\mathrm{pb}} = 217.4$ ms

Fig. 10.21: Snapshots of the entropy in the x-y plane of ELEPHANT at different times post bounce using 500 m grid resolution.

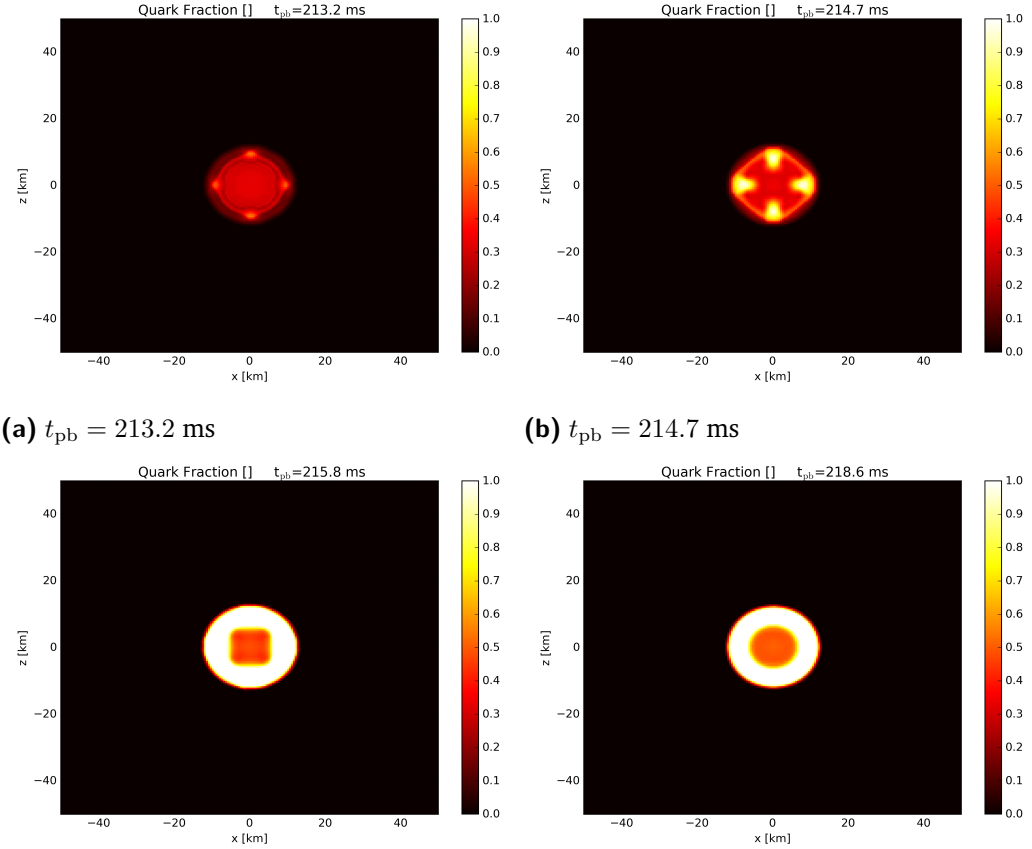

(a) $t_{\mathrm{pb}} = 213.2$ ms **(b)** $t_{\mathrm{pb}} = 214.7$ ms

(c) $t_{\mathrm{pb}} = 215.8$ ms **(d)** $t_{\mathrm{pb}} = 218.6$ ms

Fig. 10.22: Snapshots of the quark mass fraction in the x-y plane of ELEPHANT at different times post bounce using 500 m grid resolution.

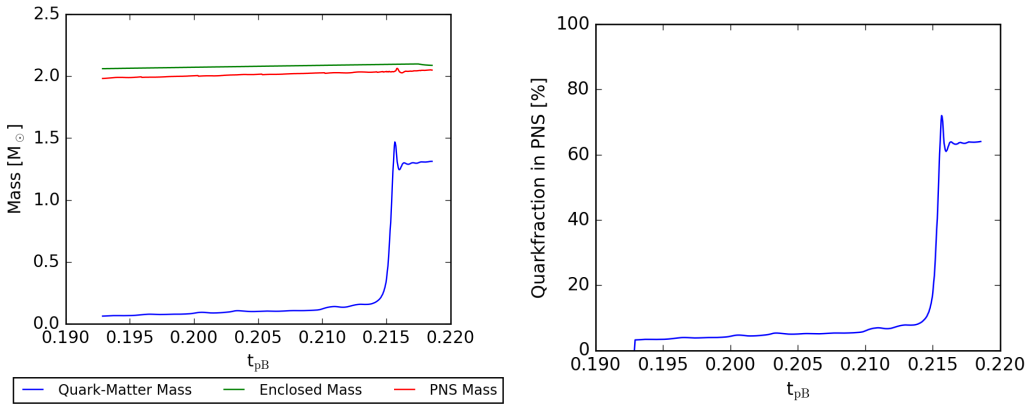

(a) **(b)**

Fig. 10.23: Evolution of the quark mass fraction.

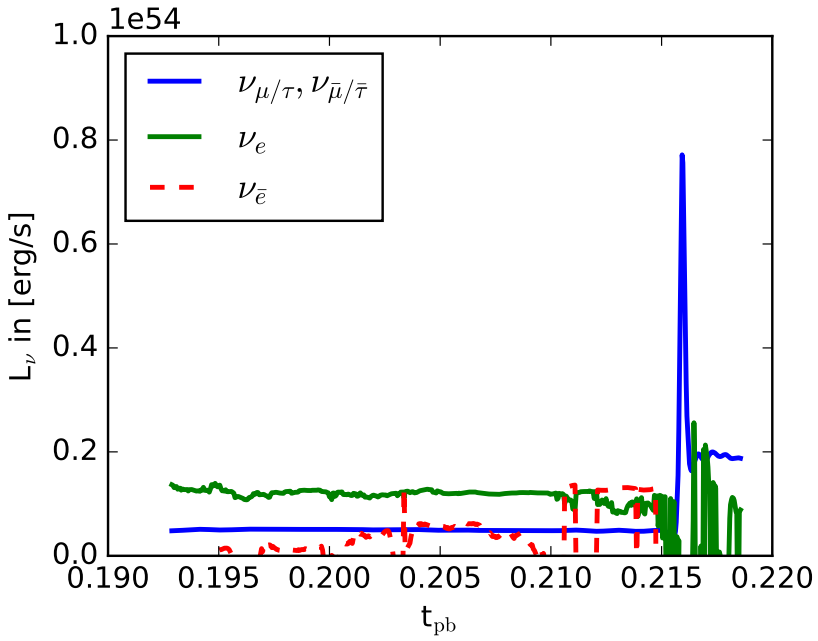

Fig. 10.24: Neutrino luminosities for the different treated neutrino flavors in the spherically restarted 40 $M_\odot$ simulation using 500 m grid resolution.

Figure 10.24 shows the neutrino luminosities of all treated neutrino types. Again, the μ/τ neutrino signal shows a clear peak of around $8 \cdot 10^{53}$ erg/s. However, the IDSA seems to have severe problems treating the ν_e and $\bar{\nu}_e$ neutrinos. Compared to the 1 km grid resolution run the problems using 500 m are even bigger: Strong oscillations already set in before the collapse, so no clear peak is at the second collapse is recognizable. This might indicate that, apart from the problems already mentioned in Sec. 10.2.2, the time stepping for the IDSA chooses to large values. This can be easily tested in the near future.

Conclusions II

11

> *What's this: ☹ → ☺?*
> *It's a "face"-transition!*
>
> **— F.-K. Thielemann**

In the second part of this thesis, the subject of multi-dimensional core-collapse supernova simulations was addressed, especially the application of BASQUARK in the 3D supernova code ELEPHANT. This is the first time a hybrid supernova equation of state is applied in a 3D core-collapse supernova simulation.

In Chapter 8, a short overview over the 3D core-collapse supernova code ELEPHANT was given. ELEPHANT consists of a central 3D domain which is embedded in a larger spherical domain described by the spherical code AGILE-IDSA. AGILE-IDSA describes the boundary conditions of the 3D domain. We consider ELEPHANT as a very suitable code to simulate core-collapse supernovae when using a hybrid supernova equation of state. ELEPHANT is a fast and efficient code which is parallelized using methods such as MPI, OpenMP, and OpenACC. The neutrino transport, which represents the computationally most expensive part of the code, is approximated using several schemes such as parametrized deleptonization, the IDSA, and a μ/τ-neutrino leakage scheme. These approximations result in huge speed-up of the code compared to a full solution of the Boltzmann equation. ELEPHANT is not a fully relativistic code, but strong gravitational fields are treated efficiently using a modified gravitational potential that includes GR corrections. Since ELEPHANT is rather fast and not as computationally expensive as other supernova codes (e.g. FLASH [50, 49, 159]), it is suitable for simulations up to several hundred milliseconds post bounce. Two upgrades had to be implemented to consider quark matter in ELEPHANT: A separate quark routine has been implemented to calculate and output the quark matter fraction in the 3D domain for a detailed post processing. Additionally, we had to split the equation of state treatment of the 3D domain and AGILE-IDSA: While we use the BASQUARK EOS in the 3D domain, AGILE-IDSA is run with the HS(DD2) EOS. This is procedure is applied to prevent a second collapse of AGILE-IDSA which in turn would lead to false boundary conditions of the 3D domain.

In Chapter 9, we presented the method and the results of a newly developed method called the *spherical restart method*. The original idea of the application of this method was to restart an ELEPHANT simulation at late post-bounce times, without weeks of preceding calculations, to test the code there, i.e. before a suspected second collapse. Since in ELEPHANT, AGILE-IDSA is always running in the background

treating the outer layers and the boundaries of the 3D domain, we can simply map a spherical profile, created in a separate external AGILE-IDSA run, into ELEPHANT. However, the mapping from the unequally-spaced AGILE-IDSA grid to the equally spaced ELEPHANT grid leads to a profile which is in the wrong hydrodynamical equilibrium. During an initial phase of the spherical restart, ELEPHANT tries to adjust the profile to a new hydrodynamical equilibrium. To prevent an artificial explosion caused by these adjustments, we introduced a damping mechanism in the 3D domain, valid during the first couple of hundred time steps. The damping criterion of this mechanism depends on the local speed of sound and the matter velocity of the initial profile. Initially, a profile with reference velocities, calculated with the damping criterion, is saved. In the following, any velocities that exceed these reference velocities are set back to the saved values. This method allows the protoneutron star to adjust to the new hydrodynamical equilibrium while damping the artificial shock waves caused by the adjustment.

The results obtained using this method are very promising: The relaxation of the system (with activated damping mechanism) takes place on a time scale of approximately $10 - 15$ ms. During this time, the central part of the protoneutron star adjusts to its new stable configuration i.a. through convection in the protoneutron star. After this relaxation, the damping mechanism is turned off and the system is evolved naturally. During this time, convection starts to build up in the high entropy regions, pushing the standing accretion front outwards. After another 50 ms of simulation time, the spherically averaged profiles of the restarted run imitate well the profiles obtained by a consistently run ab-initio simulation. Remaining differences between the profiles of these two runs are mainly caused by the different collapse behavior of the two codes.

Of the two damping parameters, especially the speed-of-sound-dependent parameter is very sensitive. If the values are chosen too high, the protoneutron star is not damped enough and strong shock waves are sent outwards. These in turn have to be decelerated by a strong velocity criterion. If the parameter is chosen too restrictive, the protoneutron star is overly damped and hindered in his natural adjustment. Especially the shock front is not able to expand to larger radii. This problem could be solved by gradually adjusting the parameter too higher values.

Very interesting results were obtained when ELEPHANT was spherically restarted from a spherical profile of the AGILE-IDSA, run in the background of ELEPHANT. The profiles of the background AGILE-IDSA differ from the profiles of the standard AGILE-IDSA: During the collapse phase of ELEPHANT, the spherically averaged profiles of ELEPHANT are transferred into the background AGILE-IDSA to achieve the same bounce times. A spherical restart from such a profile leads, after the relaxation and a few tenths of milliseconds of evolution, to an extremely good agreement of the spherically averaged radial profiles, between the restarted and the fully executed

ELEPHANT run. This result implies that the spherically-averaged 3D profiles in the post-bounce phase depend essentially on the evolution up to bounce, and not much on the following post-bounce evolution.
Since the spherically averaged profiles agree that good, the spherical restart method can as well be used to increase the resolution at any time post bounce. Using this method, interesting resolution studies might be performed in the post-bounce phase without using a vast amount of computational resources.

The spherical restart method could further be improved also considering rotation: predetermined rotation could be mapped in the simulation. Additionally, no magnetic fields are included so far, but might also be considered by an artificial profile. The damping procedure could also be used to remap 3D simulation data in the post-bounce phase to investigate higher resolutions. The damping procedure could suppress eventual artifacts caused by the rearrangement data to a different grid structure. Even though the spherical restart method was developed for ELEPHANT, it might as well be used for any other hydrodynamical core-collapse supernova code.

Chapter 10 dealt with the application of our new hybrid supernova equation of state BASQUARK in ELEPHANT. This is the first time that quark matter is investigated in a 3D core-collapse supernova simulation. In a first step we run two low resolution simulations (2 km) with BASQUARK using a 15 $M_\odot$ and a 40 $M_\odot$ progenitor. The 15 $M_\odot$ progenitor is expected to explode by the neutrino-driven mechanism, using a hadronic equation of state [128, 121, 109]. On the other hand, the 40 $M_\odot$ progenitor is expected to collapse into a black hole using a hadronic equation of state. In spherically symmetric simulations using BASQUARK, both progenitors showed explosions caused by the QCD phase-transition mechanism. It is therefore very interesting to investigate the effect of quarks in a multi-dimensional treatment. The low resolution for the initial runs was chosen so the simulations proceed reasonably fast in the post-bounce phase. This allowed us to get first information about the evolution.

In both simulations (15 $M_\odot$ and 40 $M_\odot$ progenitors) using BASQUARK, quark matter already appeared at significantly earlier post-bounce times than in the spherical simulations. This is caused by the higher present densities and the lower electron fractions. The appearance of quark matter leads to a more compact core of the protoneutron star which as a consequence influences the succeeding post-bounce evolution. In comparison to the spherical simulations, using BASQUARK in ELEPHANT quark matter appears first in the center and not off center.

In the case of the 15 $M_\odot$ progenitor, the post-bounce evolution in the beginning largely resembles the situation found in a typical neutrino-driven mechanism with the exception that quark matter is present. No collapse of the protoneutron star is found. The simulation ultimately shows an explosion due to gradually increasing oscillations of the protoneutron star. These oscillations drive shock fronts into the

standing accretion shock which in turn is pushed outwards. We believe that this oscillation behavior is caused by the low resolution, as we have seen a similar behavior with the same resolution using HS(DD2). But, without a higher resolution run this question cannot be definitely answered. However, the evolution before the unexpected oscillations of the protoneutron star indicates a neutrino driven explosion mechanism.

The 40 $M_\odot$ progenitor ultimately explodes because of strong oscillations of the protoneutron star, too. Compared to the 15 $M_\odot$ progenitor, the oscillations start not gradually but with a pronounced increase in the central density. A more detailed analysis of the radial profiles revealed that there is the beginning of a collapse at $t_{\mathrm{pb}} \sim 157$ ms, but the collapse does not behave like the collapse of the protoneutron star in the spherical simulations: The increase in the central density is not as pronounced as in spherical simulations, the quark matter fraction does not rise up to values of 1, and the shock front builds not at the boarder of the quark mixed phase but several tenths of kilometers further outside. Nevertheless, the 40 $M_\odot$ progenitor shows indications of a collapse which might fail due to the too low resolution. We can conclude that higher resolution is crucial for our core-collapse supernova simulations.

In the second half of Chapter 10, we applied the spherical restart method with the aim of a better resolution at the expected collapse. As mentioned above, compared to a full ab-initio run the spherical restart run does not consider rotation and magnetic fields. In a first attempt, we executed a spherical restart simulation using 2 km resolution. The radial profiles of the spherical restart and the ab-intio simulation at the onset of the collapse coincide extremely well. Surprisingly, the restarted simulation shows a clearer collapse behavior to higher central densities, and quark fractions of up to 1. The shock front is still built at too large radii, but in summary the collapse behavior resembled more a second collapse known from spherical simulations. Nevertheless, the outward moving shock wave is too weak to trigger an explosion. A couple of milliseconds after the second collapse, the protoneutron star becomes unstable: The central density decreases, a huge fraction of the quark matter is reconverted into hadronic matter, and the outer layers of the protoneutron star are expelled in a shock wave, leading to an explosion of the system. This behavior is most likely caused by the low resolution which is not able to handle the steep occurring gradients of the new protoneutron-star configuration. The runs with higher resolution summarized below support this statement.

In summary we can state that a spherical restart simulation with 2 km resolution shows part of the second collapse behavior known from spherical simulations but shows significant problems due to the low resolution. The different collapse behavior between the spherical restart simulation and the ab-initio calculation is unexpected and should be investigated in more detail. Since the radial profiles before the

second collapse (see Fig. 10.11) show an extremely good agreement between the simulations, the source probably is a multi-dimensional effect. At present, we can only speculate about the reasons: The slow rotation in the ab-initio calculations might additionally perturb the center of the protoneutron star, preventing a full collapse with this poor resolution. Contrariwise, the relaxation at the beginning of the spherical restart run might produce an initially more stable configuration. At the moment, we can only speculate about the influence of the magnetic fields on the collapse behavior, too. These effects could be systematically investigated running multiple simulations: Ab in-initio simulations could be run without magnetic fields and/or without initial rotation to examine the effects of the two initial conditions and compare it to the spherical restart runs. Spherical restart simulations could be started earlier to give the system more time to perturb and investigate the effect on the collapse behavior. However, it is questionable if it is worth to do this detailed investigation using 2 km spatial resolution, as we know of the problems caused by the low resolution during and after the second collapse.

In a second attempt we performed a spherical restart using 1 km resolution. Using the increased resolution, a higher maximum density during the second collapse is reached and the newly configured protoneutron star remains stable afterwards. The radial profiles of the second collapse reveal a similar pattern as known from the spherical simulations. The protoneutron star with a high quark matter fraction (~ 60 %) is well resolved. The pressure wave finally forms close to the quark mixed phase, the position also observed in spherical simulations. The outward moving shock wave is strong enough to transform the standing accretion front into a moving shock front which ultimately leads to an explosion. The pattern of the expanding shock wave is very spherical. This might be connected with the fact that the previous standing accretion front did also show little perturbation. Interestingly, within the expanding shock wave patterns known from Rayleigh-Taylor instabilities become visible. This simulation is the first to simulate the collapse of the protoneutron star with a succeeding explosion in three dimensions!

The neutrino signal shows an strong peak in the $\mu - \tau$ luminosities ($8.4 \cdot 10^{53}$ erg/s). We find another pronounced peak of the $\bar{\nu}_e$ luminosities. However, the $\bar{\nu}_e$ luminosities show negative values after the second collapse which is most likely not physical. Either, this indicates a problem with the quark rates or a problem with the IDSA. A detailed investigation of the neutrino rates and neutrino transport is necessary in the future.

In a final attempt we performed a spherical restart using a spatial resolution of 500 m. This run with higher resolution confirms the results already obtained using 1 km resolution. The maximum central density obtained during the second collapse is slightly higher than the one obtained with 1 km resolution. The newly configured protoneutron star remains stable afterwards having a quark matter fraction of around

65 %. This slightly higher quark fraction is due to the better resolved core. The radial profiles confirm well the results of the 1 km resolution run. However, the biggest improvements of the higher resolution were found in the discussed entropy slices: 500 m grid resolution leads to the development distinct convection. This was not the case using only 1 km resolution. The convection removes almost all of the spherical artifacts and also leads to deformation of the standing accretion front. Finally, the expanding shock wave is less spherical than in the 1 km resolution. Again, the merged shock wave has enough energy to trigger an explosion. In the backwash of the expanding merged shock wave we find again features of Rayleigh-Taylor instabilities. These nice results once more show the importance of a high enough spatial resolution.

The neutrino signal shows again a clear peak in the $\mu - \tau$ neutrino luminosities treated by the leakage scheme. However, the μ_e and $\bar{\mu}_e$ signal treated by the IDSA shows strong oscillations even before the collapse of the protoneutron star. This might, additionally to the already discussed problem with the neutrino rates, indicate a too large time stepping in the neutrino transport.

To sum up the discussion: A spherical restart using 1 km or even 500 m resolution seems to describe correctly the collapse of the protoneutron star and the succeeding explosion of a 40 $M_\odot$ star. The resolution is sufficient to resolve the protoneutron star in a correct and stable manner. 500 m resolution seems to be a good resolution to also treat the convections correctly. In a next step we would have to check if we can observe the same features in a full ab-initio calculation or if we would still meet similar problems as found in the 2 km ab-initio runs. In the future it might be interesting to test other progenitors, which eventually show even stronger perturbed standing accretion shocks before the second collapse, and investigate the effect on the shock evolution.

Summary and Outlook

12

> *Ich hab' getan, was ich nicht lassen konnte.*
>
> **— Wilhelm Tell**
> Aus Schiller's gleichnamigen Werk

In Chapter 7 and 11, a detailed summary and conclusion of the first and second part of this thesis was provided. This last chapter shall provide a brief summary and conclusion on the entire thesis.

The final goal of the first part of this thesis was to construct a new hybrid supernova equation of state that is in good agreement with current experimental and observation constraints, i.e. the 2 $M_\odot$ neutrons star mass constraint. Additionally, the future hybrid supernova equation of state should be constructed such that the known QCD core-collapse supernova mechanism is expected to occur in spherical simulations.

In a first step, we systematically investigated the mass-radius relations of cold hybrid stars by the variation of the phase-transition parameters. We initially used the HS(DD2) EOS to describe the hadronic matter and the CSS EOS with $c^2_{\mathrm{QM}} = 1/3$ (which has been shown to be transferable into a bag model) to describe the quark matter. We successfully determined the hybrid star configurations that satisfy the 2 $M_\odot$ neutron star mass constraint and show a third family feature in their mass-radius relation. Finally, we presented the parameter set to construct the new hybrid supernova equation of state BASQUARK. Furthermore, we investigated the possibility of multiple phase transition in cold hybrid stars: Apart from the regular HQ phase transitions we found for $c^2_{\mathrm{QM}} = 1/3$ additionally HQHQ and QHQ phase transitions and in case of $c^2_{\mathrm{QM}} = 1$ additionally HQH phase transitions. The parameter set for the new supernova equation of state is not affected by these multiple phase transitions. We extended our analysis by considering hyperons in the hadronic matter, using the BHB$\Lambda\phi$ EOS. We found that BASQUARK is not affected by hyperons. Finally, we investigated the limiting case of $c^2_{\mathrm{QM}} = 1$ for quark matter. We found that a speed of sound $c^2_{\mathrm{QM}} > 1/3$ increases the number of possibilities for new hybrid supernova equations of state significantly. In addition, our results show that using the BHB$\Lambda\phi$ EOS in future hybrid supernova equations of state represents a valid option.

On the basis of the example case obtained during the systematic analysis of the cold hybrid stars, we constructed the new hybrid supernova equation of state BASQUARK. A first analysis with the spherical core-collapse supernova code AGILE-BOLTZTRAN with a 15 $M_\odot$ progenitor showed an explosion, triggered by the QCD core-collapse supernova mechanism. Hence, BASQUARK represents the first hybrid supernova

equation of state that fulfills the 2 $M_\odot$ neutron star mass constraint and is able to trigger an explosion in spherical symmetry.

The second part of this thesis was dedicated to the analysis of BASQUARK in three-dimensional core-collapse supernova simulations using the code ELEPHANT. We developed a new method called the *spherical restart method* which allows us to restart ELEPHANT from a spherical profile produced in a standard AGILE-IDSA simulation. With this method we can test our code at several hundreds of milliseconds post-bounce without using a vast amount of computational resources. The spherically averaged profiles of such a restarted run are able to imitate profiles obtained in a full simulation well. The results are even better if a spherical restart is performed from a profile produced by the background AGILE-IDSA of ELEPHANT, normally used to treat the boundary conditions of the 3D domain. In contrast to the standard AGILE-IDSA, the background AGILE-IDSA contains the spherically averaged 3D data of ELEPHANT up to bounce. The spherical restart from such a background AGILE-IDSA profile produces almost identical spherically-averaged profiles as obtained in full ab-initio simulations. In the future, this exceptionally good agreement of the profiles will allow us to do detailed resolution studies.

Finally, we tested BASQUARK in ELEPHANT using a 15 $M_\odot$ and a 40 $M_\odot$ progenitor. Our ab-initio simulations with a resolution of 2 km ultimately showed explosions due to heavy oscillations of the protoneutron star. We concluded that this behavior probably is due to the low resolution and not robust, hence. Nevertheless, we found indications that the 15 $M_\odot$ progenitor probably underlies the delayed neutrino-driven mechanism while the 40 $M_\odot$ progenitor showed indications of a second collapse of the star.

As a consequence, we used our spherical restart method to investigate the suspected collapse of the protoneutron star in the 40 $M_\odot$ run. Using a 2 km resolution, we found a collapse but the resolution was too coarse to resolve the steep gradients in the profiles properly. As a result the reconfigured protoneutron star was unstable. With 1 km resolution, we were able to correctly simulate a collapse of the protoneutron star with a subsequent explosion using the spherical restart method. The best results using the spherical restart method where obtained with a resolution of 500 m. This additionally allowed the convection to develop properly. This confirms the need for sufficient resolution to simulate this scenario in three dimensions.

The results presented in this work represent a first step towards new investigations of quark matter in core-collapse supernova simulations:

- BASQUARK represents the first new hybrid supernova equation of state that is in good agreement with experimental and observational constraints. On the basis of the results of this work we are able to additionally calculate variations of it; e.g. using different phase-transition parameter configurations;

alternatively including hyperons with BHB$\Lambda\phi$; or considering $c^2_{\mathrm{QM}} > 1/3$. We need to further investigate BASQUARK itself: A detailed analysis of its thermodynamical properties needs to be performed to complete the analysis of our core-collapse supernova simulation done with AGILE-BOLTZTRAN. In addition, a systematic progenitor scan would be of great interest and might provide additional information on the progenitor dependence of the QCD core-collapse supernova mechanism.

- The simulations of ELEPHANT with BASQUARK are the first simulations of its kind that consider quark matter in a 3D core-collapse supernova simulation. Our results are still very preliminary, but give some clear indications on what to focus in the future: The need for runs with higher resolution is indisputable, as our results using the spherical restart method showed. We need to run full simulations with at least 1 km (better 500 m) resolution to be able to provide a detailed analysis. The influence of rotation and magnetic fields has to be investigated systematically running several simulations with different combinations of these two parameters, essentially on/off configurations. On the other hand, it might be interesting to use our spherical restart method to execute high-resolution simulations of the collapse of the protoneutron star. This might give some more information on convergence of the code when resolving the collapse and subsequent explosion.
- Moreover, we have to investigate in more detail the possible influence of included neutrino-quark rates in the simulations. Besides this, the investigation of the IDSA treatment in the context of hybrid core-collapse supernova simulations is missing so far.

In the end, we can only validate our results using experimental and observational data. The most important information would come from the observation of a new core-collapse supernova in, or close-by, our galaxy. Today, it would be possible to measure its signal using a multi-messenger approach determining quantities such as the neutrino signal, the electro-magnetic signals, and eventually its gravitational-wave signal. The combined information of such measurements would provide crucial information on the core-collapse supernova mechanism and the underlying equation of state. Ultimately, this would allow us to draw detailed conclusions about the possible appearance of quark matter and its influence on the explosion dynamics in core-collapse supernovae.

Oliver Philipp Heinimann

Curriculum Vitae

Personal Data

Date of birth: 24/09/1989
Hometown: Zunzgen
Nationality: Swiss

Academic Education

04/2014 – 03/2017 **Ph.D. in Theoretical Physics**, *University of Basel*.
Thesis title: *Hadron-Quark Phase Transitions in Hybrid Stars and Core-Collapse Supernovae*
Grade: *summa cum laude*
Part of the Computational Toolbox Ph.D. program

09/2012 – 03/2014 **Master of Science in Physics**, *University of Basel*.
Specialized in theoretical physics
Thesis title: *Hybrid Stars: Exploring the Limits*
Overall average grade: 6 / 6

09/2009 – 08/2012 **Bachelor of Science in Physics**, *University of Basel*.
Overall average grade: 5.5 / 6

01/2009 – 07/2009 Kingscliff, Australia (6 months stay as a full-time competitive swimmer)

09/2005 – 12/2008 **Matura / A-levels**, *Gymnasium Liestal*.
Major module: applied mathematics and physics
Average grades in final school report: 5.4 / 6, honoured as a top five student

Schools, Workshops, and Conferences

10/2016 **Annual Meeting**, *SSAA*, Davos.
Invited talk at the annual meeting of the Swiss Society for Astrophysics and Astronomy.

06/2016 **Workshop**, *MRACCS Workshop*, NAOJ, Tokio.
Workshop title : Many Riddles About Core-Collapse Supernovae, 1 Bethe and Beyond.
Talk with title: The hadron-quark phase transition in core-collapse supernovae: Working towards a new hybrid supernova equation of state.

04/2016 **Conference**, *Annual New Compstar Conference*, Istanbul.
Talk with title: Hadron-quark phase transition in hybrid stars and first insights for generating a new supernova equation of state. Distinction for top Ph.D. talk.

07/2015 **Workshop**, *OpenACC Eurohack*, Lugano.
GPU parallelization of IDSA-Code to be compatible with Piz Daint at CSCS.

05/2015 **Workshop**, *MICRA Workshop*, Stockholm.
Workshop on Microphysics In Computational Relativistic Astrophysics. Talk with title: Hadron-quark phase transitions in hybrid stars and first insights for generating a new supernova equation of state.

04/2015 **Tutorial**, *Scientific Data Visualization Tutorial*, CSCS, Lugano.
Introduction to 3D data visualization with Python, Paraview, and Visit.

12/2014 **Workshop**, *NEOS 2014*, Frankfurt.
Workshop title: Nuclear Equation of State for Compact Stars and Supernovae. Provided talk with the title: Hadron-Quark Phase Transition in Hybrid Stars.

09/2014 **Ph.D. School**, *New CompStar School*, Barcelona.
School title: The many faces of compact stars. Compact objects in different astrophysical scenarios. For this purpose, a large list of topics were addressed by renowned international experts: accretion theory, binaries, neutron stars thermal emission, equations of state, microquasar jets, neutron star cooling, radio-pulsars, magnetospheres, compact stars as gravitational wave sources, GRBs, Supernovae and their environments, etc.

06/2014 **Ph.D. School**, *CSCS-USI Summer School*, Serpiano/Lugano.
Summer school focused on parallel programming with MPI, OpenMP, CUDA, and OpenACC.

Teaching Assistant

Fall term 2016	Astrophysical Plasmas
Spring term 2016	Electrodynamics
Fall term 2015	Theoretical Mechanics
Spring term 2015	Electrodynamics
Fall term 2014	General Relativity

Computer Skills

Programming	FORTRAN 90, BASH, Python, OpenMP, MPI, OpenACC
Packages	Matlab, Maple, Mathematica, LaTeX
Visualization	YT, Paraview (basic)
Operating Systems	Linux, Windows
Office	Word, Power Point, Excel, Access
2015-2017	User of Cray XC30/XC50 ("Piz Daint") at CSCS, Lugano. Performed extensive parallel magneto-hydrodynamical simulations.

Publications

O. Heinimann, M. Hempel, and F.-K. Thielemann. Towards generating a new supernova equation of state: A systematic analysis of cold hybrid stars. *Phys. Rev. D*, Nov. 2016

M. Hempel, O. Heinimann, A. Yudin, I. Iosilevskiy, M. Liebendörfer, and F.-K. Thielemann. Hot third family of compact stars and the possibility of core-collapse supernova explosions. *Phys. Rev. D*, Nov. 2016

O. Heinimann, M. Hempel, and F.-K. Thielemann. A systematic analysis of hybrid stars using a hadronic equation of state suitable for core-collapse supernovae. *J. Phys. Soc. Conf. Proc.*, 2017

M. Hempel, O. Heinimann, A. Yudin, I. Iosilevskiy, M. Liebendörfer, and F.-K. Thielemann. New aspects of the QCD phase transition in proto-neutron stars and core-collapse supernovae. *J. Phys. Conf. Ser.*, 2017

Languages

German **Writing and speaking: native speaker**

English **Writing and speaking: fluent**

French **Writing and speaking: good**

References

Prof. Dr. F.-K. Thielemann

Prof. Dr. M. Liebendörfer

PD Dr. M. Hempel

More information available on request.

Bibliography

[1] E. B. Abdikamalov, C. D. Ott, L. Rezzolla, et al. „Axisymmetric general relativistic simulations of the accretion-induced collapse of white dwarfs“. In: *Phys. Rev. D* 81.4, 044012 (Feb. 2010), p. 044012.

[2] S. Akiyama, J. C. Wheeler, D. L. Meier, and I. Lichtenstadt. „The Magnetorotational Instability in Core-Collapse Supernova Explosions“. In: *Astrophys. J.* 584 (Feb. 2003), pp. 954–970.

[3] M. Alford and S. Reddy. „Compact stars with color superconducting quark matter“. In: *Phys. Rev. D* 67.7, 074024 (Apr. 2003), p. 074024.

[4] M. Alford, M. Braby, M. Paris, and S. Reddy. „Hybrid Stars that Masquerade as Neutron Stars“. In: *Astrophys. J.* 629 (Aug. 2005), pp. 969–978.

[5] M. G. Alford and S. Han. „Characteristics of hybrid compact stars with a sharp hadron-quark interface“. In: *Eur. Phys. J. A* 52, 62 (Mar. 2016), p. 62.

[6] M. G. Alford, G. F. Burgio, S. Han, G. Taranto, and D. Zappalà. „Constraining and applying a generic high-density equation of state“. In: 92.8, 083002 (2015), p. 083002.

[7] Mark G. Alford, Sophia Han, and Madappa Prakash. „Generic conditions for stable hybrid stars“. In: *Phys. Rev. D* 88 (8 Oct. 2013), p. 083013.

[8] D. Alvarez-Castillo, S. Benic, D. Blaschke, S. Han, and S. Typel. „Neutron star mass limit at 2 $M_\odot$ supports the existence of a CEP“. In: *Eur. Phys. J. A* 52, 232 (Aug. 2016), p. 232.

[9] C. Amsler, M. Doser, M. Antonelli, et al. „Review of Particle Physics“. In: *Phys. Lett. B* 667 (Sept. 2008), pp. 1–6.

[10] I. Angeli and K. P. Marinova. „Table of experimental nuclear ground state charge radii: An update“. In: *Atomic Data and Nuclear Data Tables* 99 (Jan. 2013), pp. 69–95.

[11] J. Antoniadis, P. C. C. Freire, N. Wex, et al. „A Massive Pulsar in a Compact Relativistic Binary“. In: *Science* 340 (Apr. 2013), p. 448.

[12] W. D. Arnett. „Neutrino escape, nuclear dissociation, and core collapse and/or explosion“. In: *Astrophys. J. Lett.* 263 (Dec. 1982), pp. L55–L57.

[13] G. Audi, A. H. Wapstra, and C. Thibault. „The AME2003 atomic mass evaluation . (II). Tables, graphs and references“. In: *Nucl. Phys. A* 729 (Dec. 2003), pp. 337–676.

[14] G. Audi, W. M., W. A. H., et al. „The Ame2012 atomic mass evaluation“. In: *Chin. Phys. C* 36 (Dec. 2012), p. 002.

[15]W. Baade and F. Zwicky. „Cosmic Rays from Super-novae“. In: *Proceedings of the National Academy of Science* 20 (May 1934), pp. 259–263.

[16]W. Baade and F. Zwicky. „On Super-novae“. In: *Proceedings of the National Academy of Science* 20 (May 1934), pp. 254–259.

[17]S. A. Balbus and J. F. Hawley. „Instability, turbulence, and enhanced transport in accretion disks“. In: *Rev. Mod. Phys.* 70 (Jan. 1998), pp. 1–53.

[18]S. Banik, M. Hempel, and D. Bandyopadhyay. „New Hyperon Equations of State for Supernovae and Neutron Stars in Density-dependent Hadron Field Theory“. In: *Astrophys. J. Suppl.* 214, 22 (Oct. 2014), p. 22.

[19]E. Baron and J. Cooperstein. „The effect of iron core structure on supernovae“. In: *Astrophys. J.* 353 (Apr. 1990), pp. 597–611.

[20]S. Benić, D. Blaschke, D. E. Alvarez-Castillo, T. Fischer, and S. Typel. „A new quark-hadron hybrid equation of state for astrophysics. I. High-mass twin compact stars“. In: *Astron. Astrophys.* 577, A40 (May 2015), A40.

[21]Sanjin Benić. „Heavy hybrid stars from multi-quark interactions“. English. In: *Eur. Phys. J. A* 50.7, 111 (2014).

[22]H. Berninger, E. Frenod, M. Gander, M. Liebendorfer, and J. Michaud. „Derivation of the Isotropic Diffusion Source Approximation (IDSA) for Supernova Neutrino Transport by Asymptotic Expansions“. In: *SIAM Journal on Mathematical Analysis* 45 (Dec. 2013), pp. 3229–3265.

[23]H. A. Bethe. „Supernova mechanisms“. In: *Rev. Mod. Phys.* 62 (Oct. 1990), pp. 801–866.

[24]H. A. Bethe and J. R. Wilson. „Revival of a stalled supernova shock by neutrino heating“. In: *Astrophys. J.* 295 (Aug. 1985), pp. 14–23.

[25]G. S. Bisnovatyi-Kogan, I. P. Popov, and A. A. Samokhin. „The magnetohydrodynamic rotational model of supernova explosion“. In: *Astro. Phys. Sp. Sci.* 41 (June 1976), pp. 287–320.

[26]D. Blaschke and D. E. Alvarez-Castillo. „High-mass twins resolution of the recon-finement, masquerade and hyperon puzzles of compact star interiors“. In: *American Institute of Physics Conference Series* 1701, 020013 (Jan. 2016), p. 020013.

[27]D. Blaschke, D. E. Alvarez-Castillo, and S. Benic. „Mass-radius constraints for compact stars and a critical endpoint“. In: *ArXiv e-prints* (Oct. 2013).

[28]A. R. Bodmer. „Collapsed Nuclei“. In: *Phys. Rev. D* 4 (Sept. 1971), pp. 1601–1606.

[29]S. W. Bruenn. „Stellar core collapse - Numerical model and infall epoch“. In: *Astrophys. J. Suppl.* 58 (Aug. 1985), pp. 771–841.

[30]S. W. Bruenn, K. R. De Nisco, and A. Mezzacappa. „General Relativistic Effects in the Core Collapse Supernova Mechanism“. In: *Astrophys. J.* 560 (Oct. 2001), pp. 326–338.

[31]R. Buras, H.-T. Janka, M. Rampp, and K. Kifonidis. „Two-dimensional hydrodynamic core-collapse supernova simulations with spectral neutrino transport. II. Models for different progenitor stars“. In: *Astron. Astrophys.* 457 (Oct. 2006), pp. 281–308.

[32]G. F. Burgio and D. Zappalà. „Hybrid star structure with the Field Correlator Method“. In: *Eur. Phys. J. A* 52, 60 (Mar. 2016), p. 60.

[33]A. Burrows. „Supernova explosions in the Universe“. In: *Nature* 403 (Feb. 2000), pp. 727–733.

[34]A. Burrows. „Supernova neutrinos“. In: *Astrophys. J.* 334 (Nov. 1988), pp. 891–908.

[35]A. Burrows, E. Livne, L. Dessart, C. D. Ott, and J. Murphy. „A New Mechanism for Core-Collapse Supernova Explosions“. In: *Astrophys. J.* 640 (Apr. 2006), pp. 878–890.

[36]A. Burrows, E. Livne, L. Dessart, C. D. Ott, and J. Murphy. „Features of the Acoustic Mechanism of Core-Collapse Supernova Explosions“. In: *Astrophys. J.* 655 (Jan. 2007), pp. 416–433.

[37]A. Burrows, J. Hayes, and B. A. Fryxell. „On the Nature of Core-Collapse Supernova Explosions“. In: *Astrophys. J.* 450 (Sept. 1995), p. 830.

[38]A. Burrows, L. Dessart, E. Livne, C. D. Ott, and J. Murphy. „Simulations of Magnetically Driven Supernova and Hypernova Explosions in the Context of Rapid Rotation“. In: *Astrophys. J.* 664 (July 2007), pp. 416–434.

[39]R. M. Cabezon, D. Garcia-Senz, and J. Figueira. „Recent advances in the smoothed-particle hydrodynamics technique: Building the code SPHYNX“. In: *ArXiv e-prints* (July 2016).

[40]E. Cappellaro and M. Turatto. „Supernova Types and Rates“. In: *The Influence of Binaries on Stellar Population Studies*. Ed. by D. Vanbeveren. Vol. 264. Astrophysics and Space Science Library. 2001, p. 199.

[41]N. Chamel and P. Haensel. „Physics of Neutron Star Crusts“. In: *Living Reviews in Relativity* 11, 10 (Dec. 2008), p. 10.

[42]N. Chamel, A. F. Fantina, J. M. Pearson, and S. Goriely. „Phase transitions in dense matter and the maximum mass of neutron stars“. In: *Astron. Astrophys.* 553, A22 (May 2013), A22.

[43]S. Chandrasekhar. „An Integral Theorem on the Equilibrium of a Star“. In: *Astrophys. J.* 87 (June 1938), p. 535.

[44]Barbara Chapman, Gabriele Jost, and Ruud van der Pas. *Using OpenMP: Portable Shared Memory Parallel Programming (Scientific and Engineering Computation)*. The MIT Press, 2007.

[45]D. Chatterjee and I. Vidaña. „Do hyperons exist in the interior of neutron stars?“ In: *Eur. Phys. J. A* 52, 29 (Feb. 2016), p. 29.

[46]A. Chodos, R. L. Jaffe, K. Johnson, C. B. Thorn, and V. F. Weisskopf. „New extended model of hadrons“. In: *Phys. Rev. D* 9 (June 1974), pp. 3471–3495.

[47]S. A. Colgate. „Hot bubbles drive explosions“. In: *Nature* 341 (Oct. 1989), pp. 489–490.

[48]S. A. Colgate and R. H. White. „The Hydrodynamic Behavior of Supernovae Explosions“. In: *Astrophys. J.* 143 (Mar. 1966), p. 626.

[49]S. M. Couch and E. P. O'Connor. „High-resolution Three-dimensional Simulations of Core-collapse Supernovae in Multiple Progenitors“. In: *Astrophys. J.* 785, 123 (Apr. 2014), p. 123.

[50]S. M. Couch and C. D. Ott. „Revival of the Stalled Core-collapse Supernova Shock Triggered by Precollapse Asphericity in the Progenitor Star“. In: *Astrophys. J. Lett.* 778, L7 (Nov. 2013), p. L7.

[51]R. Courant, K. Friedrichs, and H. Lewy. „Über die partiellen Differenzengleichungen der mathematischen Physik“. In: *Math. Ann.* 100 (1928), pp. 32–74.

[52]Leonardo Dagum and Ramesh Menon. „OpenMP: An Industry-Standard API for Shared-Memory Programming“. In: *IEEE Comput. Sci. Eng.* 5.1 (Jan. 1998), pp. 46–55.

[53]P. Danielewicz and J. Lee. „Symmetry energy I: Semi-infinite matter“. In: *Nucl. Phys. A* 818 (Feb. 2009), pp. 36–96.

[54]B. Dasgupta, T. Fischer, S. Horiuchi, et al. „Detecting the QCD phase transition in the next Galactic supernova neutrino burst“. In: *Phys. Rev. D* 81.10, 103005 (May 2010), p. 103005.

[55]T. Degrand, R. L. Jaffe, K. Johnson, and J. Kiskis. „Masses and other parameters of the light hadrons“. In: *Phys. Rev. D* 12 (Oct. 1975), pp. 2060–2076.

[56]P. B. Demorest, T. Pennucci, S. M. Ransom, M. S. E. Roberts, and J. W. T. Hessels. „A two-solar-mass neutron star measured using Shapiro delay“. In: *Nature* 467 (Oct. 2010), pp. 1081–1083.

[57]L. Dessart, A. Burrows, C. D. Ott, et al. „Multidimensional Simulations of the Accretion-induced Collapse of White Dwarfs to Neutron Stars“. In: *Astrophys. J.* 644 (June 2006), pp. 1063–1084.

[58]C. E. Detar and J. F. Donoghue. „Bag Models of Hadrons“. In: *Annual Review of Nuclear and Particle Science* 33 (1983), pp. 235–264.

[59]P.L. DeVries and J.E. Hasbun. *A First Course in Computational Physics*. Jones & Bartlett Learning, 2011.

[60]A. Drago and U. Tambini. „Finite temperature quark matter and supernova explosion“. In: *J. Phys. G Nucl. Phys.* 25 (May 1999), pp. 971–979.

[61]R. C. Duncan and C. Thompson. „Formation of very strongly magnetized neutron stars - Implications for gamma-ray bursts“. In: *Astrophys. J. Lett.* 392 (June 1992), pp. L9–L13.

[62]C. R. Evans and J. F. Hawley. „Simulation of magnetohydrodynamic flows - A constrained transport method“. In: *Astrophys. J.* 332 (Sept. 1988), pp. 659–677.

[63]E. Farhi and R. L. Jaffe. „Strange matter“. In: *Phys. Rev. D* 30 (Dec. 1984), pp. 2379–2390.

[64]A. V. Filippenko. „Optical Spectra of Supernovae“. In: *Ann. Rev. Astron. Astrophys.* 35 (1997), pp. 309–355.

[65]T. Fischer, I. Sagert, G. Pagliara, et al. „Core-collapse Supernova Explosions Triggered by a Quark-Hadron Phase Transition During the Early Post-bounce Phase“. In: *Astrophys. J. Suppl.* 194, 39 (June 2011), p. 39.

[66]T. Fischer, D. Blaschke, M. Hempel, et al. „Core collapse supernovae in the QCD phase diagram“. In: *Physics of Atomic Nuclei* 75 (May 2012), pp. 613–620.

[67]T. Fischer, T. Klähn, I. Sagert, M. Hempel, and D. Blaschke. „Quark Matter in Core Collapse Supernova Simulations“. In: *Acta Phys. Polon. Supp.* 7.1 (2014), pp. 153–161.

[68]T. Fischer, I. Sagert, M. Hempel, et al. „Signals of the QCD phase transition in core collapse supernovae – microphysical input and implications on the supernova dynamics“. In: *Classical Quant. Grav.* 27.11 (June 2010), p. 114102.

[69]Tobias Fischer, Matthias Hempel, Irina Sagert, Yudai Suwa, and Jürgen Schaffner-Bielich. „Symmetry energy impact in simulations of core-collapse supernovae“. English. In: *Eur. Phys. J. A* 50.2, 46 (2014).

[70]E. Fonseca, T. T. Pennucci, J. A. Ellis, et al. „The NANOGrav Nine-year Data Set: Mass and Geometric Measurements of Binary Millisecond Pulsars“. In: *ArXiv e-prints* (Mar. 2016).

[71]Message P Forum. *MPI: A Message-Passing Interface Standard*. Tech. rep. Knoxville, TN, USA, 1994.

[72]B. Freedman and L. McLerran. „Quark star phenomenology“. In: *Phys. Rev. D* 17 (Feb. 1978), pp. 1109–1122.

[73]C. L. Fryer. „Neutron Star Kicks from Asymmetric Collapse“. In: *Astrophys. J. Lett.* 601 (Feb. 2004), pp. L175–L178.

[74]C. L. Fryer and M. S. Warren. „Modeling Core-Collapse Supernovae in Three Dimensions“. In: *Astrophys. J. Lett.* 574 (July 2002), pp. L65–L68.

[75]S. Gandolfi, A. Gezerlis, and J. Carlson. „Neutron Matter from Low to High Density“. In: *Ann. Rev. Nuc. Part. Sci.* 65 (Oct. 2015), pp. 303–328.

[76]N. A. Gentile, M. B. Aufderheide, G. J. Mathews, F. D. Swesty, and G. M. Fuller. „The QCD phase transition and supernova core collapse“. In: *Astrophys. J.* 414 (Sept. 1993), pp. 701–711.

[77]Ulrich H. Gerlach. „Equation of State at Supranuclear Densities and the Existence of a Third Family of Superdense Stars“. In: *Phys. Rev.* 172.5 (1968), pp. 1325–1330.

[78]N. Glendenning. *Compact Stars. Nuclear Physics, Particle Physics and General Relativity.* 1996, p. 90.

[79]P. Goldreich and S. V. Weber. „Homologously collapsing stellar cores“. In: *Astrophys. J.* 238 (June 1980), pp. 991–997.

[80]W. Gropp, E. Lusk, and A. Skjellum. *Using MPI: Portable Programming with the Message-Passing Interface*. 1999.

[81]P. Haensel, J. L. Zdunik, M. Bejger, and J. M. Lattimer. „Keplerian frequency of uniformly rotating neutron stars and strange stars“. In: 502 (Aug. 2009), pp. 605–610.

[82]M. Hamuy. „Observed and Physical Properties of Core-Collapse Supernovae“. In: *Astrophys. J.* 582 (Jan. 2003), pp. 905–914.

[83]C. Hartnack, H. Oeschler, and J. Aichelin. „Hadronic Matter Is Soft“. In: *Phys. Rev. Lett.* 96.1, 012302 (Jan. 2006), p. 012302.

[84]A. Heger, C. L. Fryer, S. E. Woosley, N. Langer, and D. H. Hartmann. „How Massive Single Stars End Their Life“. In: *Astrophys. J.* 591 (July 2003), pp. 288–300.

[85]A. Heger, S. E. Woosley, and H. C. Spruit. „Presupernova Evolution of Differentially Rotating Massive Stars Including Magnetic Fields“. In: *Astrophys. J.* 626 (June 2005), pp. 350–363.

[86]O. Heinimann. „Hybrid Stars - Exploring the Limits“. MA thesis. University of Basel, 2014.

[87]O. Heinimann, M. Hempel, and F.-K. Thielemann. „Towards generating a new supernova equation of state: A systematic analysis of cold hybrid stars“. In: *Phys. Rev. D* 94.10, 103008 (Nov. 2016), p. 103008.

[88]C. O. Heinke and W. C. G. Ho. „Direct Observation of the Cooling of the Cassiopeia A Neutron Star“. In: *Astrophys. J. Lett.* 719 (Aug. 2010), pp. L167–L171.

[89]M. Hempel. „Nucleon self-energies for supernova equations of state“. In: *Phys. Rev. C* 91.5, 055807 (May 2015), p. 055807.

[90]M. Hempel and J. Schaffner-Bielich. „A statistical model for a complete supernova equation of state“. In: *Nucl. Phys. A* 837 (June 2010), pp. 210–254.

[91]M. Hempel, G. Pagliara, and J. Schaffner-Bielich. „Conditions for phase equilibrium in supernovae, protoneutron, and neutron stars“. In: *Phys. Rev. D* 80.12, 125014 (Dec. 2009), p. 125014.

[92]M. Hempel, K. Hagel, J. Natowitz, G. Röpke, and S. Typel. „Constraining supernova equations of state with equilibrium constants from heavy-ion collisions“. In: *Phys. Rev. C* 91 (4 2015), p. 045805.

[93]M. Hempel, O. Heinimann, A. Yudin, et al. „Hot third family of compact stars and the possibility of core-collapse supernova explosions“. In: *Phys. Rev. D* 94.10, 103001 (Nov. 2016), p. 103001.

[94]M. Hempel, T. Fischer, J. Schaffner-Bielich, and M. Liebendörfer. „New Equations of State in Simulations of Core-collapse Supernovae“. In: *Astrophys. J.* 748, 70 (Mar. 2012), p. 70.

[95]M. Hempel, O. Heinimann, A. Yudin, et al. „The phase diagram of QCD, third families of proto-compact stars, and the possibility of core-collapse supernova explosions“. In: *ArXiv e-prints* (Nov. 2015).

[96]Matthias Hempel and Jürgen Schaffner-Bielich. „A statistical model for a complete supernova equation of state“. In: *Nuclear Physics A* 837.3–4 (2010), pp. 210 –254.

[97]M. Herant, W. Benz, W. R. Hix, C. L. Fryer, and S. A. Colgate. „Inside the supernova: A powerful convective engine“. In: *Astrophys. J.* 435 (Nov. 1994), pp. 339–361.

[98]A. Hewish, S. J. Bell, J. D. H. Pilkington, P. F. Scott, and R. A. Collins. „Observation of a Rapidly Pulsating Radio Source“. In: *Nature* 217 (Feb. 1968), pp. 709–713.

[99]W. Hillebrandt. „An exploding 10 solar mass star - A model for the Crab supernova“. In: *Astron. Astrophys.* 110 (June 1982), pp. L3–L6.

[100]K. Hirata, T. Kajita, M. Koshiba, M. Nakahata, and Y. Oyama. „Observation of a neutrino burst from the supernova SN1987A“. In: *Phys. Rev. Lett.* 58 (Apr. 1987), pp. 1490–1493.

[101]K. S. Hirata, T. Kajita, M. Koshiba, et al. „Observation in the Kamiokande-II detector of the neutrino burst from supernova SN1987A“. In: *Phys. Rev. D* 38 (July 1988), pp. 448–458.

[102]C. Iliadis. *Nuclear Physics of Stars*. Wiley-VCH Verlag, 2007.

[103]N. Itoh. „Hydrostatic Equilibrium of Hypothetical Quark Stars“. In: *Prog. Theor. Phys.* 44 (July 1970), pp. 291–292.

[104]N. Itoh, H. Hayashi, A. Nishikawa, and Y. Kohyama. „Neutrino Energy Loss in Stellar Interiors. VII. Pair, Photo-, Plasma, Bremsstrahlung, and Recombination Neutrino Processes“. In: *Astrophys. J. Suppl.* 102 (Feb. 1996), p. 411.

[105]W. Iwakami, K. Kotake, N. Ohnishi, S. Yamada, and K. Sawada. „Three-Dimensional Simulations of Standing Accretion Shock Instability in Core-Collapse Supernovae“. In: *Astrophys. J.* 678, 1207-1222 (May 2008), pp. 1207–1222.

[106]J.D. Jackson, K. Müller, C. Witte, and M. Diestelhorst. *Klassische Elektrodynamik*. De Gruyter Studium. De Gruyter, 2014.

[107]H.-T. Janka. „Explosion Mechanisms of Core-Collapse Supernovae“. In: *Ann. Rev. Nuc. Part. Sci.* 62 (Nov. 2012), pp. 407–451.

[108]H.-T. Janka and E. Mueller. „Neutrino heating, convection, and the mechanism of Type-II supernova explosions.“ In: *Astron. Astrophys.* 306 (Feb. 1996), p. 167.

[109]H.-T. Janka, T. Melson, and A. Summa. „Physics of Core-Collapse Supernovae in Three Dimensions: A Sneak Preview“. In: *Annual Review of Nuclear and Particle Science* 66 (Oct. 2016), pp. 341–375.

[110]H.-T. Janka, K. Langanke, A. Marek, G. Martínez-Pinedo, and B. Müller. „Theory of core-collapse supernovae“. In: *Physics Reports* 442 (Apr. 2007), pp. 38–74.

[111]D. L. Kaplan, V. B. Bhalerao, M. H. van Kerkwijk, et al. „A Metal-rich Low-gravity Companion to a Massive Millisecond Pulsar“. In: *Astrophys. J.* 765, 158 (Mar. 2013), p. 158.

[112]R. Käppeli. „Numerical methods for 3D magneto-rotational core-collapse supernova simulation with jet formation“. PhD thesis. University of Basel, 2013.

[113]R. Käppeli, S. C. Whitehouse, S. Scheidegger, U.-L. Pen, and M. Liebendörfer. „FISH: A Three-dimensional Parallel Magnetohydrodynamics Code for Astrophysical Applications“. In: *Astrophys. J. Suppl.* 195, 20 (Aug. 2011), p. 20.

[114]F. S. Kitaura, H.-T. Janka, and W. Hillebrandt. „Explosions of O-Ne-Mg cores, the Crab supernova, and subluminous type II-P supernovae“. In: *Astron. Astrophys.* 450 (2006), pp. 345–350.

[115]T. Klähn and T. Fischer. „Vector Interaction Enhanced Bag Model for Astrophysical Applications“. In: *Astrophys. J.* 810, 134 (Sept. 2015), p. 134.

[116]T. Klähn, T. Fischer, and M. Hempel. „Simultaneous chiral symmetry restoration and deconfinement - Consequences for the QCD phase diagram“. In: *ArXiv e-prints* (Mar. 2016).

[117]K. Kotake, K. Sato, and K. Takahashi. „Explosion mechanism, neutrino burst and gravitational wave in core-collapse supernovae“. In: *Reports on Progress in Physics* 69 (Apr. 2006), pp. 971–1143.

[118]R.M. Kulsrud. *Plasma Physics for Astrophysics*. Princeton series in astrophysics. Princeton University Press, 2005.

[119]A. Kurkela and A. Vuorinen. „Cool quark matter“. In: *ArXiv e-prints* (Mar. 2016).

[120]A. Kurkela, P. Romatschke, and A. Vuorinen. „Cold quark matter“. In: *Phys. Rev. D* 81.10, 105021 (May 2010), p. 105021.

[121]T. Kuroda, K. Kotake, and T. Takiwaki. „A New Gravitational-wave Signature from Standing Accretion Shock Instability in Supernovae“. In: *Astrophys. J. Lett.* 829, L14 (Sept. 2016), p. L14.

[122]G. A. Lalazissis, S. Raman, and P. Ring. „Ground-State Properties of Even-Even Nuclei in the Relativistic Mean-Field Theory“. In: *Atomic Data and Nuclear Data Tables* 71 (1999), p. 1.

[123]R. Lastowiecki, D. Blaschke, H. Grigorian, and S. Typel. „Strangeness in the cores of neutron stars“. In: *Acta Phys. Polon. Suppl.* 5.2 (2012), p. 535.

[124]J. M. Lattimer. „The Nuclear Equation of State and Neutron Star Masses“. In: *Annual Review of Nuclear and Particle Science* 62 (Nov. 2012), pp. 485–515.

[125]J. M. Lattimer and F. Douglas Swesty. „A generalized equation of state for hot, dense matter“. In: *Nucl. Phys. A* 535 (Dec. 1991), pp. 331–376.

[126]J. M. Lattimer and Y. Lim. „Constraining the Symmetry Parameters of the Nuclear Interaction“. In: *Astrophys. J.* 771, 51 (July 2013), p. 51.

[127]B. Leibundgut. „Type Ia Supernovae“. In: *Astron. Astrophys. Rev.* 10 (2000), pp. 179–209.

[128]E. J. Lentz, S. W. Bruenn, W. R. Hix, et al. „Three-dimensional Core-collapse Supernova Simulated Using a 15 solar Mass Progenitor“. In: *Astrophys. J. Lett.* 807, L31 (July 2015), p. L31.

[129]M. Liebendörfer. „A Simple Parameterization of the Consequences of Deleptonization for Simulations of Stellar Core Collapse“. In: *Astrophys. J.* 633 (Nov. 2005), pp. 1042–1051.

[130]M. Liebendörfer, O. E. B. Messer, A. Mezzacappa, et al. „A Finite Difference Representation of Neutrino Radiation Hydrodynamics in Spherically Symmetric General Relativistic Spacetime“. In: *Astrophys. J. Suppl.* 150 (Jan. 2004), pp. 263–316.

[131]M. Liebendörfer, S. Rosswog, and F.-K. Thielemann. „An Adaptive Grid, Implicit Code for Spherically Symmetric, General Relativistic Hydrodynamics in Comoving Coordinates“. In: *Astrophys. J. Suppl.* 141 (July 2002), pp. 229–246.

[132]M. Liebendörfer, U.-L. Pen, and C. Thompson. „Efficient approximations of neutrino physics for three-dimensional simulations of stellar core collapse“. In: *International Symposium on Nuclear Astrophysics - Nuclei in the Cosmos*. 2006, p. 132.1.

[133]M. Liebendörfer, A. Mezzacappa, F.-K. Thielemann, et al. „Probing the gravitational well: No supernova explosion in spherical symmetry with general relativistic Boltzmann neutrino transport“. In: *Phys. Rev. D* 63.10, 103004 (May 2001), p. 103004.

[134]M. Liebendörfer, M. Rampp, H.-T. Janka, and A. Mezzacappa. „Supernova Simulations with Boltzmann Neutrino Transport: A Comparison of Methods“. In: *Astrophys. J.* 620 (Feb. 2005), pp. 840–860.

[135]M. Liebendörfer, S. C. Whitehouse, and T. Fischer. „The Isotropic Diffusion Source Approximation for Supernova Neutrino Transport“. In: *Astrophys. J.* 698 (June 2009), pp. 1174–1190.

[136]D. Lonardoni, A. Lovato, S. Gandolfi, and F. Pederiva. „Hyperon Puzzle: Hints from Quantum Monte Carlo Calculations“. In: *Phys. Rev. Lett.* 114.9, 092301 (Mar. 2015), p. 092301.

[137]A. Marek and H.-T. Janka. „Delayed Neutrino-Driven Supernova Explosions Aided by the Standing Accretion-Shock Instability“. In: *Astrophys. J.* 694 (Mar. 2009), pp. 664–696.

[138]A. Marek, H. Dimmelmeier, H.-T. Janka, E. Müller, and R. Buras. „Exploring the relativistic regime with Newtonian hydrodynamics: an improved effective gravitational potential for supernova simulations“. In: *Astron. Astrophys.* 445 (Jan. 2006), pp. 273–289.

[139]L. A. Marschall. *The supernova story*. 1988.

[140]K. Masuda, T. Hatsuda, and T. Takatsuka. „Hadron-quark Crossover and Massive Hybrid Stars with Strangeness“. In: *Astrophys. J.* 764, 12 (Feb. 2013), p. 12.

[141]K. Masuda, T. Hatsuda, and T. Takatsuka. „Hyperon puzzle, hadron-quark crossover and massive neutron stars“. In: *Eur. Phys. J. A* 52, 65 (Mar. 2016), p. 65.

[142]D. L. Meier, R. I. Epstein, W. D. Arnett, and D. N. Schramm. „Magnetohydrodynamic phenomena in collapsing stellar cores“. In: *Astrophys. J.* 204 (Mar. 1976), pp. 869–878.

[143]D. Mihalas and B. W. Mihalas. *Foundations of radiation hydrodynamics*. 1984.

[144]M. C. Miller. „Astrophysical Constraints on Dense Matter in Neutron Stars“. In: *ArXiv e-prints* (Nov. 2013).

[145]R. Minkowski. „Spectra of Supernovae“. In: *Pub. Astron. Soc. Pac.* 53 (Aug. 1941), p. 224.

[146]P. Möller, J. R. Nix, W. D. Myers, and W. J. Swiatecki. „Nuclear Ground-State Masses and Deformations“. In: *Atomic Data and Nuclear Data Tables* 59 (1995), p. 185.

[147]E. Müller. „Simulation of Astrophysical Fluid Flow“. In: *Saas-Fee Advanced Course 27: Computational Methods for Astrophysical Fluid Flow.* Ed. by O. Steiner and A. Gautschy. 1998, p. 343.

[148]J. W. Murphy and A. Burrows. „Criteria for Core-Collapse Supernova Explosions by the Neutrino Mechanism“. In: *Astrophys. J.* 688, 1159-1175 (Dec. 2008), pp. 1159–1175.

[149]K. Nakazato, K. Sumiyoshi, and S. Yamada. „Astrophysical implications of equation of state for hadron-quark mixed phase: Compact stars and stellar collapses“. In: *Phys. Rev. D* 77.10, 103006 (May 2008), p. 103006.

[150]K. Nakazato, K. Sumiyoshi, and S. Yamada. „Stellar core collapse with hadron-quark phase transition“. In: *Astron. Astrophys.* 558, A50 (Oct. 2013), A50.

[151]M. Obergaulinger, P. Cerdá-Durán, E. Müller, and M. A. Aloy. „Semi-global simulations of the magneto-rotational instability in core collapse supernovae“. In: *Astron. Astrophys.* 498 (Apr. 2009), pp. 241–271.

[152]E. O'Connor and C. D. Ott. „Black Hole Formation in Failing Core-Collapse Supernovae“. In: *Astrophys. J.* 730, 70 (Apr. 2011), p. 70.

[153]M. Oertel, M. Hempel, T. Klähn, and S. Typel. „Equations of state for supernovae and compact stars“. In: *Reviews of Modern Physics* 89.1, 015007 (Jan. 2017), p. 015007.

[154]*OpenACC Homepage*. Accessed Jan. 13th, 2017.

[155]J. R. Oppenheimer and G. M. Volkoff. „On Massive Neutron Cores“. In: *Phys. Rev.* 55 (Feb. 1939), pp. 374–381.

[156]T. Padmanabhan. *Theoretical Astrophysics - Volume 2, Stars and Stellar Systems*. July 2001, p. 594.

[157]G. Pagliara, M. Hempel, and J. Schaffner-Bielich. „New Possible Quark-Hadron Mixed Phase in Protoneutron Stars“. In: *Phys. Rev. Lett.* 103.17, 171102 (Oct. 2009), p. 171102.

[158]K.-C. Pan, R. Cabezon, M. Liebendörfer, et al. „Core collapse supernova in the hall of mirrors. A three-dimensional code-comparison project“. In: (in prep).

[159]K.-C. Pan, M. Liebendörfer, M. Hempel, and F.-K. Thielemann. „Two-dimensional Core-collapse Supernova Simulations with the Isotropic Diffusion Source Approximation for Neutrino Transport“. In: *Astrophys. J.* 817, 72 (Jan. 2016), p. 72.

[160]U.-L. Pen, P. Arras, and S. Wong. „A Free, Fast, Simple, and Efficient Total Variation Diminishing Magnetohydrodynamic Code“. In: *Astrophys. J. Suppl.* 149 (Dec. 2003), pp. 447–455.

[161]A. Perego. „Neutrino treatment in multidimensional astrophysical simulations: a new spectral scheme“. PhD thesis. University of Basel, 2014.

[162]A. Perego, S. Rosswog, R. M. Cabezón, et al. „Neutrino-driven winds from neutron star merger remnants“. In: *Mon. Not. R. Astron. Soc.* 443 (Oct. 2014), pp. 3134–3156.

[163]B. Peres, M. Oertel, and J. Novak. „Influence of pions and hyperons on stellar black hole formation“. In: *Phys. Rev. D* 87.4, 043006 (Feb. 2013), p. 043006.

[164]S. Perlmutter, G. Aldering, G. Goldhaber, et al. „Measurements of Ω and Λ from 42 High-Redshift Supernovae“. In: *Astrophys. J.* 517 (June 1999), pp. 565–586.

[165]J. Piekarewicz. „Do we understand the incompressibility of neutron-rich matter?“ In: *J. Phys. G Nucl. Phys.* 37.6, 064038 (June 2010), p. 064038.

[166]A. Y. Potekhin. „Atmospheres and radiating surfaces of neutron stars“. In: *Physics Uspekhi* 57, 735-770 (Aug. 2014), pp. 735–770.

[167]B. Povh, K. Rith, C. Scholz, and F. Zetsche. *Teilchen und Kerne*. 2006.

[168]W.H. Press. *Numerical Recipes 3rd Edition: The Art of Scientific Computing*. Cambridge University Press, 2007.

[169]L. Qin, K. Hagel, R. Wada, et al. „Laboratory Tests of Low Density Astrophysical Nuclear Equations of State“. In: *Phys. Rev. Lett.* 108.17, 172701 (Apr. 2012), p. 172701.

[170]D. Radice, S. M. Couch, and C. D. Ott. „Implicit large eddy simulations of anisotropic weakly compressible turbulence with application to core-collapse supernovae“. In: *Comp. Astro. and Cosm.* 2, 7 (Aug. 2015), p. 7.

[171]D. Radice, C. D. Ott, E. Abdikamalov, et al. „Neutrino-driven Convection in Core-collapse Supernovae: High-resolution Simulations“. In: *Astrophys. J.* 820, 76 (Mar. 2016), p. 76.

[172]I. F. Ranea-Sandoval, S. Han, M. G. Orsaria, et al. „Constant-sound-speed parametrization for Nambu-Jona-Lasinio models of quark matter in hybrid stars“. In: *Phys. Rev. C* 93.4, 045812 (Apr. 2016), p. 045812.

[173]R. W. Romani, A. V. Filippenko, J. M. Silverman, et al. „PSR J1311-3430: A Heavy-weight Neutron Star with a Flyweight Helium Companion“. In: *Astrophys. J. Lett.* 760, L36 (Dec. 2012), p. L36.

[174]I. Sagert, T. Fischer, M. Hempel, et al. „Signals of the QCD Phase Transition in Core-Collapse Supernovae“. In: *Phys. Rev. Lett.* 102.8, 081101 (Feb. 2009), p. 081101.

[175]I. Sagert, T. Fischer, M. Hempel, et al. „Strange matter in core-collapse supernovae“. In: *Acta Phys. Polon.* B43 (2012), pp. 741–748.

[176]L. Scheck, H.-T. Janka, T. Foglizzo, and K. Kifonidis. „Multidimensional supernova simulations with approximative neutrino transport. II. Convection and the advective-acoustic cycle in the supernova core“. In: *Astron. Astrophys.* 477 (Jan. 2008), pp. 931–952.

[177]S. Scheidegger. „Gravitational waves from 3D MHD core-collapse supernova simulations with neutrino transport“. PhD thesis. University of Basel, 2011.

[178]K. Schertler, C. Greiner, J. Schaffner-Bielich, and M. H. Thoma. „Quark phases in neutron stars and a third family of compact stars as signature for phase transitions“. In: *Nucl. Phys. A* 677 (Sept. 2000), pp. 463–490.

[179]H.-J. Schulze. „Neutron star structure with hyperons and quarks“. In: *J. Phys. Conf. Ser.* 336.1 (2011), p. 012022.

[180]Z. F. Seidov. „The Stability of a Star with a Phase Change in General Relativity Theory“. In: *Soviet Astronomy* 15 (Oct. 1971), p. 347.

[181]S. L. Shapiro and S. A. Teukolsky. *Black holes, white dwarfs, and neutron stars: The physics of compact objects*. 1983.

[182]H. Shen, H. Toki, K. Oyamatsu, and K. Sumiyoshi. „Relativistic Equation of State for Core-collapse Supernova Simulations“. In: *Astrophys. J. Suppl.* 197, 20 (Dec. 2011), p. 20.

[183]H. Shen, H. Toki, K. Oyamatsu, and K. Sumiyoshi. „Relativistic equation of state of nuclear matter for supernova and neutron star.“ In: *Nucl. Phys. A* 637 (July 1998), pp. 435–450.

[184]H. Shen, H. Toki, K. Oyamatsu, and K. Sumiyoshi. „Relativistic Equation of State of Nuclear Matter for Supernova Explosion“. In: *Prog. Theor. Phys.* 100 (Nov. 1998), pp. 1013–1031.

[185]R. R. Silbar and S. Reddy. „Neutron stars for undergraduates“. In: *Am. J. Phys.* 72 (July 2004), pp. 892–905.

[186]H. Sotani, K. Iida, K. Oyamatsu, and A. Ohnishi. „Mass and radius formulas for low-mass neutron stars“. In: *Prog. Theor. Exp. Phys.* 2014.5, 051E01 (May 2014), 051E01.

[187]A. W. Steiner, M. Prakash, and J. M. Lattimer. „Quark-hadron phase transitions in Young and old neutron stars“. In: *Phys. Lett. B* 486 (Aug. 2000), pp. 239–248.

[188]A. W. Steiner, J. M. Lattimer, and E. F. Brown. „The Equation of State from Observed Masses and Radii of Neutron Stars“. In: *Astrophys. J.* 722 (Oct. 2010), pp. 33–54.

[189]Y. Sugahara and H. Toki. „Relativistic mean-field theory for unstable nuclei with non-linear σ and ω terms“. In: *Nuclear Physics A* 579 (Oct. 1994), pp. 557–572.

[190]T. Sukhbold, T. Ertl, S. E. Woosley, J. M. Brown, and H.-T. Janka. „Core-collapse Supernovae from 9 to 120 Solar Masses Based on Neutrino-powered Explosions“. In: *Astrophys. J.* 821, 38 (Apr. 2016), p. 38.

[191]K. Sumiyoshi and S. Yamada. „Neutrino Transfer in Three Dimensions for Core-collapse Supernovae. I. Static Configurations“. In: *Astrophys. J. Suppl.* 199, 17 (Mar. 2012), p. 17.

[192]K. Sumiyoshi, S. Yamada, and H. Suzuki. „Dynamics and Neutrino Signal of Black Hole Formation in Nonrotating Failed Supernovae. I. Equation of State Dependence“. In: *Astrophys. J.* 667 (Sept. 2007), pp. 382–394.

[193]M. Takahara and K. Sato. „Collapse of the Neutron Star Induced by Phase Transitions and Neutrino Emission from Supernova 1987A“. In: *IAU Colloq. 108: Atmospheric Diagnostics of Stellar Evolution*. Ed. by K. Nomoto. Vol. 305. Lecture Notes in Physics, Berlin Springer Verlag. 1988, p. 430.

[194]M. Takahara and K. Sato. „Phase Transitions in the Newly-Born Neutron Star and Neutrino Emissionsfrom SN1987A“. In: *Prog. Theor. Phys.* 80 (Nov. 1988), pp. 861–867.

[195]M. Takahara and K. Sato. „Supernova explosions and the soft equation of state“. In: *Astrophys. J.* 335 (Dec. 1988), pp. 301–305.

[196]T. Takiwaki, K. Kotake, and K. Sato. „Special Relativistic Simulations of Magnetically Dominated Jets in Collapsing Massive Stars“. In: *Astrophys. J.* 691 (Feb. 2009), pp. 1360–1379.

[197]A. Tamii, I. Poltoratska, P. von Neumann-Cosel, et al. „Complete Electric Dipole Response and the Neutron Skin in Pb208“. In: *Phys. Rev. Lett.* 107.6, 062502 (Aug. 2011), p. 062502.

[198]The HDF Group. *Hierarchical Data Format, version 5*. /HDF5/. 1997-2016.

[199]R. C. Tolman. „Static Solutions of Einstein's Field Equations for Spheres of Fluid“. In: *Phys. Rev.* 55 (Feb. 1939), pp. 364–373.

[200]L. Trippa, G. Colò, and E. Vigezzi. „Giant dipole resonance as a quantitative constraint on the symmetry energy“. In: *Phys. Rev. C* 77.6, 061304 (June 2008), p. 061304.

[201]M. Turatto. „Classification of Supernovae“. In: *Supernovae and Gamma-Ray Bursters*. Ed. by K. Weiler. Vol. 598. Lecture Notes in Physics, Berlin Springer Verlag. 2003, pp. 21–36.

[202]S. Typel, M. Oertel, and T. Klaehn. „CompOSE - CompStar Online Supernovae Equations of State“. In: *ArXiv e-prints* (July 2013).

[203]S. Typel, M. Oertel, and T. Klähn. „CompOSE CompStar online supernova equations of state harmonising the concert of nuclear physics and astrophysics compose.obspm.fr“. In: *Physics of Particles and Nuclei* 46 (July 2015), pp. 633–664.

[204]S. Typel, G. Röpke, T. Klähn, D. Blaschke, and H. H. Wolter. „Composition and thermodynamics of nuclear matter with light clusters“. In: *Phys. Rev. C* 81 (1 2010), p. 015803.

[205]M. H. van Kerkwijk, R. P. Breton, and S. R. Kulkarni. „Evidence for a Massive Neutron Star from a Radial-velocity Study of the Companion to the Black-widow Pulsar PSR B1957+20“. In: *Astrophys. J.* 728, 95 (Feb. 2011), p. 95.

[206]B. Wehmeyer, M. Pignatari, and F.-K. Thielemann. „Galactic evolution of rapid neutron capture process abundances: the inhomogeneous approach“. In: *Mon. Not. R. Astron. Soc.* 452 (Sept. 2015), pp. 1970–1981.

[207]N. N. Weinberg and E. Quataert. „Non-linear saturation of g-modes in proto-neutron stars: quieting the acoustic engine“. In: *Mon. Not. R. Astron. Soc.* 387 (June 2008), pp. L64–L68.

[208]S. Weissenborn, I. Sagert, G. Pagliara, M. Hempel, and J. Schaffner-Bielich. „Quark Matter in Massive Compact Stars“. In: *Astrophys. J. Lett.* 740, L14 (Oct. 2011), p. L14.

[209]Edward Witten. „Cosmic separation of phases“. In: *Phys. Rev. D* 30 (2 1984), pp. 272–285.

[210]S. E. Woosley and J. S. Bloom. „The Supernova Gamma-Ray Burst Connection“. In: *Ann. Rev. Astron. Astrophys.* 44 (Sept. 2006), pp. 507–556.

[211]S. E. Woosley and A. Heger. „Nucleosynthesis and remnants in massive stars of solar metallicity“. In: *Phys. Rep.* 442 (Apr. 2007), pp. 269–283.

[212]S. E. Woosley and T. A. Weaver. „The Evolution and Explosion of Massive Stars. II. Explosive Hydrodynamics and Nucleosynthesis“. In: *Astrophys. J. Suppl.* 101 (Nov. 1995), p. 181.

[213]S. E. Woosley and T. A. Weaver. „The physics of supernova explosions“. In: *Ann. Rev. Astron. Astrophys.* 24 (1986), pp. 205–253.

[214]S. E. Woosley, A. Heger, and T. A. Weaver. „The evolution and explosion of massive stars“. In: *Reviews of Modern Physics* 74 (Nov. 2002), pp. 1015–1071.

[215]N. Yasutake, K. Kotake, M.-A. Hashimoto, and S. Yamada. „Effects of QCD phase transition on gravitational radiation from two-dimensional collapse and bounce of massive stars“. In: *Phys. Rev. D* 75.8, 084012 (Apr. 2007), p. 084012.

[216]A. Zacchi, R. Stiele, and J. Schaffner-Bielich. „Compact stars in a SU(3) quark-meson model“. In: *Phys. Rev. D* 92.4, 045022 (Aug. 2015), p. 045022.

[217]A. Zacchi, M. Hanauske, and J. Schaffner-Bielich. „Stable hybrid stars within a SU(3) quark-meson-model“. In: *Phys. Rev. D* 93.6, 065011 (Mar. 2016), p. 065011.

[218]J. L. Zdunik and P. Haensel. „Maximum mass of neutron stars and strange neutron-star cores“. In: *Astron. Astrophys.* 551, A61 (Mar. 2013), A61.

This thesis was typeset with LaTeX 2$_\varepsilon$ and the (modified) Clean Thesis template, found at `http://cleanthesis.der-ric.de/`.